The impact of supernova remnants on interstellar dust within the Large Magellanic Cloud

Maša Lakićević

A thesis submitted for the Degree of Doctor of Philosophy to the Research Institute for the Environment, Physical Sciences and Applied Mathematics, University of Keele.

June 2015

Abstract

This thesis presents the first population study of supernova remnants (SNRs) in one whole galaxy – the Large Magellanic Cloud (LMC) on submm and FIR wavelengths. The first part is about the dust production in supernovae (SNe) and SNRs, based on several observations of SN 1987A on mm and submm wavelengths that I made using the *ATCA* and *APEX* telescopes. SN 1987A is found to produce $\sim$0.7 $M_\odot$ of dust, which is 2 orders of magnitude higher than the masses found in most of other SN/SNR observations. I constrained the spectral energy distribution (SED) of SN 1987A, confirming *Herschel* data using better resolution, but did not manage to resolve the object. These data were used in the preparation of the *ALMA* observations (Kamenetzky et al. 2013; Indebetouw et al. 2014).

The second part of the thesis is the population study of all LMC SNRs using *Herschel* and *Spitzer* data, which resulted in the conclusion that SNRs are significant dust destroyers. This conclusion is based on dust mass maps of SNRs and their surroundings which have shown that there is less dust within SNRs than outside. My study shows that a SNR in the LMC removes on average 4–6 $M_\odot$. I conclude that SNRs might not be the main suppliers of dust in galaxies, and that it is possible that other sources of dust production are needed to explain the origin of the dust at high red-shifts. I estimate the mass of sputtered dust from all SNRs in LMC to be $\sim 373^{+746}_{-249}$ $M_\odot$, a dust destruction rate in the LMC of $\sim 0.037^{+0.074}_{-0.025}$ $M_\odot$ yr^{-1} due to SNRs and an average lifetime for interstellar dust in the regions close to SNRs of $\sim 2^{+4}_{-1.3} \times 10^7$ yr.

Acknowledgements

I wish to express my deep sense of gratitude to my supervisor Jacco Th. van Loon on the great help during all my PhD in the new ideas, large contribution in my work, great trust in me from the very beginning and a strong support. I am also grateful to my second supervisor, Ferdinando Patat and to European Southern Organisation, as well as to Keele University for providing me the funding for this work. I thank my collaborators Thomas Stanke, Carlos de Breuck, Lister Staveley-Smith, Giovanna Zanardo, Toby Potter, Julia Kamenetzky, Miroslav Filipović. I thank Dejan Urošević and Bojan Arbutina, who introduced me into the field of supernova remnants (SNRs) during my Master studies. My study of SNRs using *Herschel* and *Spitzer* data would not be possible without the help of the members of *HERITAGE* team, Margaret Meixner, Karl Gordon, Caroline Bot, Julia Duval, Karl Misselt, Mikako Matsuura, Remy Indebetouw, and others. Special thanks goes to Lian Bryant for careful reading of my thesis. I am grateful to all my friends and colleagues at ESO and at Keele University that were listening my ideas and problems and sharing their experiences with me. Finally, thanks to my examiners Haley Gomez and James Reeves for making my thesis more accurate and for teaching me very important things.

Maša Lakićević
M. Sci., University of Belgrade
Keele Astrophysics Group
20 February 2015

Contents

List of Figures

List of Tables

1 Introduction

1.1 Galaxies and Dust

1.1.1 Dust formation and role in galaxies

In local late-type galaxies, the interstellar medium (ISM) amounts to $\sim$ 10% of the baryonic mass. The ISM includes gas mixed with tiny solid particles – dust – with sizes ranging from a few atoms up to $\sim$ 10 μm, composed on various elements such as carbon, oxygen, silicon, magnesium, and iron and PAH[1] molecules. The mass in dust is typically 0.5 to 1% of the ISM mass (Franceschini 2000), with the remainder being in the gaseous phase. The dust mass is found to be linearly proportional to the gas metallicity and equal to 40% of the total mass in heavy elements in a present-day galaxy (Peeples et al. 2014).

A detailed account of the most important processes in the dust and gas life cycle can be found in Dwek (1998). This cycle starts by dust production in supernova remnants (SNRs), stellar winds, and dense molecular clouds, but it may continue by grain destruction by sputtering and evaporative grain-grain collisions in SNRs which then returns these elements back to the gas phase.

Dust plays an important role in both the evolution of the ISM in galaxies and the Universe as a whole. The dust grains are expelled into the surroundings by SNRs and stellar winds and mixed with the local ISM. Stars eject about 40% of their initial mass into the ISM and thus enrich the surroundings with new chemical species and fresh dust grains. The dust particles absorb the light from various sources and convert it to IR radiation, blocking optical light since their size is similar to these wavelengths. In star formation dust acts as a catalyst for the formation of H_2 molecules, which are

[1]Polycyclic aromatic hydrocarbon (PAH), also polyaromatic hydrocarbon, is a compound containing only carbon and hydrogen, composed of multiple aromatic rings. A PAH contains $\sim$50 C-atoms. PAHs are very easily formed in hot (T$\sim$2000 K) carbon and hydrogen rich gases. Interstellar PAHs are observed at mid-IR (MIR) wavelengths.

efficient coolants, giving dense clouds a chance to contract and create new stars. The complex organic molecules necessary for life may have formed in the protoplanetary disk of dust grains surrounding the stars. It is believed that PAHs could be a step along the path toward amino acids and nucleotides, parts of proteins and DNA and probably associated with forming of new stars and exoplanets (Gudipati & Yang 2012). Another important role of the dust in disks is that at larger radii (>100 R_{star}), dust grains shield the envelope from the penetration by the interstellar radiation field (ISRF) allowing molecular species to survive and complex molecules to form (Casoli, Lequeux & David 1998).

Two processes can lead to increase in size and mass of grains in interstellar clouds, i) coagulation where two low velocity grains collide and stick together and ii) the formation of an ice mantle around the refractory core via physical or chemical adsorption (attracting to a surface). The first process forms porous grains consisting of various sub-grains of different composition, whereas the second process will accrete the abundant species, mainly H, O, C and N, onto grain surfaces (Casoli, Lequeux & David 1998).

Dust formation occurs in regions where the densities are high enough, there are heavy elements and the temperatures are below the vaporization temperature for grains, so that the processes of nucleation[2], condensation (change from gas into liquid phase), accretion and coagulation (change from a fluid into a thickened mass) can proceed. The astrophysical objects that have required conditions to form the dust are cool and dense atmospheres of asymptotic giant branch[3] (AGB) stars, more massive red supergiants (RSGs), the winds of certain types of Wolf-Rayet stars, molecular clouds, envelopes of protostars, novae and young SNRs (Casoli, Lequeux & David 1998). Beside type-II supernovae, which are considered as the most important dust producers in the early Universe (Nozawa et al. 2003; Dwek, Galliano & Jones 2007; Mattsson 2011),

[2]Nucleation is the process of forming a nucleus. It is the initial process in crystallization. It is the process in which ions, atoms, or molecules arrange themselves in a pattern characteristic of a crystalline solid, forming a site in which additional particles deposit as the crystal grows.

[3]AGB stars are intermediate mass stars of $\sim$ 1–8 $M_{\odot}$ which have gone through hydrogen and helium burning stages (Krishna 2005).

many authors claim that stars of a few solar masses ($M < 8$ M$_\odot$) are important dust producers in the local Universe since stars of higher mass are too rare (Franceschini 2000) and the contribution of the dust from other sources is modest. However, Peeples et al. (2014) have shown that most of the O, and all Fe is provided by core-collapse SN, that most of carbon is formed from AGB stars and type II SNe, ^{12}C is from stars with M<6 M$_\odot$, while ^{16}O is formed mostly from stars >8 M$_\odot$. Since ^{16}O made in massive stars makes up 1% of ISM mass and is a primary element – massive stars could be a responsible for almost all oxygen – therefore could be a responsible for a lot of dust (also see Tinsley 1980). Finally, it is uncertain if the dust which can be formed in the winds of massive stars (such as η Carina, whose dust mass is $\sim$0.4 M$_\odot$; Gomez et al. 2010) survives the shock wave of the subsequent SN explosion (Mattsson 2011).

However, in most of the parts of the ISM, the densities and the temperatures are in general too low to trigger the condensation of solids, while sputtering, shattering, vaporisation and other destructive processes are dominant, usually as a consequence of shock waves from SNRs and stellar winds (see Section 1.3.4). The dust composition and distribution in the ISM is the balance between the formation and destruction processes.

Compared to the outflows of evolved stars where the dust formation is a continuous process, in Wolf-Rayet, Coronae Borealis stars and novae, the dust is formed rapidly, in episodic outbursts, allowing monitoring of growth and development of the newly formed grains.

Dust formation in SNe/SNRs is a well-known and confirmed phenomenon, but it is still a not completely understood process. It is certain that several months after the explosion significant amounts of dust $\sim 10^{-2}$–10^{-3} M$_\odot$ are formed (Kotak et al. 2006; Fabbri et al. 2011), but it is still not understood when it stops forming, whether it survives the reverse shock and how it is connected with SN conditions and/or the type.

For comparison with SNe, it is worth mentioning that in novae dust formation typically occurs between one and five months after the outburst. The observations show that this time-scale depends on the rate that the nova fades in the optical, with

dust condensation time being longer for slower novae (Williams et al. 2013). There appears to be a strong correlation between time of condensation and the time it takes for the brightness of a nova to decline by two magnitudes. This relationship has not been explained theoretically.

1.1.2 Dust at far-infra-red wavelengths

This thesis is based on far-infra-red (FIR) and (sub)mm wavelengths which are used to study interstellar dust in the directon of SNRs in the LMC. The emission is composed of two components. The first dust component consists of larger grains, at temperatures close to the temperature of dust heated by the ISRF in galaxies (20 K). This cold dust radiates at $\lambda > 60$ μm and makes up $\simeq$90% of the dust mass in most galaxies (Dunne & Eales 2001). The second dust component is a bit warmer, at 40–70 K it radiates at $\lambda \leq 100$ μm and it is composed of smaller grains. At wavelengths ≥ 24 μm, we see interstellar dust, either warmed up collisionally by SNRs (Williams 2010), or on the temperature of the ISRF; while at shorter wavelengths ($\leq$24 μm) we detect dust, PAHs and there are also some other sources of radiation (see Section 1.3.1; Seok, Koo & Onaka 2013). Energy absorbed in the optical or UV or due to collisions between dust grains or electrons is re-radiated as thermal dust emission at FIR and (sub)mm wavelengths, with the spectral energy distribution (SED) well described by a modified black-body function (Sections 2.2 and 2.2.1). Modified black-body function has the shape:

$$F_{\nu}^{IR} \propto B_{\nu}(T)\nu^{-\alpha_{IR}} \tag{1.1}$$

where the coefficient α_{IR} is often between -1 and -2. I use this formula for all fitting in Chapter 3 and Chapter 4. For more details on the assumptions of the dust characteristics and deriving the final formula see Section 2.2.1.

1.1.3 The Large Magellanic Cloud

The Large and Small Magellanic Clouds (LMC and SMC) are irregular dwarf galaxies visible only from the Southern hemisphere, members of our Local Group, maybe orbiting the Milky Way (MW) galaxy. Until the discovery of the Sagittarius Dwarf Elliptical Galaxy in 1994, they were considered to be the closest known galaxies to our own. The Magellanic Clouds are far from the Galactic Plane, there is little foreground contamination from interstellar clouds and the distances to their objects can be assumed to be identical.

The LMC is a good laboratory for the life cycle of baryonic matter, because of its proximity of 50 kpc (Walker 2012) and favourable viewing angle permitting the studies of resolved stellar populations and interstellar clouds (Meixner et al. 2006). The ISM in the MW and in the SMC are confused in infra-red (IR) images due to crowding along the line of sight. In contrast, all LMC features are at approximately the same distance from the Sun, and there is typically only one substantial cloud along a given line of sight, so their relative masses and luminosities are directly measurable.

MCs have sub-solar metallicity of $0.5Z_{\rm solar}$ (LMC) and $0.2Z_{\rm solar}$ (SMC) that is similar to the mean metallicity of the ISM during the epoch of peak star formation in the Universe (red-shift of $\sim$ 1.5) and the dust-to-gas mass ratio have real spatial variations being $\sim$ 2-4 times lower than the value for the solar neighborhood resulting in substantially higher ambient UV fields than in the solar neighbourhood (Meixner et al. 2006). The lower metallicity results in lower dust content in both galaxies compared to the MW which allow us to probe conditions similar to the highest redshift, metal poor galaxies.

Studying the MC offers a unique opportunity to study star formation and evolution outside of the MW, containing numerous young stars and star clusters, as well as some much older stars and planetary nebulae. Catalogues of SNRs in MCs are equally important as the catalogues of MW SNRs since they do not suffer from distance dependent selection effect (see Section 1.2.5).

1.2 Introduction to Supernovae and Supernova Remnants

1.2.1 The observations of SNe and SNRs from historical times to today

The SN has a specific light curve whose maximum luminosity is quite high as much as that of its host galaxy. If a SN event occurs in our galaxy, it may be easily visible to the naked eye, even during the daytime for many months. The remnants formed after the SN explosions are called supernova remnants (SNRs). SNe events have been observed and recorded since ancient times; there are around ten well-known SN events that happened in our Galaxy observed in human history that are connected with existing young SNRs.

SNRs, the expanding shocks of material, remain visible dozens of thousands of years after the explosions, spreading chemical elements over thousands of cubic light-years and heating the ISM through fast shock waves and strong radiation. SNRs provide a record of SNe that have exploded in gas-rich environment in the past $\sim 10^4$ yr (Van den Bergh 2004). The classical SNR signatures are bright X-ray emission, conspicuous radio radiation (non-thermal, synchrotron emission), enhanced [SII]/H_α ratio, > 0.4 (Mathewson & Clarke 1973) and sometimes shells are visible in optical wavelengths (in early years after the explosion or in radiative phase).

Nowadays more than 200 SNRs are known in the Galaxy, while a few hundred extragalactic SN events have been reported every year (Uchida 2009). The frequency and the types of SNe in a galaxy are related to the structure, kinematics, metallicity, galactic age, star formation and all other galactic properties (McWilliam 2010). Furthermore, the SN rate determines the flux of cosmic-rays of galactic origin (Uchida 2009). They mentioned that the estimated average Galactic SN rate was 2.5 SNe per century. For the LMC, the rate was estimated to be 1 SN per century and the star-formation rate (SFR) to be 0.7 ± 0.2 $M_\odot$ yr^{-1}. The SMC SN rate is once every 350 yr and the SFR was estimated to be 0.15 ± 0.05 $M_\odot$ yr^{-1} (Filipović et al. 1998b).

SN events seem not to be observed in our Galaxy since A.D. 1604, but this fact may be simply because the visible light from the SNe were obscured by the line-of-sight dense ISM. For example, the explosion of Cas A was possibly not observed by eye (although it might have been recorded by John Flamsteed in 1680) and we know that the remnant is around 300 years old and that it is one of the brightest SNRs nowadays. Also, the explosion of SNR G1.9+0.3 was not seen until detected in radio bands despite being $\sim$ 100 yr old (Reynolds et al. 2008).

Although they are visible at many wavelengths, most SNRs are detected at radio and X-ray wavelengths. However, the comparison and modelling of SNR radiation is easier done in radio because X-ray radiation can be synchrothron (non-thermal) and Bremsstrahlung (thermal), while most of radio radiation is purely synchrotron. The radio synchrotron radiation occurs in places where accelerated particles orbit around the lines of the magnetic field of the shock front of a SNR. This radiation is non-thermal and polarised. After some time, the aged particles diffuse away from the shock area and radiate over a much wider area, producing diffuse emission (Han et al. 2013). The synchrotron emission can be described by the relation:

$$S_\nu \propto \nu^{-\alpha}, \tag{1.2}$$

where S_ν is the radio flux density, ν – frequency and α – spectral index, and $0 < \alpha < 1$. The spectral index determines the steepness of the spectrum of a SNR and the remnants are mostly the brightest at longer wavelengths (although there are some findings of a curvature of slope on the longest wavelengths). Higher energy particles lose their energy faster than the lower ones, so that the aged particles will diffuse out and produce extended emission with a steeper spectrum, while PWNs (pulsar wind nebulas) and young and bright objects will a have shallower slope. The spectrum of SNR radio emission has a typical spectral index of $\alpha = 0.4$ to 0.8 for most SNRs from Sedov to later phases. Some objects have unusually low spectral index (lower than 0.3), which is often the case for PWNs[4].

[4]Objects with too small spectral index ($0 < \alpha < 0.3$) are either PWNs (Vukotić 2006) or could be

1.2.2 Impact of SNRs on the ISM

SNe are the cataclysmic ends of life of various types of stars, seeding the Universe with the chemical elements necessary to form other stars, planets, and life. All chemical elements are formed in stars or SNe, distributed through the ISM by SNe/SNRs or stellar winds and spread over large distances. SN explosions are among the most energetic events in the Universe, having energies $\sim 10^{51} - 10^{53}$ ergs, being the most important sources of energy in galaxies, together with active galactic nuclei. They significantly influence their environment by removing matter out from the centre, warming up the ISM and their circumstellar medium (CSM), destroying the parent stars, forming strong magnetic fields, sputtering surrounding dust and creating dust from the star's remainders, in the early stages. These events can blow material out of galaxies, as well as suppress or enhance star formation (Leão et al. 2003). Recently, it has been observationally proven that SNRs are accelerating high velocity cosmic rays (Nikolić et al. 2013) which can also influence the life on planets, dust lifetime and various other phenomena. Eventually, the remnants mix with the ISM which later can collapse to form interstellar clouds from which new stars and planets can be formed.

1.2.3 Classification and Origin of Supernovae

1.2.3.1 End of the life of stars

Stars that begin their main-sequence lives with a mass of less than about 8 $M_\odot$ (majority of stars) spend most of their lives in the hydrogen burning phase. When their hydrogen runs out, they will swell into red giants, increasing in volume by a factor of > 1000 (stars with masses <0.5 $M_\odot$ will not even have enough power to reach this stage). The red giant phase is typically characterized by a helium core surrounded by a hydrogen burning shell. When the core contracts and heats to temperatures above $\sim 10^8$ K, helium burning will begin, fusing helium to carbon. Some stars will have

classified only as SNR candidates (see for example Filipović et al. 2005).

enough material to pass through helium burning phases, or even carbon or oxygen burning, until the fuel in the core is used up, when they collapse and the outer layers of the star are ejected. Collapse continues until the degenerate pressure of electrons in the plasma is sufficient to balance the gravitational forces, creating a *white dwarf* (WD) star. A typical WD has a mass of $\sim 0.6-0.7$ $M_{\odot}$, the size of the Earth (R$\sim$ 6000 km) and an average density is $\sim 10^6$ g cm^{-3}.

Stars above ~ 8 $M_{\odot}$ are hot enough at their cores to fuse hydrogen into helium, helium into carbon, carbon into oxygen, neon, silicon, sulphur and other elements. When iron is reached, the core collapses in upon itself on time-scales of the order of a second, combining electrons with protons to form neutrons, the electron degeneracy limit has been passed and the collapse continues until it is stopped by neutron degeneracy. Once nuclear density ($\sim 10^{15}$ g cm^{-3}) is reached, the degeneracy pressure of neutrons is sufficient to halt the collapse, and the core becomes a proto-neutron star. The remaining in-falling material from the core bounces off of this now hard core, ejecting the outer layers of the star in a fantastic explosion known as a core-collapse (CC) SN. The proto-neutron star forms a neutron star (NS), a stellar remnant of mass ~ 1 $M_{\odot}$ and R$\sim$ 10 km, with a density of $\sim 10^{15}$ g cm^{-3}. For highly massive stars, it is possible that even neutron degeneracy pressure cannot halt the collapse of the core, and a stellar-mass black hole is formed.

Type II SNe result from the CC of stars of mass greater than 8 $M_{\odot}$, but generally not more than $\sim 25-30$ $M_{\odot}$. They yield roughly the same amount of kinetic energy ($\sim 10^{51}$ ergs) as do type Ia SNe (see below), but their overall energetics are much greater, as most of the energy (99%) of CC SNe is carried off in neutrinos. Type II SNe leave behind a neutron star (NS) that is typically ~ 1.4 $M_{\odot}$. Type Ib and Ic SNe are believed to be the result of stars with a progenitor mass of $\geq$ 25–30 $M_{\odot}$. According to theory they leave behind a NS or stellar-mass black hole. Some of SN Ic progenitor stars are believed to have a main sequence mass $>$ 100–250 $M_{\odot}$ (Yoshida, Okita & Umeda 2014) and many of them have been connected with γ- ray bursts (Andersen et al. 2004; Hjorth et al. 2003).

The occurance and the evolution of NSs within SNRs is still not understood yet,

but the example of the young NS formed in the Cas A SNR has given many answers (Heinke & Ho 2010). That object is the youngest NS observed so far (less than 330 yr) with a very low magnetic field (B$< 10^{11}$ G). By virtue of its proximity the NS was observed to have a decreasing temperature in the past $\sim$ 10 years. In SN 1987A there still has not been found any NS or pulsar (PSR), see Chapter 3. The Crab Nebula ($\sim$1000 yrs) has a fast rotating PSR, thought to being producing flares.

Type Ia SNe are formed in binary (or more complex) systems. If a WD is contained in a binary system with a companion star that enters its red giant phase (or has even slightly evolved off the main sequence), and the separation between the stars is sufficiently close, the WD can gravitationally strip matter from its companion. Mass transfer occurs between the two stars, with the WD growing in mass via an accretion disk. WDs can only exist up to the *Chandrasekhar limit* ($\sim$ 1.4 $M_\odot$) and a WD pushed over this limit will become unstable, igniting a deflagration[5], or subsonic burning, of material in the star. This deflagration will lead to a detonation[6], a supersonic thermonuclear explosion of the entire WD. This is how SNe Ia are created, in the so called *single degenerate* scenario. The entire 1.4 $M_\odot$ of material is ejected into the surrounding medium at speeds of $\sim$ 10 000 km s^{-1}, releasing about 10^{51} ergs of kinetic energy. A second possible mechanism for triggering a SN Ia is the merger of two WDs who lost their angular momentum on the gravitational drag, whose combined mass exceeds the Chandrasekhar limit (so called *double degenerate* scenario). Type Ia SNe leave behind no compact remnant and since all WDs are thought to explode at a similar mass and their light curves are quite similar in peak brightness, they are used as a standard candle to determine distances to host galaxies. Type Ia spectra show no hydrogen because WDs are made mostly of carbon and oxygen, nearly all of which is burned to nickel in the explosion and have a strong [Si II] line at 615 nm.

[5]Deflagration is subsonic combustion propagating through heat transfer.
[6]Detonation is supersonic and propagates through shock.

1.2.3.2 Supernova Classifications

Historically, the SN classification scheme distinguishes Type I and Type II which is based solely on the existence of hydrogen lines in their spectra; Type I SNe show no hydrogen Balmer lines, Type II do. Except that SNII had different brightness curves, while SNI seemed like a homogeneous class of objects. Later, two sub-classes of the type I were discovered: SNIa (the only type of SNe present in elliptical galaxies) and SNIb (also found around HII regions and in the spiral arms; progenitors of the latter are young massive stars that lost their envelope, stripped-envelope SNe). SNIa originate from old, population II stars (from WDs in close binary systems) and SNII and Ib originate from gravitational collapse of young, massive stars. Later, a third class was discovered, SNIc, having no He nor H lines, from massive stars that lost their He and H envelopes. SNe II are a very heterogeneous class having several sub-classes: SNII-L (after maximum the brightness decreases linearly); SNII-P (plateau present on the brightness curve as a consequence of the recombination of H in the envelope during the expansion); SNIIb - weak H lines; SNII-n have narrow emission lines because of the interaction with CSM; and peculiar SNII (SN 1987A belongs to this type; Lyman, Bersier & James 2014). In Fig. 1.1 I give a diagram summarising this classification.

In the sample of 132 SNe in the Local Universe Smartt et al. (2009) determined the relative rates of each sub-type of the explosion, finding that 27% are type Ia while the rest are core-collapse SNe which break down into 59% II-P and 29% Ib/c, with the remainder being IIb (5%), IIn(4%) and II-L (3%).

1.2.3.3 Type of the Supernova Remnants

SNRs are harder to type the older they are, since they have mixed up with ISM. The methods of typing of SNRs include analysis of the amounts of the nucleosynthesis products of the ejecta, study of SN light echoes[7] (analysis of the spectrum of the

[7] A light echo is produced when a sudden flash or burst of light, such as that observed in supernovae, is reflected off a source and arrives at the viewer after a considerably longer duration than if it would

reflected light from echoes of SNRs as old as 100–1000 yr can be used for spectral identification of the SN; Rest et al. 2008), the association with a NS/PWN/PSR or the observing of the local star types. The typing of SNRs, based on the study of the stellar population around SNRs relies on knowing that high-mass stars (usually progenitors of CC SNR) are rarely formed in isolation, but cluster in OB associations, environments of active star formation, close to stars and HII regions while the progenitors of Ia are often isolated, far away from their place of birth, but can be in various environments. One such study was done by Chu & Kennicutt (1988). Also, studies of the X-ray and IR morphologies of SNRs suggest that type Ia and CC SNRs have distinct symmetries – type Ia are more spherical than the CC SNRs (Peters et al. 2013).

Unlike in SNe, in SNRs, before the radiative phase, radiation comes primarily from hydrogen Balmer lines (transitions from $n \geq 3 \rightarrow 2$), such as H_α, $\lambda = 656.3$ nm, and H_β, $\lambda = 486.1$ nm. This requires the presence of neutral hydrogen ahead of the shock, which is much more easily attained in the case of a type Ia than a type CC, since CC ionize the surrounding medium, either with ionizing radiation from the progenitor, or a flash of ultraviolet (UV) radiation at the moment of explosion. Charge exchange between slow neutral atoms and fast protons behind the shock produces fast-moving neutral atoms, generating a broad H_α line, with a narrow component arising from stationary neutral atoms in the post-shock medium (Williams 2010). That is why SNRs Ia are called "Balmer-dominated".

Another classification of SNRs is morphological, based on their shape: 1) shell SNRs and 2) plerionic or filled-centre. For shell SNRs at radio frequencies the most dominant radiation is behind the shock wave (for example E0102–72), while in plerions a central synchrotron nebula (originating from the PWN) is visible. The remnants where both structures are observable are composite type (B0540–69.3, Kes 75, Vink 2012). Crab Nebula is an example of a plerion without a shell (Vukotić 2006).

Classification of SNRs based on the spectral characteristics is as follows: 1) Balmer-dominated, 2) Oxygen-rich, 3) Plerionic/composite and 4) Evolved remnants

have taken on a direct path.

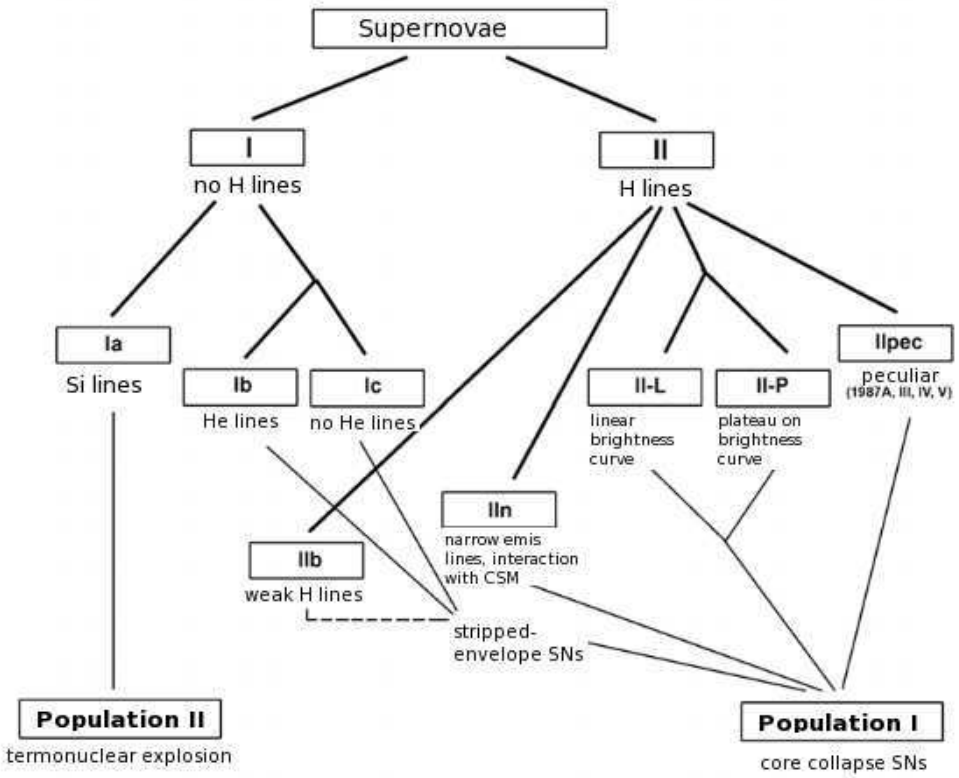

Figure 1.1: Classification of SNe, taken from Arbutina (2005).

(Mathewson et al. 1983). Balmer SNRs are usually connected with SNIa, Oxygen-rich SNRs originate from SNIb – explosion of a massive O or a Wolf-Rayet star (Arbutina & Urošević 2005) and their emission is mainly from the interaction with CSM. Plerions are from SNII events – explosion of a massive B star, having additional energy input from the rotational energy losses of a stellar remnant – NS or PSR – plus the shock wave powered shell. All three groups in the end become evolved remnants. Based on all the facts that we have, there is an additional class of SNRs that could be added to the previous four, an extreme class of SNIc with higher than normal expansion velocities, also known as SNId (Fryer 2004), that should be connected to the remnants of hypernovae[8] (Arbutina 2005). Also, SNIc should be added to the Oxygen rich SNRs.

Forest, Spenny & Johnson (1988) have proven that SNRs in the LMC are commonly associated with HII regions which is a sign of dominance of CC over Ia SN types, but it is still not known if this result is influenced by the fact that the SNRs in dense regions are more likely to be detected. Nowadays, in the sample of known SNRs in the LMC, we still have more CC than Ia SNRs, but their ratio is not precisely known because for older SNRs it is hard to determine the type. The typing of SNRs in our data sample is explained in Section 4.1.1.

Desai et al. (2010) investigated the physical associations between star formation and 45 SNRs within the LMC, finding seven SNRs associated with both Young Stellar Objects (YSOs) and molecular clouds, three SNRs associated with YSOs but not molecular clouds, and eight SNRs near molecular clouds but not associated with YSOs. They concluded that the association between the YSOs and SNRs cannot be convincingly established. However, they argue that 15 SNRs that are near molecular clouds may trigger star formation in the future when the SNR shocks have slowed down to <45 km s^{-1}.

An alternative way of typing SNRs could be attempted using the $\Sigma - D$ relation (see Section 1.2.6) or guessed by observing the ISM density around SNRs (see Chapter

[8]Hypernovae are thought to be the unusually energetic Type Ib/c SNe that are sometimes associated with $\gamma-$ray bursts.

4).

Estimating ages of SNRs is usually done by deriving the Sedov age from the shock velocity that was found by measuring the width of spectral lines (H_α for example; see Smith et al. 1991), by the pulsar connected to the remnant, from analysis of non-thermal X- ray filaments (Bamba, Yamazaki & Hiraga 2005), and often by applying the measured diameter and velocity in various models.

1.2.4 Hydrodynamic Evolution of SNRs

When a star explodes as a SN, the delivered kinetic energy is $10^{51} - 10^{53}$ erg. SNRs continue to be visible several dozens of thousands of years after the explosion before they lose all characteristics that make them distinguishable from, and mix with the ISM, while their diameters can reach several hundreds of parsecs. The evolution of a SNR has four phases:

- Free-expansion phase
- Sedov (adiabatic) phase
- Radiative (iso-thermal) phase
- Dissipation phase

In the first phase, right after the explosion, the blast wave is formed and the ejecta is scattered into the ISM. Since this phase lasts as long as the ejected mass, M_{ej}, is significantly greater than the mass of the ISM it sweeps up, M_{sw}, crudely speaking, there is no appreciable slowing of the ejecta by the ambient medium. Since $E_{SN} = M_{ej}V^2/2$, where E_{SN} is the explosion energy of the initial event, and V the velocity of the expansion, thus $V \propto (2E_{SN}/M_{ej})^{1/2}$ in the free expansion phase. The SNR is spreading into the ISM with an almost constant velocity of $\sim 10\,000$ km s^{-1}, in a typical density of 1 cm^{-3}, driving a strong shock at the leading edge. How long this phase lasts depends on both the ejected mass of the SN and the density of the CSM in front of the shock, and can be from a few days to several hundreds of years.

As the shock continues to expand and sweep up material it encounters, the accumulated mass becomes non-negligible, and gradually causes the shock to slow. The ejecta behind the shock, however, are still travelling at a free-expansion velocity, and slam into the decelerating material ahead of it. This causes a reverse shock to form. The duration of the reverse shock phase can last tens to thousands of years.

When the mass swept up by the blast wave becomes more than 3 times higher than the mass that was ejected in the explosion, $M_{sw} \approx 3M_{ej}$, the Sedov-Taylor phase begins. The reverse shock is propagating all the way back through the ejecta and dissipates. The space between swept-up and ejected material is a contact discontinuity. By now, the blast wave is significantly decelerated. This phase is the longest (it can last $\sim 10^5$ years) and it is likely that a sample of SNRs in the LMC would exist in this phase (Badenes, Maoz & Draine 2010; Chapter 4). In the Sedov phase the interior of the SNR is so hot that the energy losses by radiation are very small (all atoms are ionized, there is no recombination). Therefore, this pressure-driven expansion phase is often called adiabatic, since the cooling of the gas is only due to the expansion. The relation between remnant radius, R and its age, t can be described by a self-similar Sedov solution (Sedov 1959):

$$R \propto \left(\frac{E_{SN}}{\rho}\right)^{1/5} t^{2/5}, \tag{1.3}$$

where ρ is the density of the ISM.

The radiative phase (or momentum-conserving phase) begins when the SNR loses approximately half of the kinetic energy released in the explosion and the radiative losses become important. The interior of the SNR is much colder, the temperature of the post-shock gas drops below 10^6 K, the SNR is expanding according to $R \propto t^{1/4}$ and the forward shock speed is only a few hundred km s^{-1}. The energy of the shock wave is being radiated, so the shell is always on the same temperature and this phase is therefore called 'isothermal'. The total momentum of the shock wave $4/3\pi R_s^3 \rho V$ is constant in time in this phase. As the gas temperature drops further, the material usually becomes visible in the form of optical radiation.

Finally, some $10^4 - 10^6$ yr after the explosion, when the velocity of the shock wave falls below the speed of sound ($\sim$ 10 km s^{-1}), the dissipation phase starts, the remnant begins to fade away and becomes part of the ISM.

1.2.5 The LMC and its SNRs

The LMC is convenient for studing SNRs because these observations are relatively free of Galactic confusion, far enough so that we can assume that all SNRs are on the same distance to us (50 kpc), yet close enough that we can resolve all remnants larger than 9 pc (>90% of objects), even with the poor resolution that we use in this work (36.3″; Chapter 4). Thus many of its SNRs are well-studied objects in existing catalogues. These SNRs create a significant sample of objects, belonging to a dwarf galaxy of low metallicity, with progenitor stars of moderate masses. The LMC is actively forming stars and so the SNe that explode include both Ia and CC SNe.

Data sets of Galactic SNRs suffer from a severe Malmquist bias: intrinsically bright SNRs are favoured because they are sampled from a larger spatial volume compared to any given flux limited survey. The result is a bias against low surface brightness remnants such as highly evolved old SNRs (Urošević et al. 2005). On the other hand, data sets made of extragalactic SNRs do not suffer from distance dependent selection effects, since these SNRs are at the same distance and therefore sampled from the same volume. However, they do suffer from other selection effects – from limitations in sensitivity and resolution, as well as from source confusion. All these selection effects cause samples of extragalactic SNRs to span a shorter range of both diameters and surface brightness.

In Fig. 1.2 the whole population of SNRs in the LMC that are used in this thesis and observed with the *Herschel Space Observatory* (Section 2.1.1.1, Pilbratt et al. 2010) is shown. The remnants are distributed all over the galaxy, although they tend to be located more often in denser environments. The list of all LMC remnants that I have investigated in this thesis is given in Table 4.1.

Many SNRs from the LMC are very well-studied, especially the younger ones

and the ones in higher density because more information is conserved. SNRs are observed at many frequencies; their types, ages, progenitors, physical characteristics and compositions are discussed. Although most SNRs are visible at radio wavelengths more often than at any other wavelength, some SNRs are visible in X-rays, but faint or invisible at radio and optical frequencies e.g. the sources in Maggi et al. (2014), or SNR 0103−726 in the SMC. The lesser known sources in the LMC are older shells that swept up so much ISM that not much could be concluded on their progenitor stars or age and they have cooled down and faded at most of the wavelengths.

One should be aware that in this sample many SNRs, especially of type Ia are probably undetected because of the lack of ISM to interact with or they are old or there are observational difficulties like background/forgeround emission for example. In Section 4.1.1 we explain how we divide our SNR sample into 15 Type Ia and 45 core-collapse remnants.

1.2.6 $\Sigma - D$ relation

The conditions required for synchrothron radiation are accelerated particles (electrons) and a magnetic field around which they have to start spinning around. According to Alfvén theory, the magnetic field remains frozen in the plasma while the SNR is expanding, so that the total flux should remain constant if there is no decrease of energy. But, because of the energy loss, the surface brightness of SNRs is decreasing in time in the way shown by Helmboldt & Kassim (2009) for Cas A, at a more or less constant rate.

The $\Sigma-D$ relation describes the evolution of the radio surface brightness of SNRs, Σ, with the diameter, D, as SNRs spread, cool down, fade and mix with the ISM. It follows the relationship: $\Sigma \propto AD^{-\beta}$. The radio surface brightness, Σ is obtained from

$$\Sigma_\nu \left[\mathrm{Wm^{-2}Hz^{-1}sr^{-1}}\right] \;=\; 1.505 \times 10^{-19}\; \frac{F_\nu[\mathrm{Jy}]}{\Theta[']^2}, \tag{1.4}$$

where F_ν is the flux density and Θ the angular diameter of a source (Vukotić et al. 2009). Σ is used instead of flux density in order to study the evolution of remnants,

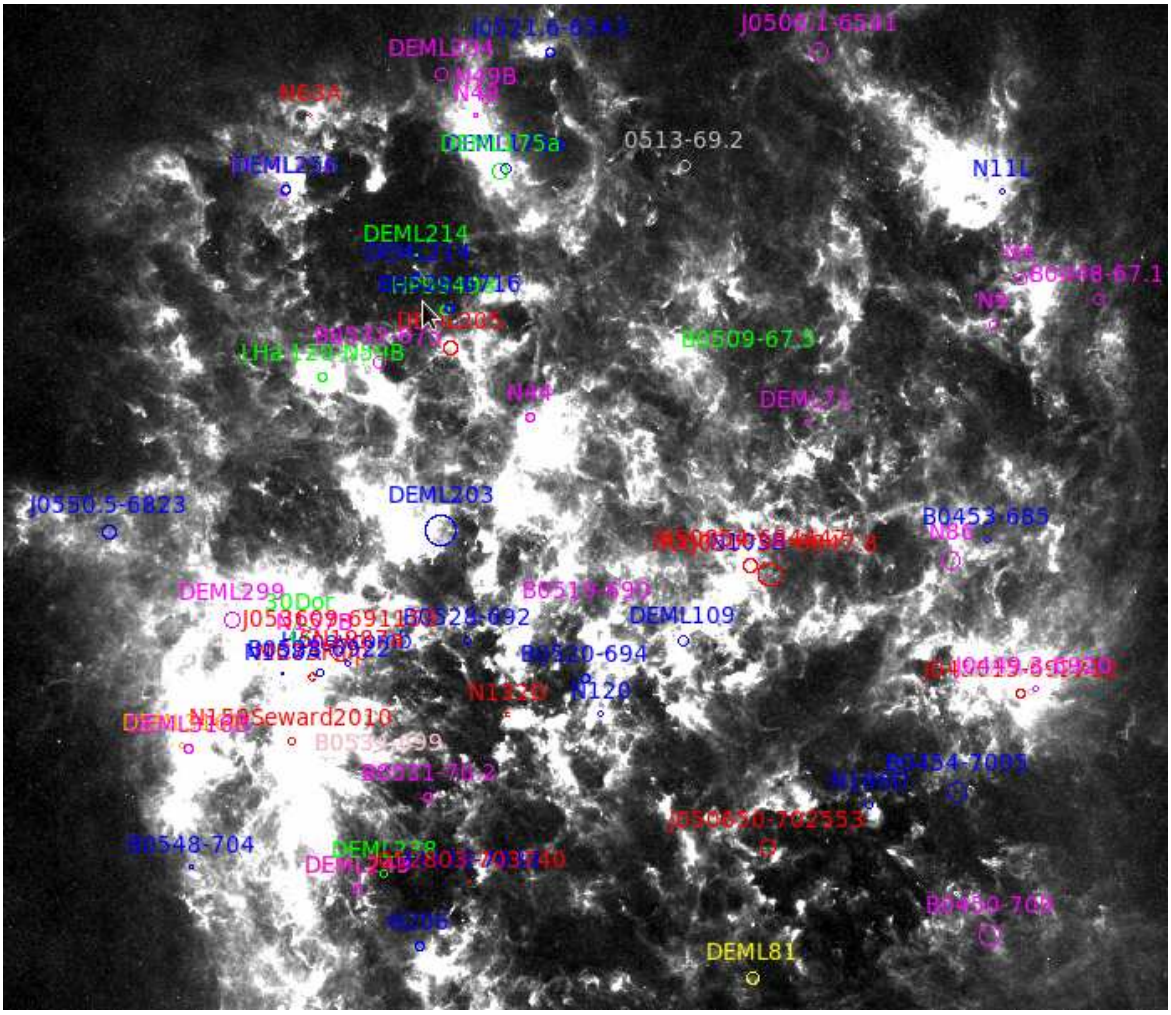

Figure 1.2: My sample of supernova remnants in the LMC; image obtained with *Herschel* at 350 μm (Meixner et al. 2013).

since fluxes depend on the diameter and Σ does not. The $\Sigma - D$ relation is traditionally used for determining the distances to SNRs. If flux density and the angle diameter are known from the observations and if we have A and β from previous estimations then D can be calculated from the $\Sigma - D$ relation and the distance d can be obtained as $d = D/\Theta[\mathrm{rad}]$. The values of A and β are calibrated values, and are not easy to calculate precisely. Their meaning will be explained below. This method of distance determination for SNRs has advantage over other methods in that the Σ of a radio SNR does not depend on its distance (Urošević et al. 2005).

The first $\Sigma - D$ relation was given by Shklovsky (1960), but it continued to be improved through the years with new observations, models and assumptions. A detailed history of theoretical and empirical $\Sigma - D$ relations is given by Urošević (2000) and some recent studies include Urošević (2003) and Arbutina & Urošević (2005). Urošević (2002) used the $\Sigma - D$ relation for proving that the origin of main Galactic radio loops (Loop I, II, III and IV) are huge ancient SNRs.

Since I am interested in the statistical study of SNRs in the LMC and since most of the SNRs in this sample are in the Sedov phase (Badenes, Maoz & Draine 2010), the most suitable theory for their radio evolution is described by Duric & Seaquist (1986). This theory describes the fading of radio surface brightness of SNRs with time (diameters) including parameters such as initial conditions, energy of the explosion, density, spectral index and magnetic field.

In the work of Berkhuijsen (1986) different important dependences are examined such as $\Sigma - D$; $n - D$ and $\Sigma - n$ where n is the density of environment around the SNR. Later these relations were slightly corrected by Bandiera & Petruk (2010) based on more precise observations. The conclusion of Bandiera & Petruk (2010) was that the $\Sigma - D$ relation was only a secondary effect of the relations between D and Σ with n, while Σ is proportional to n and D is decreasing with n. They claimed that only the $\Sigma - D$ relation of SNRs in an environment of constant density could represent one life path of one SNR, therefore they consider the usual $\Sigma - D$ relation to be too unspecific because it is influenced by different SNRs in different conditions.

On the other hand there is the approach of Arbutina & Urošević (2005), who claim

that in the relation $\log\Sigma = \log A - \beta \log D$ the parameter A depends on the environment density, energy, magnetic field and other conditions of the explosion, while the slope β is almost constant for the various groups of SNRs in typical local galaxies (MW, MCs and similar). For example, Urošević et al. (2005) found about the same slope for Σ at 1 GHz of SNRs in the LMC and SMC (2.28 ± 0.4 and 2.28 ± 0.52; while the offsets are $3.76^{+11.55}_{-2.84} \times 10^{-17}$ and $2.52^{+13.87}_{-2.13} \times 10^{-17}$, respectively). Arbutina & Urošević (2005) have obtained a similar conclusion about $\Sigma_{1\mathrm{GHz}}$. They claim that the slope β (3.3±0.4 and 3.2±0.6 for CC and Ia SNRs) explicitly does not depend on the density or the other conditions within a SNR and that the evolutionary tracks of all SNRs are parallel. Thus, SNRs with higher density and Σ (CC) are in a higher position on the $\Sigma - D$ diagram than SNRs in lower density (Ia), as the offset of CC ($2.2^{+3.1}_{-1.3} \times 10^{-15}$) is higher by two orders of magnitude than the one for Ias ($3.9^{+11.3}_{-2.9} \times 10^{-17}$). Therefore from the position of a SNR on the $\Sigma - D$ diagram it might be possible to estimate its type.

In reality, there are significant differences between the measured and theoretical $\Sigma - D$ relations. According to the theory of Duric & Seaquist (1986), based on the analytic expression of synchrotron emissivity in shocked gas (Bell 1978) and the model of the magentic field from Gull (1973), for a sample of young SNRs ($D \ll 10$ pc), β would be 5, while for somewhat older remnants it would be 3.5 (error bars are not given because these equations are derived by assuming a number of parameter values). On the contrary, the measured values of β for 10 out of 11 nearby galaxies span from 1.67 ±0.26 to 2.38 ±0.26. The exception was a star-burst galaxy, M 82, known to have a large population of much younger SNRs than the LMC (and similar galaxies), where $\beta = 3.41 \pm 0.24$ (with an offset of $2.54^{+0.51}_{-0.43} \times 10^{-15}$) – this is the only β in agreement with theoretical predictions. It follows that the empirical relations for SNRs in 10 of the 11 nearby galaxies have the approximately trivial form ($\Sigma \propto D^{-2}$) and therefore do not represent a physically meaningful relation, while M 82 has a steep slope which was expected from the theory. Urošević et al. (2005) explained this flattening as the result of selection effects from different survey sensitivities in all 10 galaxies, while they found that for M 82, the $\Sigma - D$ relation was not strongly affected by selection

effects since its SNRs are younger and brighter by more than three orders of magnitude. However, M 82's SNRs have such small diameters that they are probably still in the free expansion phase, so they must radiate more energy per volume than the ones in the LMC, thus they should have a larger span of Σ, which also might be the reason for the steeper slope.

Exploring the $\Sigma - D$ relation is important since it can tell us the history and the future of these objects, the details about the radiation mechanisms, enviroments the remnants are expanding into, how the magnetic fields evolve and how the initial conditions influence SNRs (see Duric & Seaquist 1986).

1.2.7 Observed evolution of SNe and SNRs

While fluxes of SN 1987A and SNRs of similar age still exponentially increase at all wavelengths except IR (Zanardo et al. 2010), the radio flux of a young remnant in late free expansion phase, Cas A (∼330 years) is significantly decreasing in time, ∼ 37 % in ∼50 years (Helmboldt & Kassim 2009). The secular variation of the radio flux density, d_ν has the wavelength dependence of $d_\nu[\%\ \mathrm{yr}^{-1}] \propto \nu^{-2.1}$ (Vinyaikin 2014). In SN afterglows it is even more common to see significant changes of the flux on all wavelengths.

1.2.8 Introduction to Supernova 1987A (SN 1987A)

On February 24 1987, all telescopes turned their eyes to observe the spectacular event of a SN explosion in the LMC and this object became the most studied SN ever. Its brightness peaked in May with an apparent magnitude of about 3 and slowly declined in the following months. Examination of plates of the region obtained before the SN explosion allowed the detection of the progenitor of SN 1987A, a blue super-giant (BSG) (Sk -69° 202), believed to have had an initial mass of 18–20 $M_\odot$, spectral type in the range B0.7 to B3 and luminosity class I (Van den Bergh 2004). It is now understood that BSGs are progenitors of SNe, although there is still the speculation that the

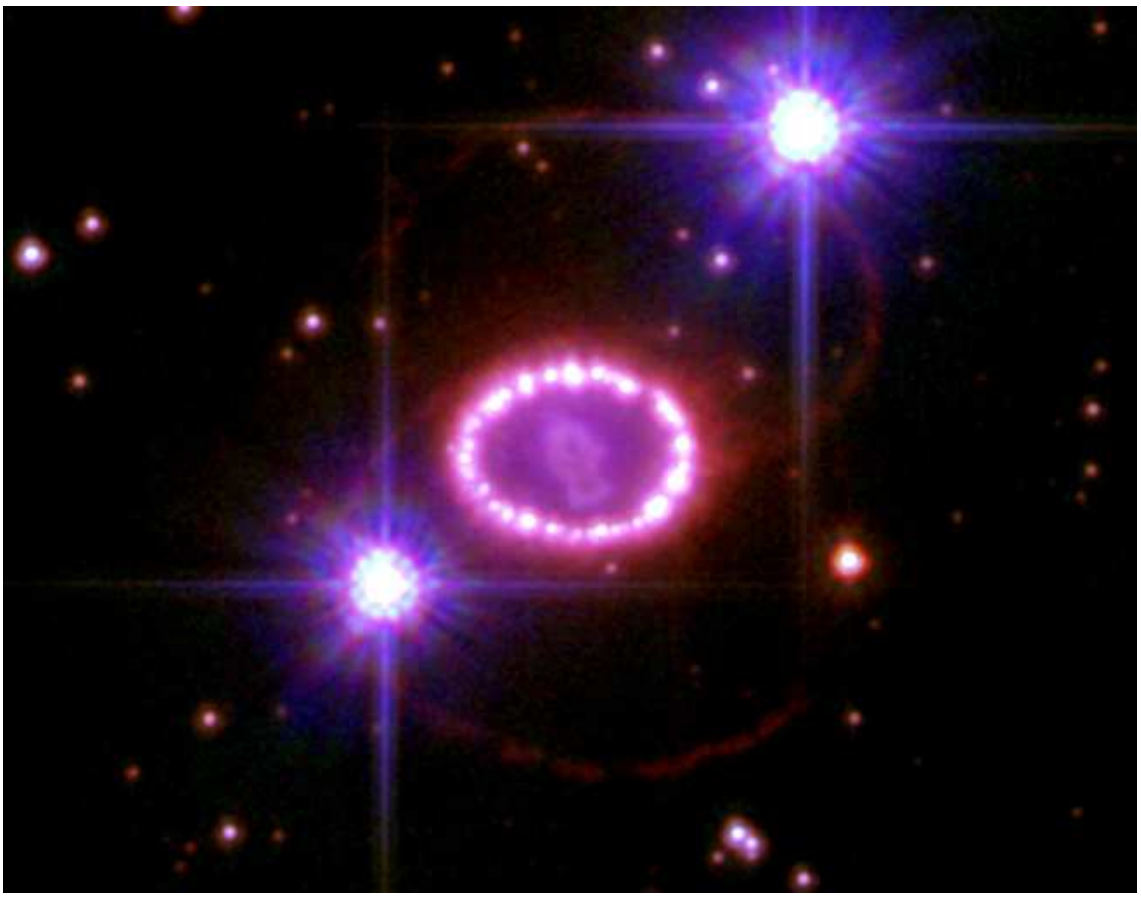

Figure 1.3: SN 1987A with *HST*. Equatorial ring is the bright ring in the center, with ejected material visible in the center of that ring. Two other rings are from sand clock-like structure of surrounding ISM (interface of fast bipolar wind of BSG progenitor, and surrounding CSM). Image taken from http://www.spacetelescope.org/images/heic0704a/.

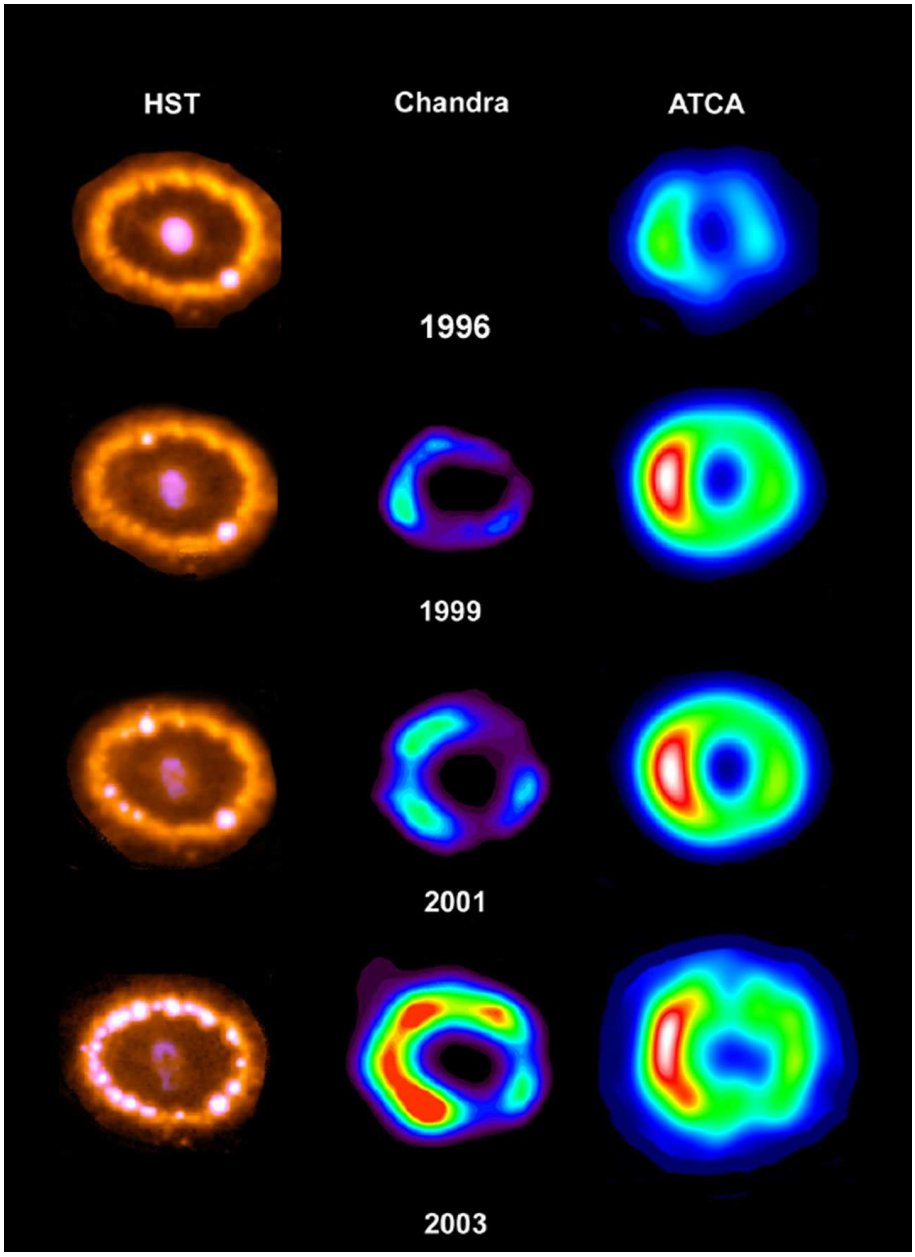

Figure 1.4: Evolution of SN 1987A from the year 1996 to 2003: *Left:* with *HST* (optical); *Center:* with *Chandra* (X-rays) and *Right:* with *ATCA* (radio). Taken from the Web-page http://www.spacetelescope.org/images/ opo0409r/; credit: R. McCray (University of Colorado), D. Burrows and S. Park (Pennsylvania State University), and R. Manchester (Australia Telescope National Facility).

evolution of such stars requires mass loss involving a binary companion. Although this SN was classified as a type II (Arnett et al. 1989), it was about one tenth as luminous as the average observed type II SN, which is probably associated with the denser surroundings.

The SN 1987A progenitor is believed to have been a RSG in a binary system, prior to becoming the BSG that vanished in the post explosion images (Barkat & Wheeler 1988), but it could also have been a fast rotating single star (van Loon 2013). From the colour-magnitude diagram of the stars from the area surrounding SN 1987A, observed with *Hubble*, it is found that in this region there are several generations of star formation with ages between 1 Myr and 150 Myr (Van den Bergh 2004). Xu & Crotts (1999) noticed interstellar velocity components at $V = +269$ and $+301$ km s^{-1} that occur within $20''$ around SN 1987A, believed to be produced by the progenitor star's RSG wind.

The emerging remnant of SN 1987A is being shaped by the impact of the initial blast wave and the expanding hot plasma upon an equatorial ring[9] (ER) of matter (see Fig. 1.3), $\sim 1.6''$ in diameter, deposited probably by the progenitor star when it was still a RSG (Bouchet et al. 2006; Dwek et al. 2010; Larsson et al. 2011). The blast wave likely reached dense circumburst regions around day 6000 and since then radiation has been exponentially increasing at all frequencies (Zanardo et al. 2010; Dwek et al. 2010). Several years after the explosion, SN 1987A had evolved from a SN radiating as a result of radioactive decays, mainly ^{56}Co and ^{44}Ti, into a remnant where the interaction of the blast wave with the CSM is causing the ER to brighten up. The ejecta themselves are due to reach the ring in the near future.

Images of this remnant evolving from the year 1996 to 2003 on optical, X-rays

[9]In case of SN 1987A, collisional interaction between the blast wave and the matter, manifested through the appearance of UV-optical hot spots strung like beads around the ring (see Fig. 1.3), but also bright at most of other wavelengths, X-rays, optical, UV, radio and at MIR wavelengths (see Fig. 1.4) is called the equatorial ring. The ER is the densest part of this SNR, visible because forward and reverse shock have excited the medium. It is a part of a system of three bright rings of material from the stellar wind of the progenitor, forming an hour-glass like configuration, at 0.67 ly from the centre of the explosion, ionized by the UV flash from the SN explosion and emitting in various emission lines (Fig. 1.3; Washimi, Shibata & Mori 1996).

and radio are shown in Fig. 1.4. The remnant is becoming brighter in X-rays and radio and the difference between the left and right lobe becomes more obvious. In optical images the ring is becoming brighter, and the ejecta become fainter for that period, but in later days (from year 2010), the brightness of the ejecta has increased again probably because it was re-heated by the radiation from the ER (Larsson et al. 2011).

At radio frequencies, the increase of flux of this object has been continuously monitored from day $\sim$ 1200 in the 1.4–9 GHz frequency range with the *ATCA*. The emission from the immediate vicinity of SN 1987A at radio frequencies is due exclusively to synchrotron radiation arising from magnetized plasma (Zanardo et al. 2010). The radio imaging of this object was recently presented by Manchester et al. (2005), Potter et al. (2009), Zanardo et al. (2010), Ng. et al. (2011), Lakićević et al. (2012b), Ng et al. (2013), Zanardo et al. (2013) and Zanardo et al. (2014). For the IR characteristics of this object, see Section 1.3.0.1 and this work (Chapter 3).

1.3 IR observations of SNe and SNRs

SNR dust research is important because they impact on dust sputtering, heating, evolution, formation and the amount in the ISM surrounding SNRs, but it may be also important since dust converts UV and visible radiation from bright objects to IR radiation. I will mention some of the most resent research about SNe/SNRs seen at IR wavelengths.

1.3.0.1 IR observations of SN 1987A: a special case study

Small amounts ($M_{\rm d} \leq 10^{-3}$ M$_{\odot}$) of warm dust formed about two years after the explosion in the ejecta of SN 1987A (Spyromilio et al. 1988; Suntzeff & Bouchet 1990; Bouchet, Danziger & Lucy 1991; Moseley et al. 1989). These observations also discovered the first molecules forming within a SN ejecta. Observing SN 1987A offered a great opportunity to study fresh SN dust, because in older remnants it becomes in-

creasingly difficult to distinguish between dust formed in the ejecta or dust swept-up from the surroundings (Rho et al. 2009; Sandstrom et al. 2009; van Loon et al. 2010; Otsuka et al. 2010; Barlow et al. 2010). The dust condensation process started around day 450–600 after the explosion (Whitelock et al. 1989) and it was thought that dust had condensed in clumps within the ejecta (Lucy et al. 1989). As the remnant cooled, dust formed and began to obscure the inner ejecta from view at optical wavelengths within the first few years (Kamenetzky et al. 2013).

The early detections of dust in SN 1987A are important to estimate the amount of dust during the period in which it is being formed, before the ejecta expands, mixes with ISM and becomes difficult to observe or get sputtered by shocks. Because of a new generation of FIR and (sub)mm telescopes, we are able to explore what has happened with dust that formed after the explosion in the following ∼27 years and to monitor what will happen next.

The warm dust component connected to SN 1987A was recently explored using *Gemini* and *Spitzer* (see Section 2.1.1.2) data, finding $\sim 10^{-6} - 2.6 \times 10^{-6}$ $M_{\odot}$ of dust located in the ER, at ∼166–180 K (Bouchet et al. 2006; Dwek et al. 2010). The strong IR emission arised from dust in the inner ER that had been collisionally heated by the shocked X-ray emitting gas, on a temperature of $\sim 10^6$ K and with density $\sim 10^4$ cm^{-3}. That dust was ejected during the pre-SN evolution of the progenitor star. The total MIR flux had increased by a factor of 5 in around five years, but since the shape of the dust spectrum had not changed, Dwek et al. (2010) concluded that the temperature and density of the soft X-ray emitting gas had not changed significantly; they found no new dust formed in the ring. Also they found another warm dust component in the ring, at 350 K, suggesting that these grains are probably smaller and might have different evolutionary paths.

The discovery of ∼0.4–0.7 $M_{\odot}$ of 20–27 K dust at the location of the remnant (Matsuura et al. 2011) challenged us to better understand this object. Matsuura et al. (2011) claimed that this dust is probably from the ejecta, because the mass is too high to be from the progenitor star. Although it was assumed and expected (from theory) that SNe could produce significant amounts of dust, this observation could not rule

out if dust formed in the ejecta or in the ER or surroundings, since *Herschel* could not resolve the object. My research of SN 1987A at mm and submm wavelengths with *APEX* (see Section 2.1.1.4) and *ATCA* (Section 2.1.1.3) are presented in Chapter 3.

Finally, *ALMA* observed this object (Kamenetzky et al. 2013; Indebetouw et al. 2014; Zanardo et al. 2014), and confirmed that $\sim$0.3 $M_{\odot}$ of dust is constrained in the ejecta.

1.3.1 Contributions to MIR radiation in SNRs from dust radiation, molecular line emission, fine-structure lines, PAH and synchrotron emission

At shorter IR wavelengths (3.6–8 μm), Reach et al. (2006) observed MIR emission of eighteen Galactic SNRs with *Spitzer*, finding molecular line emission, fine-structure lines, and PAH emission in nine, three and four SNRs respectively, but also mixed cases. None of these remnants are dominated by synchrotron radiation. Also, at 11–70 μm, Seok et al. (2008) observed 21 LMC SNRs using *AKARI*, detecting eight and finding that the emission in five objects is dominated by thermal emission from hot dust heated by X-ray emitting plasma (because MIR emissions showed morphologies similar to the X-rays).

Afterwards, Seok, Koo & Onaka (2013) observed 47 LMC SNRs with *Spitzer*, finding that the images of 29 SNRs show some features belonging to these objects. All of them show emission in the *MIPS* band at 24 μm, and 20 out of 29 show emission in one or several *IRAC* bands (4.5, 8, or 24 μm). They concluded that the *MIPS* emission of all SNRs originates from dust emission, while *IRAC* emission originates from ionic/molecular lines, PAH emission, or synchrotron emission.

They found that LMC SNRs are considerably fainter in the MIR than the Galactic SNRs and that Ia SNRs are significantly fainter than CC SNRs. It is known that the LMC dust is more silicate rich than MW (Pei 1992), but there is no evidence yet that the dust in LMC is destroyed by shocks more rapidly than in MW. Also, although the SNRs in LMC might be fainter in the FIR, that does not mean that they have less

dust.

LMC SNRs have a higher detection rate (62%) than Galactic ones (20-32%). Seok, Koo & Onaka (2013) suggest that this can be either because of less IR confusion in LMC by the Galactic disk, or because of the limited resolution of the *Infrared Astronomical Satellite* (*IRAS*).

Previous IR studies of SNRs with *IRAS* (Graham et al. 1987; Arendt 1989; Saken, Fesen & Shull 1992) and *Spitzer* (Borkowski et al. 2006; Williams, Chu & Gruendl 2006; Williams et al. 2006; Otsuka et al. 2010; Sankrit et al. 2010) have also shown that a substantial component of the MIR and FIR emission comes from dust collisionally heated by electrons and ions in hot plasma in the post-shock gas (Dwek et al. 1987; Draine 1981). Dust radiating at 24–500 μm can be from dust formed in SN/SNR ejecta or dust formed in pre-SN CSM or ISM material, or from light echos. Besides heating by the explosion, gas collisions and the ISRF, the dust heating in/around SNRs can also be stochastic[10], or heated by the synchrotron radiation from the PWN (Temim et al. 2013), or by irradiation by some other source like a star or other SN explosion. Collisional heating is assumed to be the main source of dust heating of young SNRs at wavelengths from 100–500 μm (Williams 2010), while older SNRs are heated by the ISRF and their dust is at a similar temperature to that of interstellar dust (see Chapter 4).

Collisionally heated grains in SNRs are typically warmed to temperatures of 30–70 K (Seok et al. 2008; Williams 2010), or cooler. Although IR line emission can become strong once a shock reaches its radiative phase, it usually does not exist in fast, non-radiative shocks (Williams 2010). If remnants are in the Sedov phase (Badenes, Maoz & Draine 2010), then non-radiative are dominate.

From spatial correlation of X-ray and IR emission in the shell of SNR Kes 75 (G29.7−0.3), Temim et al. (2012) found 10^{-2} $M_{\odot}$ of dust collisionally heated to ∼140 K by the X-ray emitting gas. Andersen et al. (2011) explored a sample of 14 Galactic

[10]In probability theory, a purely stochastic system is one whose state is non-deterministic (i.e., "random") so that the subsequent state of the system is determined probabilistically.

SNRs, found large grains at temperatures of 29–66 K (higher than a typical ISM temperature of 15-20 K), all these SNRs also show evidence for PAH emission, with dust moderately heated typically by 30-100 times the solar neighborhood ISRF. The Kepler SNR was observed by *Spitzer* and studied by Blair et al. (2007), who found no newly formed dust in ejecta material but significant sputtering of CSM dust (see 1.3.4). Williams et al. (2012) also used *Spitzer* data of this SNR, found the dust formed during the AGB stage, collisionaly heated to 50–150 K by slower shocks (a few hundred km s^{-1}) into moderate density material (n $\sim$ 50–250 cm^{-3}). Gomez et al. (2012a) used *Herschel* data and shown that SNR Kepler swept up CSM dust and SNR Tycho swept ISM dust.

1.3.2 Dust connected to SN/SNRs ejecta and/or interstellar environment

Models predict the total dust production in CC SN ejecta to be 0.1−1 $M_\odot$ (Kozasa et al. 2009; Nozawa et al. 2003; Cherchneff & Dwek 2010; Todini & Ferrara 2001). A somewhat newer estimate by Sarangi & Cherchneff (2013) predicts more moderate dust masses of 0.03−0.09 $M_\odot$ per SN. In their model, they include the formation of molecules and dust clusters in the ejecta, where the dust builds up from small to large mass in $\sim$5 yr after the explosion, but chemical reactions that form elements are stratified in the layers post explosion, which limits the available metals free to form dust (while other models assume all elements free to form dust). Kozasa et al. (2009) argued that the size of produced/survived dust in SNe should depend on the SN type, being affected by the gas density in the ejecta, and by the time of the arrival, and the strength of, the reverse shock.

There have been many claims of observations of dust formation in more distant SNe (Elmhamdi et al. 2003; Fox et al. 2009; Sakon et al. 2009; Inserra et al. 2011), though often SNe are seen to destroy pre-existing dust (Botticella et al. 2009; Wesson et al. 2010; Andrews et al. 2011). The amount of newly formed dust in the ejecta of several CC SN based on recent observations is usually in the range $10^{-3} - 10^{-5}$ $M_\odot$.

At epochs between 214 and 795 days after explosion, similar dust masses were found for the Type II-P SNe SN 1999em, SN 2003gd, SN 2004et and SN 2005af (Gall 2010). Also, there are many examples of dust formed in IIn SNe and luminous blue variables (LBVs)[11], while significant amounts in Ic, Ib or IIb SNe have not been observed, except in Cas A which is probably of type IIb (Krause et al. 2008). For the comprehensive detailed list of the amounts of dust observed in various SNe, see Gall (2010).

Szalai & Vinkó (2013) observed twelve type IIP SNe, older than 300 days using *Spitzer* data. Their study suggested that two SNe have formed dust in their environment, three were not identified as point sources and the MIR fluxes of the other seven might originate from pre-existing circumstellar or interstellar dust. Their conclusion is that warm new dust in the environment of SNe contributes only marginally to the cosmic dust content.

Knowing that CSM has been detected around Ia SNe (Patat et al. 2007), it is necessary to find how much of dust can surround a SN Ia, since they are used as a distance estimator. The possible dust mass in the direction of these objects is so low, that only upper limits could be placed using the best telescopes and if Ia SNe do produce some dust, it would not be easy to detect it. The sensitivity of current estimations is 1−2 orders of magnitude larger than the circumstellar (CS) dust masses expected to exist around SNe Ia, $\sim 10^{-4}$ $M_{\odot}$ (Johansson, Amanullah & Goobar 2013). They used *Herschel* data of three nearby SNe to constrain the upper limits on the amount of pre-existing dust in the CS environment, within two weeks after maximum brightness, and found it to be less than 0.1 $M_{\odot}$. Also, Gomez et al. (2012a) noticed the lack of dust production in the Galactic Ia SNRs Kepler and Tycho using *Herschel* data. They detected $\sim 10^{-3}$ $M_{\odot}$ swept-up material warmed up to ∼80-90 K, but they found no evidence of ≥ 0.07 $M_{\odot}$ of cold dust formed in Ia SNRs, which means that if there is any dust formed in the ejecta of Type Ia SN, it has significantly less mass than

[11]LBVs are massive evolved stars that show unpredictable and sometimes dramatic variations in both their spectra and their brightness.

ejecta formed after CC explosions.

As it is difficult to resolve the dust emission in young SNe (<30 yr), it is not easy to be sure if the observed dust is new dust – formed in the ejecta, or just heated pre-existing dust (Rho et al. 2009; van Loon 2010; Otsuka et al. 2010). Smith et al. (2013) have observed a SN IIn, SN 2009ip claiming that pre-SN outbursts are able to efficiently form dust into which SN ejecta and radiation will propagate. Also, Maeda et al. (2013) reported dust grains formed in a dense cooling (CSM) shell of SN 2010JL (type IIn) one and half years after the explosion. Sakon et al. (2009) suggested that although newly formed dust in SN ejecta is $10^{-3} - 10^{-5}$ $M_{\odot}$, a significant amount of dust is also condensed in the mass-loss wind of SN 2006JC, prior to the SN explosion.

Non-detection of the cold dust in SNe does not necessary mean that these objects do not form significant quantities of dust, as (a) they are young (< 5 yr) and the dust needs time to condense (Gall et al. 2014; Wesson et al. 2015), (b) there is no resolved submm information for these sources so the current observations could be only lower limits.

Many studies describe the small amounts of warm dust ($\sim 10^{-3}$-10^{-2} $M_{\odot}$) formed in the ejecta in young SNRs, like Cas A (Rho et al. 2008; Nozawa et al. 2010), Crab (Temim et al. 2012; Temim et al. 2013), E0102 (Stanimirović et al. 2005; Sandstrom et al. 2009), N 132D and G11.2−0.3 (Rho et al. 2009), Kepler's SNR (Morgan et al. 2003) and B0540−69.3 (Williams et al. 2008). Since the warm dust masses were too low compared to models, it was expected that there could be colder ejecta dust, detectable at only FIR/submm wavelengths.

A significant quantity of dust was explored in Cas A using *SCUBA* polarimethry (Dunne et al. 2009), while Barlow et al. (2010) used *Herschel* data and found for the first time a cold dust component at ∼35 K located interior to the reverse shock with a mass ∼0.075 $M_{\odot}$. Matsuura et al. (2011) detected ∼0.4 $M_{\odot}$ of cold dust in SN 1987A while Gomez et al. (2012b) detected ∼0.1 $M_{\odot}$ of ∼33 K dust in the Crab Nebula, which suggested that dust formation in SNe is efficient. However, not many other SNRs have been detected to produce significant amounts of cold dust so far, but this is limited by the confusion along the line of sight towards SNRs in our Galaxy.

Then, many examples of large amounts of dust present in high-redshift (z) galaxies and quasars were found, with ages of less than 1 Gyr which corresponds to $z \geq 6$ (Gall 2010; Mattsson 2011). Since at high-z there are not many AGB stars, as they have had no time to form, and AGB stars are considered to be the most important dust sources in the local Universe (see Gall, Hjorth & Andersen 2011 and references within), there was a need to explain the existence of dust at high-z. Therefore, SNe were expected to be the main dust producers in high-z galaxies (Morgan & Edmunds 2003) and this expectation was strongly supported by the detection of $\sim$1 $M_\odot$ of dust in the ejecta of SN 1987A (Matsuura et al. 2011; Lakićević et al. 2011; Lakićević et al. 2012a; Lakićević et al. 2012b; Indebetouw et al. 2014).

However, the masses of warm and cold dust detected in SNe/SNRs and surroundings were too low – $10^{-6} - 10^{-3}$ $M_\odot$ (except for SN 1987A, Crab Nebula and Cas A), much lower than the expectations from models and much below that needed to explain the existence of the dust at high-z (Silvia, Smith & Shull 2010). Therefore, SN 1987A is a special object for understanding this problem. Questions still remain, e.g., whether selection effects are a problem for detecting the cold dust in SNe/SNRs or whether the dust in SN 1987A, Cas A and the Crab Nebula will have a short lifetime if ultimately dust is destroyed by the reverse shocks.

1.3.3 Molecules formation in SNe/SNRs

Besides dust production, SNe/SNRs produce molecules. The ejecta of at least eight SNe have been observed in the vibrational transitions of CO within the first few years after their explosion (Cherchneff & Sarangi 2011). Therefore, SNe could be important sites of molecule formation resulting in species such as CO, SiO, SiS, O_2, SO, and CO_2 (Cherchneff & Lilly 2008; Rho et al. 2012).

In the Cas A remnant, Rho et al. (2012) detected vibrationally excited ^{12}CO with a mass of $\sim 10^{-6}$ $M_\odot$ and temperature as high as 900−1400 K, using *AKARI*. The observed positions include both shocked and unshocked ejecta at the center, indicating that CO molecules form in the ejecta in the early phase, suggesting that significant

amounts of carbon may have been locked up in CO soon after the explosion (330 yrs ago). Therefore, less carbon is available to form carbonaceous dust in SNe than is currently thought and some of the ejecta mass could be in molecular form. Surprisingly, CO was not efficiently destroyed by reactions with ionized He or the energetic electrons created by the decay of radioactive nuclei. Finally, Wallstrom et al. (2013) reported the rotational emission from CO in a knot in the Cas A remnant, detected with *Herschel*, believed to be reformed in the post-shock gas in the past several years (∼300 yrs after the explosion).

Rho et al. (2011) found processing of PAH molecules in SNR N132D and ∼14 other SNRs. They claimed that PAHs in this remnant have survived behind the forward shock, and that both large and small PAHs survive in low velocity shocks. Also, they found a strong correlation between PAH detection and carbonaceous small grains, while a few SNRs with dominant silicate dust lack PAH features.

Not only SNRs, stars and molecular clouds are significant molecule producers. Around 180 various molecules have been detected so far in the ISM (Belloche et al. 2014). In the meteorites found on Earth, there were identified more than 80 amino acids (the building blocks of proteins). It is still not understood how widespread these complex organic molecules are in galaxies and how complex these molecules formed in ISM can be.

1.3.4 Dust destruction, heating and cooling in SNRs

Many studies have predicted and modelled that shocks can sputter the interstellar dust and thus potentially modify its abundance and size distribution, as well as heat up the dust (Jones et al. 1994; Borkowski & Dwek 1995; Williams, Chu & Gruendl 2006; Borkowski et al. 2006; Reach et al. 2006; Guillet, Jones & Pineau des Forêts 2009; Williams 2010; Andersen et al. 2011; Rho et al. 2011). For a homogeneous ISM and under the assumption that silicon and carbon grains are equally mixed, Dwek, Galliano & Jones (2007) demonstrated that the mass of the ISM completely cleared of dust through one single SNR could be $\sim$ 1200 $M_{\odot}$. Andersen et al. (2011) studied Galactic

SNRs that interact with molecular clouds and found evidence for dust processing by shocks. SN/SNR shocks are one of the primary sites for destroying, fragmenting and altering interstellar PAHs and dust.

The same collisions that heat grains can also destroy them via sputtering. The most common ways for sputtering of grains in SNRs are thermal sputtering, when energetic particles knock atoms off the grain surface (Casoli, Lequeux & David 1998), more often in fast shocks, $v > 150$ km s^{-1} and grain–grain collisions, dominant in slower shocks, ≤ 50–80 km s^{-1} (Jones et al. 1994), often called shattering. Sputtering is most effective on small grains (SG) (Andersen et al. 2011), resulting in a deficit of SG in SNRs compared to the ISM. Shattering destroys primarily big grains (BG), such as silicates, as opposed to, for instance, graphitic grains. BG become SG which produces an increased SG-to-BG ratio (Andersen et al. 2011). While sputtering is a well-understood process by theory and experiment, grain-fragmentation and vaporisation by grain-grain collisions are less understood since the experimental data can not be applied to the realm of sub-micron interstellar dust particles. It is known that magnetic field frozen into the gas causes charged grains to gyrate and accelerate behind the shock front and results in the enhancement of the sputtering rate and the grain-grain collision frequency (Nozawa & Kozasa 2006).

For sub-micron interstellar grains present in SNR shocks, grain cooling is proportional to their volume, while collisional heating increases with the grain geometrical cross section (Sankrit et al. 2010). Small grains emit their energy at higher temperatures than large grains because of their larger surface-to-volume ratios. Dust sputtering by thermal ions is more effective in destroying small grains than large grains also because of the higher surface-to-volume ratios.

The sputtering of circumstellar dust in the Kepler SNR (SN 1604) was investigated by Blair et al. (2007) by modelling the ratio of fluxes at 70 and 24 μm. They estimated the current mass of warm dust of 5.4 $\times 10^{-4}$ M$_{\odot}$ and inferred an original mass before sputtering to be of about 3×10^{-3} M$_{\odot}$.

Arendt et al. (2010) used *Spitzer* data, pointing out the interaction between the shock of young SNR Puppis A (3700 years old) and a molecular cloud, concluding that

a significant amount of PAHs is destroyed and that approximately 25% of the mass of the dust was destroyed in that place.

Sankrit et al. (2010) used *Spitzer* images of the SNR Cygnus Loop, ∼10 000 years old (Uchida et al. 2009), measuring the ratio of the flux densities on 70 and 24 μm in the post-shock region. This ratio rises from about 14 at a distance of 0.1′ behind the shock front to about 22 in a zone of 0.75′ further downstream, as grains are heated and destroyed in the hot plasma. Dust is destroyed by the shocks of velocity about 350 km s^{-1}. They suggest that also non-thermal sputtering (sputtering due to motion of the grains relative to the gas, where dust grains enter the shock with some velocity) contributes significantly to the dust destruction in the shocked region. Their model suggests that about 35% by mass of the grains are destroyed over a 0.14 pc region behind a shock front in about 1350 years.

1.4 Objectives of the thesis work

The question of the dust production in SNe and SNRs is important because they might be significant producers of the dust in galaxies as well as in the early Universe. In this thesis, I am trying to investigate whether SNRs produce dust, how much is formed and how long does it survive? Could we observe this dust with *Herschel* or with other instruments? If such dust exists, how much is created in the SN and how much in the SNR phase? Would SNRs show something that SN observations have not shown? How much of interstellar dust is destroyed in SNRs? What is the lifetime of interstellar dust in various galaxies? Is sputtering stronger in more massive and dense galaxies? How does the dust production/survival depend on the SN/SNR type? Could SNe explain the dust at high redshifts? How do the interstellar environments of SNRs differ according to SNR type?

To this end, I explored dust production in SN 1987A since it is the only SNR in the LMC observed to produce cold dust. It was not known at the time whether the dust was produced from SNe ejecta or from the surrounding ISM.

In Chapter 3, I describe my observations and analysis of the data of SN 1987A at FIR, submm and mm wavelengths (using *Herschel*, *APEX* and *ATCA* data) which contributed to an important scientific result, the first observational confirmation of dust production in the ejecta revealed using resolved images of the SNR with the *ALMA* telescope. This work has enormous scientific significance as it is a proof of an important astrophysical phenomenon, but is possible due to recent advances in (sub)mm astronomy which has opened new horizons – observations seemed impossible ten years ago.

In Chapter 4, I perform a population study of LMC SNRs using data from *Spitzer* and *Herschel*. Since LMC SNRs were not detected with *Herschel* data at first sight (except in SN 1987A), in this thesis I have attempted to find any signatures that SNe/SNRs would have on the dust properties of the LMC, in terms of both production and sputtering. Several previous *Spitzer* measurements concluded that significant sputtering of warm dust had taken place, but did not measure this for the cold dust (which makes up $\simeq$90% of the dust mass in most galaxies; Dunne & Eales 2001). Using *Herschel data*, I find that SNRs are still net dust destroyers and estimate the amounts of dust sputtered. I also estimated how much of the cold dust is sputtered by the whole population of SNRs in the LMC and derived the lifetime of the dust in SNR environments.

2 Instrumentation and methodology

2.1 Description of the instruments that I use in this work

In this thesis I used data from the *Herschel* and *Spitzer* telescopes, which are single-dish, space borne observatories, observing on FIR and MIR wavelengths. The second group of telescopes here are ground-based (sub-)mm and cm telescopes, including the *ALMA* and *ATCA* interferometers, respectively, and a submm single dish, *APEX*. For the background emission to be low enough, the *Spitzer Space Telescope* and *Herschel Space Observatory* are cooled to very low temperatures by evaporating liquid helium. While *Spitzer* uses cameras and *ALMA* and *ATCA* use receivers, *Herschel* and *APEX* use bolometers as detectors.

A bolometer is a device for measuring the power of incident electromagnetic radiation via the heating of a material with a temperature-dependent electrical resistance. For submm wavelengths (from around 200 μm to 1 mm), bolometers are among the most sensitive available detectors. To achieve the best sensitivity, they must be cooled down to a fraction of a degree above absolute zero (typically from 50–300 mK). Notable examples of bolometers in astronomy are the *Herschel Space Observatory*, the *James Clerk Maxwell Telescope*, the *Stratospheric Observatory for Infra-red Astronomy* (*SOFIA*) and *APEX*.

2.1.1 Observation techniques at MIR, FIR and submm wavelengths

2.1.1.1 *Herschel Space Observatory*

The *Herschel Space Observatory* (Pilbratt et al. 2010) was active from 2009 to 2013, having the largest single mirror ever built for a space telescope during that time (3.5 meters) and instruments sensitive to the FIR and submm wavebands (55−672 μm).

The light reflected by the mirror was focused onto three instruments, whose detectors were kept at temperatures below 2 K. The instruments were cooled with 2 300 litres of liquid helium at 1.4 K. The supply of helium was the fundamental limit to the lifetime of the telescope.

Herschel was sited at the second Lagrangian point (L2) of the Earth-Sun system, 1 500 000 kilometres from Earth. *Herschel* is named after Sir William Herschel, the discoverer of the infra-red spectrum and planet Uranus, and his sister and collaborator Caroline Herschel. *Herschel* was used for observing of objects in the Solar System, the MW, studying galactic formation and evolution, star formation and its interaction with the ISM and molecular chemistry across the Universe.

Herschel had three scientific instruments: *HIFI* (Heterodyne Instrument for the Far Infra-red) – a very high resolution heterodyne spectrometer, *PACS* (Photo-detector Array Camera and Spectrometer) – an imaging photometer and medium resolution grating spectrometer, and *SPIRE* (Spectral and Photometric Imaging Receiver) – an imaging photometer and an imaging Fourier transform spectrometer. The three instruments complement each other providing imaging capability in six bands with centre wavelengths of 70, 100, 160, 250, 350, and 500 μm and imaging spectroscopy over the entire *Herschel* wavelength coverage. The resolution of *PACS* camera was $6.7'' \times 6.9''$ and $10.6'' \times 12.1''$ at 100 and 160 μm, respectively. The resolution of *SPIRE* camera was $18.2''$, $24.9''$ and $36.3''$ for at 250, 350, 500 μm, respectively.

In this thesis, I used data from the *Herschel Observatory open time key program*, entitled *HERschel Inventory of The Agents of Galaxy Evolution* (*HERITAGE*), mapping the LMC and SMC (Meixner et al. 2013; Gordon et al. 2011). *Heritage* performed a uniform survey of the LMC and SMC with *SPIRE* at 250, 350, and 500 μm and with *PACS* at 100 and 160 μm (Meixner et al. 2013).

2.1.1.2 *Spitzer Space Telescope*

The *Spitzer Space Telescope* was launched in August of 2003 and began full-time science operations in 2004. The main goals of *Spitzer* were to investigate dust processes in stars,

young stellar objects, ISM, galaxies and planets. *Spitzer* follows a heliocentric orbit that recedes away from Earth at the rate of 0.1 astronomical units (AU) per year. Both the Earth and the Moon are bright IR sources, and the telescope had to be placed far away from both to achieve its desired sensitivity.

There are three instruments on *Spitzer*. *Infra-red Array Camera* (*IRAC*) is a near-IR and MIR camera which operates simultaneously at four wavelengths. Four channels (3.6, 4.5, 5.8 and 8 μm), provide photometric capabilities with angular resolution of 1.8″. The *Infra-red Spectrograph* (*IRS*) is an IR spectrometer which operates at the wavelengths 5–40 μm. The *Multiband Imaging Photometer for Spitzer* (*MIPS*) has three detector arrays for photometric imaging in the FIR, centred at 24, 70 and 160 μm, with resolutions of 6″, 18″ and 40″, respectively.

The spacecraft consists of an 85-cm telescope with 3 separate instruments which can be placed in the field of view at any given time. A sun-shield, which always faces the Sun, protects the entire system, acting as the first line of defence against photons that would warm the telescope and damage the instruments. The telescope was cryogenically cooled, with liquid helium, keeping the detectors at 4.2 K, necessary for science observations in the MIR and FIR. The coolant ran out in May of 2009. Thus began the "warm mission" of *Spitzer*, in which it is possible to observe only at the shortest IR wavelengths (3.6 and 4.5 μm), with the *IRAC* instrument; although expected to last until 2013 it is still functional.

In this work I use data from the *Surveying the Agents of a Galaxy's Evolution* (*SAGE*) project, in the LMC. The survey covered $7^\circ \times 7^\circ$ of the LMC using the *IRAC* (3.6, 4.5, 5.8, and 8 μm) and *MIPS* (24, 70, and 160 μm) instruments (Meixner et al. 2006) though here, I use the 24 and 70 μm data. The scientific goals of *SAGE* were to study of star formation, evolved stars, and ISM.

2.1.1.3 *ATCA* (*Australia Telescope Compact Array*)

The *Australia Telescope Compact Array* (*ATCA*) is an array of six 22-m antennae used for radio astronomy, about 500 km North-West of Sydney, operating from 1988. The

first five antennae can be moved along its 3 km railtracks to change the beam size or resolution available at each observing frequency, while the sixth antenna is in a fixed position a further 3 km from the end of that railtrack. The *ATCA* operates in the millimetre and centimetre wavebands, specifically those centred around 20, 13, 6, 3, 1.2, 0.7 and 0.3 cm. The *ATCA* is operated in one of 17 standard configurations (which are in use for typically 3 weeks at a time) ranging from maximum baselines of 75 meters up to 6 km. *ATCA* is used for the studying of synchrotron and free-free radiation, both for imaging and spectral lines.

The field of view (primary beam, HPBW[1]) ranges from $\sim 30''$ at 3 mm to $\sim 42'$ at 16 cm. The resolution (HPBW, synthesized beam) ranges from $\sim 1''$ at 3 mm to $\sim 9''$ at 16 cm. The flux sensitivity (1 σ Gausian-noise level) obtained in 12 hr ranges from 83 μJy/beam for 3 mm to 4 μJy/beam at 16 cm.

2.1.1.4 *APEX* (*Atacama Pathfinder EXperiment*)

APEX (*Atacama Pathfinder Experiment*), is a collaboration between the Max Planck Institut für Radioastronomie (MPIfR), Onsala Space Observatory (OSO), and the European Southern Observatory (ESO) to construct and operate a single dish, ground based antenna. *APEX* is a radio telescope located at 5 100 meters above sea level, at the Llano de Chajnantor Observatory in the Atacama desert. The main dish has a diameter of 12 meters and consists of 264 aluminium panels with an average surface accuracy of 17 μm. *APEX* observes at submm wavelengths (0.2–1.5 mm) – between FIR light and radio waves (Siringo et al. 2009). The telescope was officially inaugurated on September 25, 2005. The *APEX* telescope served as a pathfinder for subsequent (sub)mm and (far)IR missions, *ALMA*, *Herschel* and *SOFIA*, by exploring their wavelength windows.

The first instrument on *APEX* used in this thesis is *the Large APEX Bolometer Camera* (*LABOCA*), observing at 345 GHz (870 μm), with 295 composite bolometers

[1]HPBW is half power beam width. The same parameter is often mentioned as a FWHP (full width to half power).

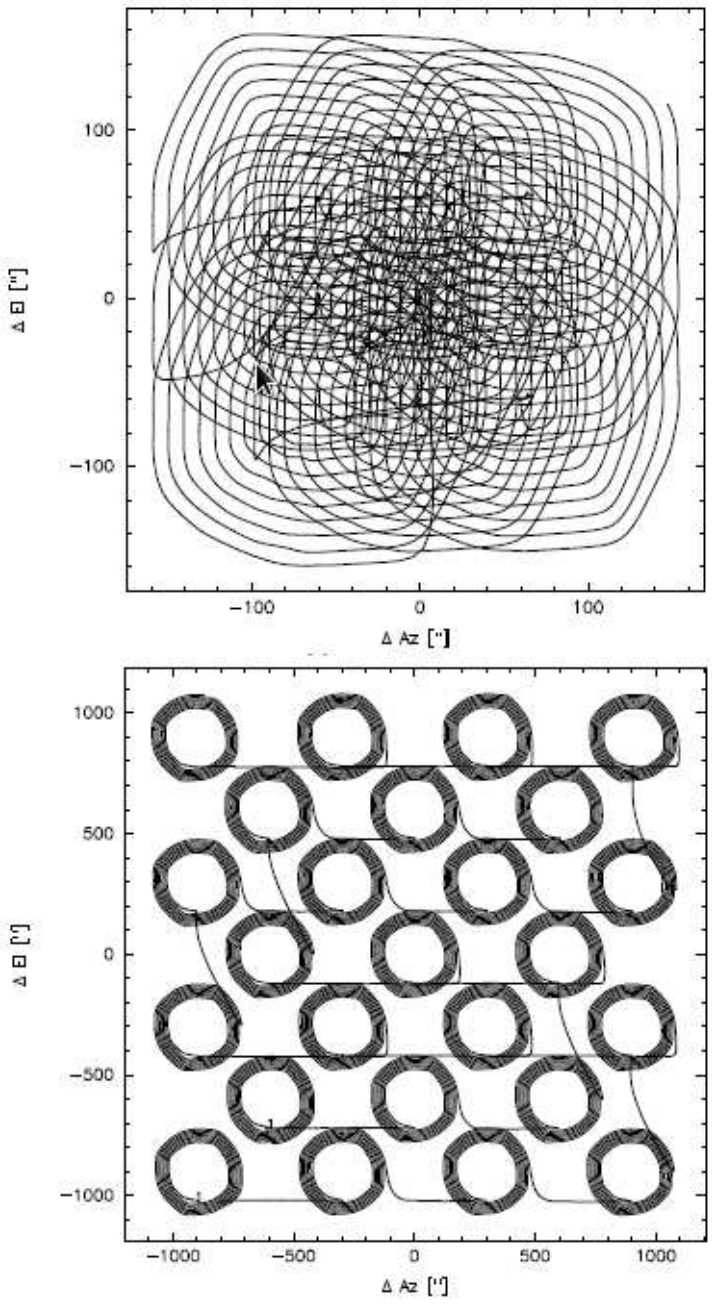

Figure 2.1: Examples of raster-spiral patterns with the *APEX* telescope, taken from Siringo et al. (2009). In the top panel the compact pattern is shown, optimized to map the field of view of *LABOCA*. In the bottom panel the large scale map is shown, consisting of 25 raster positions, covering a larger field of $0.5° \times 0.5°$.

arranged in an hexagonal layout with a field of view of $11' \times 11'$. In order to detect the tiny temperature changes caused by the faint submm radiation, each of these bolometers is cooled to less than 0.3 K above absolute zero. The angular resolution is $18.6''$ and the sensitivity is 40 mJy $s^{1/2}$[2].

The second instrument on *APEX* used is the *Submillimetre APEX Bolometer Camera* (*SABOCA*), a 39 bolometer array operating at 850 GHz (350 μm), within a 120-GHz wide band ($\Delta\nu/\nu \approx 1/7$) (Siringo et al. 2010). *SABOCA* was provided with a hardware/software infrastructure similar to that of *LABOCA*. The angular resolution was $\sim 8''$, field of view was $1.5'$ and the average sensitivity is 750 mJy $s^{1/2}$.

The main obstacle to observations at these wavelengths is bright emission from the water vapour in the Earth's atmosphere. This is exacerbated by the amount of water vapour along the line of sight can change quickly, giving rise to instabilities in emission and transmission, called *skynoise*. The technique that *LABOCA* uses to minimize these effects is called *fast scanning*; the bolometers look simultaneously at different points of the sky, therefore chopping is not needed. The contribution of the atmosphere and a part of the instrumental noise is strongly correlated in all bolometers and a post-detection analysis of the correlation across the array makes it possible to extract the signals of astronomical interest from the atmospheric foregrounds (Siringo et al. 2009).

The *LABOCA* control system currently supports two basic scanning modes: spiral scanning patterns and on the-fly (OTF) maps (*SABOCA* has similar scanning modes, but scaled to the different size of the beam and array). Spirals are done with a constant angular speed and an increasing radius. The spiral patterns are kept compact (maximum radius $\leq 2'$), where most of the time is spent on the integration of the central $11'$ of the array. Spiral modes are preferred for pointing scans on sources with flux densities down to a few Jy. For fainter sources, the basic spiral pattern can be combined with a raster mapping mode (raster-spirals), resulting in even denser sampling

[2]That sensitivity is the flux density per second integration time of a point source that generates a signal with a signal-to-noise ratio of one.

and longer integration time (see Fig. 2.1, top panel, from Siringo et al. 2009). These compact raster-spirals give excellent results for sources smaller than the field of view of *LABOCA* and they are suitable for fainter sources. The bottom panel of Fig. 2.1 shows an example of a raster of spirals optimized to give an homogeneous coverage across a field much larger than the field of view, the so-called mapping mode. In this case the spiral starts with a large radius and follows an almost circular pattern.

OTF scans are rectangular scanning patterns produced moving back-and-forth along alternating rows with constant speed and accelerating only at the turnarounds. OTF patterns are typically used to map sky areas much larger than the field of view, up to $\sim 2^{\circ}$.

Atmospheric absorption attenuates the astronomical signals as $e^{-\tau}$, where τ is the dimensionless optical depth (Siringo et al. 2009). The accuracy of calibration depends on the precision of the determination of τ. τ is determined in two different ways. The first one is from precipitable water vapour (PWV) level measured every minute along the line of sight. PWV is converted to τ using an atmospheric transmission model and the passband (range of frequencies or wavelengths that can pass through a filter without being attenuated) of *APEX*. The second method uses skydips, scans that measure the power of the atmospheric emission as a function of the airmass while tipping the telescope from high to low elevation. As the telescope moves from high to low elevation, τ increases with airmass. The increasing atmospheric load produces an increase of signal, in sky temperature (T_{eff}). The dependence of T_{eff} on elevation is fitted to determine the zenith opacity τ.

2.1.1.5 *ALMA* (*Atacama Large Millimeter/submillimeter Array*)

ALMA (the *Atacama Large Millimeter/submillimeter Array*) is one of the largest ground-based astronomical projects of this decade and is the major new facility for observations in the mm/submm regime, also placed on the Chajnantor plateau in the Chilean Andes. *ALMA* is a single radio telescope composed of 66 high-precision antennas, an astronomical interferometer, operating at wavelengths of 0.3 to 9.6 mm.

Its main 12-metre array has fifty antennas, 12 metres in diameter, acting together as a single telescope. An additional compact array of four 12-metre and twelve 7-metre antennas complements this. The antennas are spread across the desert plateau over distances from 150 metres to 16 kilometres, which gives unprecedented sensitivity and a spatial resolution up to 10 milliarcseconds, ten times better than the *Very Large Array* and five times better than the *Hubble Space Telescope*.

2.1.2 Radio Telescopes

Radio telescopes have two basic components: (1) a large radio antenna and (2) a sensitive radiometer or radio receiver. The sensitivity of a radio telescope depends on the area and efficiency of the antenna and the sensitivity of the radio receiver used to amplify and detect the signals. For broadband continuum emission the sensitivity also depends on the bandwidth of the receiver. The most familiar type of radio telescope is the radio reflector consisting of a parabolic antenna – the so-called dish. A digital computer is used to drive the telescope to follow the motion of a radio source across the sky. The performance of a radio telescope is limited by various factors: the accuracy of the reflecting surface, the effect of wind load, thermal deformations that cause differential expansion and contraction, and deflections due to changes in gravitational forces as the antenna is pointed to different parts of the sky.

The angular resolution, or ability of a radio telescope to distinguish fine detail in the sky, depends on the wavelength of observations divided by the size of the instrument, $R = 2 \times 10^5 \lambda/D$ (factor 2×10^5 is the conversion from radians to arc seconds, 1 rad=206265″). Because radio telescopes operate at long wavelengths, radio telescopes must be much larger in size than other telescopes. The high angular resolution of radio telescopes is achieved by using the principles of interferometry to synthesize a very large effective aperture from a number of small elements so that $R = 2 \times 10^5 \lambda/B$, where B is the baseline or the telescope separation. Most radio arrays have angular resolution between 0.1 and 10″.

In my work I used the radio telescopes *ATCA*, *ALMA* and *APEX*, of which the

first two are interferometers. Arrays of antennas are constructed to synthesize a large aperture using several small antennas, aided by the rotation of Earth. Movable antenna elements combined with the rotation of the Earth and long observing time can sample a sufficient number of Fourier components with which to synthesize the effect of a large aperture and thereby reconstruct high-resolution images of the radio sky.

In a simple two-element radio interferometer (Fig. 2.2), the signals from the radio source alternately arrive in phase and out of phase as the Earth rotates (and changes the source inclination angle Θ) which causes changes in the path difference from the source to the two elements of the interferometer. If B is the distance between the antennas, the path difference between the two signals is $P = B\ \mathrm{Cos}\Theta$. If the P is a whole number of λ, radio waves detected by two telescopes are in phase and the combined signal has maximum intensity, which is called constructive interference. If the P is a whole number of $\lambda/2$ then the waves are out of phase, cancel each other and the combined signal has minimum intensity and that is destructive interference. This produces interference fringes in a manner similar to that in an optical interferometer. At each telescope the incoming radio waves are detected at the telescope focus and are converted into electrical signals. These signals are sent to a correlator where they are sampled and combined. In the correlator the signals are multiplied together and are averaged over a sampling time and the correlated signal is called the source visibility. The visibility amplitude is a measure of the detected flux density from the source. The visibility phase provides information on the source position. The visibility amplitudes and phases are stored for later analysis.

Single-baseline interferometers can be used to measure the positions of unresolved sources, to an accuracy comparable to the angular resolution. To make an image of a more complex radio source, it is necessary to use an array of radio telescopes which has a number of baselines of different lengths. The longer baselines resolve the small-scale structure in the source. The shorter baselines provide information on the larger scale structures. Each interferometer pair measures one "Fourier component" of the brightness distribution of the radio source, measuring at one discrete spatial frequency. Spatial frequency describes how fast the brightness changes with the direction (angle)

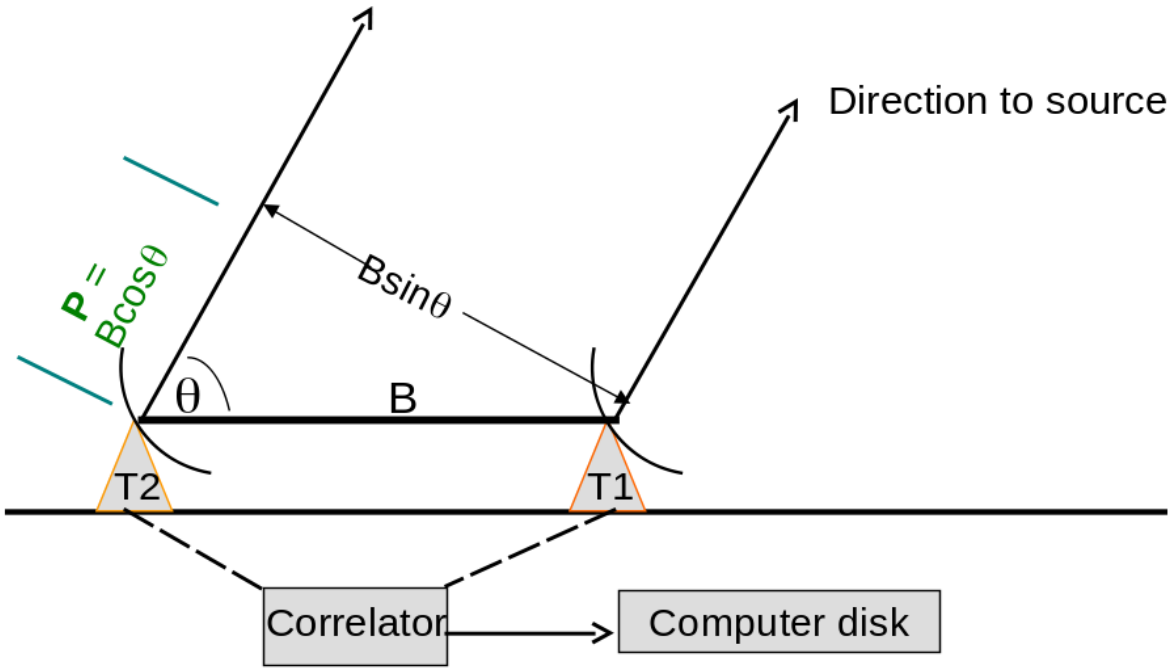

Figure 2.2: A simple two-element radio interferometer, consisting of two radio telescopes at the distance B. The angle Θ is changing as the Earth rotates. The image is taken from www.atnf.csiro.au/people/Julie.Grant/astrotech/radio_intro_Swinburne.ppt.

of observation.

As the Earth rotates the direction of the baselines as seen from the source changes. Over an interval of twelve hours, each baseline will have all possible orientations relative to the source (Fig. 2.3i). Note that it is the projected baseline that changes.

We call the aperture plane the plane at the origin of a rectangular coordinate system (u,v,w) with w pointing towards the source. Thus, the projected baseline can be specified using (u,v) coordinates. u gives the East-West component, and v gives the North-South component of the baseline. As seen from the source, each baseline traces out an ellipse in the (u,v) plane with one telescope at the centre of that ellipse (Fig. 2.3ii). Only if the source is on the celestial pole, the projections to (u,v) plane will be a circle, while if the source is on the celestial equator, the projections would be a line (Fig. 2.3iv), therefore in this case it is necessary to have some antennas separated along North-South axis, to have better covering of (u,v) plane.

Similarly, let the two dimensional electric field distribution on the sky be centred on another coordinate system (l,m), see Fig. 2.3iii. On the (u,v) plane, the electric field distribution $\epsilon(u, v)$ is a result of the electric field distribution $V(l, m)$ on the sky. Auto-correlation[3] and the Fourier transformation of $\epsilon(u, v)$ would give us $I(l, m)$, the intensity field distribution of the source. This is the relation between the intensity map of radio source on the sky with the aperture illumination.

The correlation products between any pair of antennae are used to fill the (u,v) plane. The (u,v) coordinates are baseline distances and they are expressed in units of kilo-wavelengths (Fig. 2.4). For example at 6 cm, 100 kλ is equal to 6 km. If there are n antennae in the array, the number of cross correlation terms is $n(n-1)/2$, and that is the number of the baselines for that array. For an East-West array of telescopes like

[3]Cross-correlation is a measure of similarity between two waveforms as a function of a time-lag applied to one of them. For two continuous functions of time t denoted as $f(t)$ and $g(t)$, the cross-correlation $r(\tau)$ is expressed as

$$r(\tau) = \int_{-\infty}^{\infty} f^*(\tau) g(t+\tau) d\tau \tag{2.1}$$

where f^* is the complex conjugate of f. A special case of cross-correlation is the auto-correlation where the signal is correlated with itself.

the *ATCA*, the 15 baselines trace out a set of 15 concentric ellipses in the (*u*,*v*) plane in 12 h (Fig. 2.4).

The connection between the real sky brightness, $I(l, m)$ and the visibility (measured by the interferometer) $\nu(u, v, w)$, is the Fourier transform:

$$\nu(u, v) = \int\int \frac{A'I(l, m)}{\sqrt{(1 - l^2 - m^2)}} e^{-2\pi i(ul+vm)} dldm, \tag{2.2}$$

where $A'(l, m)$ is the primary beam response.

Finally, the resolution of a radio telescope can be obtained using the formula for diffraction through a circular aperture as $R = 1.22\lambda/B$, where the factor 1.22 is derived from a calculation of the position of the first dark circular ring surrounding the central Airy disc[4] of the diffraction pattern.

2.2 Modelling the spectral energy distribution

In this thesis I mostly model the radiation at ≥ 100 μm from different sources. This includes dust emission which is modeled using a modified blackbody, heated by the ISRF or collisions (Section 1.3.1).

In addition to the mechanisms described in Section 1.3.1, at these wavelengths synchrotron radiation and/or some Bremsstrahlung (free-free) radiation can also contribute. Synchrotron originates from accelerated particles orbiting around magnetic field lines, and is very important in SNRs (see Section 1.2.1). Free-free emission is produced by the deceleration of any charged particle when deflected by another charged particle and has a continuous spectrum. The upper limit of free-free emission is estimated only in my work on SN 1987A (Chapter 3) and was found to be negligible. The synchrotron contribution was also only estimated for SN 1987A, since it is not easy to estimate this component for old SNRs, because the radiation from the dust that we

[4]The diffraction pattern resulting from a uniformly-illuminated circular aperture has a bright region in the center, known as the Airy disk which together with the series of concentric bright rings around is called the Airy pattern.

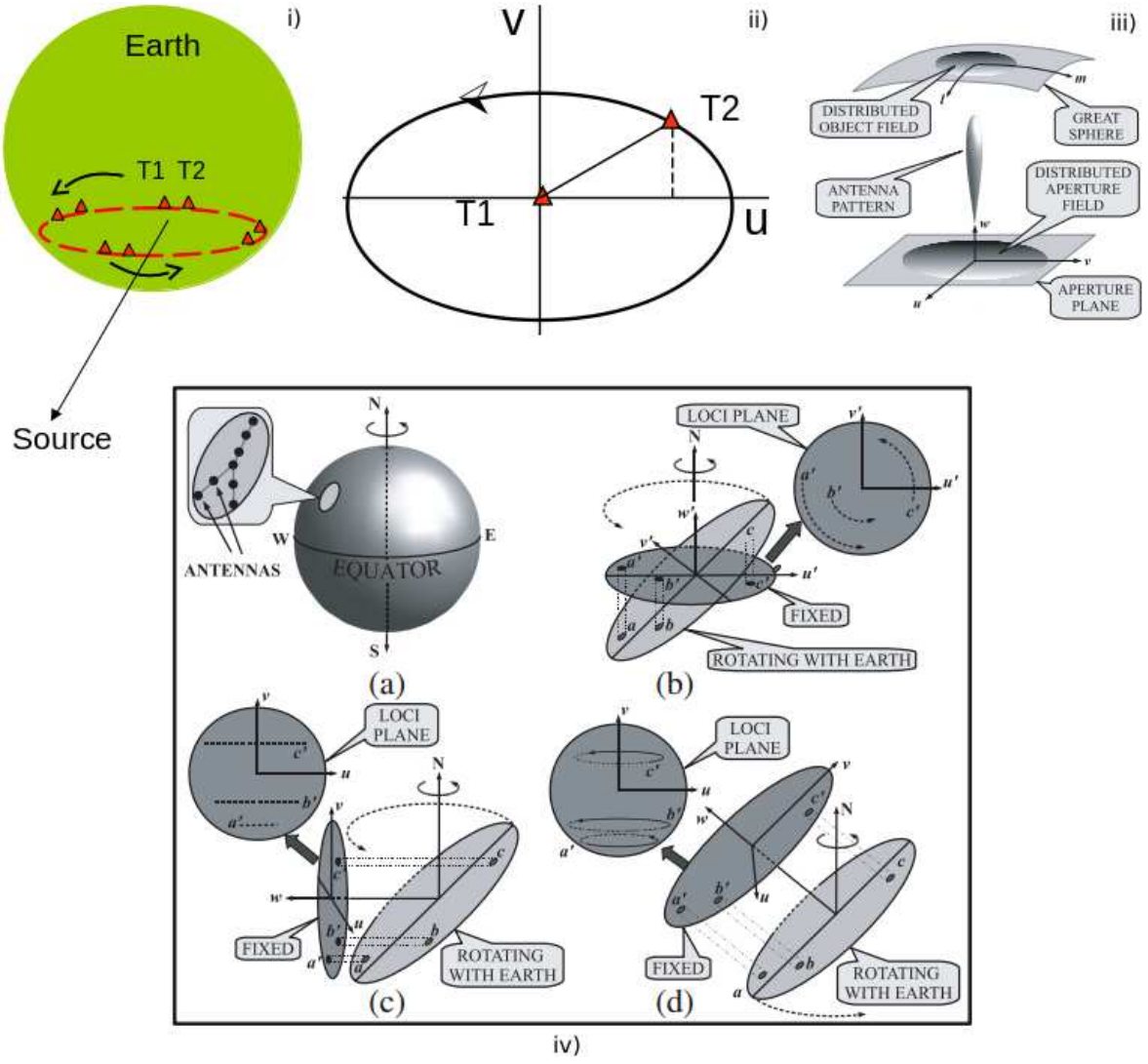

Figure 2.3: In panel *i*): sketch of how the baseline of an interferometer will have all possible orientations rotating with Earth in 12 hours and thus the projections of the baseline will make ellipses in the (u,v) plane with one telescope at the centre of the ellipse; *ii*): As seen from the source, each baseline traces out an ellipse with one telescope at the centre of the ellipse, in the (u,v) plane; *iii*); (u,v) plane compared to a parallel coordinate system, connected to the source, (l,m) and *iv*): *a*): An array of antennas rotates with the Earth rotation. Observing a radio source towards *b*): celestial North Pole; *c*): along the celestial equator; *d*): along a celestial latitude in between. Panels *iii* and *iv* are taken from Joardar et al. (2010).

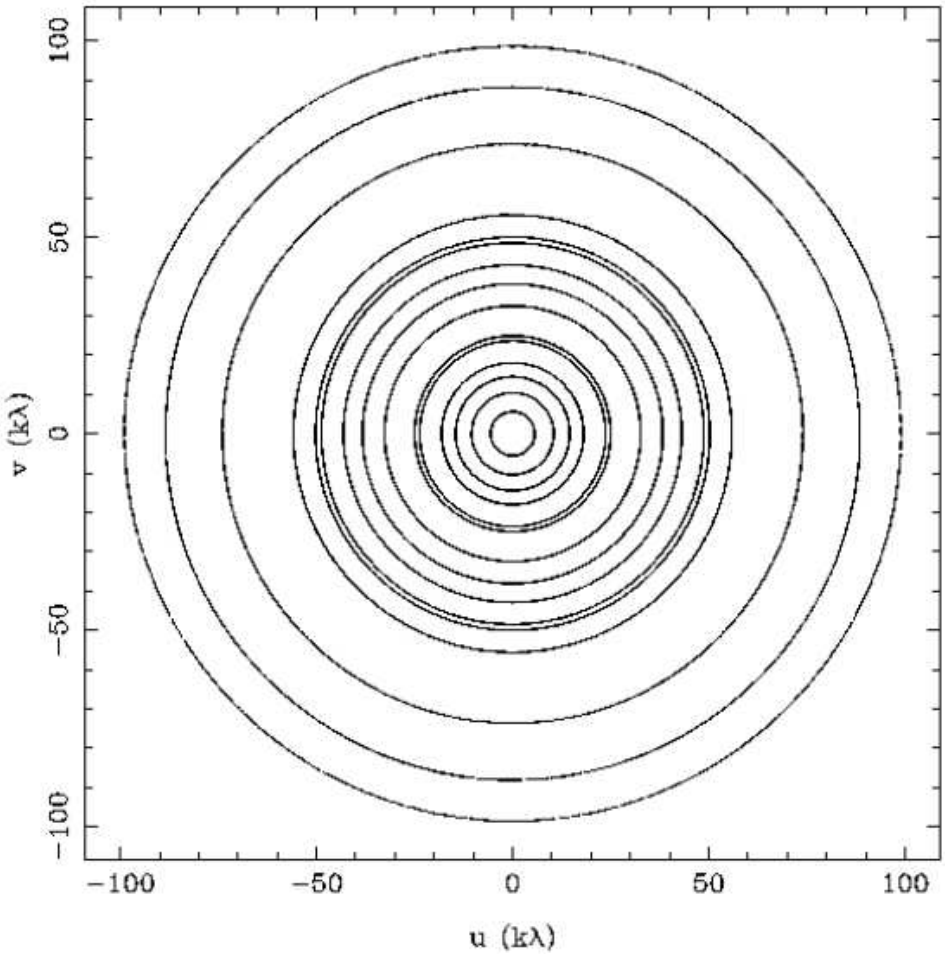

Figure 2.4: The correlation products between any pair of antennas are used to fill the (u,v) plane. In the image we see the (u,v) coverage for the *ATCA* telescope, which are 15 concentric circles (or ellipses) that the baselines make in 12 h. The (u,v) coordinates have dimensions in number of wavelengths. The image is taken from www.atnf.csiro.au/people/Julie.Grant/astrotech/radio_intro_Swinburne.ppt.

measure does not usually correlate with radio signatures of the SNR, the remnants are not detected at FIR wavelengths and very often we do not know if the FIR radiation does or does not belong to the SNRs, but to the surrounding or foreground/background dust. It would be possible to estimate synchrotron radiation by extrapolating the radio spectral index. Gordon et al. (2014) shows that the model of modified black body describes our data well, therefore the contribution of other types of radiation does not exceed more than 10–20%.

2.2.1 Modelling dust emission with a modified black body

To model dust collisionally heated by SNR shocks (to 20–70 K) or at similar temperatures to interstellar dust (∼20 K). I use Planck's black body formula

$$B_\nu(\nu, T_d) = \frac{2h\nu^3}{c^2} \frac{1}{e^{\frac{h\nu}{KT}} - 1}, \tag{2.3}$$

which is modified by a power-law $F_\nu(\nu) \propto B_\nu(\nu, T)\kappa(\nu) \propto \nu^{(3-\alpha_{IR})}$, where $\kappa(\nu)$ is the frequency-dependent mass-absorption coefficient (emissivity),

$$\kappa(\nu) = 0.6086 \times 10^{-18} \times \nu^{-\alpha_{IR}} \tag{2.4}$$

in $\mathrm{m^2\ kg^{-1}}$ derived from

$$\kappa(\lambda) = \kappa_0 \left(\frac{\lambda}{\lambda_0}\right)^{\alpha_{IR}}, \tag{2.5}$$

where $\kappa_0 = 0.1\ \mathrm{m^2\ kg^{-1}}$ and $\lambda_0 = 0.001$ m. The SED of the entire cloud of dust particles is described by the same shape as long as the cloud is optically thin. Adopted values of emissivity index α_{IR} are usually in the range $[-1, -2]$. For simplicity and because it is consistent with determinations for Galactic interstellar cirrus (Planck's collaboration, 2014), in this work I have adopted the case of $\alpha_{IR} = -1.5$.

The simple form of the SED (spectral energy distribution) of an emitting source is given by

$$F_\nu^{IR} = \frac{\int f_\nu d\nu}{L} 4\pi\kappa_\nu B_\nu M_D, \tag{2.6}$$

where B_ν is the Planck function, L is the luminosity, M_D is the mass of the observed dust, F_ν^{IR} is the flux in W m^{-2} Hz^{-1}, κ_ν is in m^2 kg^{-1} and f_ν is the function that describes the radiation on various frequencies. Since the luminosity of the source can be written as $L = 4\pi d^2 \int f_\nu d\nu$, where d is the distance to the source, the equation from above can be expressed as

$$M_D = \frac{F_\nu d^2}{\kappa_\nu B_\nu}. \tag{2.7}$$

When I put in Planck's formula $B(\nu, T)$, the previous expression becomes

$$F_\nu = M_D \frac{\kappa_\nu}{d^2} \frac{2h\nu^3}{c^2} \left(e^{\frac{h\nu}{KT}} - 1\right)^{-1}. \tag{2.8}$$

Converting the previous expression to Jy and to the units of solar mass, in kg, and expressing $\kappa(\nu)$ from eq. 2.4, I get

$$F_\nu[\mathrm{Jy}] = M_D[M_\odot] \frac{0.6086 \times 10^{-18} \nu^{-\alpha_{IR}}}{d^2} \frac{2h\nu^3}{c^2} \left(e^{\frac{h\nu}{KT}} - 1\right)^{-1} \cdot 1.9891 \cdot 10^{30} \cdot 10^{26}, \tag{2.9}$$

in which I replace and d =50 000 pc for the LMC. Therefore, for $\alpha_{IR} = -1.5$, I find the formula:

$$F_\nu[\mathrm{Jy}] = 10^{-54} \times 0.749 \times M_D[\mathrm{M}_\odot] \nu^{4.5} \left(e^{\frac{h\nu}{KT}} - 1\right)^{-1}. \tag{2.10}$$

I use the eq. 2.10 in Chapter 4 to perform fitting of a one-component modified black-body using all *Herschel* data-points from 100 to 500 μm, in order to produce maps of mass and temperature. I use *Spitzer* data at 24 and 70 μm in Chapter 4 only for the flux ratio maps, but not for producing maps of mass and temperature since they trace the warm dust component. I do not perform fitting of a two-component modified black body because of the big uncertainties that would exist for the warm component.

Note that the value of κ that we use here is twice larger than in the most literature. Most of the authors quote κ = 0.05-0.07 m^2 kg^{-1} at $\sim$ 850 μm (Draine & Li 2001; James et al. 2002). Therefore in this thesis we might underestimate the dust masses by a factor of two compared to other works.

It should be added that some observations of evolved stars, ISM and other objects have shown the existence of excess flux at 500 μm or that another dust component might be needed to fit the SED for $\lambda > 300$ μm, but it was not clear whether that is caused

by the calibration, background, by a second component of very cold dust (T<8 K) or by something else. Therefore, Gordon et al. (2014) have analysed not only the simple emissivity law model (that I use here), but also the more sophisticated models of broken emissivity law and model of two dust components on different temperatures modified by a non-broken emissivity law. They argue that submm excess is more likely to be due to emissivity variations with wavelength than a second population of extremely colder dust.

2.2.2 Making maps of mass, temperature and the flux ratio of SNRs and their surroundings

In Chapter 4, we use *Herschel* images to fit SEDs from 100–500 μm, pixel by pixel and we produce flux ratio maps. To do this the images at different wavelengths need to be on the same resolution and to have the same pixel size. Firstly I performed the convolution of images of all remnants on 24, 70, 100, 160, 250 and 350 μm with the kernel (Gaussian) to the resolution of the image at 500 μm (beam 36.3$''$), because this is the poorest resolution of all images. All maps have been rebinned and regridded to 14$''$ pixel. However, afterwards I adopted and used the data prepared by Gordon et al. (2014), who convolved with the kernels from Aniano et al. (2008), subtracting the foreground/background such as residual foreground MW cirrus emission and confusion noise of unresolved background galaxies and rebinning. For the ratio maps in this work I use similar maps of *MIPS* data at 24 and 70 μm.

For producing mass and temperature maps, I use only pixels with flux higher than 3σ where the uncertainties are different for each wavelength and pixel (see the estimation of the uncertainties below). If the flux of a pixel is below that limit, then it is added to the fluxes of other faint pixels and the value of the average faint pixel is found, which is then fit using only the calibration uncertainties (as the background uncertainties become negligible in the approximation).

Before fitting the SEDs pixel-by-pixel, I converted the intensity of the *Herschel* images from MJy sr^{-1} to Jy pixel^{-1}, by multiplying the pixel values from the images

by the steradian area of the 14″ pixel.

For *MIPS* data at 24 and 70 μm I calculated the error of each pixel by adding in quadrature the calibration uncertainty of 2% and 5%, respectively and background noise measured away from the galaxy (see below; Gordon et al. 2007; priv. comm. with K. Gordon). Similarly, calibrational errors for *PACS* and *SPIRE* of 10% and 8%, respectively (priv. comm. with K. Gordon and J. Roman-Duval; Bendo et al. 2015), are combined in quadrature with the background uncertainty. For the background uncertainties, I used [1.77, 0.85, 1.63, 1.39, 0.98, 0.51, 0.24] MJy sr^{-1} for wavelengths 24, 70, 100, 160, 250, 350 and 500 μm, respectively (Gordon et al. 2014; priv. comm. with K. Gordon). Notice here that the background uncertainties are very high for 24 μm data, that they can be of the order of magnitude of the actual fluxes (see Chapter 4).

I use formula 2.10 to perform fitting of a one-component modified black-body through *Herschel* data-points 100–500 μm, in order to produce maps of mass and temperature. I use the program *mpfit*, written by Markwardt (2009), performing χ^2 minimisation in *IDL*, modelling each pixel separately. The two free parameters, the temperature and mass, initially were set to $T = 20$ K and $M = 1$ M$_\odot$. I further constrained the temperature to be ≥ 3 K (cosmic microwave background) and $\leq 25\,000$ K – all grains will have sublimated by $T \sim 1500$ K; and the mass to be $\geq 10^{-5}$ M$_\odot$ and ≤ 180 M$_\odot$. The degrees of freedom are calculated by subtracting the number of free parameters from the number of data points, which is in my case $5 - 2 = 3$.

Firstly I performed the fitting without colour correction, then I computed the colour corrections to that model (using the *IDL* wrapper distributed with the DustEM code and described in Compiègne et al. 2011). Finally, I applied the fit to data that were divided by that colour correction. The colour correction is in the most extreme cases ∼4 %, but most often less than 1%. In Fig. 4.16 one can see the example of the resulting maps of mass and temperature made for SNR N 49. These maps and their uncertainties are shown and described in Chapter 4.

2.3 Catalogues of SNRs in the MCs on various frequencies

To be sure about the positions of the SNRs in the MCs, since FIR maps do not show clear detections, I have used many different papers and all existing catalogues on SNRs observed at different wavelengths. The list of SNRs is growing every day with new discoveries, but in recent times most of the discovered SNRs are only visible at certain wavelengths. Some objects that I included in this work are SNR candidates, although they are listed as SNRs in Badenes, Maoz & Draine (2010). Here I describe the existing catalogues of MC SNRs that I used in order to make my sample of SNRs. Sometimes there is confusion between various catalogues, detecting two different remnants under the same name (because remnants often get their names from neighbouring HII regions), partly overlapping SNRs, errors in the coordinates, real differences in the positions at different wavelengths, or finally some remnants only exist only in certain catalogues.

The study of SMC SNRs by Filipović et al. (2005) showed that most of the known SNRs are visible at radio, X-ray and optical frequencies, but there are often exceptions. Some SNRs are visible only in X-rays, a significant number of them are not visible optically and only one is found to be invisible in X-rays, but visible in optical and radio radiation. The recent study by Maggi et al. (2014) presents four SNRs observed in X-rays that were not detected in radio.

Most of the information about SNRs can be found at radio frequencies. At radio frequencies we see the synchrotron radiation of SNRs, which means that we distinguish objects that have a magnetic field and relativistic electrons to circulate around the magnetic field lines and radiate perpendicularly to the direction of the magnetic field. This radiation is polarised, non-thermal and it follows the law given by equation 1.2. Radio catalogues that I use here are Payne et al. (2004), Payne et al. (2007), Payne, White & Filipović (2008), Filipović et al. (2005), Filipović et al. (2008), Filipović et al. (1998a), Filipović et al. (1995), the unpublished new catalogue of Miroslav Filipović,

as well as many different papers about one or few SNRs.

While doing this work I have access to radio and Magellanic Cloud Emission-line Survey (*MCELS*; which provides images in narrow-band filters, [S II], Hα and [O III], made using the 0.6 m University of Michigan/CTIO Curtis Schmidt telescope). This data was kindly provided by Miroslav Filipović, which helped me to see the remnants, since they are not visible in FIR.

In the early stages of SNR life they are dominated by thermal X-rays, later becoming non-thermal X-rays; young SNRs have both. X-ray astronomy of SNRs began with using the *Einstein* telescope (see Berkhuijsen 1986), and later with *ROSAT*, *XMM* and *Chandra*. The most famous X-ray catalogues of MC SNRs are the *ROSAT* catalogue (Williams et al. 1999), available at http://www.physics.rutgers.edu/~jackph/ science/MCSNRs_atlas.html and the *Chandra* catalogue, http://hea-www.harvard.edu/ ChandraSNR/gallery_lmc.html.

Beside the detection of Balmer lines present in many young Ia SNRs, for most of the remnants that are optically visible, it is believed that they have already entered the radiative phase (Smith et al. 1991). During the radiative phase, strong optical lines are seen from a variety of atomic species, most strongly from H_α and singly-ionized sulfur (S II). The most famous optical catalogues are Mathewson et al. (1983), Mathewson et al. (1984) and Mathewson, Ford & Tuohy (1985) and Desai et al. (2010).

Graham et al. (1987) published *IRAS* data of four SNRs in LMC. The most famous newer IR catalogues of MC SNRs are Seok et al. (2008) and Seok, Koo & Onaka (2013).

The most famous UV catalogue is Blair et al. (2006). They have detected 15 out of 39 SNRs. Finally, I used the two mixed catalogues of MC SNRs, e.g. Badenes, Maoz & Draine (2010) and the online MCSNR catalogue: http://hoth.ccssc.org/mcsnr/[5], consisting of the information obtained using various frequencies. This thesis contains the first FIR atlas of SNRs in the LMC.

[5]This page is not longer accessible.

3 SN 1987A on FIR and (sub)mm wavelengths

In this Chapter, we present the series of papers, in chronological order, about the various observations of SN 1987A at (sub)mm wavelengths. Sections 3.1, 3.2, 3.3 and 3.4 details results from 2011 and 2012, while Section 3.5 presents the newer *ALMA* results.

3.0.1 Introduction to FIR and (sub)mm observations of SN 1987A

The SN explosions of massive stars are a potentially important source of dust, with estimates ranging from $0.2-4$ $M_{\odot}$ (Dunne et al. 2003) to much lower measured amounts < 0.01 $M_{\odot}$ (Sandstrom et al. 2009). These kinds of measurements are complicated, because SNRs are frequently witnessed to hit surrounding dust clouds (e.g., N 49 in the LMC – van Loon et al. 2010; Otsuka et al. 2010). My research of SN 1987A started around the same time when Matsuura et al. (2011) were discovering ~ 0.7 $M_{\odot}$ of cold (~ 20 K) dust using *Herschel* images, and interpreted it as freshly-synthesized in the ejecta of SN 1987A, without being able to resolve it. I have attempted to obtain higher spatial resolution data constraining the location of the dust within this compact SNR. Furthermore, I wanted to explore if there are changes in the FIR and (sub)mm emission. The idea was to better constrain the SED, exploring if there are some characteristics of this object that can be found using better resolution at similar and longer wavelengths than the ones of *Herschel* (100–500 μm).

3.1 The first observations of SN 1987A at 870 μm and 3 mm

In this section I present the observations of SN 1987A at 0.87 mm and 3.2 mm, constituting the first detections of SN 1987A at wavelengths $0.35< \lambda <8$ mm which were published in Lakićević et al. (2011).

3.1.1 *LABOCA, APEX* observations of SN 1987A at 0.87 mm, from May 2007

The *APEX* observations of SN 1987A were taken from the ESO (European Southern Observatory) archive. The instrument used was the *LABOCA* camera at a wavelength of 0.87 mm (345 GHz, with a bandwidth of 60 GHz). The object was observed on 30 May 2007, for the first time at this wavelength. The total on-source integration time was 2 hr. The field was imaged in raster-map mode (to fill the spaces between the 295 bolometer array elements) over $\sim$15$'$ diameter, centred on the coordinates of this object (RA: $05^{\rm h}$ $35^{\rm m}$ $16.8^{\rm s}$, Dec: -69° $15'$ $00''$). The beamsize has a FWHM of $18''$.

The data were reduced using the *Bolometer array Analysis* (*BoA*) software, following standard submm calibration procedures (similar as in Section 3.3.1). The individual raster-map scans were first corrected for attenuation by the Earth's atmosphere, signal calibration factors, and response variations across the bolometer array. Then, the voltages were converted to flux densities using the conversion factor determined from measurements of planets during commissioning of *APEX*. Afterwards, a series of 20 iterations of $\kappa-\sigma$ clipping were performed to remove noise spikes that deviate from the mean by more than $\kappa \times \sigma$ (where $\kappa \geq 4$ and σ is standard deviation of all data), taking known bad channels into account. The individual maps were then combined into a single image. The image was smoothed with a Gaussian kernel of $\sigma = 1$ pixel with FWHM of $14''$, using the *Munich Interactive Data Analysis Software* (*MIDAS*), and the resolution of the final image is thus $23''$.

The resulting image, Fig. 3.1 shows SN 1987A at 870 μm, in resolution of $\sim$23$''$

(although we also had looked at the original image, which has resolution of $\sim$18″). The remnant is faint compared to surrounding dusty clouds, but it is clearly detected. Although the *Herschel* resolution at 100 μm (6.75″) was much better than this image ($\sim$18″) – but not at 500 μm (36.3″) – and at 100 μm the object is a point source (Matsuura et al. 2011), our data in Fig. 3.1 suggests that SN 1987A is part of some bigger elongated structure extending $\sim$0.5′ towards the South-West. This made me wonder if this object is resolved at this wavelength. We were not sure if *APEX* detects the same dust as *Herschel* or if there is some difference.

The brightest part of this image belongs to the molecular cloud complex on the North-East corner toward 30 Dor, where the giant, dense shell of the old SNR B0536−6914 lies. This source is not obviously distinguishable from interstellar dust at FIR wavelengths (which is also the case for most of the other SNRs in the LMC, which will be discussed later). Another SNR, on the South-East from the position of SN 1987A is SNR Honeycomb, or B0536−69.3 (Chu et al. 1995), which is not detected here (although see Chapter 4, Fig. A.10).

We used the CENTER/MOMENT task from *MIDAS* to measure the flux density of SN 1987A from a Gaussian fit to be 21 ± 4 mJy. Attempts to measure the flux density using different software has suggested an accuracy of $\sim$ 10% but the highly structured background has led us to adopt a more conservative value of $\sim$ 20%. The *MIDAS* task that I used also returned a value of 16″ for the FWHM, which was in fair agreement with the angular resolution of the telescope, lending support to the detection of a point source at the position of SN 1987A.

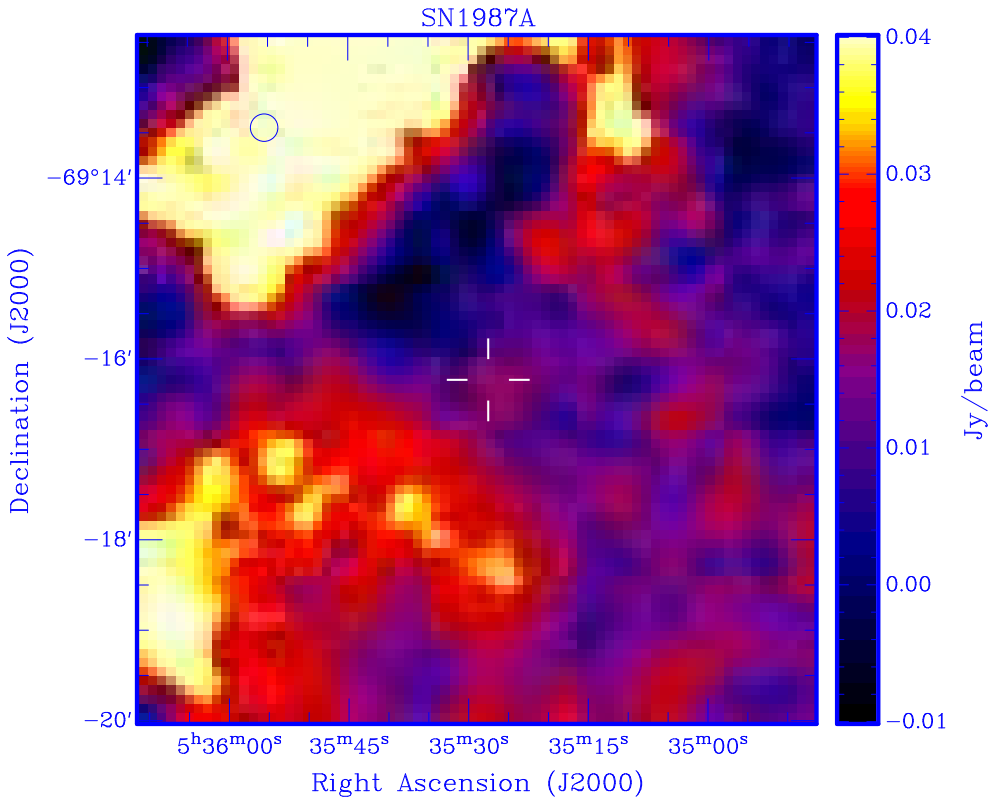

Figure 3.1: *APEX* image of SN 1987A at 345 GHz/0.87 mm, obtained in May 2007; resolution of this image was 23″ (it was smoothed). The position of SN 1987A is indicated with a cross; the beam is drawn in the upper left corner.

3.1.2 *ATCA* observations of SN 1987A at 3 mm, from July 2005

SN 1987A was observed with the *ATCA* (*Australia Telescope Compact Array*) on 11–12 July 2005, with the 3-mm receiver in two frequency bands, one between 93.45–93.56 GHz (peak reception at 93.49 GHz) and another between 95.5–95.6 GHz (peak reception at 95.57 GHz). The observations were carried out with the most compact antenna configuration, H75, with an on-source observing time of ∼8 h. I analyzed these data since they have not previously appeared in the refereed literature.

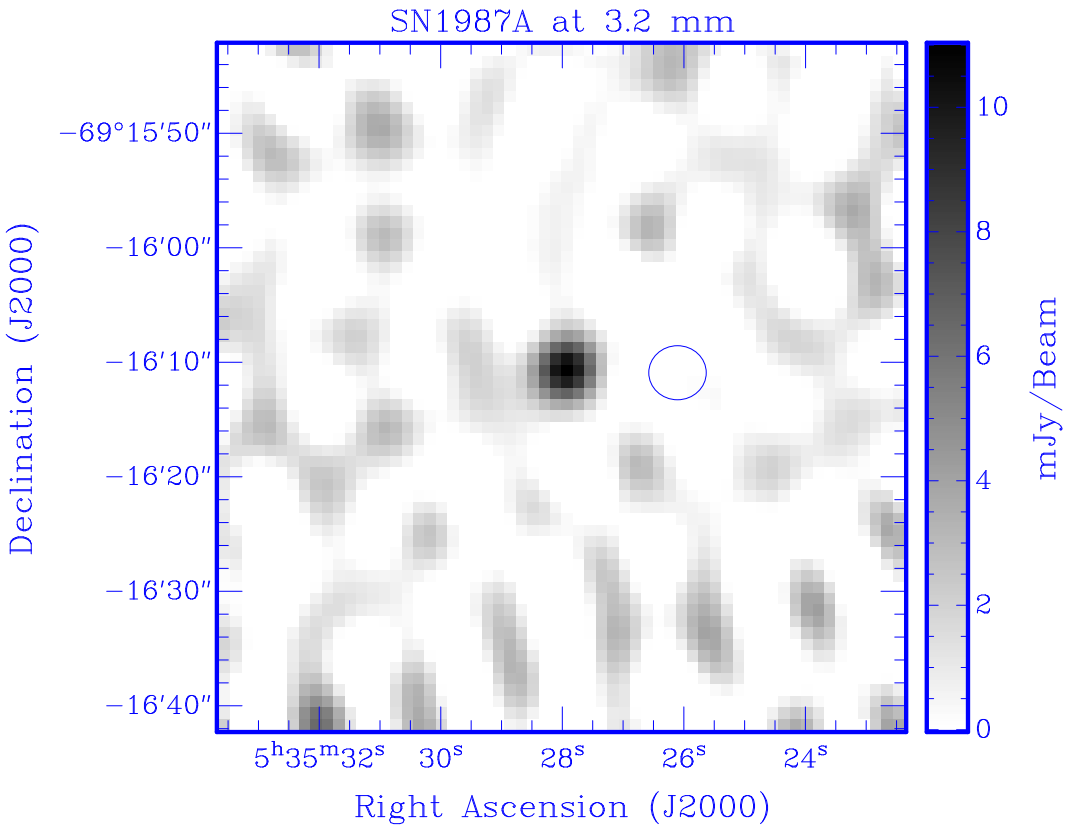

Figure 3.2: *ATCA* image of SN 1987A at 94.5 GHz/3.2 mm, obtained in July 2005. The synthesized beam is drawn just next to it. FWHM was $5'' \times 4.7''$.

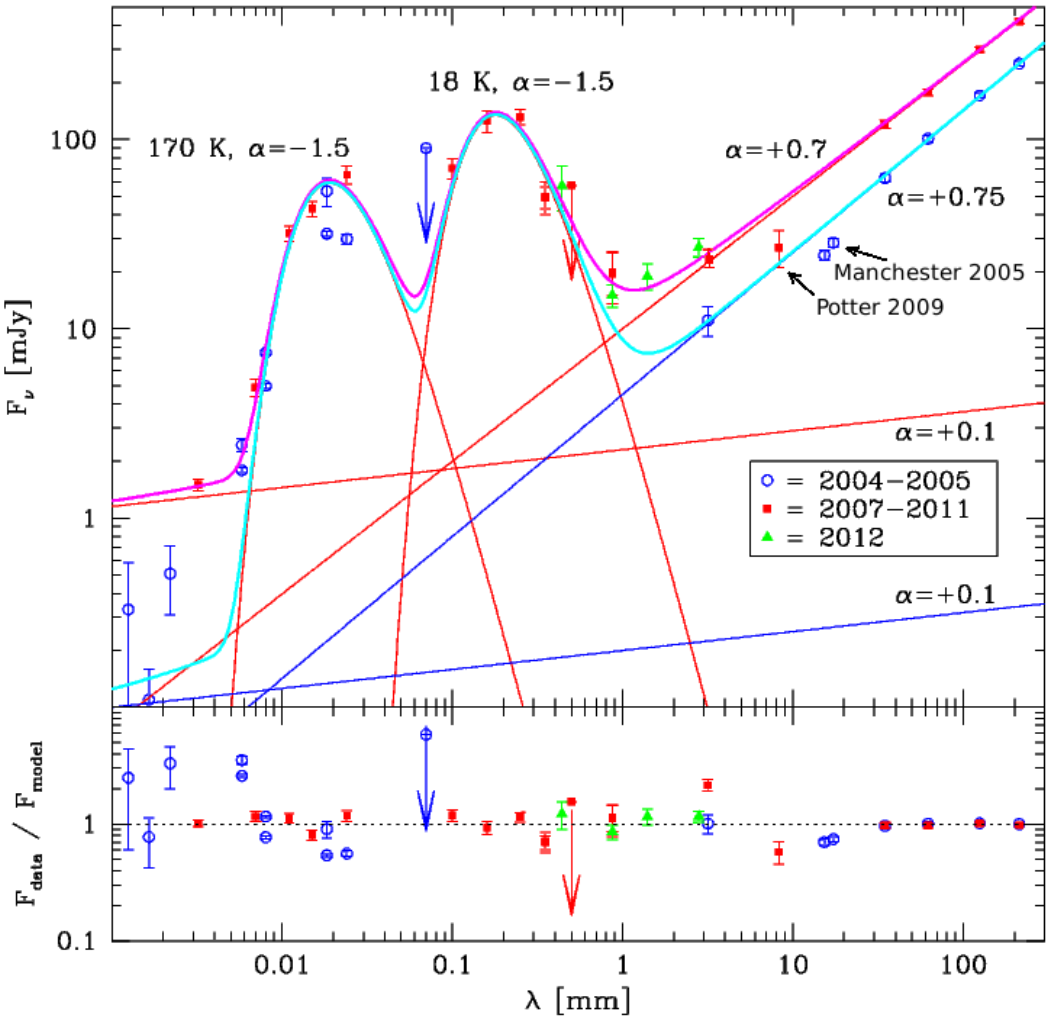

Figure 3.3: SED fit for the observations from Lakićević et al. (2011), while later the data from Lakićević et al. (2012a), Lakićević et al. (2012b), and Indebetouw et al. (2014) were added. Overplotted are modified blackbodies to represent two dust components, two steep radio powerlaws to represent synchrotron radiation, and two shallow powerlaws to represent free-free radiation. Cyan and magenta curves represent the sum of all emission for the 2004–5 and 2007–10 period, respectively, with residuals plotted underneath. Green data-points are added later as they are *ALMA* data from Indebetouw et al. (2014). All these data are listed in Table 3.1.

Table 3.1: All observations of SN 1987A, as shown in Fig. 3.3.

$\lambda[\mu m]$	F[Jy]	ΔF[Jy]	day	comments	reference
2.14e5	0.422	0.013	8014	1.4 GHz *ATCA*	Zanardo et al. (2010)
2.14e5	0.2515	0.0076	6690	1.4 GHz *ATCA*	Zanardo et al. (2010)
1.25e5	0.299	0.009	8014	2.4 GHz *ATCA*	Zanardo et al. (2010)
1.25e5	0.1710	0.0052	6690	2.4 GHz *ATCA*	Zanardo et al. (2010)
6.23e4	0.178	0.007	8014	4.8 GHz *ATCA*	Zanardo et al. (2010)
6.23e4	0.1009	0.004	6690	4.8 GHz *ATCA*	Zanardo et al. (2010)
3.48e4	0.120	0.006	8014	8.6 GHz *ATCA*	Zanardo et al. (2010)
3.48e4	0.0625	0.0031	6690	8.6 GHz *ATCA*	Zanardo et al. (2010)
1.73e4	0.0285	0.0015	6001	17.3 GHz *ATCA*	Manchester et al. (2005)
1.53e4	0.0245	0.0015	6001	19.6 GHz *ATCA*	Manchester et al. (2005)
8.28e3	0.027	0.006	7905	36.2 GHz *ATCA*	Potter et al. (2009)
2.8e3	0.027	0.003	9001	110 GHz *ALMA*	Indebetouw et al. (2014)
1.4e3	0.019	0.003	9001	215 GHz *ALMA*	Indebetouw et al. (2014)
870e3	0.015	0.002	9001	345 GHz *ALMA*	Indebetouw et al. (2014)
440e3	0.057	0.015	9001	680 GHz *ALMA*	Indebetouw et al. (2014)
3.17e3	0.0112	0.0020	6713	94.5 GHz *ATCA*	Lakićević et al. (2011)
3.17e3	0.0237	0.0026	6713	94.5 GHz *ATCA*	Lakićević et al. (2012a)
870	0.021	0.004	7385	345 GHz *APEX*	Lakićević et al. (2011)
870	0.0196	0.006	7385	345 GHz *LABOCA*	Lakićević et al. (2012b)
500	<0.0573	0.0000	8516	*Herschel*	Matsuura et al. (2011), upper limit
350	0.05	0.01	8938	857 GHz *SABOCA*	Lakićević et al. (2012a)
350	0.0493	0.0065	8516	*Herschel*	Matsuura et al. (2011)
250	0.1317	0.0121	8516	*Herschel*	Matsuura et al. (2011)
160	0.1253	0.0161	8516	*Herschel*	Matsuura et al. (2011)
100	0.0705	0.0085	8516	*Herschel*	Matsuura et al. (2011)
70	<0.09	0.0000	6184	*Spitzer*	Dwek et al. (2010), upper limit
24	0.065	0.007	7192	*AKARI*	Seok et al. (2008)
24	0.0298	0.0017	6184	*Spitzer*	Bouchet et al. (2006)
18.3	0.0534	0.009	6526	*TReCS*[1]	Bouchet et al. (2006)
18.3	0.0318	0.001	6190	*TReCS*	Bouchet et al. (2006)
15	0.043	0.004	7192	*AKARI*	Seok et al. (2008)
11	0.032	0.003	7192	*AKARI*	Seok et al. (2008)
8	7.48e-3	1.9e-4	6487	*Spitzer*	Bouchet et al. (2006)
8	4.98e-3	1.6e-4	6130	*Spitzer*	Bouchet et al. (2006)
7	4.9e-3	0.5e-3	7192	*AKARI*	Seok et al. (2008)
5.8	2.44e-3	1.9e-4	6487	*Spitzer*	Bouchet et al. (2006)
5.8	1.79e-3	0.6e-4	6130	*Spitzer*	Bouchet et al. (2006)
3.2	1.5e-3	0.1e-3	7192	*AKARI*	Seok et al. (2008)
2.2	5.1e-4	0.2e-3	6525	*CTIO*[2]	Bouchet et al. (2006)
1.65	1.1e-4	0.5e-4	6525	*CTIO*	Bouchet et al. (2006)
1.25	3.3e-4	2.5e-4	6525	*CTIO*	Bouchet et al. (2006)

Note: The fluxes from Indebetouw et al. (2014) are obtained by summing the fluxes from the torus and the ejecta.

1 – *TReCS* (Thermal-Region Camera Spectrograph) is a mid-infrared imager and long-slit spectrograph built by the University of Florida for Gemini South.

2 – *CTIO* – Cerro Tololo Inter-American Observatory.

The bands were reduced simultaneously using standard procedures within the *MIRIAD*[1] software, and ultimately merged. Firstly, the signal was corrected for elevation-dependent attenuation using up-to-date antenna reconfiguration files with the task ATFIX. The phase stability (measurement of the interferometer amplitude/phase calibration) and antenna tracking were investigated and found to be mostly within 0.2–0.5 mm and (typically) $0.3 - 0.6''$ to (occasionally) $\sim 3''$. Data obtained when the telescope had tracking errors of $> 3''$ were flagged as bad, with the task UVFLAG. Secondly, the task MFCAL was used to calibrate the bandpasses[2] and antenna phase offsets against observations of the primary reference sources 1921–293 (at the start) and 1253–055 (at the end), and the phase variations against regular observations of the secondary reference sources 0637–752 and 0454–810. Absolute flux calibration was achieved using the task MFBOOT against an observation of the planet Uranus. The flux calibration appeared reliable at a 10–20% level. Thirdly, the signal as a function of baseline in the (u,v) plane (visibilities) was inverted using a standard fast-Fourier transform with the task INVERT, where the visibilities were weighted according to the noise variance (system temperature) but otherwise uniformly across a 1-arcmin field chosen to effectively suppress the sidelobes. A multi-frequency synthesis approach was taken, producing an image at 94.5 GHz (3.2 mm) with an rms[3] noise level of 2.0 mJy beam^{-1}. This map was cleaned with the tasks CLEAN and RESTOR, employing a Högbom scheme (Högbom 1974). The resulting beam has a FWHM of $5.0'' \times 4.7''$ in RA and Dec. The calibrated image is shown in Fig. 3.2, where SN 1987A is clearly detected as an unresolved source at a level of 11.2 $\pm$2.0 mJy.

[1] http://www.atnf.csiro.au/computing/software/miriad/

[2] A band-pass filter is a device that passes frequencies within a certain range and rejects (attenuates) frequencies outside that range.

[3] rms (root mean square) voltage is measuring the thermal noise generated by the random thermal motion of charge carriers (usually electrons), inside an electrical conductor, which happens regardless of any applied voltage. This noise depends of resistance, bandwidth and the resistor's absolute temperature.

3.1.3 Discussion about these data

3.1.3.1 Bridging the IR and radio spectral energy distributions

APEX 0.87 mm and *ATCA* 3.2 mm detections bridge the big gap of a factor > 20 in wavelength, between on the one hand the radio emission detected down to $\lambda = 0.8$ cm (Potter et al. 2009), which are explained by synchrotron radiation of the SNR (generated by free charge in a magnetic field) and FIR emission detected up to 350 μm (Matsuura et al. 2011) attributed to thermal radiation from dust grains, on the other. The full spectral energy distribution (SED) is shown in Fig. 3.3. The initial IR data are taken from Bouchet et al. (2006), Seok et al. (2008), Dwek et al. (2010), Matsuura et al. (2011) and Lakićević et al. (2011) while radio data are from Manchester et al. (2005), Potter et al. (2009), Zanardo et al. (2010) and this work (Lakićević et al. 2011), and the fit is from this work. The data from later works Lakićević et al. (2012a), Lakićević et al. (2012b) and Indebetouw et al. (2014) (green triangles) are also shown to avoid repeating the same plot in the following sections. All these data points are listed in Table 3.1.

I grouped the latest data in two categories according to the time of observation, 2004–2005 and 2007–2010, because Zanardo et al. (2010) and Dwek et al. (2010) have shown that the brightness on radio and IR wavelengths is increasing in the last years (or decades), respectively. We found that our *APEX* detection agrees with a modified black body curve (which fits all the other IR data) while our *ATCA* data agree with a power-low synchrotron radiation, together with other radio data on the right side of the plot.

Here I use the model that FIR-submm emission is represented very well by a modified Planck's curve of thermal dust emission:

$$F_\nu^{IR} \propto B_\nu(T)\nu^{-\alpha_{IR}}, \tag{3.1}$$

for a dust temperature of 18 K and coefficient $\alpha_{IR} = -1.5$, similar to the work of Matsuura et al. (2011). One should notice that Matsuura et al. (2011) did not use the flux density at 500 μm for producing their fits because they did not detect SN 1987A at

3σ at that wavelength. The MIR emission can be matched with thermal dust emission of identical α_{IR}, but with $T = 170$ K and a total emitting dust mass of $\sim 10^{-6}$ $M_{\odot}$. More details about the warm component in this SNR can be found in Bouchet et al. (2006), Dwek et al. (2010) and Matsuura et al. (2011), as well as in Section 1.3.0.1.

While it was shown that warm dust component from Fig. 3.3 changes flux in recent years (Dwek et al. 2010), and while radio fluxes were exponentionaly growing (Zanardo et al. 2010), this work examines the behaviour of the cold dust component, since at the time of writing this paper, in 2011, we still did not know if the brightness of thermal radiation of cold dust in SN 1987A changes on timescales of a few years. We were still not sure if the dust is in the ejecta or surroundings, if it is in the process of forming dust or undergoing destruction and how fast this could be happening. After my analysis of the *APEX* data, compared to *Herschel* data, we understood that if some change exists, it is not big, although the error of the *APEX* data was estimated to be $\sim$20% ($\sim$4 mJy), while the *Herschel* error is $\sim$13% (for 160 μm *PACS* data; Matsuura et al. 2011; Section 3.2).

The emission at longer wavelength, together with our 3-mm data-point is fitted with a powerlaw $F_{\nu}^{\rm radio} \propto \lambda^{\alpha_{\rm radio}}$, where $\alpha_{\rm radio}$ is the spectral index (see eq. 1.2). A value for $\alpha_{\rm radio} \approx 0.75$ during 2004−2005 produces an excellent fit to the 3–21 cm data, as well as our new measurement at 3.2 mm, while for the period from 2007−2010 the best fit is when $\alpha_{\rm radio} \approx 0.7$. The absolute value of spectral index had decreased for 18% from the year 2002 to 2010 (Zanardo et al. 2010), in contrast to predictions from the models by Berezhko & Ksenofontov (2006). Thus, we have noticed that the data points of Manchester et al. (2005) and from Potter et al. (2009) are fainter than expected from the extrapolations of the corresponding power law components (see Fig. 3.3) and this is likely due to the difficulties of conserving flux at the longest baselines in radio interferometry (Staveley-Smith priv. comm.).

Comparing to the possible very low flux value due to modified black body emission at 3.2 mm (Fig. 3.3), and since this data-point lies on the powerlaw slope predicted by other authors, we concluded that this measured radiation at 3.2 mm belongs only to synchrotron radiation, without the need to to invoke either mm emission from dust

(see Bot et al. 2010), or free-free (f-f) emission from a hot plasma. Therefore, 94 GHz is the highest radio frequency that this SNR is observed so far, although as the radio flux will grow in the future, we can expect that synchrotron radiation will be observable on even shorter wavelengths.

In order to check if f-f emission could significantly contribute to our 870 μm measurement, f-f radiation following the relationship $F_\nu^{f-f} \propto \lambda^{\alpha_{ff}}$, where $\alpha_{ff} \approx 0.1$, is plotted in Fig. 3.3. Note that this refers to the optically thin case (in the end of this section I will estimate that within SN 1987A the optical depth, τ is $\sim 10^{-6}$, therefore it is not optically thick), but this typically happens at wavelengths $\gg$ cm or at high energies – which is not the case at IR-radio wavelengths. From Fig. 3.3 it can be seen that the f-f contribution is constrained by the near-IR data (this may include the contributions from hot dust and/or atomic line emission). The excellent description of the SED by the cold dust and synchrotron components leaves room for only a fraction of the measured flux density at 0.87 mm to arise from any additional component; in the most extreme case, $\sim$2 mJy at 1 mm is caused by f-f emission. Since the 0.87 mm datum is positioned on the well-constrained tail of the modified Planck's curve, there is little room for variations in its slope to affect the estimation of the limit of f-f emission.

Now I will show that the contribution of f-f emission to the flux at 870 μm is small, in a different way. Radiation transfer through plasma can be written as

$$I_\nu = \int_0^{\tau_\nu} B_\nu(T) e^{-\tau_\nu}\, d\tau_\nu, \tag{3.2}$$

where the optical depth is

$$\tau_\nu = 8.24 \times 10^{-2} T^{-1.35} \nu^{-2.1} E_{\rm c} \tag{3.3}$$

(Osterbrock 1974), where ν is in GHz and the continuum emission measure is $E_{\rm c} = \int n_+ n_e ds$, in cm^{-6} pc. The density n is here expressed in cm^{-3} and the pathlength, s is measured in pc. s is the size of the ionized ejecta, which is $\sim$ 0.1 pc. Assuming that 1 M$_\odot$ of ionized ejecta lies within the region of dimensions l $\sim$0.1 pc, and using the formula

$$n = \frac{1{\rm M}_\odot}{{\rm m_H}(4\pi/3)(l/2)^3}, \tag{3.4}$$

where m_H is the mass of the proton (mass of the hydrogen atom), the density (more precisely number of particles per cm^3) of the ionized ejecta is from $7.84 \times 10^5 gcm^{-3}$ (for $l = 0.1$ pc) to $6.27 \times 10^3 gcm^{-3}$ (for $l = 0.5$ pc), therefore $n_+ \sim n_e \sim 10^4 - 10^5$ cm^{-3}. Thus, I find that E_c is 10^7 cm^{-6} pc. Knowing that the ejecta consist of heavier elements like Fe and C, having more stripped electrons per nuclei (which is the factor of 10 to multiply the numerator of eq. 3.4), but also more massive nuclei (which would change m_H in the denominator to some larger number), predicts a minimum value of n_+ to be ∼10 times lower.

The solution to the radiation transfer equation in the isothermal case (constant T) is

$$T_{b,\nu} = \int_0^{\tau_\nu} T e^{-\tau_\nu} \, d\tau_\nu = T[1 - e^{-\tau_\nu}], \tag{3.5}$$

where the brightness temperature is defined as $T_{b,\nu} = c^2 I_\nu / (2\nu^2 k)$. This last formula presents the shape of Planck's law in case of low frequency and high temperatures (the Rayleigh-Jeans law), when $h\nu \ll KT$.

At high frequencies,

$$\lim_{\tau_\nu \to 0} T_{b,\nu} = T\tau_\nu. \tag{3.6}$$

If the temperature of the ionized ejecta is $T \sim 10^5$ K and $\nu = 345$ GHz, we can find τ_ν from eq. 3.3 to be $\sim 10^{-6}$. Using these results and eq. 3.6, one can estimate that $T_{b,345GHz} \sim 0.1$ K.

Now, from $I_\nu = 2T_b k\nu^2/c^2$ I can calculate that I_ν is 0.276×10^9 Jy and then knowing that the ejecta subtend 0.1 $arcsec^2$ on the sky (which is 2.3×10^{-11} sr), from the formula $F_\nu = I_\nu D[\text{sr}]$, I can calculate the flux F_{300GHz} to be ~ 1 mJy. This has a very similar magnitude to the observationally derived limit we set on the f-f component. However, the shock-ionized plasma mass associated with the ER is estimated to be only ∼0.06 $M_\odot$ at densities of 10^{3-4} cm^{-3} (Mattila et al. 2010), therefore its f-f emission is expected to be two orders of magnitude fainter than in the above scenario. Combined with the case where n_+ is ∼10 times lower, the estimation of f-f emission would be also 100 times lower, ∼0.01 mJy.

Now, we will assume the f-f emission we estimated (F_{300GHz} =2 mJy; see Fig 3.3)

and use it to estimate the density of SN 1987A. If we obtain reasonable densities, then our f-f estimation is more likely to be correct. The luminosity per frequency interval can be found as

$$L = F \times 4\pi d^2 = 5.98 \times 10^{14}\mathrm{WHz}^{-1}, \tag{3.7}$$

where $d = 50$ kpc is the distance to the LMC. If we assume that the ejecta is placed within R =0.1 pc radius, the plasma emissivity is equal to the power radiated divided by unit of volume,

$$j(\nu) = L(4\pi R^3/3)^{-1} = 4.86 \times 10^{-33}\mathrm{WHz}^{-1}\mathrm{m}^{-3}. \tag{3.8}$$

As the observed brightness temperature, $T_{\mathrm{b,345GHz}}$ of 0.1 K is many orders of magnitude less than the actual ejecta temperature, the plasma is optically thin. Therefore, for a hot, optically thin plasma, thermal Bremsstrahlung plasma emissivity can be found as

$$j(\nu)d\nu = 6.8 \times 10^{-51} Z^2 T^{-1/2} n_j n_e \times g(\nu, T) \times e^{-h\nu/KT}\mathrm{WHz}^{-1}\mathrm{m}^{-3}d\nu, \tag{3.9}$$

(van Paradijs & Bleeker 1999) where j is the emissivity in units of W m^{-3} Hz^{-1}, while n_j and n_e are ion/electron densities in particles per cubic metre, $g(\nu, T)$ is the Gaunt factor (at frequencies $h\nu \ll KT$ it has only a logarithmic dependence on frequency; we will adopt $g(\nu, T) \approx 1$), Z is the average atomic charge of the plasma nuclei (i.e. Z =1 for pure H; $Z = 2$ for pure He etc.; we will adopt Z =1.2 for gas with hydrogen, oxygen and carbon) and the plasma temperature of ionised ejecta is $T = 10^5$K. From equations 3.8 and 3.9, and adopting $n_j \approx n_e$, we find $n \approx 10^4\mathrm{cm}^{-3}$. This result is as expected from equation 3.4, therefore our upper limit estimate of flux of f-f emission in SN 1987A is realistic.

3.1.3.2 The location and origin of cold dust around SN 1987A

As *APEX* has superior resolution compared to *Herschel* images at 350 and 500 μm, I had clearly confirmed that most of the detected cold dust ($T \approx 18$ K) appeared to be concentrated within a region $\ll 23''$ (5 pc) across, but also my *APEX* image revealed diffuse emission to the South-West of SN 1987A. This reason made us still suspect if

the 18-K emission arises from part of a larger dust complex than SN ejecta, in radiation equilibrium with the ambient interstellar radiation field. Finally, no such structures are seen in the more sensitive *ATCA* image at 3.2 mm, which suggested that if the source is extended, the extension is more likely to be dust emission ($\alpha_{IR} < 0$) than f-f emission ($\alpha > 0$).

3.2 Detection of cold dust in SN 1987A with the *Herschel Space Observatory*

This section briefly describes the results of Matsuura et al. (2011), who used *Herschel* observations of SN 1987A from 100 to 500 μm, to conclude that 0.4–0.7 $M_\odot$ of cold dust ($\sim$20 K) is connected to this object, claiming that this dust is formed in the ejecta of the SN. I have contributed to this paper, in particular by ruling out that the FIR emission could be due to f-f radiation or synchrotron radiation.

3.2.1 Observations and results

SN 1987A was observed as part of the *HERschel Inventory of The Agents of Galaxy Evolution* (*Heritage*) in the MCs open time key program, using the *Herschel Space Observatory*'s imaging instruments, *PACS*, and *SPIRE*. The survey covered 5 bands, *PACS* for 100 and 160 μm, and *SPIRE* for 250, 350, and 500 μm with angular resolutions of $6\farcs69 \times 6\farcs89$, $10\farcs65 \times 12\farcs13$, $18\farcs2$, $24\farcs9$ and $36\farcs3$, respectively. SN 1987A was observed on April 30$^{\rm th}$ and August 5$^{\rm th}$, 2010 (days 8467 and 8564 after the explosion). The *PACS* and *SPIRE* images of the combined two epochs reveal SN 1987A as a faint but detectable point source coincident with the *VLBI* measured coordinates. The two observations were combined because there were no substantial changes in the fluxes seen in the two epochs.

In the 100 and 160 μm images, SN 1987A is clearly detected as a point source that is well separated from the nearby interstellar medium (ISM) dust. In the 250-μm image SN 1987A appears as a point source, but the SN begins to merge with the nearby ISM dust emission at 350 μm, and blends completely at 500 μm owing to the increasing beam size at longer wavelengths. The *Hubble*, *Spitzer Space Telescope* and *Herschel Space Observatory* images (Fig. 3.4) show that SN 1987A is located in a region with relatively low amounts of ISM gas and dust. On panels (A) and (B) there are *Hubble* and *Heritage Team* images, on (C)-(D) *Spitzer* images (Dwek et al. 2010), and on (E)-(H) *Herschel* images of the remnant from 100 to 350 μm. The 500 μm image

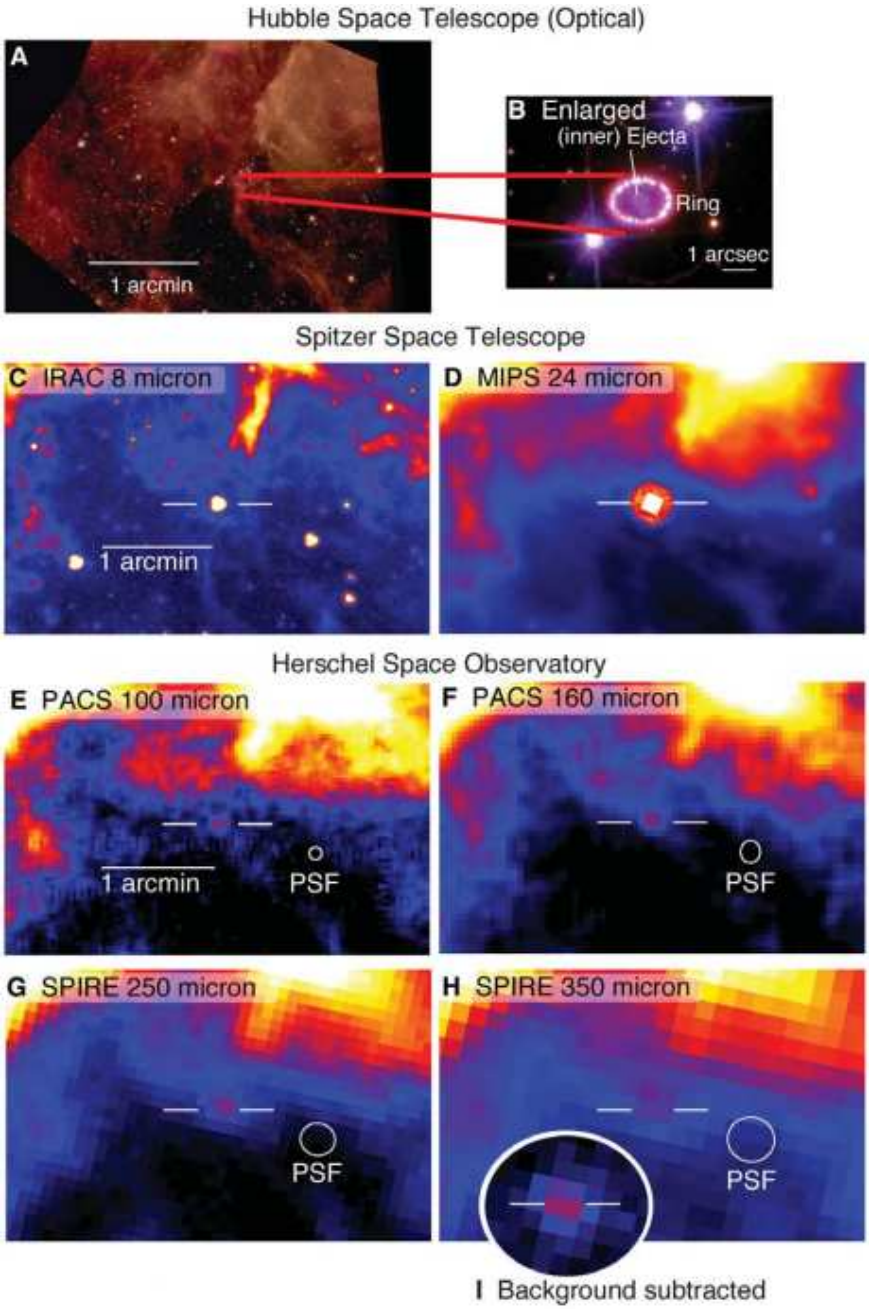

Figure 3.4: (A) and (B) show *HST* optical image, (C) and (D) *Spitzer* and (E) to (H) *Herschel* images of SN 1987A. North is top, and East is left. (I) Background-subtracted 350-μm image. The circles (PSFs) show the resolution of the *Herschel* instruments. [Source: panel (*A*): the *Hubble Heritage Team (AURA/STScI/NASA)*; (*B*): *NASA, ESA*, P. Challis and R. Kirshner (*Harvard-Smithsonian Center for Astrophysics*).] The image is taken from Matsuura et al. (2011).

Band [μm]	Flux[mJy]
PACS 100	70.5 ± 8.5
PACS 160	125.3 ± 16.1
SPIRE 250	131.7 ± 12.1
SPIRE 350	49.3 ± 6.5
SPIRE 500	$< 57.3^{*}$

Table 3.2: The measured *PACS* and *SPIRE* flux densities of SN 1987A. The uncertainties from the source extraction are added in quadrature with the absolute errors in the flux calibration, which are estimated to be 10% for the *PACS* bands and 7% for the *SPIRE* bands. * is for 3-sigma upper limit. The table is taken from Matsuura et al. (2011).

was omitted from the SED fitting in this paper since the source does not stand out, and because of the possibility of excess on 500 μm or other types of radiation (see Section 2.2.1, Gordon et al. 2014).

Photometry is obtained from the processed *Herschel* images assuming SN 1987A is unresolved and the fluxes are shown in Table 3.2.

3.2.2 The origin of the FIR/submm emission

The blackbody-like shape of the FIR/submm SED in Fig. 3.3 suggests continuous emission from dust although synchrotron emission and line emission from the same gas that produces the UV, optical and near-IR lines are also possible. Matsuura et al. (2011) estimated that the expected intensities of the strongest ionized lines are equivalent to a 0.2 % contribution to the total *Herschel* fluxes and therefore they make a negligible contribution to the FIR/submm fluxes. Also, it is believed that it is unlikely that the contribution of radiatively cooling gas shocked by the ejecta/ring interaction contributes significantly to the line emission, because the forbidden lines are collisionally de-excited in the high-density shocked gas.

Continuum synchrotron radiation can also contribute to the emission in the *Her-*

schel bands. The radio fluxes are extrapolated to FIR wavelengths using a power-law (Fig. 3.3). The predicted *Herschel* flux densities from synchrotron radiation are two orders of magnitude lower than those we measured at λ =100-350 μm, implying that the emission observed with *Herschel* is mostly due to the continuum emission from dust.

3.2.3 The origin of the cold dust in the ejecta

Matsuura et al. (2011) explored various dust compositions and origins (echos, ejecta, dust from progenitor red supergiant phase, ambient ISM dust) and found that the total dust mass is about $0.4 - 0.7$ $M_\odot$, while the temperature is 17 to 23 K, and that it is probably associated with cold dust in the SN ejecta.

Support for the presence of large amounts of dust in the ejecta may come from *HST* observations of the ejecta H_α profile in 2004 and 2010 (Larsson et al. 2011) which show the red-ward part of the profile to be largely missing, which could be interpreted as implying that emission from material at the far side of the ejecta suffers more extinction by intervening dust than material at the front side.

The derived dust mass is about 10^3 times larger and about twenty times colder than that measured at MIR wavelengths around 600 days after the explosion, soon after it first condensed out of the ejecta (Wooden et al. 1993; Whitelock et al. 1989). It is possible this all this dust mass existed at day 600, or that this dust mass grew by accretion over the past 20 years, or that initially optical/IR-thick dust-bearing clumps may have become optically thin at FIR and submm wavelengths.

The result obtained in this work strongly impacted the current understanding of the evolution of dust in galaxies. In the LMC, the rate of type II SNe is estimated to be one per 300 years (Maoz & Badenes 2010). If all type II SNe form typically 0.4 $M_\odot$ of dust, the overall SN dust injection rate into the ISM would be more than 10^{-3} $M_\odot$ yr^{-1}. This is about ten times higher than the dust inputs measured from AGB stars in the LMC (Matsuura et al. 2009). With such high efficiency and with a dust lifetime of 2×10^8–4×10^8 years (Jones, Tielens & Hollenbach 1996), it would be possible to explain

a substantial fraction of the dust in the LMC (about 1×10^6 $M_\odot$; Bernard et al. 2008) by a stellar origin.

The main conclusion of this important paper was that if the dust is not significantly destroyed during its injection into the ISM and by interstellar shocks or the reverse shock, production of 0.1–1.0 $M_\odot$ of dust per SN is consistent with that required to explain the dust masses in high-redshift galaxies (Morgan & Edmunds 2003; Dwek & Cherchneff 2011). In that case SNe may be significant contributors of dust detected in such galaxies.

3.3 The observations of SN 1987A at 870 and 350 μm from 2011

In continuation of my study of SN 1987A, I observed the object with *APEX*: on 870 μm with the *LABOCA* camera (I repeated a similar observation to the one that I described in Section 3.1) and on 350 μm with *SABOCA* for the first time. This study was published in Lakićević et al. (2012a). The aim was confirmation of the previous unusual measurement with *LABOCA*, which seemed unresolved (with evidence for extended interstellar emission) and a comparison with previous measurements to probe any evolution of the dust. Also, I wanted to achieve the three times higher angular resolution which *SABOCA* offers compared to *SPIRE* on 350 μm. At the time, these data were providing an important zero-spacing value[4] for planned observations with the *ALMA* as well.

I led the the programme ESO088.D-0252, P.I. Maša Lakićević, which observed SN 1987A in July and September 2011 under excellent weather conditions – the precipitable water vapour (PWV) column was <0.2 mm for most of the *SABOCA* observations and <0.5 mm for the *LABOCA* observations.

[4]Zero-spacing problem is the problem of any purely interferometric set of the data – data has a hole in the center of the (u,v) plane whose radius corresponds to the minimum projected spacing between antennas. This information may be obtained by a single dish mapping with a telescope of sufficient diameter (Sutton 2012).

3.3.1 *LABOCA* observations at 870 μm

SN 1987A was re-observed with *LABOCA* at a wavelength of 870 μm (345 GHz) within a 60-GHz wide band ($\Delta\nu/\nu \approx 1/6$). The on-source integration time was 5 h (6.1 h including overheads). The field was imaged in spiral raster map mode. The beam has a FWHM of $\sim 19.2''$.

The data were reduced with the *BOlometer array Analysis* (*BoA*) software. The data were first corrected for atmospheric attenuation determined through skydips, applying a correction derived from observations of planets and secondary flux calibrators taken at similar elevation as the target. Then were applied several rounds of correlated flux variation ("skynoise") removal, despiking, removal of noisy bolometers, and baseline subtractions, before maps of the individual scans were created. These were then combined. The resulting map was then smoothed, and values below zero set to zero, and used as a source model for the next iteration. The model was subtracted from the data before skynoise, spike and baseline removal and added back before creating the next map. In total 35 iterations were performed, with increasing skynoise, spike and baseline removal settings while reducing the smoothing. This procedure allows one to recover extended structures, reduces the negative "bowls" seen frequently in bolometer on-the-fly maps, and reduces the noise, while yielding a final map at the full spatial resolution of the instrument.

The image was smoothed with half a beam and the resulting beam size was $20''.4$ (Fig. 3.5). The source appears to sit on filamentary emission extending towards the South-West, similar to that reported by Lakićević et al. (2011).

The flux density of the central point source is $F_{870} = 19.6 \pm 5.6$ mJy, where the uncertainty combines the rms noise level of 4 mJy (8 mJy in the unsmoothed map) and *LABOCA*'s absolute calibration uncertainty of $\sim$20%. This brightness is consistent within the errors with the result from Lakićević et al. (2011), which was 21 ± 4 mJy, observed in 2007.

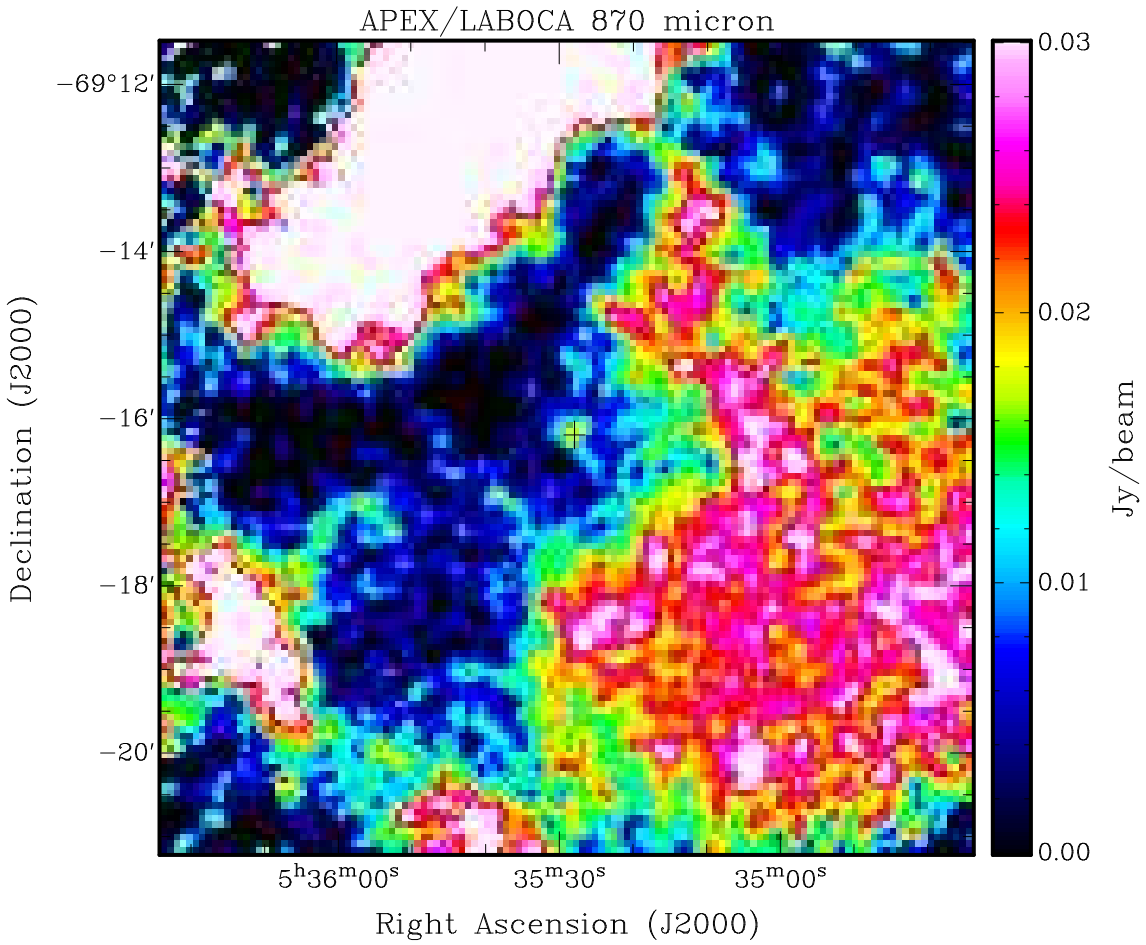

Figure 3.5: *APEX/LABOCA* image of SN 1987A at 870 μm, in July and September 2011. FWHM was 20″.4. The black cross indicates the position of the object.

3.3.2 *SABOCA* observations at 350 μm

The on-source integration time was 15.6 h (22.7 h including overheads). The field was imaged in spiral raster map mode. The beam has a FWHM of $7.''8 \pm 0.''5$, 2.5 times better spatial resolution compared to *LABOCA*, three times better compared to *Herschel SPIRE*, and similar to the 2005 *ATCA* image at 3 mm. These observations had very good quality and high signal to noise (S/N) ratio because of great weather

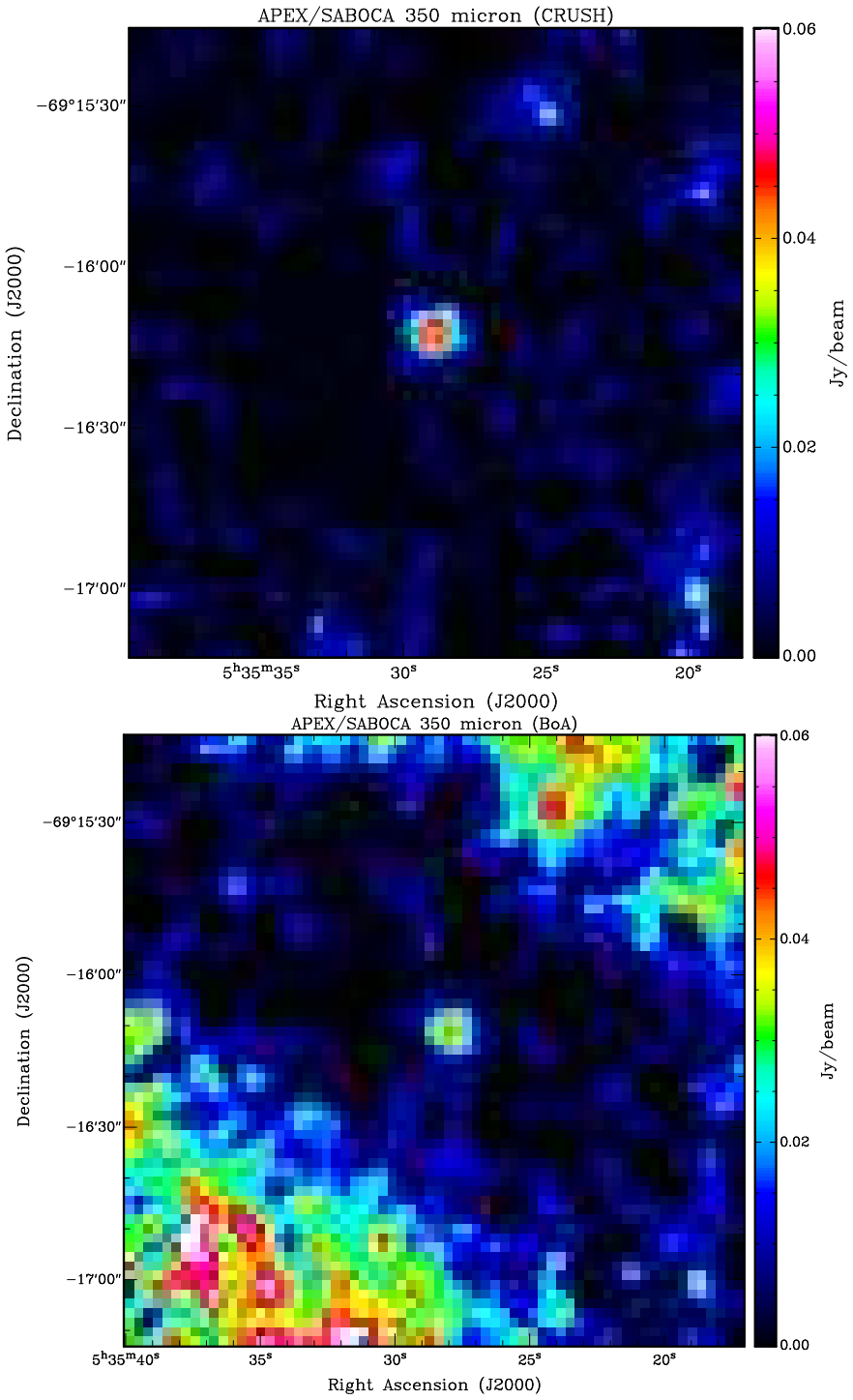

Figure 3.6: SN 1987A observed with *SABOCA* at *APEX*, on 350 μm, in July and September 2011, *Top:* reduced with *CRUSH* and *Bottom:* reduced with *BoA*. FWHM was $8''.4$.

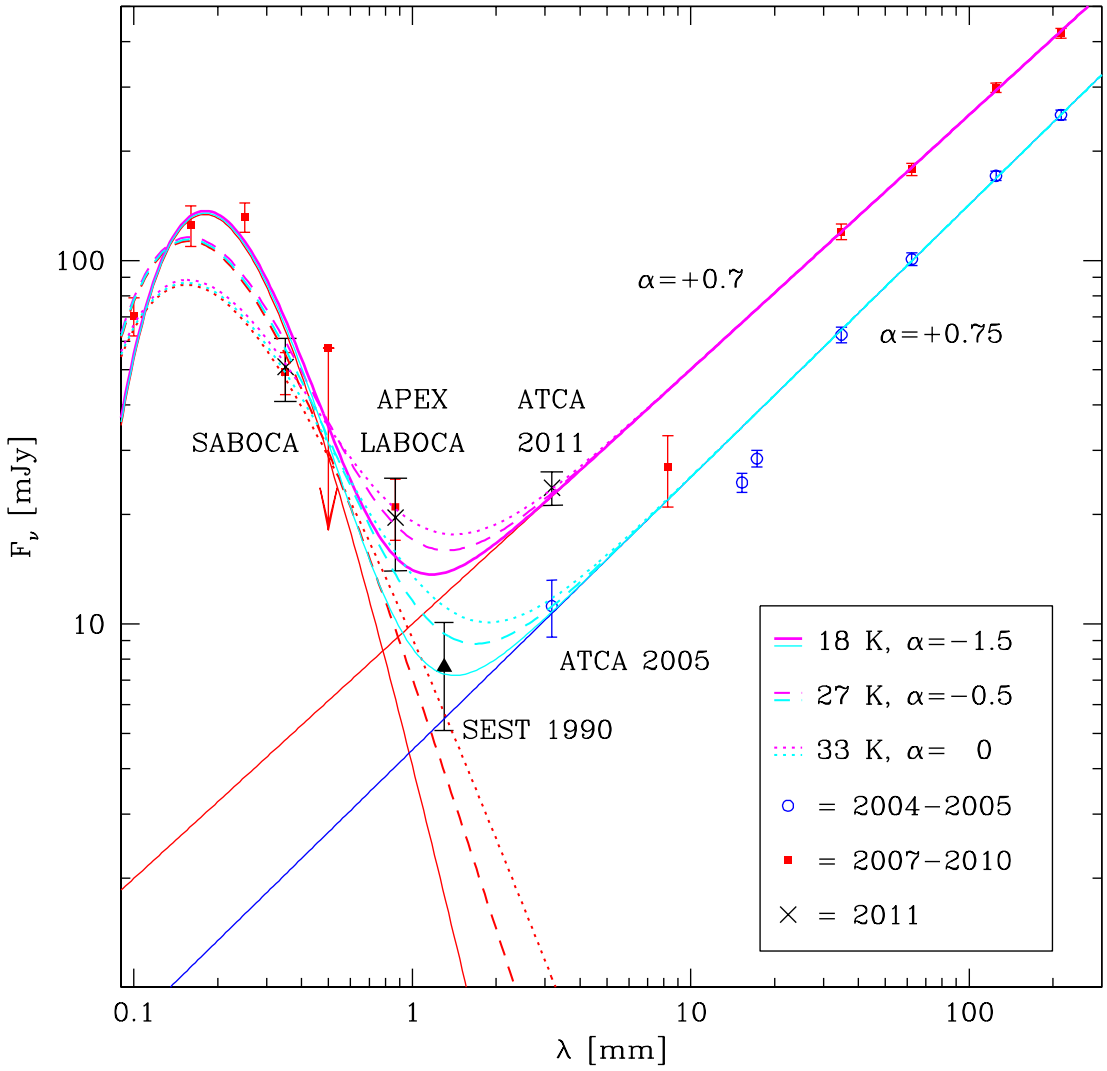

Figure 3.7: SED of SN 1987A in case that $\alpha_{IR} = 0$, T=33 K, and 160 and 250-μm fluxes are ignored, dotted line; that $\alpha_{IR} = -0.5$, T= 27 K, and 160 and 250-μm fluxes are ignored, dashed line and that $\alpha_{IR} = -1.5$, all wavelengths 100-350 μm are included, T=18 K, full line. See χ^2, reduced χ^2 value, χ^2_{RED} and included data-points of these fits in Table 3.3. The blue lines are fit through the data from 2004-2005, while pink lines are fit through data from 2007-2011. Data: Biermann et al. (1992); Zanardo et al. (2010); Matsuura et al. (2011); Lakićević et al. (2011), Lakićević et al. (2012a) and Lakićević et al. (2012b).

conditions, and high brightness of the object at 350 μm.

The data reduction was performed with two different packages – *BoA* and *CRUSH* (*Comprehensive Reduction Utility for SHARC-2*; Kovács 2008) which use different algorithms. In *CRUSH*, we used the faint source reduction option, with a source size filtering of 10″, and ran 20 iterations. The image, smoothed with half a beam, is presented in Fig. 3.6. Since the pointing in September was slightly offset from that in July, the data from July and September were reduced separately and the September data were shifted to match the July data and averaged. The resulting beam has an effective FWHM of 8.″4. The flux density of the unresolved source at the position of SN 1987A on the combined image is $F_{350,\mathrm{CRUSH}} = 58 \pm 13$ mJy, where the uncertainty combines the rms noise level of 6 mJy and *SABOCA*'s absolute calibration uncertainty of 20%.

The data reduction strategy within *BoA* corresponds to the one used for *LABOCA*, except that the atmospheric opacities were determined from measurements of the amount of PWV done in parallel to the observations, using an atmospheric model (ATM). Because the calibration measurements were made at the same time as the observations and at the same azimuth and elevation, they yield a more accurate opacity correction. The image obtained using *BoA*, smoothed with half a beam, is presented in Fig. 3.6. Here, the July and September data were aligned and placed at the centre of the image *before* the reduction. The measured flux density of SN 1987A is now $F_{350,\mathrm{BoA}} = 44 \pm 7$ mJy.

The maps reduced with *BoA* and *CRUSH* differ slightly in the flux level, probably due to the different calibration strategies (*CRUSH* uses opacities derived from skydips). The flux densities are consistent within the calibration uncertainties of $\sim$ 20-30%. The extended emission in the *BoA* reduced image is not evident in the *CRUSH* reduced map, because here the algorithm is optimised to remove correlated signal variations from the data time streams, which includes extended emission structures on scales of $\sim 0.5'$-$1'$.

The images from the two reduction techniques both confirm that the object at the position of SN 1987A is a point source. The detection is of much higher significance

than the uncertainty in the flux density suggests, because the latter includes systematic uncertainties mainly in the flux calibration. For the flux density we adopt the average from the two reductions, $F_{350} = 51 \pm 10$ mJy, where the uncertainty is the average from the individual uncertainties as they are strongly correlated. This is remarkably close to the *Herschel* measurement from 2010, 49.3 ± 6.5 mJy.

3.3.3 Discussion of the new data

3.3.3.1 Time needed for the dust to cool down

Here I discuss the time needed for the dust to cool down in the absence of additional collisional heating. The cooling of a spherical grain of diameter a and temperature $T_{\rm d}$, and luminosity, $L_{\rm d} = 4\pi(a/2)^2\sigma T_{\rm d}^4$, results in a heat loss of $L_{\rm d} \equiv {\rm d}Q/{\rm d}t = -mC{\rm d}T_{\rm d}/{\rm d}t$, where m is the mass of the grain and C its heat capacity. From these two equations it can be derived that

$$\frac{dT}{dt} = \frac{-4\pi(a/2)^2\sigma T_{\rm d}^4}{mc} = -\frac{4\pi(a/2)^2\sigma T_{\rm d}^4}{4/3\pi(a/2)^3\rho C} = \frac{-6\sigma T_{\rm d}^4}{a\rho C}, \tag{3.10}$$

if I write mass as $4/3(a/2)^3\rho\pi$. The expression can be written as

$$\frac{dT}{T_{\rm d}^4} = \frac{-6\sigma}{a\rho C}dt \Leftrightarrow \int_0^x \frac{dT}{T_{\rm d}^4} = \int_0^x \frac{-6\sigma}{a\rho C}dt. \tag{3.11}$$

If I integrate and if I choose that $t_0 = 0$ to $t_x = t$, I will have

$$\frac{1}{3T_{\rm d}^3(0)} - \frac{1}{3T_{\rm d}^3(t)} = \frac{-6\sigma}{a\rho C}t, \tag{3.12}$$

from which it is easy to obtain

$$T_{\rm d}(t) = \left(\frac{1}{T_{\rm d}^3(0)} + \frac{18\sigma}{a\rho C}t\right)^{-1/3}, \tag{3.13}$$

where one can find that the initial temperature, $T_{\rm d}(0)$ ($\sim$ 1000 K, for example) rapidly vanishes, and is not very important, therefore

$$T_{\rm d}(t) \simeq \left(\frac{a\rho C}{18\sigma}\right)^{1/3} t^{-1/3}. \tag{3.14}$$

Replacing ρ ∼3000 kg m^{-3}, $C \sim 10^3$ J K^{-1} kg^{-1}, t =24 yr= 10^9 s, $\sigma = 5.67 \times 10^{-8}$ J K^{-4} m^{-2} s^{-1} and a =10^{-7} m into the previous equation I can obtain $T_{\rm d}(t) \simeq 0.07$ K (or ≃0.14 K for a =10^{-6}m). From eq. 3.14, $t = \frac{a\rho C}{18\sigma} T_{\rm d}^{-3}$, therefore I find that the dust would cool down to the temperature of the cosmic microwave background (3 K) in 10^4-10^5 s, within a matter of hours. At first, collisions with the electrons prevent this from happening, but as the remnant gets older, the ejecta expands, the gas cools, so the gas and grains detach when the density falls below 10^5 cm^{-3}. In Section 3.1.3.1 we have shown the density of the ionized ejecta of SN 1987A is $n \sim 10^4 - 10^5$ cm^{-3}.

I will give a brief explanation for this. If the density of particles (mainly gas atoms) is 10^5 cm^{-3}, each particle has a volume of 10^{-5} cm^3, which corresponds to a radius of 0.013 cm, therefore the distance between particles is l ∼0.026 cm. The average kinetic energy of the particles can be written as $\langle mV^2/2 \rangle = kT$, where k is the Boltzmann constant, 1.38×10^{-23} J K^{-1}. If m is a mass of a hydrogen atom, 1.67×10^{-27} kg, from there can be derived that $V \sim 5 \times 10^4$ cm s^{-1} to be the atomic speed. Dividing V and l one gets that there are ∼2×10^6 collisions s^{-1} in such gas. If the grain size is ∼0.1 μm, with a density a few g cm^{-3}, then a grain would weigh $\sim 10^{10}\times$ m$_{\rm atom}$. In order to have the grains in the equipartition stage where as much mass has hit the grain as the grain itself has, 10^{10}/number of collisions $\sim 10^4$ s are needed. That is how the collisions keep the dust at the warm temperature and it does not cool down so quickly. However, when the density drops below 10^5 cm^{-3}, l will be longer while the number of collisions will be lower, thus the time between the collisions will be longer than 10^4 s, therefore dust will cool down, grains and the dust will detach, but the ISRF will still keep the dust at a temperature $10 < T_{\rm d} < 30$ K.

In this section we ignored collisional heating in order to explore the case of dust being in the low density gas, although we are aware that Bouchet et al. (2006) demonstrate that collisional heating still can dominate at T$_{\rm d}$ <50 K, for grains with radius 0.1 μm, log(Te)<5.5 and log(n$_e$)< 2.4. Also, we ignored the case of the possible heating due to radioactive decay of this object (Matsuura et al. 2011; Matsuura et al. 2015).

3.3.3.2 Spectral energy distribution

The new measurements on 870 and 350 μm are compatible with the previous fluxes with *APEX* (Lakićević et al. 2011) and *Herschel* (Matsuura et al. 2011), respectively. Therefore, we concluded that there is no evidence for an evolution of the dust on those timescales (1–4 yr) within the uncertainty of the measurements.

Lakićević et al. (2011) used a modified black-body with $\alpha_{IR} = -1.5$ and obtained a temperature of 18 K and mass ≈ 0.5 $M_{\odot}$, similar to the result of Matsuura et al. (2011). If we extrapolate a powerlaw $F_{\nu} \propto \lambda^{\alpha}$ with slope $\alpha = +0.7$ (Fig. 3.3), one can get an estimate of the synchrotron emission contribution of ∼5 and ∼9 mJy at 0.35 and 0.87 mm.

The *Herschel* data could be affected by line emission close to SN 1987A: the 160-μm band includes the [C II] 158-μm and [N II] 205-μm lines, while the 250-μm band includes three highly excited ^{12}CO lines with another ^{12}CO line and the [N II] line at the edges of the band. In warm gas, these ^{12}CO transitions can be brighter than those at longer wavelengths, and the 350- and 500-μm bands each only include two ^{12}CO lines which additionally reduces the contribution from line emission from $\lambda > 300$ μm. While $\chi^2_{RED} = 4.20$ ($\chi^2 = 12.61$) for $\alpha_{IR} = -1.5$ if only *Herschel* data at 100-350 μm are included in fitting (Fig. 3.7; Table 3.3), when I assume the very extreme case that $\alpha_{IR} = 0$[5] (Paradis et al. 2011) and that the temperature is 33 K, I obtain a better fit ($\chi^2_{RED} = 1.36$; $\chi^2 = 5.45$) for the 100, 350 and 870 μm measurements, leaving the 160 and 250 μm measurements discrepant. A compromise between these two cases was obtained for $\alpha_{IR} = -0.5$, at 27 K ($\chi^2_{RED} = 3.02$; $\chi^2 = 12.07$; Fig. 3.7; Table 3.3) and is a better fit to the 160 μm data. The fit for α_{IR} =0 (and though to a lesser degree, the fit for $\alpha_{IR} = -0.5$) agrees with the measurement at 1.3 mm made in 1990 (Biermann et al. 1992) hinting that the cold dust has been unaltered since day 1290 and that it might well have already been in place prior to the explosion. The three fits at the

[5]The remark of Dr. Haley Gomez is that the assumption that $\alpha_{IR} = 0$ is unphysical (unless there is evidence of this kind of dust in the literature) since even fluffy aggregates (typically α_{IR} =[-1,-1.5]) and iron whiskers do not have $\alpha_{IR} = 0$.

Table 3.3: The first 3 rows show the data points included in the fits displayed in Fig. 3.7, temperatures, χ^2, χ^2_{RED} and α_{IR} values from this work. The second 3 rows show the fits where all data points are included.

Data points included	Temp. [K]	χ^2	χ^2_{RED}	α_{IR}
Herschel 100, 160, 250 and 350 μm	18	12.61	4.20	-1.5
Herschel 100, 350 + *APEX*: 350 + 870 μm $\times$2	33	5.45	1.36	0
Herschel 100, 350 + *APEX*: 350 + 870 μm $\times$2	27	12.07	3.02	-0.5
All data 100-870 μm	18	33.17	4.74	-1.5
All data 100-870 μm	33	23.26	3.32	0
All data 100-870 μm	27	24.93	3.56	-0.5

temperatures 18, 33 and 27 K and with α_{IR} of -1.5, 0 and -0.5, through all data-points from 100-870 μm (since flux at 500 μm is the upper limit, we adopt the error of 100% for that data point) are given in the end of the Table 3.3. They suggest that including 870-μm data-points into the fits give different results from the work of Matsuura et al. (2011), which could be because of synchrotron contribution of $\sim 1/3$ of the flux at that wavelength or because of lower precision of these measurements.

Mennella et al. (1998) find $\kappa \sim 10$–10^3 cm^2 g^{-1} at FIR-mm wavelengths, depending on grain composition. Smaller grains, needles, or fluffy grains all increase the surface-to-mass ratio and hence κ, thus the mass would become lower, perhaps low enough to be from progenitor mass loss. Indeed, for SNe of type IIb – probably a good match to SN 1987A, Nozawa et al. (2010) predict grains of only 0.001–0.003 μm size, and Wickramasinghe & Wickramasinghe (1993) explained the mm radiation from SN 1987A in 1990 by iron whiskers with $\kappa \sim 10^7$ cm^2 g^{-1} at FIR-mm wavelengths. Though, Gomez et al. (2006) have shown that to radiate this efficiently, iron whiskers have to be unphysically small and thin and would not survive in the solid phase in the plasma.

Here we will explore the possibility that grains are as small as $a = 0.1$ μm, $T = 33$ K and $\alpha_{IR} = 0$. The absorption efficiency, $Q_{\rm abs} = C_{\rm abs}/C_{\rm geo}$, where $C_{\rm abs}$ is the absorption cross section and $C_{\rm geo} = \pi a^2$ geometric cross section (for a sphere). The

expression for κ is

$$\kappa = \frac{C_{\rm abs}}{\rm mass} = \frac{Q_{\rm abs} \times C_{\rm geo}}{\rm mass} = \frac{Q_{\rm abs}\pi a^2}{\rm mass} = \frac{Q_{\rm abs}\pi a^2}{4/3\pi a^3 \rho} = \frac{3Q_{\rm abs}}{4\rho a}. \quad (3.15)$$

For silicate grains at T <50 K, the maximum $Q_{\rm abs}$ can be estimated using Figure 5b from Draine & Lee (1984). At λ = 100 μm, they have $\lambda Q_{abs}/a$ =1 which leads to maximal $Q_{abs} \approx 10^{-3}$. Using this value in eq. 3.15, we can get maximal $\kappa \approx 25$ cm^2 g^{-1}. If we ignore the *Herschel* 160, 250 and 500- μm data, we obtain a dust mass in SN 1987A of 0.068 M$_\odot$, with χ^2_{RED} =1.82 (χ^2 = 5.45). In Lakićević et al. (2012a) we have found that this mass could be ∼0.008 M$_\odot$, but there we have used several assumptions that are less likely, like that $\kappa \sim 10^5$ cm^2 g^{-1} and $\alpha_{IR} = 0$.

The scenario of ignoring 160 and 250-μm more accurate space telescope data, using only *Herschel* data at 100 and 350 and *APEX* data at 350 and 870 μm, is not very likely. To produce our 33 K model, the *Herschel* 160 and 250 μm fluxes would have to be contaminated by around 28% and 47% by line emission, respectively. When our initial results were published (Lakićević et al. 2012a), we did not know that CO only contributes < 10% of flux at >350 m (Kamenetzky et al. 2013) and that there is only seen 1–10% contribution from line emission to fluxes at >50 μm in the Crab Nebula (Gomez et al. 2012b), so this derivation is likely to be unrealistic.

Furthermore, if dust emits as a $\alpha_{IR} = 0$ and is not iron whiskers then this can only come from larger than typical grains, e.g. a $\gg$ 1 μm. In fact α_{IR} is only higher than -1 for grains with $a_{\rm max} > 3 \times$ wavelength suggesting these grains must be >3 mm (Draine & Fraisse 2009). Changing the grain size to mm would lead to a κ 2-4 orders of magnitude lower than the one derived in this section. The dust mass would therefore be 2 orders of magnitude higher than quoted for the different grain size alone.

3.4 Resolving SN 1987A at 3 mm with the *Australia Telescope Compact Array*

The remnant of SN 1987A was first successfully observed at 3 mm wavelengths in 2005 with *ATCA* on short baselines with integrated flux density of 11.2 ± 2.0 mJy but was unresolved with $5''$ beam (Lakićević et al. 2011). Here, I describe the work of Lakićević et al. (2012b) in which I have spatially resolved this remnant for the first time at this wavelength. The source was only detected because its brightness increased and because of an upgrade to the interferometer (the Compact Array Broadband Backend – CABB; Wilson et al. 2011) which provided a factor of 4 increase in the continuum sensitivity and therefore reducing the required observing time for a given continuum sensitivity by a factor 16.

The ability to resolve the remnant at high radio frequencies is crucial in investigating the different sources of emission within the remnant, and as such the new *ATCA* observations were also a useful complement to future observations with *ALMA* (Kamenetzky et al. 2013; Indebetouw et al. 2014; Zanardo et al. 2014).

3.4.1 Observation and data reduction

I observed SN 1987A at 3-mm wavelength with the *ATCA* over three 12-h sessions, on 2011 June 30, July 1 and August 2 (programme C2495; P.I. J. van Loon) - days 8892, 8893 and 8925 since explosion – with the five antennae equipped with receivers operating in the 3-mm band (85-105 GHz). The array was in the 750B array configuration on June 30 and July 1, with baselines between 61 and 765 m, and in the H168 array configuration on August 2, with baselines between 61 and 192 m. Observations were performed in 2-GHz wide bands centred on frequencies of 93 and 95 GHz. All three sessions were characterised by stable atmospheric conditions, with very low PWV on June 30 and July 1.

The bandpass calibrator, PKS B1921−293 was used on June 30 and August 2, while PKS B0637−752 was used on July 1. The phase calibrator PKS B0530−727 was

observed for 1.5 min per 2 min integration time on the source, while the pointing calibrator PKS B0637−752 was observed for 2 min at approximately hourly intervals. Uranus was used as flux density calibrator. Observations of SNR 1987A were centred on RA $5^{\rm h}35^{\rm m}27^{\rm s}.975$, Dec $-69^\circ\ 16'\ 11''.08$ (J2000), as from Potter et al. (2009).

The data were processed using the *MIRIAD* package. The task *ATFIX* was first used to correct the system temperatures, instrumental phases and baseline lengths. The data were examined, and scans during poor atmospheric phase stability were rejected. To maximise the S/N ratio, robust weighting was used to invert the calibrated *uv* data at both frequencies, with weighting parameter 0.5 (Briggs 1995). A preliminary *CLEAN* model (Högbom 1974) was constructed by using a small number of iterations (viz. 200). The source had sufficient S/N for phase self-calibration, which was performed with a 2-min solution interval. Subsequently, deconvolution was performed using the maximum entropy method (MEM; Gull & Daniell 1978). For the final image the MEM model of the combined datasets was restored to a diffraction-limited circular beam with FWHM of $0.''7$ – i.e. the synthesized beamsize of the 750B array – and regridded at a pixel scale of $0.''01$. Fig. 3.8 shows the Stokes-I continuum image; the off-source rms noise is ≈ 0.5 mJy beam^{-1} and we determined an integrated flux density of SNR 1987A of 23.7 ± 2.6 mJy.

To construct a spectral index image, we also reduced observations at 3 cm performed on 2011 January 25 (Ng et al. 2013). The reduction procedures included application of uniform weighting, one iteration of phase self-calibration over a 5-min solution interval and MEM deconvolution. As for the 3-mm image, the 3-cm image was restored with a $0.''7$ circular beam and regridded at a pixel scale of $0.''01$.

3.4.2 Discussion

Compared to July 2005 (Lakićević et al. 2011), the flux density in 2011 had increased 2.1 ± 0.4 times (Fig. 3.3). The new 3-mm measurement lies on the position expected from extrapolation of a power-law fit to data at $\lambda > 30$ cm of the form $S_\nu \propto \lambda^\alpha$, with spectral index $\alpha = 0.7$ (note that the July 2005 measurement at 3 mm (Lakićević et al.

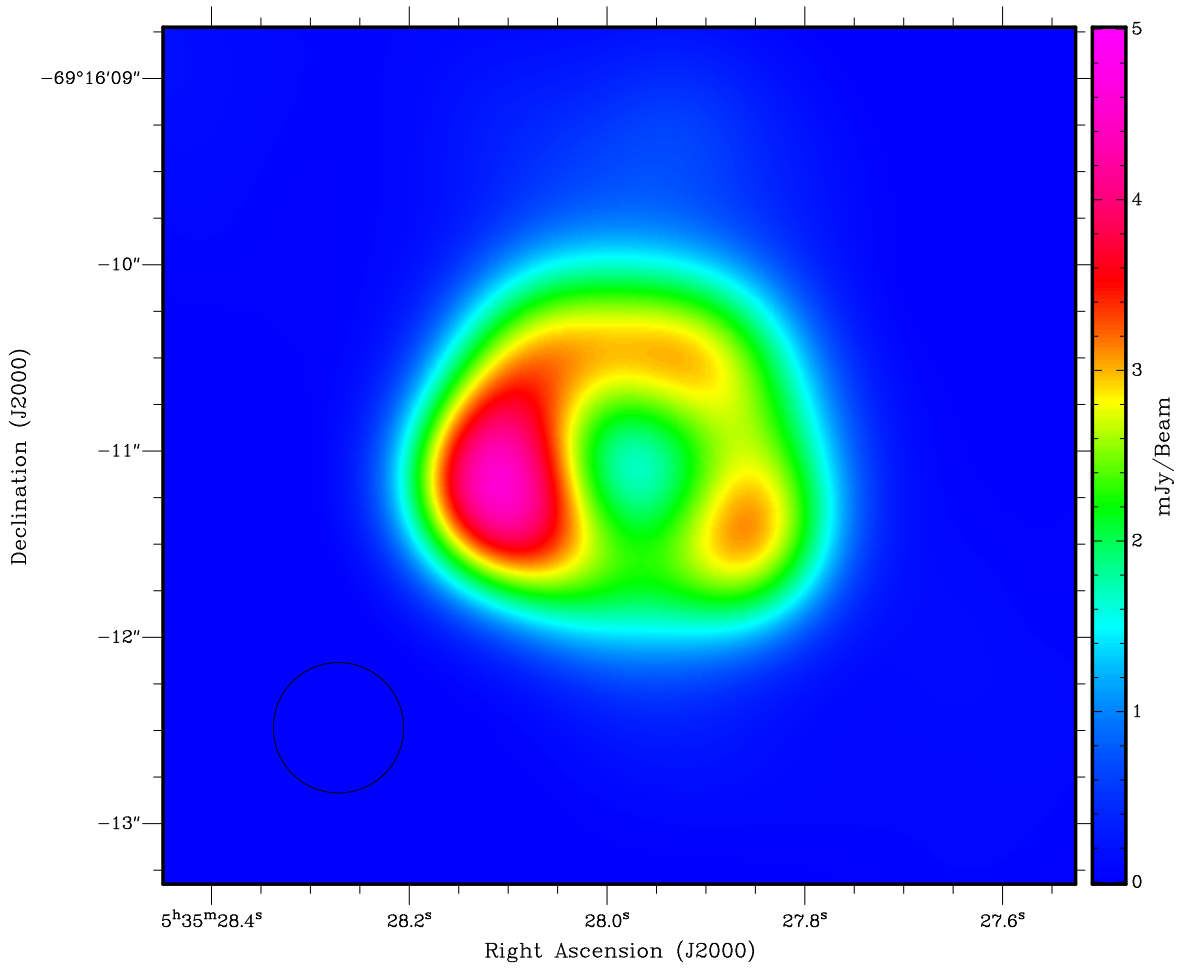

Figure 3.8: Diffraction-limited Stokes-I continuum image of SNR 1987A at 3 mm from observations made on 2011 June 30, July 1 and August 2. The image is restored to a 0.″7 circular beam (plotted in the lower left corner). The off-source rms noise is ≈0.5 mJy beam^{-1}. The size of the image is 4.90″×4.59″.

2012b) obeyed a power law with $\alpha = 0.75$ when compared to other radio data at the same epoch). We remind the reader that the 7- and 12-mm band flux densities (from Manchester et al. 2005 and from Potter et al. 2009) are lower than expected from the power law obeyed by the longer-wavelength data (see Section 3.1.3.1).

At 0.″7 resolution the 3-mm emission from SNR 1987A is clearly resolved (Fig. 3.8), making it the highest radio frequency at which this was accomplished at the time. The 3-mm image shows similarities with the images at 7 and 12 mm and 3 cm (Potter et al. 2009; Manchester et al. 2005; Ng et al. 2008). The emission is broadly distributed along the equatorial ring, but unlike the optical images the radio appearance is asymmetric with the emission peaking in the Eastern lobe and the flux ratio between the Eastern and Western halves of the image is ≈ 1.3. By fitting an optically thin shell, this asymmetry was found to be ≈ 1.3 at 7 mm (Potter et al. 2009) and 1.4 at 3 cm (Ng et al. 2008). Radial profiles are constructed across the SNR and the maximum asymmetry with respect to the *VLBI* position in the 3-mm image occurs near position angle 90° (i.e. due East-West), where it reaches a ratio of ≈ 1.6 (Fig. 3.9).

The flux density in the centre is ≈1.6 mJy, but this includes a contribution from surrounding emission due to beam smearing. The emission peaks at ±0.″6 from the centre, at ≈ 3 mJy beam^{-1} (Fig. 3.9). These show two Gaussians of peak intensities 4.5 and 2.5 mJy and FWHM 0.″7 separated by 1.″2, the formula for a Gaussian for $x = 0$ (in the middle of the two peaks) is:

$$f(x) = \frac{1}{\sigma\sqrt{2\pi}} e^{-\frac{(x-\mu)^2}{2\sigma^2}}, \tag{3.16}$$

for the two Gaussians. Since we have *mean* or *expectation* μ =0.6, we find a *standard deviation* $\sigma \approx 0.3$ (since $FWHM = 2\sqrt{2ln2}\sigma$, and $\frac{1}{\sigma\sqrt{2\pi}}$ =1.33 mJy). I find that at $x = 0$, the intensity level is ≈0.36 mJy. This leaves room for additional emission in the centre at a level of ≈1.2 mJy, which may be compared with the 2-σ rms noise of ≈1 mJy. Given the crudeness of this estimate I settle on an upper limit of 1 mJy at 2-σ significance. This is below the upper limit of ∼2 mJy placed on contributions from f-f emission to the mm emission by Lakićević et al. (2011). Lakićević et al. (2011) estimated that the cold dust (∼18 K) seen at FIR and submm wavelengths would

contribute ~ 0.1 mJy at 3 mm.

The 3-mm image is compared with the 3-cm image in Fig. 3.10 and these form the basis for the spectral index image (Fig. 3.11). The spectral index α was determined from the ratio of the two images, as $\alpha = \log(S_1)\log(S_2)/(\log(\nu_1)\log(\nu_2))$, where the flux levels exceed 3-σ though we conclude that near the outer edge of the displayed region the low flux level combined with the imperfections in the image reconstruction can easily lead to strong variations in the flux ratio between independent images. We observe the following: (1) the brightest radio emission is characterised by $-0.95 < \alpha < -0.75$; and (2) the centre has a shallower spectrum, with $\alpha \sim -0.65$, similar to the tentative result obtained at cm wavelengths (Potter et al. 2009).

Diffusive shock acceleration theory (Jones & Ellison 1991) yields $\alpha = (1-\gamma)/2$, where γ is the power-law index of the momentum distribution of the accelerated electrons, $N \propto p^{\gamma}$ and depends only on the shock compression ratio, r, as $\gamma = (r+2)/(r-1)$. Supersonic[6] shocks are easily established in SNRs, and lead to $1 < r \leq 4$, i.e. $\alpha \leq -0.5$ ($r > 4$ is possible for relativistic and/or non-adiabatic shocks). We conclude that the strongest mm-emission, with $-0.95 < \alpha < -0.75$, arises from moderately-weak shocks with $2.6 < r < 3.0$. The central region could signify the emergence of a pulsar wind nebula (as seen in Crab Nebula's PWN; Bandiera, Neri & Cesaroni 2002) with strong shocks ($r \sim 3.3$), or some non-synchrotronic emission, e.g., f-f emission with $\alpha \sim -0.1$ (indeed, the ejecta are clearly visible in *Hubble Space Telescope* images). Also, it is possible the emission from grains with high emissivity at mm wavelengths (Lakićević et al. 2012a; Wickramasinghe & Wickramasinghe 1993), but the spectral index value in the image centre in the edges of the SNR is uncertain since the sensitivities of the two measurements could be different and the fluxes are low.

[6]Supersonic speed is a rate of travel of an object that exceeds the local speed of sound. Mach number is representing the ratio of speed of an object moving through a fluid and the local speed of sound, $M = V/V_{\rm sound}$. For sonic speeds, Mach number is 1, for supersonic speeds, it is from >1 to 5, and for hypersonic it is from 5 to 10.

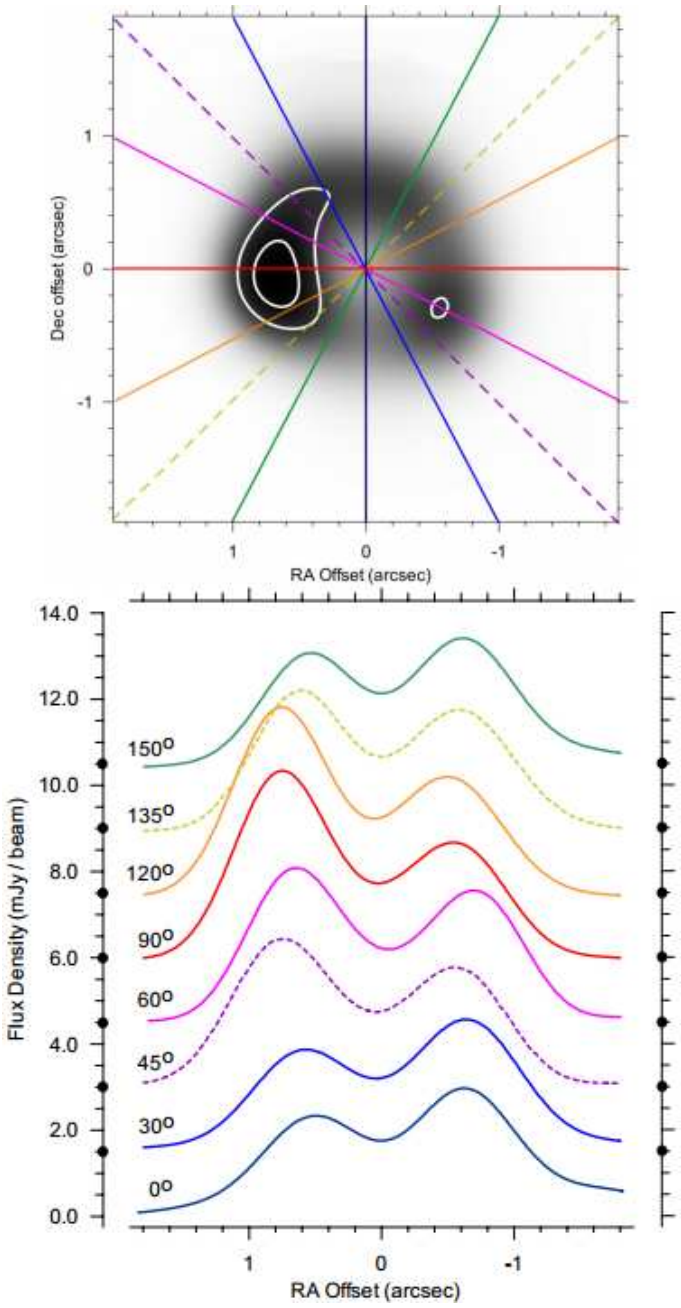

Figure 3.9: Radial slices through the 3-mm image at 8 position angles. The black dots on vertical axes on the bottom panel indicate the position of the zero for each slice. The top image is overlaid with 70% and 90% flux density levels (white contours), where maximal flux is 4.5 mJy beam^{-1}. The image centre is shifted to the *VLBI* position of SN 1987A determined by Reynolds et al. (1995) (RA $05^{\rm h}35^{\rm m}27.968^{\rm s}$, Dec $-69°16'11.09''$ (J2000)).

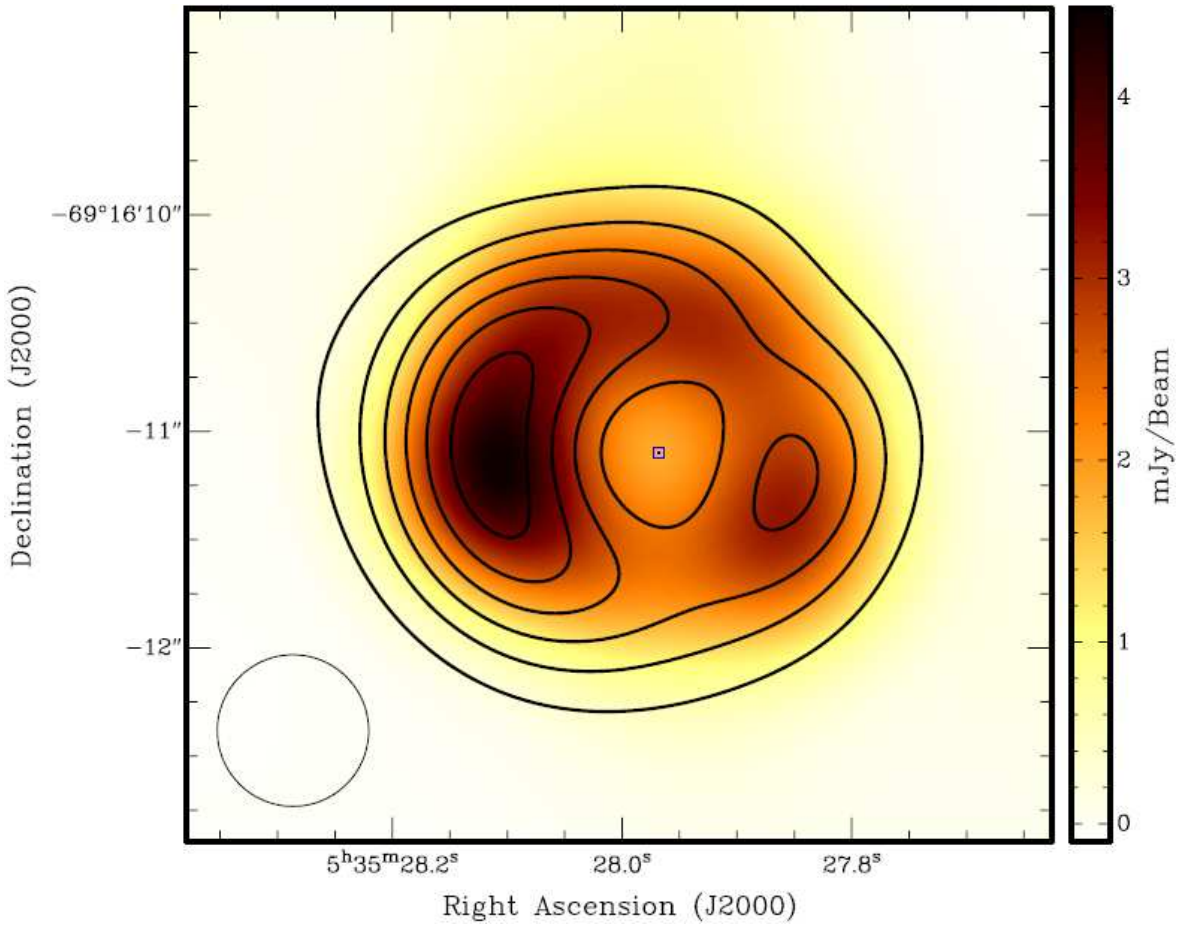

Figure 3.10: 3-mm image with contours of the 3-cm image derived from observations performed on 2011 January 25 (Ng et al. 2013), where the contours correspond to 20% flux-density intervals, while the outer contour is at the level of less than 3 mJy beam^{-1} and the typical rms noise level for 3-cm image is 0.05 mJy beam^{-1}. Both the 3-mm and 3-cm images were restored with a 0.″7 circular beam and are centred on the *VLBI* position of SN 1987A determined by Reynolds et al. (1995) (blue square).

There is striking resemblance between the 3-mm image from 2011 (Fig. 3.8) and the earliest, deconvolved X-ray images, kindly provided by David Burrows and Eveline Helder, taken with the *Chandra* satellite in 1999 and 2000 (Burrows et al. 2000; Park et al. 2002; Racusin et al. 2009), when the blast wave had just reached the inner rim

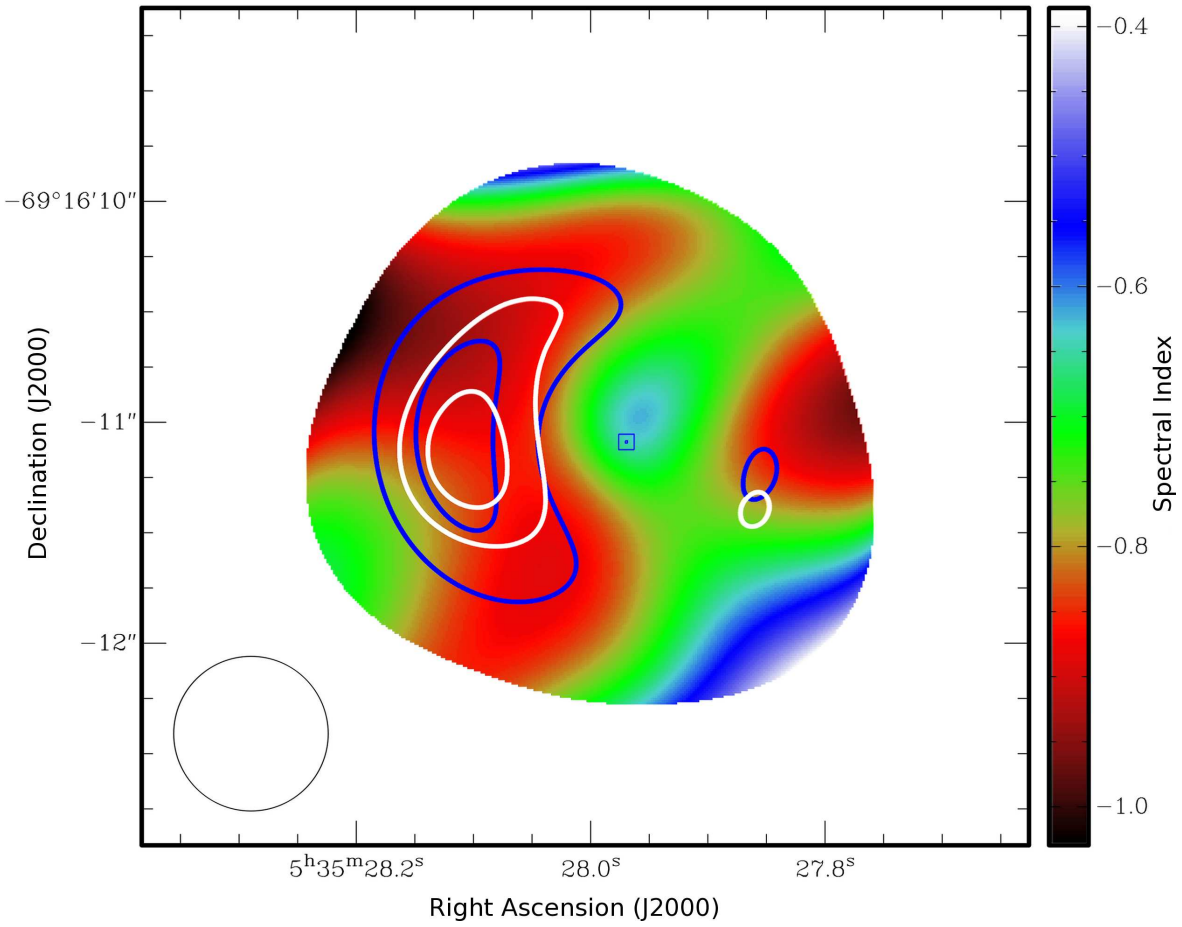

Figure 3.11: 3-mm – 3-cm spectral index image. The spectral index α is deffined as $S_\nu \propto \nu^\alpha$ and was determined from the ratio of the 3-cm image from observations performed on 2011 January 25 (Ng et al. 2013) and the 3-mm image from observations around July 2011. Both images were restored on a 0.″7 circular beam and centred on the *VLBI* position of SN 1987A determined by Reynolds et al. (1995) (blue square). Contours representing the 70% and 90% flux density levels (white: 3 mm; blue: 3 cm) are shown.

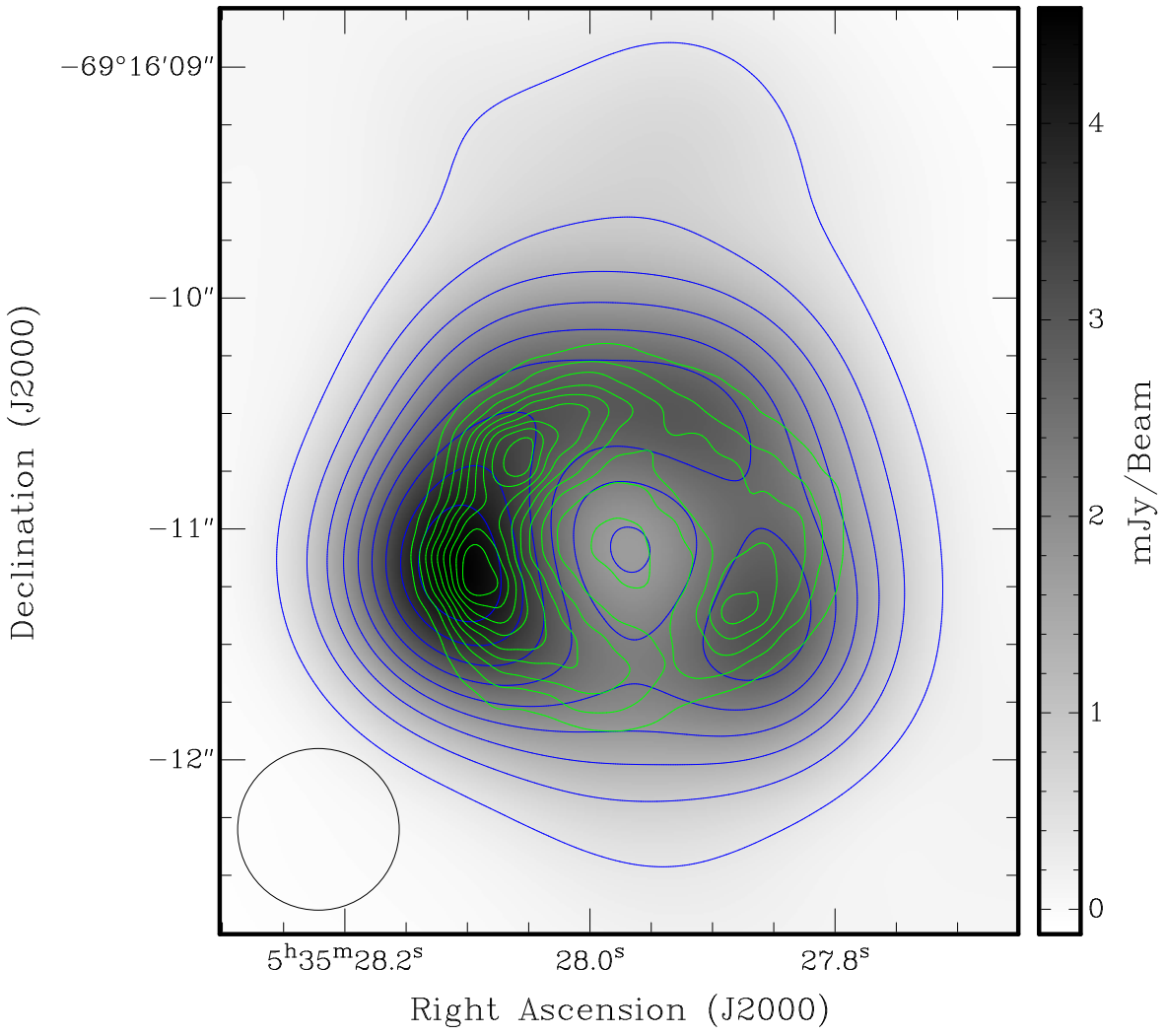

Figure 3.12: The 3-mm image of SNR 1987A from 2011 (greyscale and blue contours; the beam is plotted in the lower left corner), overlain with (green) contours of the average of the deconvolved 0.3-8 keV *Chandra* X-ray images from October 1999, January 2000 and December 2000 (Burrows et al. 2000; Park et al. 2002). Contours are between 10% and 90% of the maximum flux of the image with 10% intervals. For 3-mm image, 10% is 0.45 mJy beam^{-1}, while 2σ rms noise level is $\approx$1 mJy beam^{-1}. For the X-ray image, the level of 10% is 0.8×10^{-6} mJy beam^{-1}. The size of the image is $3.55''\times4.01''$.

of the flash-ionized ring (Fig. 3.12). In particular, the peaks in the mm emission in the East and South-West correspond to similar peaks in the X-ray emission at that time. The X-ray images are broad-band, 0.3–8 keV, and were averaged and aligned with the 3-mm image. The correspondence between the high-frequency radio structures and former X-ray structures is remarkable given that radio synchrotron emission depends on the magnetic field strength and is highly anisotropic.

However, the resemblance between the mm emission and X-rays has diminished since 2000, because the X-ray images have become dominated by soft, X-ray emission from hot gas behind the forward shock distributed more uniformly along the ring (Racusin et al. 2009; Zhekov et al. 2010a). This gives us an important conclusion that has often been discussed, that in the early stages of the life of a SNR, the X-ray spectrum is dominated by hard, non-thermal, synchrotron radiation, while later, it becomes more dominated by soft X-ray emission. Though, in the life of a mature SNR which is cooling down, in its radiative phase, or later (or some $\geq$15 000 yr after the explosion), thermal X-rays will vanish sooner than non-thermal and radio radiation.

3.5 SN 1987A resolved with *ALMA*

I have participated in *ALMA* studies of SN 1987A, which I briefly summarise below.

3.5.1 CO and SiO rotational emission from the debris of SN 1987A with the *ALMA*

A small mass (10^{-3} $M_\odot$) of hot (3200–4000 K), vibrationally excited CO was seen 192 days after the explosion in SN 1987A (Liu, Dalgarno & Lepp 1992; Spyromilio & Leibundgut 1996), but the emission faded below detection limits after ~600 days, when the gas became too cool to excite vibrational transitions (Liu & Dalgarno 1995; 700 K at 800 days). Emission from freshly formed warm (<900 K) CO and SiO molecules has been observed at IR wavelengths in SN 1987A and several other SNe, some hundred

days after the SN explosion (Wallstrom et al. 2013). Theoretical models predict that CO formation would continue after that time, yielding ~ 0.1 $M_\odot$ of CO (Cherchneff & Dwek 2009).

Kamenetzky et al. (2013) performed spectroscopy and imaging observations with *ALMA*, *APEX* and *Herschel* of rotational transitions of cold CO and SiO in SN 1987A, for the first time and they located the emission of these molecules within $1''$ of the central debris, finding at least 0.01 $M_\odot$ of CO at a temperature >14 K, ∼25 yrs after the explosion. SiO was detected by chance, thus only the red wing of SiO emission is observed, so it was not possible to measure the full flux in that line. These observations confirm the presence of cold molecular gas within SNRs and provide insight into the physical conditions and chemical processes in the ejecta.

Soon after the paper of Kamenetzky et al. (2013) came out, Wallstrom et al. (2013) reported rotational CO emission in the knots of Cas A, detected with *Herschel*, believed to have reformed in the post-shock gas. The gas is warm (two components at ∼400 and 2000 K) and dense $\sim 10^{6-7}$ cm^{-3}.

3.5.2 Dust production and particle acceleration in SN 1987A revealed with *ALMA*

Indebetouw et al. (2014) observed SN 1987A at 450 μm, 870 μm, 1.4 mm, and 2.8 mm, using *ALMA*, finally resolving the object at FIR and (sub)mm wavelengths. SN 1987A was observed during 2012 multiple times with ∼20 antennae in configurations containing baselines between ∼20 m and ∼400 m. In Fig. 3.3, data from this paper are shown as green triangles. The *ALMA* data lie within the error bars of the fit from Lakićević et al. (2011), for the years 2007–2010.

The images at 450 μm, 870 μm and 1.4 mm separate emission from the torus (equatorial ring) and inner ejecta. The radiation from the torus is from synchrotron emission, while the radiation from the central part (ejecta) is the dust and can be well fit with a modified black body. On Fig. 3.13 (taken from Zanardo et al. 2014), the brown-yellow color scale presents the 870-μm *ALMA* $0.3''$-beam image whereas it is

clearly visible that the ejecta is resolved from the ring. The *HST* image is given by the light blue contours. Fig. 3.13 should be compared with the one we made in the same wavelength, at 2011, Fig. 3.1. The *ALMA*, *Herschel* and *APEX* photometry can be fitted with 0.23±0.05 $M_\odot$ of amorphous carbon dust at 26±3 K (half the amount that Matsuura et al. 2011 estimated, at somewhat higher temperature).

ALMA observations (Kamenetzky et al. 2013; Indebetouw et al. 2014) finally confirmed that the dust lies in the ejecta of this object; while synchrotron radiation is placed in the ring (Matsuura et al. 2011; Lakićević et al. 2011; Lakićević et al. 2012a; Lakićević et al. 2012b). They better constrained the SED and succesfully detected molecules formed in the ejected material.

3.5.3 Comments on molecule production in SN 1987A

The detection of CO and SiO in SN ejecta suggests that molecular gases could lock up a significant amount of heavy elements in SN ejecta, leaving very little left for dust production (Section 1.3.3). For a progenitor of SN 1987A of 18 $M_\odot$ (Woosley, Heger & Weaver 2002), Sarangi & Cherchneff (2013) predict the formation of 0.5 $M_\odot$ of CO, ∼0.005 $M_\odot$ of C and low amounts of other elements ($< 10^{-2}$ $M_\odot$), except O_2, ∼0.77 $M_\odot$. Nevertheless, Matsuura et al. (2015) modelled the new *Herschel* observations with 0.5 $M_\odot$ of pure C, which is twice mass of C than the predicted amount in nucleosynthesis models. The results from the theoretical models do not give enough metals formed in SN 1987A to explain the high dust mass in SN ejecta (∼0.4 $M_\odot$; Matsuura et al. 2011) and they lock up high amounts of C in CO, while the observations suggest a higher mass of carbon is locked up in dust (Matsuura et al. 2011; Indebetouw et al. 2014) and lower CO mass (0.01 $M_\odot$; Kamenetzky et al. 2013). This could occur if the CO mass in ejecta of SN 1987A is overestimated in theoretical models or because CO may be dissociated by UV/radioactive photons (Clayton 2011).

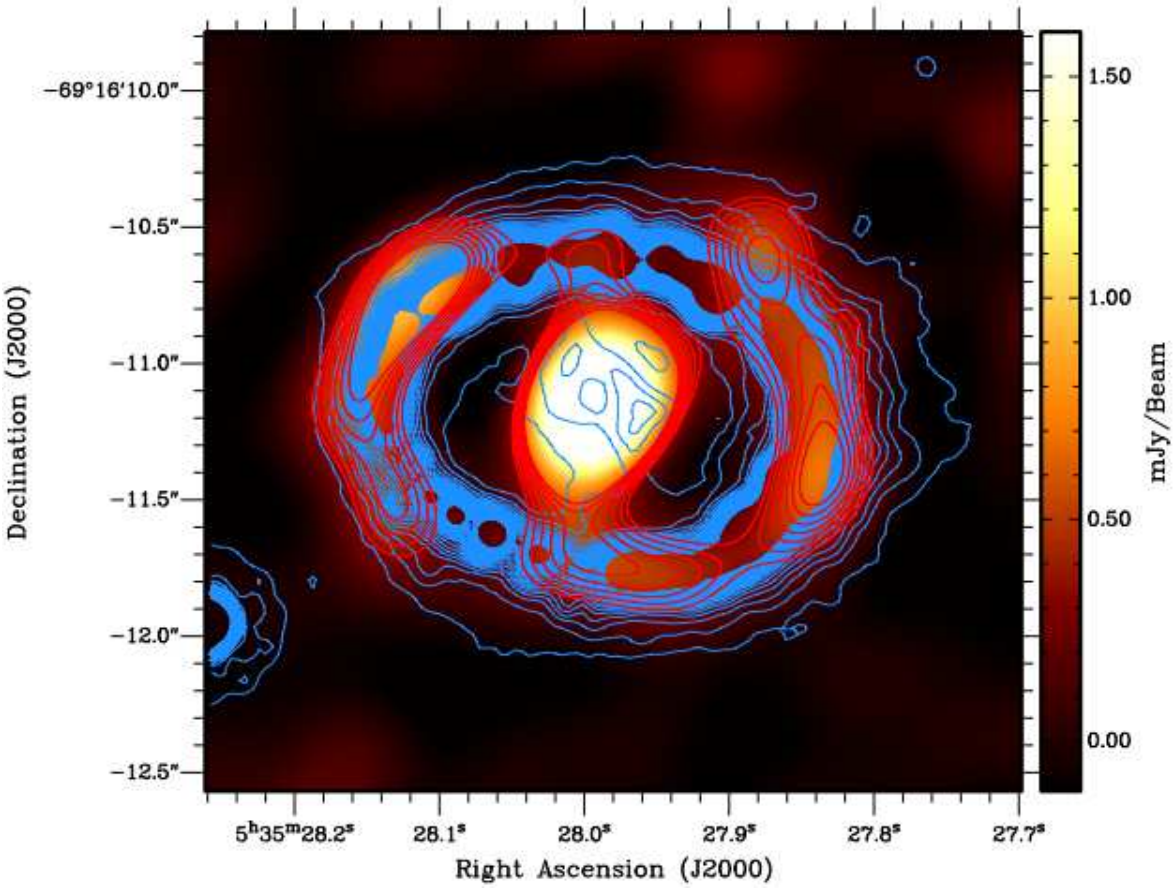

Figure 3.13: Overlay of the *HST* image of SNR 1987A (light blue contours; Larsson et al. 2011) on the 345 GHz image produced from *ALMA* observations performed in 2012 June and August (brown-yellow color scale and red contours). The *ALMA* image is resolved with 0.3″ circular beam. The image is taken from Zanardo et al. (2014).
.

3.6 Conclusions

- In Section 3.1, I presented the first submm (*APEX* at 0.87 mm) and mm (*ATCA* at 3.2 mm) observations of SN 1987A that bridge the gap in the SED between the previously detected FIR emission from dust grains (at $\lambda \leq 0.35$ mm) and radio emission from synchrotron radiation (at $\lambda \geq 0.8$ mm). They do not deviate from previous extrapolation of the FIR and radio SEDs, respectively. We assume that 3.2-mm emission is only synchrotron emission, since it agrees with previous radio data. However, I set a limit on the contribution from f-f emission from a plasma at 870 μm to be $\sim$2 mJy, from SED and from the theory.

- While the 3.2-mm *ATCA* image ($5''$ resolution) is point-like, the *APEX* 0.87-mm image ($18''$ resolution) seemed to have an extended emission from cold dust towards the South-West, which could be an interaction region between the RSG progenitor's wind and a dense medium.

- We were the first to publish the data of a SN/SNR observed with *APEX*, together with the data of this object on 3.2 mm which was the shortest and faintest synchrotron wavelength that this object was observed at, at the time of publication.

- In Section 3.2, I briefly show the results of the work of Matsuura et al. (2011), who have observed SN 1987A with *Herschel* at 100, 160, 250, 350 and 500 μm, finding $\sim$ 0.4–0.7 $M_\odot$ of the dust at 17–23 K, connected to this object, without resolving it on high wavelengths, interpreting this result as the dust condensed in the ejecta of this SN.

- In Section 3.3, I have presented my own observations of SN 1987A at wavelengths of 350 and 870 μm, obtained with the *APEX* telescope, showing very clear detections of largely unresolved emission.

- Repeated observations with the *LABOCA* instrument confirmed my previous results and convinced me that there is no evolution of the dust on the timescales of ∼4 yr above the uncertanties (20%).

- The *SABOCA* instrument had a beam size a third of that of the *Herschel* image (Matsuura et al. 2011), which constrained all emission from SN 1987A to be located within 8″ from the explosion site, but this still did not provide the answer to the question whether the emitting dust is from some echo, the dense wind material from the progenitor, pre-existing interstellar dust or in the ejecta.

- We investigated whether smaller, nonspherical, or fluffy grains could have higher κ, which would decrease the inferred dust mass, possibly enough to become consistent with pre-SN production ($\ll$0.5 $M_\odot$). In that case, the temperature may be as high as ∼33 K if the dust emits as greybody (α_{IR} =0) – though this would require a contribution from line emission to the flux within the 160- and 250-μm *Herschel* bands of 28% and 47%, respectively. However, we concluded that this scenario is not likely because $\alpha_{IR} = 0$ is not physical for grains and iron whiskers themselves would struggle to reach the κ level of 10^5, required to significantly reduce the dust mass.

- In Section 3.4 I have resolved the remnant of SN 1987A for the first time at 3-mm wavelength with *ATCA*, at a resolution of 0.″7. The image is dominated by synchrotron emission from just inside the equatorial ring, generated by moderately weak shocks.

- We noted the correspondence between the 3-mm emission and structures in the hard X-ray emission recorded in 1999 and 2000 (>10 yr before *ATCA* data). We concluded that at 1999, the X-ray emission was more non-thermal than now and that the synchrotron emission from the year 2011 possibly arises from plasma behind the reverse shock (or reflected shock; cf. Zhekov et al. 2010b).

- We set an upper limit on the emission from any dust or pulsar wind nebula in the centre, of ≈ 1 mJy (at a level of 2-σ rms noise).

- In Section 3.5 I briefly describe the *ALMA* observations of SN 1987A, which resolved SN 1987A, separating the $\sim$0.23$\pm$0.05 $M_\odot$ of dust (modelled as the amorphous carbon) at 26$\pm$3 K in the ejecta from the synchrothron radiation which belongs to the ring. They have detected 0.01 $M_\odot$ of CO at a temperature $>$14 K and also found some SiO formed in the ejecta of this object.

4 Influences of SNRs within the LMC on the ISM on FIR and submm wavelengths: SNRs as dust destroyers

In this Chapter I present the results from the paper Lakićević et al. (2015).

4.1 Introduction to my study of SNRs with *Herschel* and *Spitzer*

In this work I analyse *Spitzer* and *Herschel* observations of SNRs in the LMC at wavelengths 24, 70, 100, 160, 250, 350 and 500 μm, which are not obviously detected at wavelengths longer than 70 μm. While several ($\sim$10) young objects were detected with *IRAS*, *Spitzer* and *AKARI* at $\lambda \leq 70$ μm (Williams et al. 2006; Williams, Chu & Gruendl 2006; Borkowski et al. 2006; Seok et al. 2008), 29 SNRs analyzed in the later study of Seok, Koo & Onaka (2013), at *Herschel* wavelengths SNRs are not detected. However, instead of direct detection methods, I chose instead to investigate the influence of SNRs on their environment at FIR and submm wavelengths on different methods: comparison of FIR/submm surface brightness with SNR diameters, ages and radio surface brightness, looking for the difference between the environments of Ia and CC SNRs, finding the flux ratios of SNR images on different wavelengths (since I found that this often shows the existence of the remnant), making maps of the dust mass and temperature of these regions – which will become the first FIR/submm atlas of these objects and exploring the radial profiles of these dust mass maps.

4.1.1 Some more details about my sample of objects

In this thesis I research a sample of 61 LMC SNRs (see Table 4.1; Sections 1.2.5 and 2.3) and here will give some information about the ones that are explored because that

is useful to know when interpreting the mass and temperature maps (Section 4.2.4). Some more details about these more explored objects (diameters, ages, types, fluxes) are given in Table 4.2.

As many SNRs from my sample are mature objects, the explosion type is often not known or it is uncertain and in the literature is given that they are core-collapse (CC), Ia or that information is not known. Because I wanted to explore if the different densities of the dust surround these two types of objects, in this work I made the classification to Ia and CC SNRs. The group assumed to be type Ia are the ones that are claimed to be Ias in the literature, while for all the rest in this work I assume that they are CC. Therefore, CC in my sample may still harbour some Ias. In the literature, the type of CC SNRs (e.g. II, Ib, IIP...) is also often assumed, but it is not always very certain.

SN 1987A is described in Chapter 3. It is a young SNR in the free expansion phase and by its characteristics it does not belong to the rest of the SNRs in LMC.

N 49 (0525−661) is the brightest SNR in the LMC. It has a progenitor mass of <30 $M_{\odot}$ (Badenes et al. 2009; van Loon et al. 2010). The age of this SNR is probably about 6600 yr (Williams, Chu & Gruendl 2006). This SNR has an X-ray emitter in the North-Eastern part (Hayato et al. 2006), which is not detected at any other wavelength. An unresolved X-ray hot spot coincides with the position of the soft gamma-ray repeater (SGR) 0525−66 (Williams et al. 1999). SNR N 49 is special for FIR/submm wavelengths because it is the only detected SNR (except SN 1987A) in the MCs at *Herschel* wavelengths which is explained by the interaction of SNR with a massive and warm cloud of ISM (so called 'blob'), estimated to have ∼10 $M_{\odot}$ of dust (Otsuka et al. 2010). The 'blob' is also observed with *Spitzer*[1]. 10 $M_{\odot}$ of dust is the highest dust mass that one SN/SNR has ever been connected with.

N 158A (0540−693) is possibly of type Ib/c or IIP progenitor (Badenes et al. 2009), of 20−25 $M_{\odot}$, containing a pulsar (Hayato et al. 2006). It is an ∼1000 yr old

[1]Here I mention only *Spitzer* detections because that is connected with my work, but most of these objects are detected also at radio, X-rays and sometimes optical wavelengths.

O-rich and Crab-like remnant (Park et al. 2010). Williams et al. (2008) detected its PWN with *Spitzer* at wavelengths ≤ 24 μm, but did not find any IR detection of the shell. They found $\sim 10^{-3}$ $M_\odot$ of dust synthesized in the SNR, heated up to 50−65 K by the shock wave generated by the PWN.

0509−67.5 is a SNR of type Ia, from an old population of stars (Badenes et al. 2009), observed with *Spitzer* (Borkowski et al. 2006). Its progenitor is probably a double degenerate system (Schaefer & Pagnotta 2012).

0519−69.0 is a type Ia, from an old, metal-poor population (Badenes et al. 2009), observed with *Spitzer* (Borkowski et al. 2006). Its progenitor is probably a double degenerate system (Edwards, Pagnotta & Schaefer 2012).

N 103B (0509−68.7) is probably a Ia SNR, of 1000−1500 yr (Hughes et al. 1995), having a relatively younger and massive progenitor with substantial mass loss before the explosion (Badenes et al. 2009). Although in the direction of this remnant there is a dense cloud (see mass map in Fig. A.4, bottom), it is possible that it expands in relatively low density (Dickel & Milne 1995). The remnant is located on the NE edge of the H II region N 103 and probably part of the young star cluster NGC 1850.

DEM L71 (0505−67.9) is a type Ia, from an old, metal-poor population. Its age is ∼4400 years; it was observed with *Spitzer* by Borkowski et al. (2006). They measured ∼0.034 $M_\odot$ of warm dust within the remnant.

0453−68.5 (J0453.6−6829) is a CC SNR in a rare dusty environment, containing a PWN (Hayato et al. 2006; Williams, Chu & Gruendl 2006). The lowest age of this object is estimated to be ∼8700 yr (Williams 2010). It was observed with *Spitzer* by Williams et al. (2006).

0548−70.4 (LHG 89, RASS 298) is ∼7100 years old (Hendrick, Borkowski & Reynolds 2003), a Ia remnant, and was observed with *Spitzer* (Borkowski et al. 2006).

N 63A (0535−660) has no detected compact object, although the presence of a low-activity PWN is possible (Badenes et al. 2009). It is embedded in the large H II region N 63, and appears to be located within an OB association (Chu & Kennicutt 1988), which makes a CC type very likely. The size, morphology, and X-ray spectrum show evident signs of a complex interaction with ISM, indicating that it is expanding

into a large cavity, which suggests a massive progenitor with a fast wind and maybe a type Ib/c (Hughes, Hayashi & Koyama 1998). Also, the CC origin is plausible because of surrounding star formation (Badenes et al. 2009). The remnant was observed with *Spitzer* by Williams, Chu & Gruendl (2006).

DEM L238 (0534−70.5) and **DEM L249 (0536−70.6)** are believed to be two 'Ia prompt' objects (Borkowski, Hendrick & Reynolds 2006), from younger progenitors.

0534−699 is a type Ia of ∼10 000 yr old (Hendrick, Borkowski & Reynolds 2003).

N 159 (0540−697) is in a very complicated region, within H II complex N 159, close to the LMC X-1 source, probably CC, >18 000 yr old (Seward et al. 2010). It is quite confused in FIR. One of the brightest SNRs in radio.

DEM L241 (0536−67.6) is within the H II region DEM L241, containing an unresolved PWN. The SNR precursor star had probably a mass of up to > 25 $M_\odot$, and the age of the object is 80 000−160 000 yr (Seward et al. 2012).

N 9 (B0454−67.2) The SNR has no sign of a pulsar, its spectrum is dominated by iron lines, thus it has probably a Ia origin. This is unexpected, as the SNR's position at the edge of an H II region indicates a massive-star progenitor to be more likely (Seward et al. 2006).

N 120 (0519−697) is an ∼7000 yr old remnant, within a large nebular complex, N 120 (Reyes-Iturbide, Rosado & Velazquez 2008).

0450−70.9 (J 0450.4−7050) is one big shell resembling an old SNR. The lower limit of the estimated age is 45 000 yr. A centrally filled radio morphology can indicate the presence of a PSR, but no point source is detected in either radio or X-ray observations (Williams et al. 2004).

DEM L316A and **DEM L316B (0547−69.7)**. The former is a type Ia SNR, 27 000−39 000 yr old (Williams et al. 2005). The latter is a type II SNR. There was an unresolved question whether these two objects are interacting and how close they are (Williams & Chu 2005).

N 132D is an O-rich, CC remnant, thought to have a Ib origin and a progenitor of 25−35 $M_\odot$ (Vogt & Dopita 2011), for which it is shown that warm dust was formed in the ejecta (Rho et al. 2009). It is a young SNR (2500−3000 yr), entering the Sedov

phase and it was detected with *Spitzer* (Williams et al. 2006). Tappe, Rho & Reach (2006) reported the destruction of PAHs/grains in the SNR blast wave via thermal sputtering.

N 49B (0525−660) is a CC, 10 900 yr old (Williams 2010) from a progenitor of more than 25 $M_\odot$ (Park et al. 2003c). There is no evidence for an associated NS or its wind nebula. It was detected with *Spitzer* (Williams et al. 2006). This remnant has magnesium rich ejecta and present spectral lines from O, Ne, Si, S, and Fe.

N 23 (0506−68.0) is probably a PWN, ∼4600 yr old, and detected with *Spitzer* (Williams et al. 2006). Recently Hayato et al. (2006) detected an X-ray central compact source.

J0550−6823 (J0550−683) has no PWN detected, it is of a younger age despite its large size, and in a low density environment. It was described in Bozzetto et al. (2012b).

N 86 (0455−687) – there is not much certain information. The age is from 2 to 9×10^4 yr (Williams et al. 1999). It is not known if the remnant is still in the Sedov phase or it has entered the radiative phase.

N 11L (0454−66.5) is 7000−15 000 yr old (Williams et al. 1999); located within a region of a high density, close to the field of OB stars, and is probably of CC type (Chu & Kennicutt 1988). It is detected with *Spitzer* (Williams, Chu & Gruendl 2006).

N 186D (LHa 120−N186D, MCSNR J0459−7007, 0500−70.2) is another CC SNR (Chu & Kennicutt 1988).

0528−69.2 (LHG 40) is a type CC (Chu & Kennicutt 1988).

DEM L218 (MCELS J0530−7008) is probably a Ia (De Horta et al. 2012).

DEM L214 (J0529−6653) from MCSNR and Filipović's unpublished catalogue; it has a PSR on its NE edge (Bozzetto et al. 2012a).

DEM L214 (J0529.9−6701) from Badenes, Maoz & Draine (2010) – not much is known about this object.

N 157B (0538−691) is close to 30 Dor, with a progenitor of 20−25 $M_\odot$ (Micelotta, Brandl & Israel 2009). It is a Crab-type SNR, having an X-ray bright central PSR. It is a 5000 yr-old object (Wang et al. 2001), expanding into the hot low-density interior of

the surrounding superbubble formed by the young OB association LH 99, as revealed in *Spitzer* MIR-images (Chen et al. 2006; Williams, Chu & Gruendl 2006).

0520−69.4 (J0519−6926) – Chu & Kennicutt (1988) suggest that it is maybe a Ia.

N 44 (0523−67.9) has an age of ∼18 000 yr (Chu et al. 1993). It is hidden in one of the largest H II complexes of the LMC, N 44. There is no IR emission at *Spitzer* wavelengths from this shell (Williams, Chu & Gruendl 2006).

SNR Honeycomb is named after its interesting morphology, consisting of over 10 loops of sizes 2−3 pc expanding towards the observer at 100−200 km s^{-1}. The object is extended and optically visible, but detected only at some wavelengths, thus it is not well-studied.

N 206 (B0532−71.0) is 23 000−27 000 yr old (Williams et al. 2005), having a progenitor SN of type II and containing a moving PSR (Hayato et al. 2006).

Table: 4.1: Whole sample of the LMC SNRs that I studied.

Name	RA[h m s][a]	Dec[° ′ ″][a]	D[″][a]
J 0448.4−6660	04 48 22	−66 59 52	220
J 0449.3−6920	04 49 20	−69 20 20	133
B 0449−693[b]	04 49 40	−69 21 49	120
B 0450−6927	04 50 15	−69 22 12	210
B 0450−709	04 50 27	−70 50 15	357
LHA 120-N 4 (N 4)	04 53 14	−66 55 13	252
0453−68.5	04 53 38	−68 29 27	120
B 0454−7000	04 53 52	−70 00 13	420
LHA 120-N 9 (N 9)	04 54 33	−67 13 13	177
LHA 120-N 11L (N 11L)	04 54 49	−66 25 32	87
LHA 120-N 86 (N 86)	04 55 37	−68 38 47	348
LHA 120-N 186D (N 186D)	04 59 55	−70 07 52	150
DEM L71	05 05 42	−67 52 39	72
LHA 120-N 23 (N 23)	05 05 55	−68 01 47	111
J 0506.1−6541	05 06 05	−65 41 08	408
B 0507−7029	05 06 50	−70 25 53	330
RXJ 0507−68[b]	05 07 30	−68 47 00	450
J0508−6830[d]	05 08 49	−68 30 41	123
LHA 120-N 103B (N 103B)	05 08 59	−68 43 35	28
0509−67.5	05 09 31	−67 31 17	29
J0511−6759[d]	05 11 11	−67 59 07	108
DEM L109	05 13 14	−69 12 20	215

to be continued on next page...

Table 4.1 – *Continued from previous page*

J0514−6840[d]	05 14 15	−68 40 14	218
J0517−6759[d]	05 17 10	−67 59 03	270
LHA 120-N 120 (N 120)	05 18 41	−69 39 12	134
0519−69.0	05 19 35	−69 02 09	31
0520−69.4	05 19 44	−69 26 08	174
J 0521.6−6543	05 21 39	−65 43 07	162[e]
LHA 120-N 44 (N 44)	05 23 07	−67 53 12	228
LHA 120-N 132D (N 132D)	05 25 04	−69 38 24	114
LHA 120-N 49B (N 49B)	05 25 25	−65 59 19	168
LHA 120-N 49 (N 49)	05 26 00	−66 04 57	84
B 0528−692	05 27 39	−69 12 04	147
DEM L 204	05 27 54	−65 49 38	303
HP99498[c]	05 28 20	−67 13 40	97
B 0528−7038	05 28 03	−70 37 40	60
DEM L203	05 29 05	−68 32 30	667
DEM L214	05 29 51	−67 01 05	100
DEM L214[c]	05 29 52	−66 53 31	120
DEM L218	05 30 40	−70 07 30	213
LHA 120-N 206 (N 206)	05 31 56	−71 00 19	192
0532−67.5	05 32 30	−67 31 33	252
B 0534−69.9	05 34 02	−69 55 03	114
DEM L238	05 34 18	−70 33 26	180
SN 1987A	05 35 28	−69 16 11	2
LHA 120-N 63A (N 63A)	05 35 44	−66 02 14	66
Honeycomb	05 35 46	−69 18 02	102
DEM L241	05 36 03	−67 34 35	135
DEM L249	05 36 07	−70 38 37	180
B 0536−6914	05 36 09	−69 11 53	480
DEM L256	05 37 27	−66 27 50	204
B 0538−6922	05 37 37	−69 20 23	169
0538−693[b]	05 38 14	−69 21 36	169
LHA 120-N 157B (N 157B)	05 37 46	−69 10 28	102
LHA 120-N 159 (N 159)	05 39 59	−69 44 02	78
LHA 120-N 158A (N 158A)	05 40 11	−69 19 55	60
DEM L299	05 43 08	−68 58 18	318
DEM L316B	05 46 59	−69 42 50	84
DEM L316A	05 47 22	−69 41 26	56
0548−70.4	05 47 49	−70 24 54	102
J 0550.5−6823	05 50 30	−68 22 40	312

a - From Badenes, Maoz & Draine (2010), if not written different. *b* - This SNR is from the Blair et al. (2006) catalogue. *c* - This SNR is from Filipović's unpublished catalogue and MCSNR. *d* - From Maggi et al. (2014). *e* – From Desai et al. (2010).

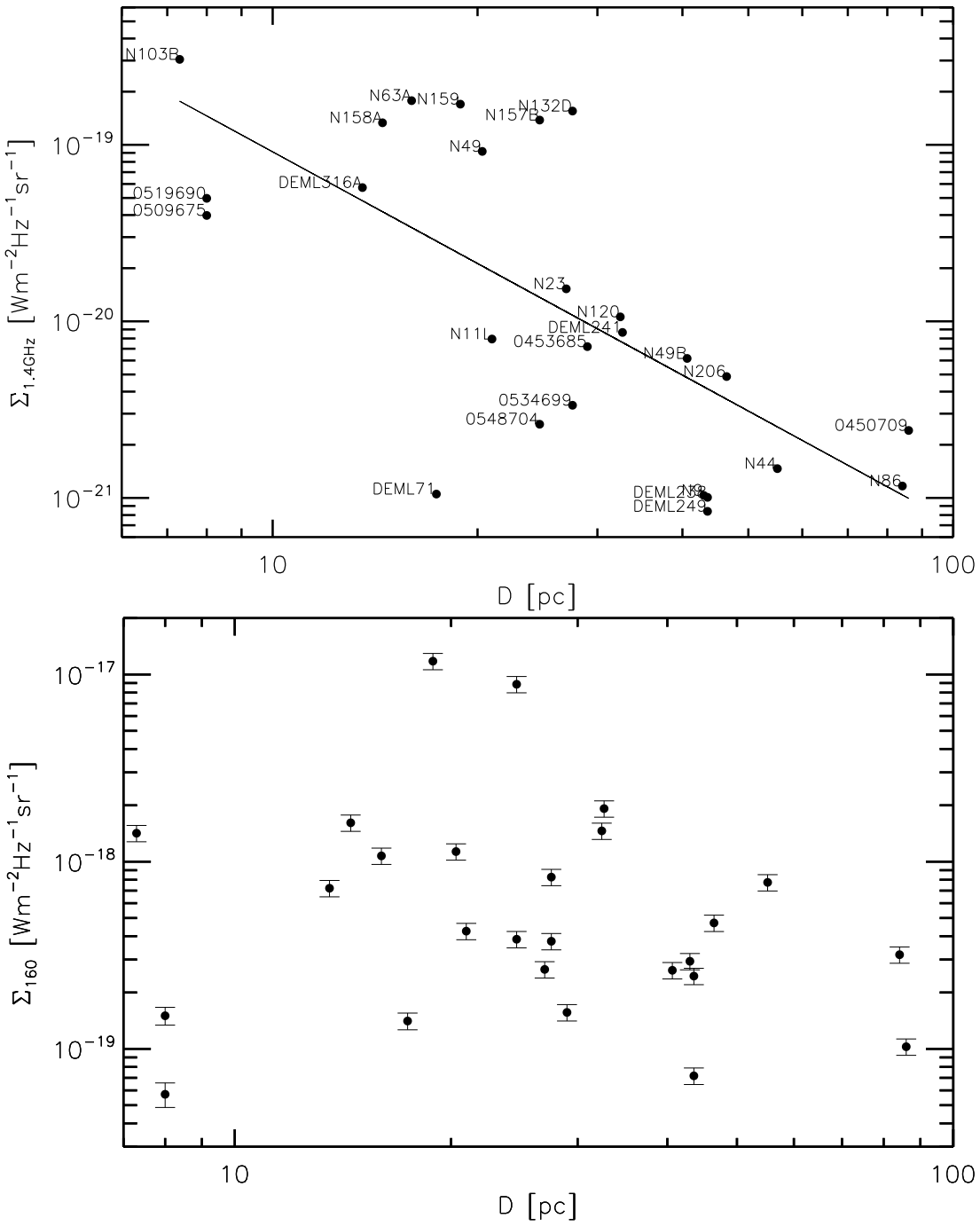

Figure 4.1: *Top:* $\Sigma_{1.4\mathrm{GHz}} - D$ relation for the sample of 26 SNRs. The radio fluxes are taken from Badenes, Maoz & Draine (2010). The line is the best linear fit through these data, presenting the relation $\Sigma_{1.4\mathrm{GHz}} = (1.2^{+3.7}_{-0.9}) \times 10^{-17} \times D^{-2.1\pm0.4}$. *Bottom:* Σ_{160} versus the diameter, D for the same sample of data. There is no obvious correlation (Table 4.3).

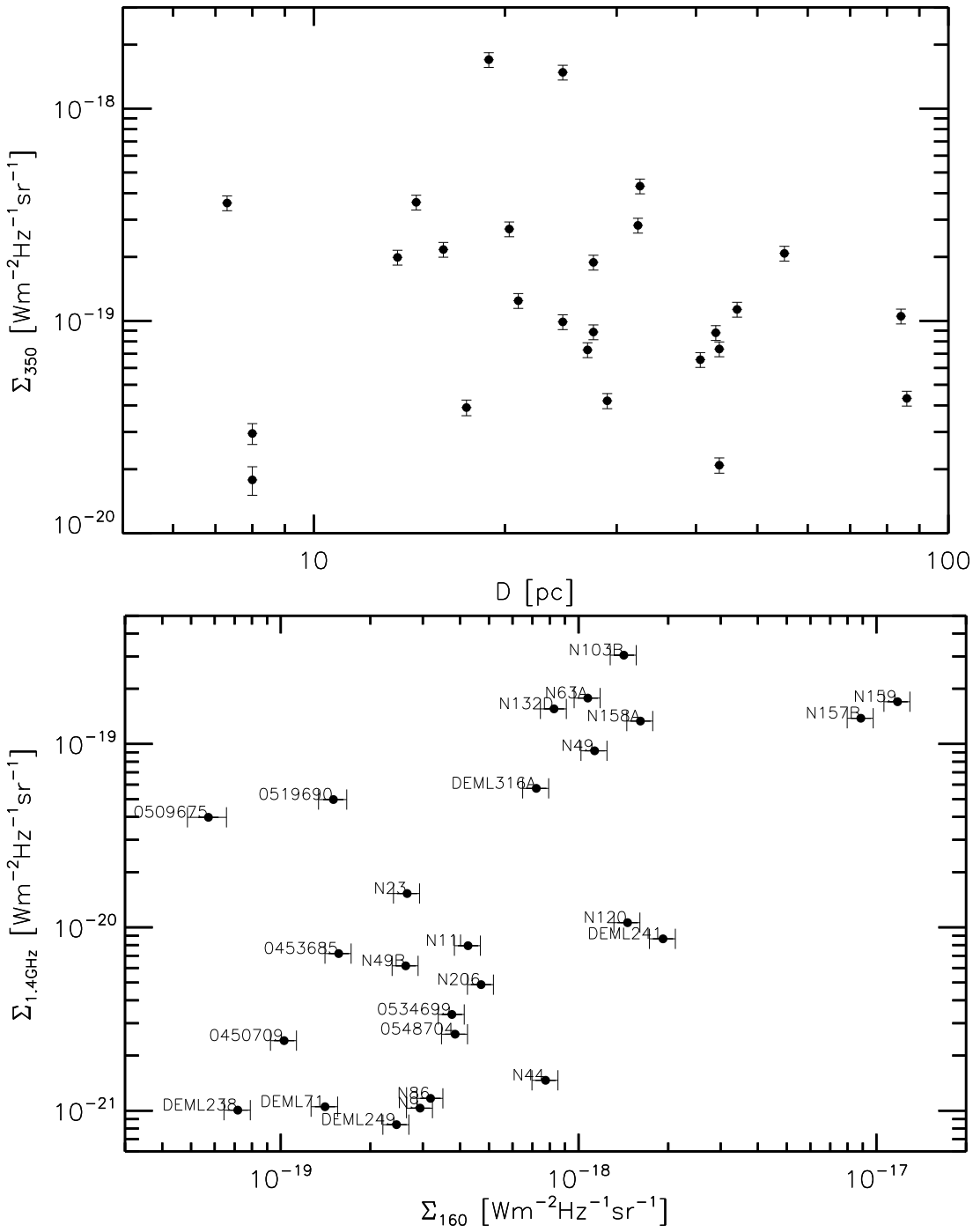

Figure 4.2: *Top:* Σ_{350} versus the diameters, D for the sample of 26 SNRs. There is no obvious correlation. *Bottom:* Σ_{160} versus $\Sigma_{1.4\mathrm{GHz}}$ for 26 SNRs. There exists some correlation, see Table 4.3.

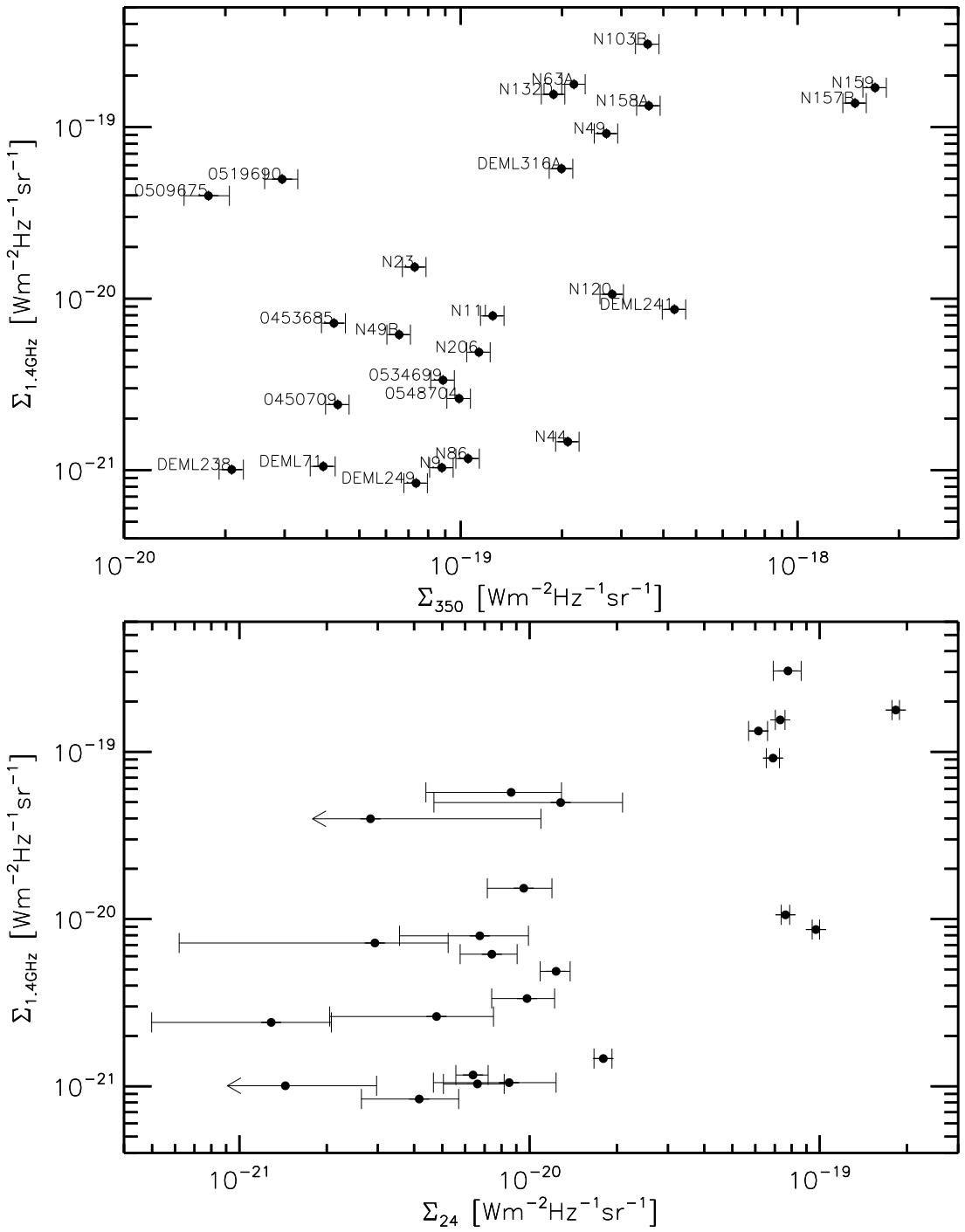

Figure 4.3: *Top:* Σ_{350} versus $\Sigma_{1.4GHz}$ for the sample of 26 SNRs. *Bottom:* Σ_{24} versus $\Sigma_{1.4GHz}$ for the same sample of data. There exist some correlations, see Table 4.3.

4.2 Results

4.2.1 Comparison of FIR/submm surface brightness with radio surface brightness, ages and diameters of SNRs

As I discussed in Section 1.2.6, the most famous relation for SNRs is the $\Sigma - D$ relation, describing the decreasing radio surface brightness, Σ, with diameter, D (Urošević 2003; Arbutina & Urošević 2005). Taking the sample of 26 SNRs in the LMC for which we have an esimate of the age from the literature, fluxes at 1.4 GHz and the coordinates from Badenes, Maoz & Draine (2010) – see Table 4.2, I performed a linear fitting to find my own $\Sigma - D$ relation (see Fig. 4.1, top) to be

$$\Sigma_{1.4\mathrm{GHz}} = (1.2^{+3.7}_{-0.9}) \times 10^{-17} \times D^{-2.1\pm0.4,} (4.1)$$

with a correlation coefficient of -0.7, which is the expected dependence for SNRs in normal galaxies (see above-mentioned papers). One can see that confirmed CC are usually above Ia SNRs of similar diameter (as we mentioned in Section 1.2.6). If some remnant is above other remnants of similar diameter (of $\sim$10 times higher Σ, like Cas A and Crab Nebula; see Berkhuijsen 1986), then it is considered to extreme, either because of a high CSM density, or because it is too young for comparison for the other SNRs in Sedov phase.

Bearing in mind the $\Sigma-$D dependence, I wanted to examine similar correlations for FIR and submm wavelengths in order to see if there exists any evolution of Σ_{FIR} in time. Fig. 4.1, bottom shows a plot of surface brightness at 160 μm, Σ_{160} versus the SNR diameters and they are not correlated (Table 4.3). The dependence of surface brightness at 350 μm, Σ_{350} versus the diameters is shown in Fig. 4.2, top. Similarly we conclude that the FIR surface brightness is not correlated with D. This is likely because the FIR/submm radiation is probably dominated by ISM rather than the SNRs. I remind the reader that I measure all interstellar dust in the LMC behind and in front of SNRs, without any subtraction and SNRs are at the same temperature as the surrounding ISM – which is usually not time varying. The temperature of the

cold interstellar dust is usually dependent on the temperature of the ISRF and surface brightness also depends strongly on the density, therefore if there is any fading, it is not very conspicuous. In Section 4.2.4.2 I estimate the temperatures of the cold dust in/around SNRs and I find that their temperature does not change more than ∼15 K from young to old remnants.

Although it is well-known that Σ_{24} does decrease with time since only young remnants are detected at that wavelength (Seok et al. 2008; Seok, Koo & Onaka 2013), I do not find the decreasing of Σ_{24} with the diameter because I have too few young and bright SNRs and too many middle age SNRs (Σ_{24} depends strongly on the density and the youngest SNRs in my sample are Ia, so they are not the brightest). The coefficients of these correlations are, thus, very low (Table 4.3). I will show below that some evolution in time probably does exist, because of cooling down and perhaps eroding of the dust.

Before I compare $\Sigma_{\rm FIR}$ and $\Sigma_{\rm radio}$ and find their correlation, I notice that the errors in fluxes of SNRs (ΔF) in these and the following plots are found by the formula

$$\Delta F = \sqrt{\Sigma F_{\rm back}^{\rm error2} + (Y \times F)^2} \tag{4.2}$$

where $Y = [0.02, 0.05, 0.1, 0.1, 0.08, 0.08, 0.08]$ corresponds to the wavelengths 24, 70, 100, 160, 250, 350 and 500 μm. Here, $F_{\rm back}^{\rm error}$ is the background noise of a pixel estimated by Gordon et al. (2014) (see Section 2.2.2), while the factor $Y \times F$ is the calibration error for the various instruments (Meixner et al. 2006; Meixner et al. 2013) and F is total flux of a SNR.

However, the comparison between $\Sigma_{\rm FIR}$ and $\Sigma_{\rm radio}$ suggests an important dependence (Fig. 4.2, bottom and Fig. 4.3, top and bottom); also see Table 4.3. This must be the consequence of the dependence of both radio and IR radiation (24−500 μm) on the density of the ISM. The correlation coefficients between $\Sigma_{\rm FIR}$ and $\Sigma_{\rm radio}$ are ∼0.55, while $\Sigma_{\rm radio}$ is somewhat stronger correlated with Σ_{24} (70%) which traces the warm dust. However, the dependence of $\Sigma_{\rm radio}$ and Σ_{24} that is obtained by Seok et al. (2008) has a correlation coefficient as big as 98%, but they have used only eight clearly detected SNRs with some flux subtraction.

Here I have to mention the work of Gonçalves (2013) who found the relation between total fluxes at MIR (24 and 70 μm) and radio (1.4 GHz) wavelengths for SNRs in the MW in the shape $F_{1.4\mathrm{GHz}}(F_{\mathrm{IR}})$ (and also found a relation between H I and MIR radiation for SNRs). The relation between radio and MIR fluxes had the slope $\sim$1 and she argued that the same relation is found for galaxies. My slopes for the dependence of $\Sigma_{1.4\mathrm{GHz}}(\Sigma_{\mathrm{FIR}})$ are 0.75$\pm$0.15, 0.88$\pm$0.24, 0.94$\pm$0.29 and 1.0$\pm$0.3 for 24, 160, 350 and 500 μm, which is similar to Gonçalves (2013) result. Note that these results are not the same as in the Table 4.3, since in that table we gave $\Sigma_{\mathrm{FIR}}(\Sigma_{1.4\mathrm{GHz}})$ dependences, but the correlation coefficients are the same as in that table.

There is one group of CC SNRs (N 49, N 63A, N 158A (0540$-$693), N 157B and N 132D) that are among the brightest in radio and FIR/submm wavelengths (Fig. 4.3) and that are believed to have massive progenitors (see Vogt & Dopita 2011 for N 132D; van Loon et al. 2010 for N 49; Hughes, Hayashi & Koyama 1998 for N 63A; Williams et al. 2008 for N158A and Micelotta, Brandl & Israel 2009 for N 157B).

The 24-μm flux may also have a contribution from line emission (see e.g. Crab Nebula; Temim et al. 2012). Among the SNRs believed to be more affected by this are N 49 and N 63A, where the line contribution is estimated to be an exceptional $\sim$ 80% (Williams, Chu & Gruendl 2006) and modest $\sim$ 10% (Caulet & Williams 2012), respectively. I corrected Σ_{24} for these two SNRs accordingly. In general, however, line emission is thought to make a negligible contribution to the 24-μm flux (Williams 2010) and I found estimates in the literature only for these two SNRs.

The diameters of SNRs are more reliable estimators of SNR ages than the ages themselves, as the ages are derived in various ways while the diameters are directly measured. Since I have already shown that Σ_{FIR} does not evolve much with the diameter (Table 4.3), from that follows that it also does not evolve with age of SNRs. However, the diameter will also depend on the ISM/CSM density and explosion energy. For completeness, here I give the comparison of Σ_{FIR} and $\Sigma_{1.4\mathrm{GHz}}$ with time. In Fig. 4.4, I show the dependence of $\Sigma_{1.4\mathrm{GHz}}$ and Σ_{24} on the age and in Fig. 4.5 the dependence of Σ_{160} and Σ_{350} on the age of the remnant for the same data sample. In Table 4.4, I give the correlation coefficients and the parameters A and B for these relatons, similarly

Table 4.2: SNRs in the LMC with known age and type from the literature.

Name	RA[h m s]	Dec[d m s]	D[pc]	age[yr]	ref.age	$F_{1.4GHz}$[Jy]	type	ref.type
0450−70.9	04 50 27	−70 50 15	86	$\leq$ 45000	29	0.56	CC	29
B 0453−68.5	04 53 38	−68 29 27	29	13000	1	0.11	CC	1
N 9	04 54 33	−67 13 13	43	30000	27	0.06	Ia?	27
N 11L	04 54 49	−66 25 32	21	11000	2	0.11	CC	9
N 86	04 55 37	−68 38 47	84	86000	2	0.26	CC?	2
DEM L71	05 05 42	−67 52 39	17	4400	3	0.01	Ia	3
N 23	05 05 55	−68 01 47	27	6300	3,4	0.35	CC	5
N 103B	05 08 59	−68 43 35	7	1000	6	0.51	Ia	6
B 0509−67.5	05 09 31	−67 31 17	8	400	7	0.08	Ia	7
N 120	05 18 41	−69 39 12	32	7300	8	0.35	CC	9
B 0519−69.0	05 19 35	−69 02 09	8	600	7	0.1	Ia	7
N 44	05 23 07	−67 53 12	55	18000	10	0.14	CC	?
N 132D	05 25 04	−69 38 24	28	2750	3	3.71	CC	11
N 49B	05 25 25	−65 59 19	41	10900	3	0.32	CC	12
N 49	05 26 00	−66 04 57	20	6600	13	1.19	CC	14
N 206	05 31 56	−71 00 19	46	25000	15	0.33	CC	15
0534−69.9	05 34 02	−69 55 03	27	10000	16	0.08	Ia	16
DEM L238	05 34 18	−70 33 26	43	13500	17	0.06	Ia	17
SN 1987A	05 35 28	−69 16 11	0.5	27	18	0.05	CC	18
N 63A	05 35 44	−66 02 14	16	3500	19	1.43	CC	19
DEM L249	05 36 07	−70 38 37	43	12500	17	0.05	Ia	17
N 157B	05 37 46	−69 10 28	25	5000	20	2.64	CC	20
N 159	05 39 59	−69 44 02	19	18000	21	1.9	CC	21
B 0540−69.3	05 40 11	−69 19 55	15	800	22	0.88	CC	5
DEM L316A	05 47 22	−69 41 26	14	33000	23	0.33	Ia	23
B 0548−70.4	05 47 49	−70 24 54	25	7100	3	0.05	CC	3
DEM L241	05 36 03	−67 34 35	33	12000	28	0.29	CC	28

The literature where I found the age and the type: (1) Haberl et al., 2012; (2) Williams et al. (1999); (3) Williams (2010); (4) Someya, Bamba & Ishida (2010); (5) Hayato et al. (2006); (6) Lewis et al. (2003); (7) Rest et al. (2005); (8) Rosado, Laval & Coarer (1993); (9) Chu & Kennicutt (1988); (10) Chu et al. (1993); (11) Vogt & Dopita (2011); (12) Park et al. (2003c); (13) Park et al. (2003a); (14) Otsuka et al. (2010); (15) Williams et al. (2005); (16) Hendrick, Borkowski & Reynolds (2003) (17) Borkowski, Hendrick & Reynolds (2006); (18) Zanardo et al. (2010); (19) Hughes, Hayashi & Koyama (1998); (20) Wang et al. (2001); (21) Seward et al. (2010); (22) Badenes et al. (2009); (23) Williams & Chu (2005); (24) Van der Heyden, Bleeker & Kaastra (2004); (25) Owen et al. (2011); (26) Park et al. (2003b); (27) Seward et al. (2006); (28) Seward et al. (2012); (29) Williams et al. (2004).

like on Table 4.3). Only $\Sigma_{1.4\mathrm{GHz}}$ decreases in time with the relation:

$$\Sigma_{1.4\mathrm{GHz}} = (0.27^{+2.29}_{-0.25}) \times 10^{-16} \times \mathrm{age[yr]}^{-0.86\pm0.25}, \tag{4.3}$$

with correlation coefficient of -0.58. Having in mind the $\Sigma_{1.4\mathrm{GHz}} - D$ relation (eq. 4.1), this is consistent with a time evolution of the diameter according to $D \propto \mathrm{age}^{0.41}$, or almost exactly the $\mathrm{age}^{2/5}$ as predicted for the Sedov phase (cf., e.g., Badenes, Maoz & Draine (2010); see eq. 1.3). Fading away of Σ_{radio} in time, while the diameter is increasing is a well-proven fact (see for example Helmboldt & Kassim (2009) and Section 1.2.6), while for the FIR/submm wavelengths we can not conclude any fading from these fits.

If there exists a slow fading of Σ at FIR/submm wavelengths it could be due to cooling down, but also maybe due to destruction of the dust by shocks, or erosion. Another approach to proving that the Σ_{FIR} of SNRs do fade in time is the following. To avoid the differences between brightnesses, for every SNR I normalised the Σ_{FIR} of SNRs at all wavelengths to the Σ_{250}. In Fig. 4.6, top I give these normalised values versus the diameter, denoted as Σ^{in}. I then put the remnants in order of increasing diameter (since this gives some crude estimation of their age) and smooth these Σs in *IDL* with a boxcar 14[2]. I show the resulting values of normalised, smoothed Σ versus diameter in Fig. 4.6, bottom. According to this comparison, moderate fading of flux can be seen at all wavelengths. Furthermore, in the same way, I found a similar behaviour of dust that surrounds SNRs, in annuli from D/2 to D/2+21pc (Fig. 4.7, top). One can see that, although outer regions (denoted as Σ^{out}) are colder than inner, environments of younger SNRs are still brighter in the FIR than the environments of older SNRs. The dust that surrounds SNRs has a similar density, composition and brightness as most of the SNRs themselves (except the youngest), so this decreasing of Σ of surrounding dust is happening for the same reason, probably due to slow cooling down, but possibly also the erosion of the dust.

[2]Which means replacing of the value of each Σ with the mean of 7 points from one side, that point and 7 points from the other side. The option *EDGE_TRUNCATE* is used in order to perform the smoothing also in the edges of the interval (the first 7 and the last 7 points).

Table 4.3: Relations between surface brightnesses (Σ) and SNR diameters. For these linear relations we tabulate the correlation coefficient, constant A and slope, B, where $\log\, y = A + B\log x$.

	$\log D$ [pc]			$\log \Sigma_{1.4\mathrm{GHz}}$		
$\log(\Sigma)$	c. corr.	A	B	c. corr.	A	B
$\log \Sigma_{24\mu\mathrm{m}}$	-0.3	-18.53 ± 0.78	-0.85 ± 0.55	0.7	-6.61 ± 2.71	0.66 ± 0.14
$\log \Sigma_{160\mu\mathrm{m}}$	-0.14	-17.88 ± 0.58	-0.29 ± 0.41	0.59	-10.49 ± 2.19	0.39 ± 0.11
$\log \Sigma_{350\mu\mathrm{m}}$	-0.09	-18.67 ± 0.51	-0.16 ± 0.36	0.55	-12.46 ± 1.98	0.3 ± 0.1
$\log \Sigma_{500\mu\mathrm{m}}$	-0.08	-23.08 ± 0.49	-0.14 ± 0.34	0.56	-17.09 ± 1.89	0.31 ± 0.09
$\log \Sigma_{1.4\mathrm{GHz}}$	-0.7	-16.94 ± 0.63	-2.1 ± 0.4			

Table 4.4: Linear dependence between Σ and the age of SNRs, as for Table 4.3.

$\log(\Sigma)$	c. corr.	A	B
$\log \Sigma_{24\mu\mathrm{m}}$	-0.23	-18.51 ± 1.08	-0.32 ± 0.28
$\log \Sigma_{160\mu\mathrm{m}}$	0.002	-18.30 ± 0.79	0.002 ± 0.202
$\log \Sigma_{350\mu\mathrm{m}}$	0.063	-19.10 ± 0.69	0.05 ± 0.18
$\log \Sigma_{500\mu\mathrm{m}}$	0.062	-23.49 ± 0.66	0.05 ± 0.17
$\log \Sigma_{1.4\mathrm{GHz}}$	-0.58	-16.56 ± 0.97	-0.86 ± 0.25

Fig. 4.6, bottom reveals different rates of cooling down at various wavelengths. While Σ_{100} and Σ_{160} are slowly changing within the lifetime of SNRs, the most significant is that Σ_{24} decreases $\sim$3 times. Less expected is the fading at submm wavelengths (350 and 500 μm), by a factor two compared to the Σ_{250} – i.e., more pronounced than at 100 and 160 μm. Perhaps free–free and/or synchrotron emission contributes at the longest wavelengths, and diminishes during the evolution of the SNR. It appears as though there is no further evolution for SNRs with $D > 70$ pc.

Finally, in Fig. 4.7, bottom, I derive the ratios of inner and outer normalised and smoothed SBs, finding that at all wavelengths there is some decrease in surface brightness inside compared to annuli outside the remnant.

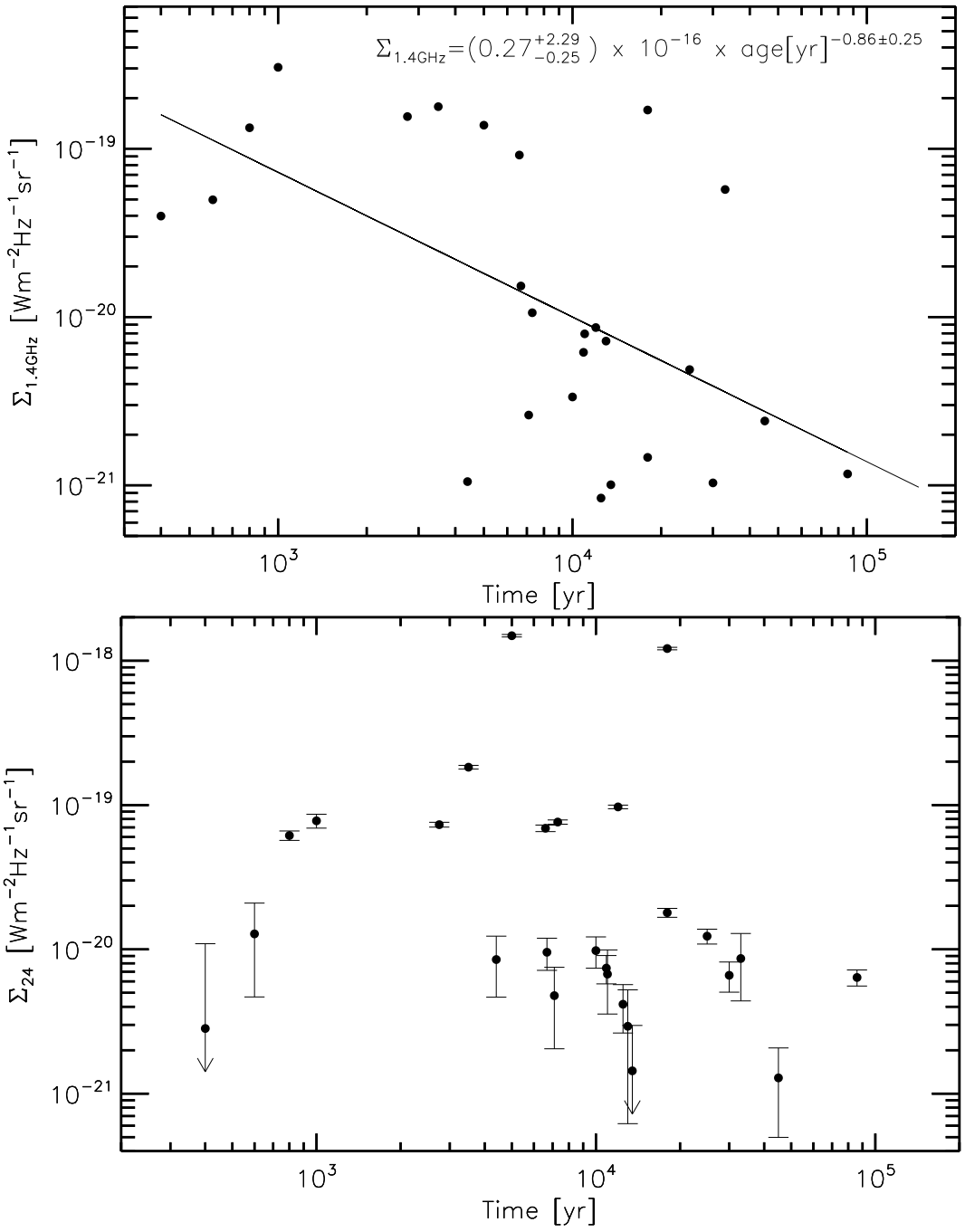

Figure 4.4: *Top:* $\Sigma_{1.4\mathrm{GHz}}$ shows a decreasing trend versus age in the shape: $\Sigma_{1.4\mathrm{GHz}} = (0.27^{+2.29}_{-0.25}) \times 10^{-16} \times \mathrm{age[yr]}^{-0.86\pm0.25}$, corr. coeff.: –0.58. *Bottom:* Σ_{24} shows no significant trend versus age (corr. coeff.: –0.23), although we know that the decrease exists because SNRs do fade on 24 μm.

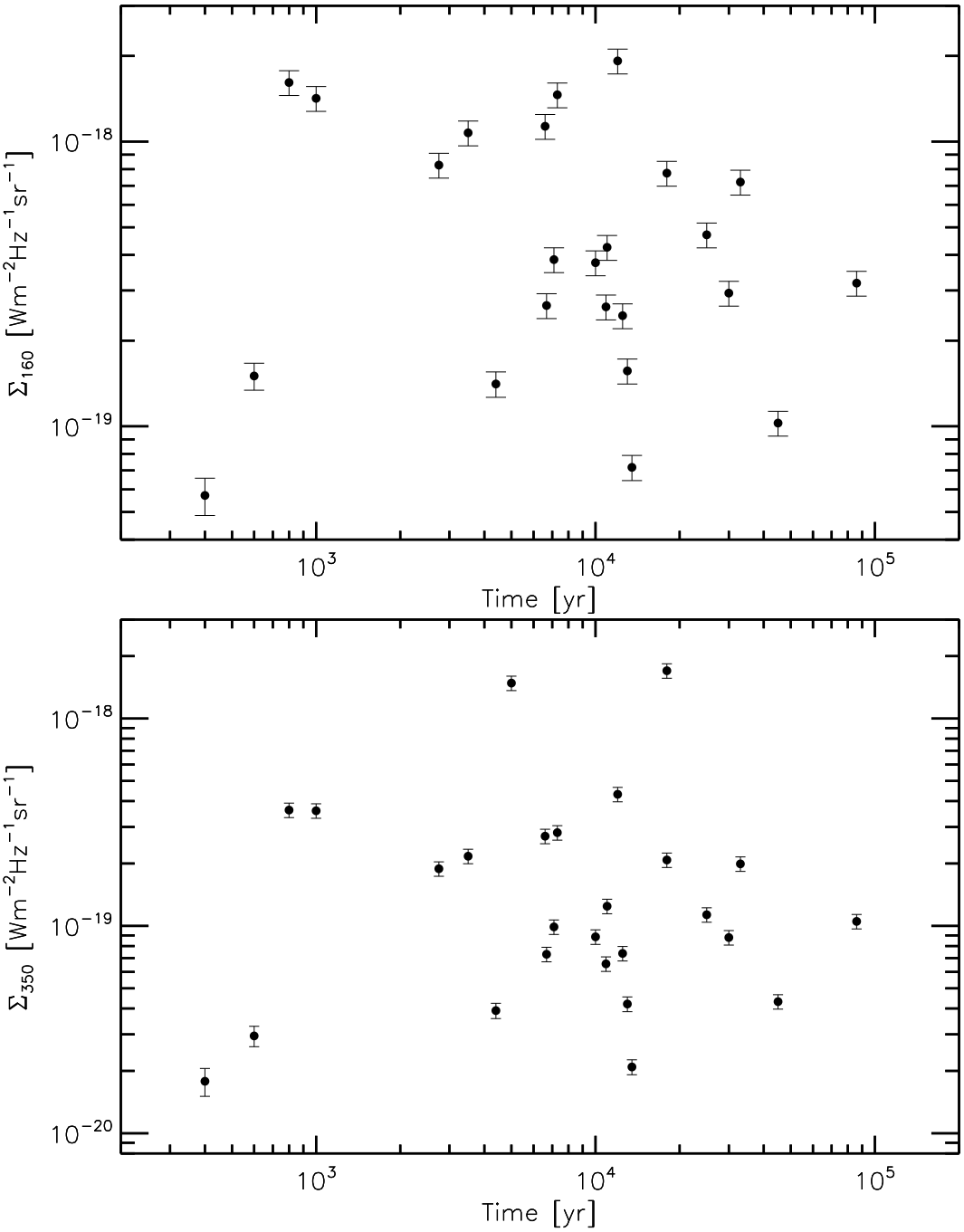

Figure 4.5: *Top:* Σ_{160} versus age. *Bottom:* Σ_{350} versus age. They do not show any trend, the correlation coefficients are only 0.002 and 0.063, respectively.

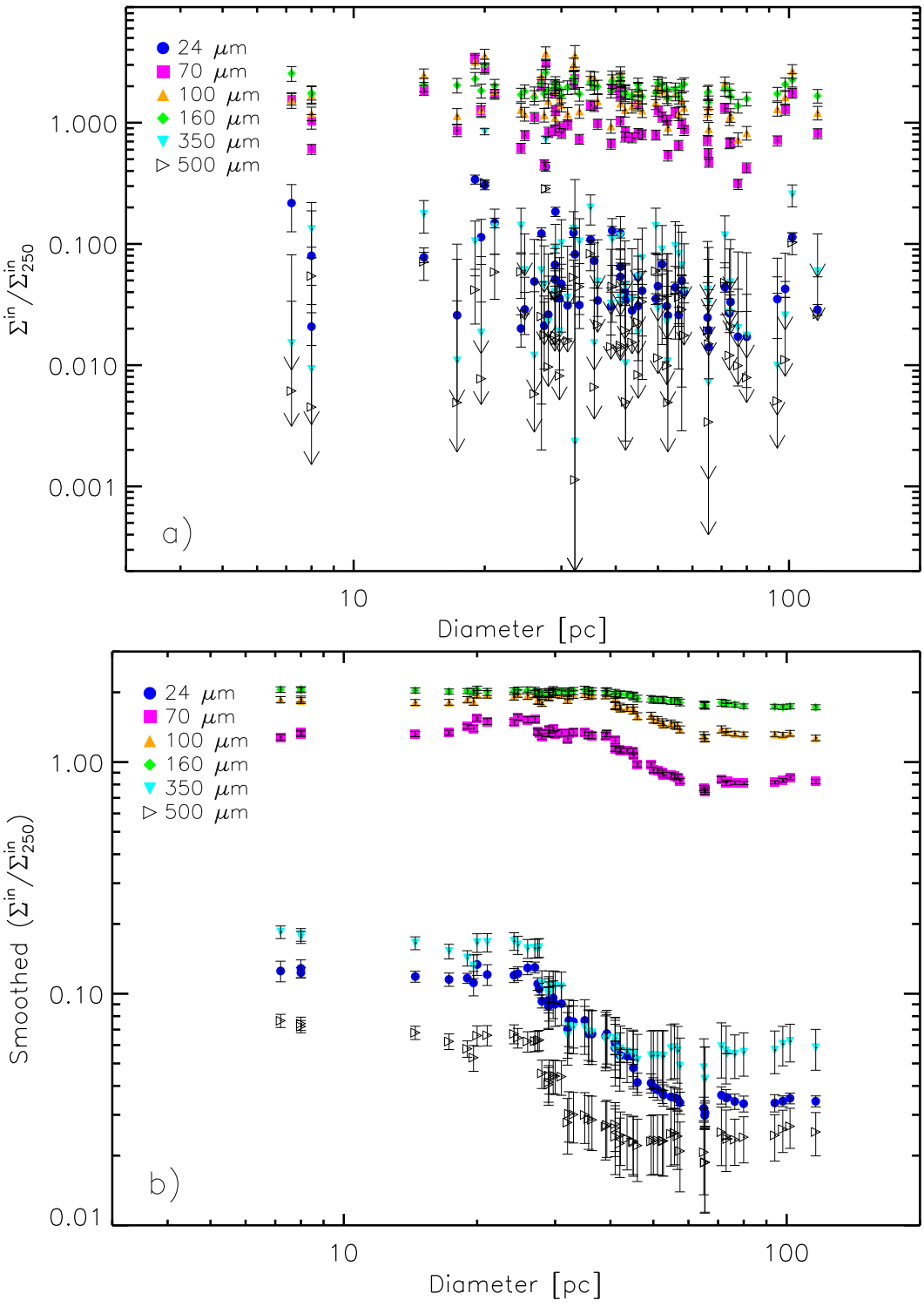

Figure 4.6: *Top:* Evolution of Σ inside SNRs ($\Sigma^{\rm in}$), normalised to $\Sigma^{\rm in}_{250}$, at 24−500 μm depending on the diameter; *Bottom:* – the same as *Top*, but smoothed.

In this Section I found that $\Sigma_{\rm FIR}$ and $\Sigma_{\rm radio}$ are somewhat dependent, but that diameters and/or ages of SNRs are not correleted with $\Sigma_{\rm FIR}$, while $\Sigma_{\rm radio}$ decreases with diameters and ages, as expected. However, after normalisation and smoothing, there is more evidence of evolution of Σ at FIR/submm wavelengths.

4.2.2 Maps of flux ratios

Bearing in mind the conclusions of Sankrit et al. (2010) and Williams (2010) about the ratios of fluxes on different wavelengths behind and in front of the shocks of young SNR (these ratios are lower within SNRs than outside of them), I made maps of the flux ratios at 70 and 24 μm ($\rm R_{70/24}$), and at 350 and 70 μm ($\rm R_{350/70}$), including all other combinations of *Herschel* and *Spitzer* wavelengths where the numerator is always at the longer wavelength than the denominator. I made these ratio maps by dividing images that were convolved to the same resolution (36.3″, the resolution of the 500 μm band).

My ratio maps also show that $\rm R_{70/24}$ and $\rm R_{350/70}$ etc. are lower within the SNRs than in the surrounding medium for almost all young SNRs. The other ratios have similar behaviour, thus I will just analyse these two. Sankrit et al. (2010) explained this phenomenon by the higher temperature in young SNRs compared to the surroundings and by sputtering of the dust in SNRs by the shocks (see Section 4.2.4). The differences between these ratios in areas within and outside of SNRs are the most obvious in ratios that contain shorter wavelengths (24 and 70 μm) e.g. for $\rm R_{70/24}$ because fluxes at these wavelengths are more sensitive to the temperature changes. Collisionally heated dust, where we observe small grains which are the easiest to sputter and heat peaks at 24 and 70 μm (Williams 2010). The 24 and 70 μm emission belongs to dust warmed up to $\sim$ 40–100 K by SNRs, while longer wavelengths trace dust at temperatures similar to the ISRF. In Section 4.2.3, I will track the evolution of these ratios in time for various SNRs.

Even if not visible in mass/temperature maps (shown in Section 4.2.4), this effect, that ratios are lower in SNRs than in outer regions, is often visible even in older

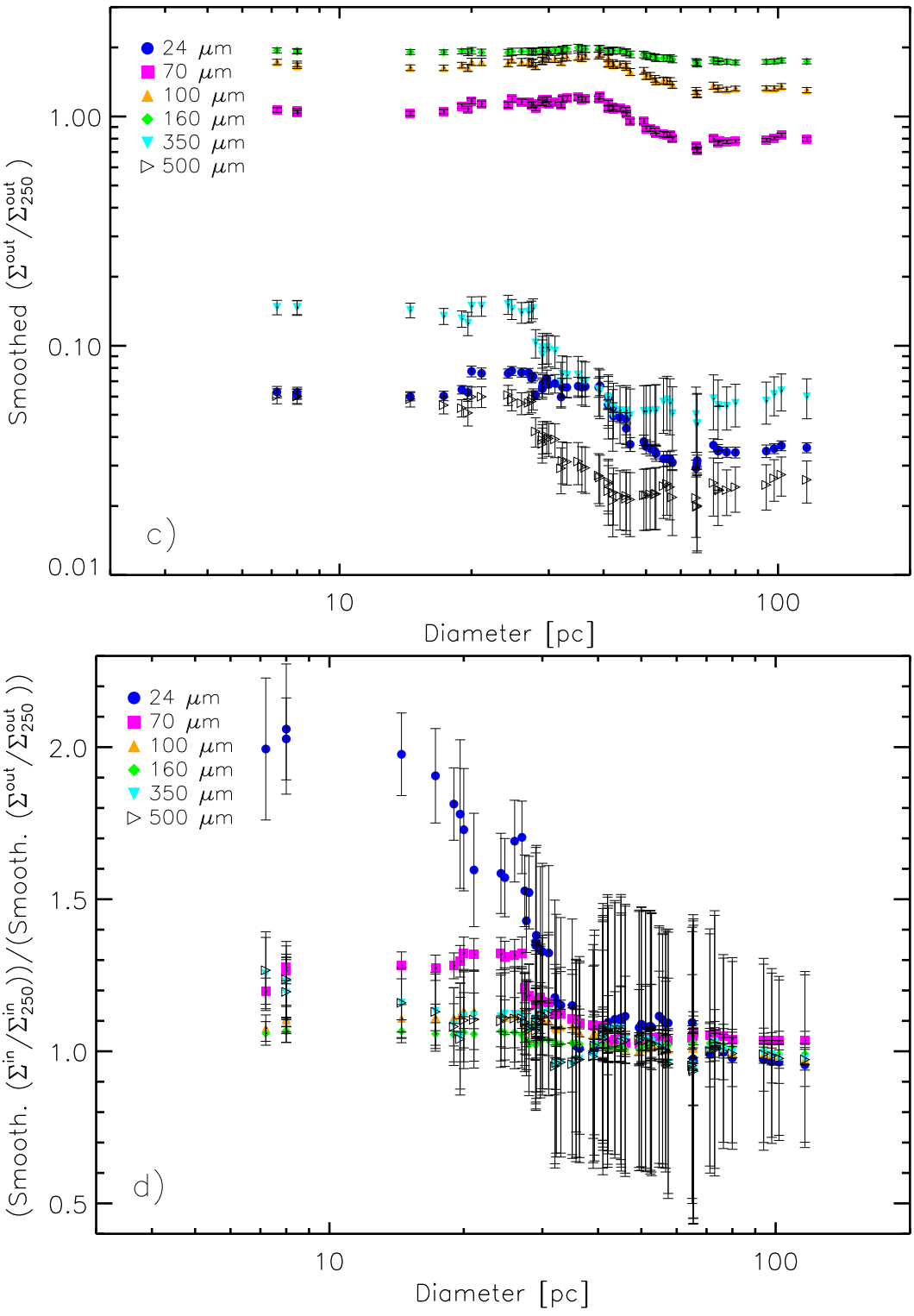

Figure 4.7: *Top:* The same as previous, but in annuli around SNRs. *Bottom:* Ratio of normalised and smoothed Σ inside and outside of the SNR.

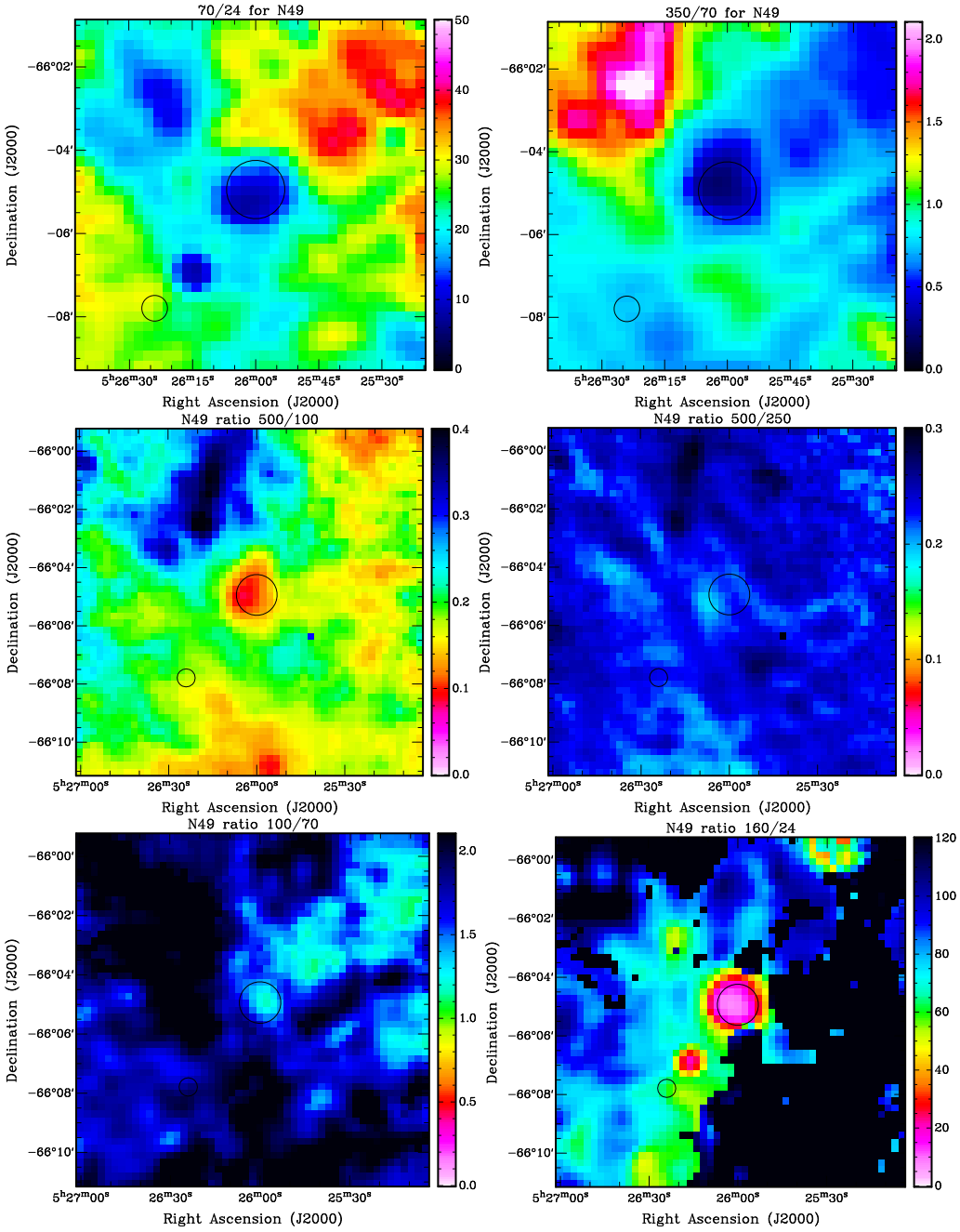

Figure 4.8: Images of fluxes ratios for SNR N 49. *Top left:* $R_{70/24}$, *top right:* $R_{350/70}$, *middle left:* $R_{500/100}$, *middle right:* $R_{500/250}$, *bottom left:* $R_{100/70}$ and *bottom right:* $R_{160/24}$. The small circle in the left corner is the beam size and bigger circle in the centre is the surface of the SNR.

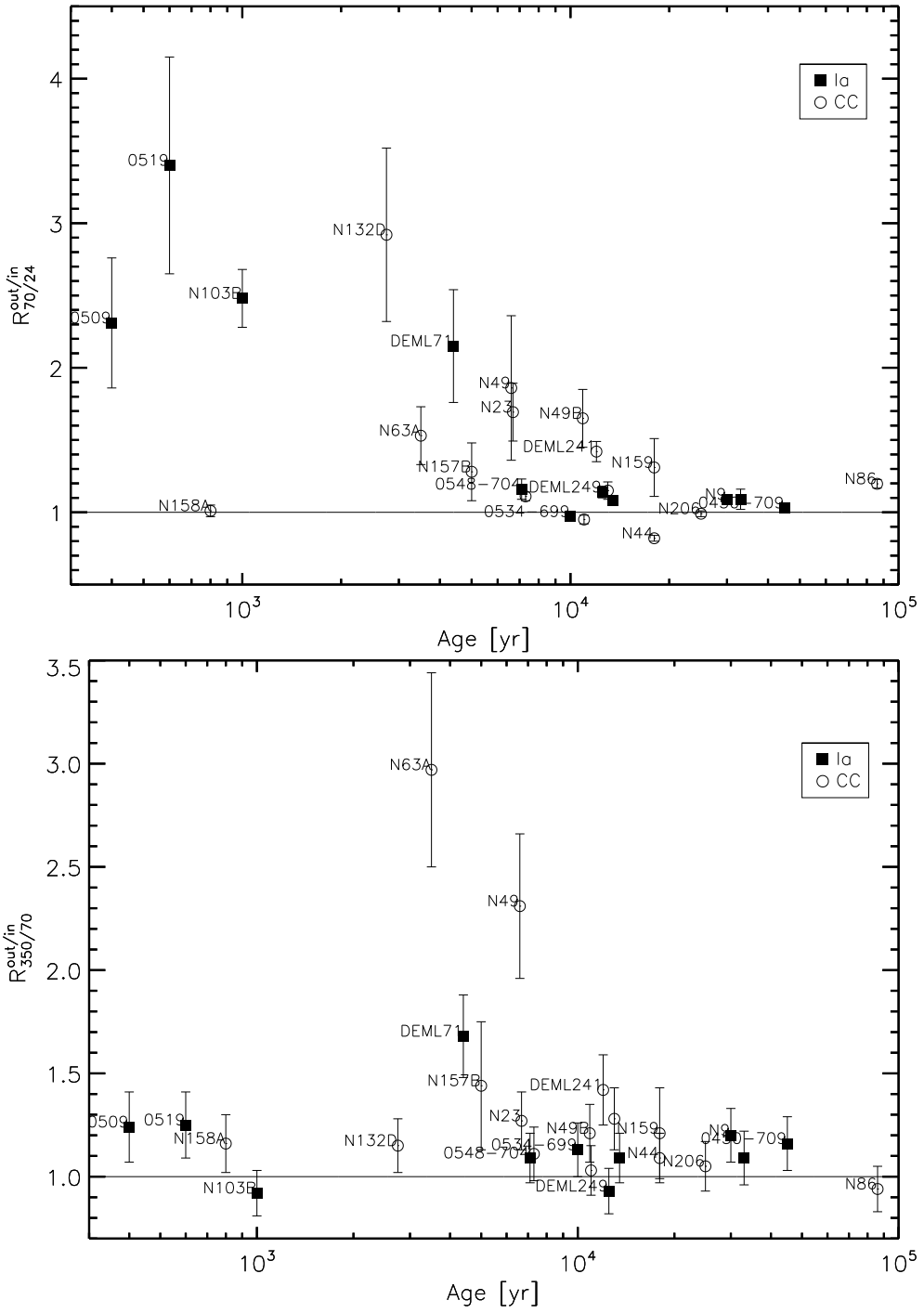

Figure 4.9: *Top:* Evolution of the ratio $R^{out/in}_{70/24}$ with SNR age; *Bottom:* Evolution of the ratio $R^{out/in}_{350/70}$ with SNR age – both for the smaller sample of SNRs (Table 4.2).

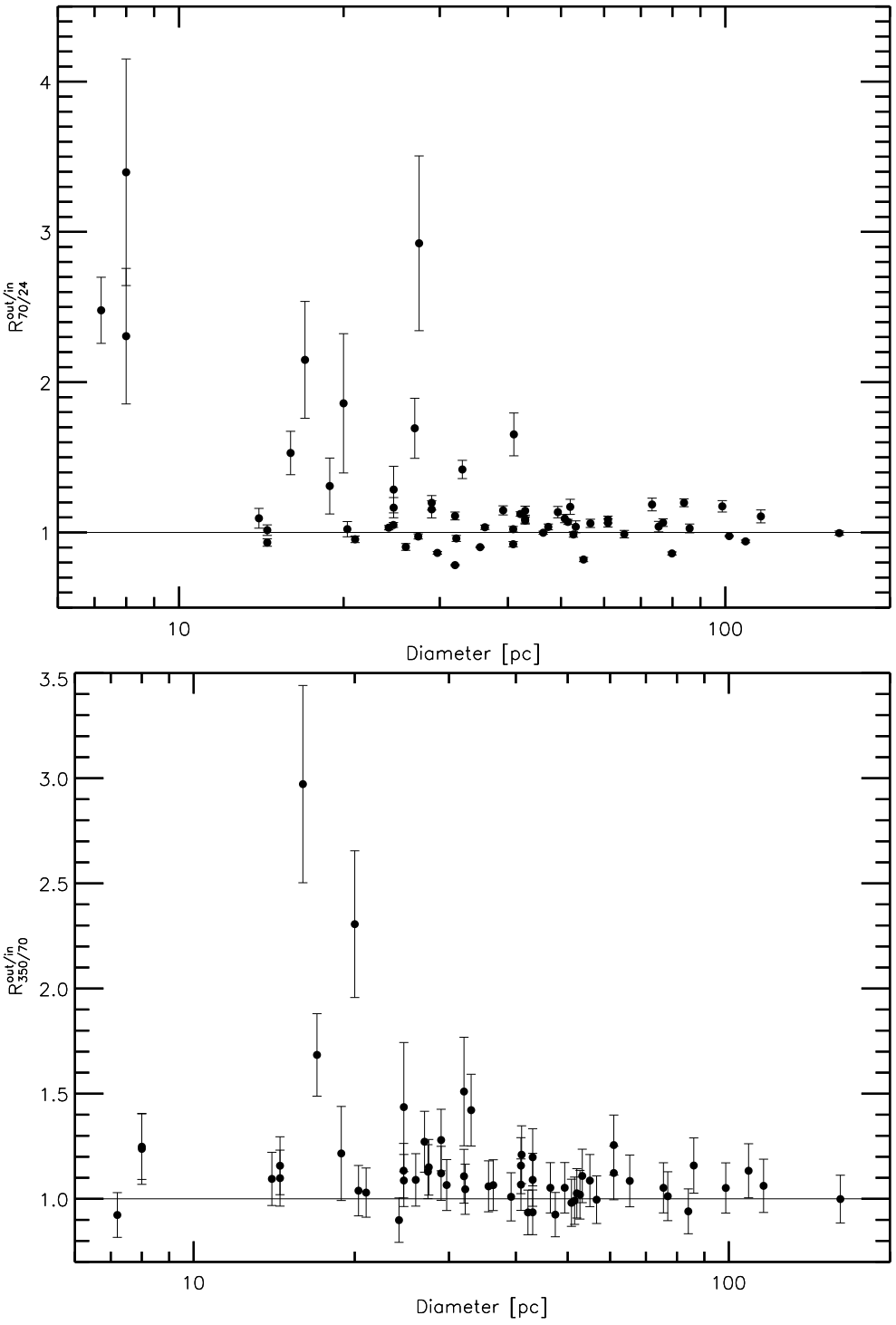

Figure 4.10: *Top:* Evolution of the ratio $R^{out/in}_{70/24}$ with diameter; *Bottom:* Evolution of the ratio $R^{out/in}_{350/70}$ with diameter – both for the whole sample of SNRs (Table 4.1).

SNRs, that have cooled down and are barely visible at most wavelengths (for example DEM L203, B 0536−6914 and B0454−7005), and in the obscured SNRs (Honeycomb; N 103B), sometimes even when they are not resolved at 500 μm. Thus, I found that these ratios are the best way to notice the SNR influence on the ISM if there is enough dust for the SNR to interact with and if back/foreground emission is not too dominant. The images of different ratios for SNR N 49, $R_{70/24}$; $R_{350/70}$; $R_{500/100}$; $R_{500/250}$; $R_{100/70}$ and $R_{160/24}$ are shown on Fig. 4.8. I provide similar images of flux ratios of the other SNRs on the attached DVD, presented in data cubes (FITS files) whose names contain the names of SNRs. Each FITS file contains the ratios in the following order: 70/24, 350/70, 500/100, 500/250, 100/70, 160/70 and 160/24. One could open these cubes with the program *DS9*, load the file under the name *lmc.reg*, see where are the actual positions of these remnants and notice that ratios are usually lower within SNRs than outside of them.

These ratio maps give us another important conclusion: they show that lower ratios are connected to the whole remnant, and not only to some envelope. As we move outwards from the centre of SNRs, the ratio increases and the difference between inner and outer ratio becomes smaller, gradually, suggesting that we observe less of the SNR and more ISM dust. If the dust affected by heating and sputtering is in some kind of envelope, surrounding the SNR, the minimum of ratio would not be in the SNR centre, but in some annulus at a certain distance from the centre.

Another use of these ratios could be to find out which candidates are really SNRs and which are not, and which of them are young. However, a few well-known SNRs do not show much signature in these ratios, because of complicated and dense surroundings.

4.2.3 Evolution of ratios of fluxes in SNRs with time

In Section 4.2.2 I demonstrated that this ratio technique reveals SNRs in the FIR. I wanted to measure how this impact of SNRs on the ISM evolves with time. Therefore, I first found $R_{70/24}$ per pixel, outside and within the SNRs, from these ratio maps, and

then in Fig. 4.9, top, I plotted the ratios for various SNRs (from the sample of SNRs in Table 4.2) versus their age, $R_{70/24}^{out/in}$. On the bottom image there are the ratios of $R_{350/70}$ per pixel outside and within SNRs, versus SNR age, $R_{350/70}^{out/in}$, for the same sample of SNRs.

The plots (Fig. 4.9) show a decreasing of $R_{70/24}^{out/in}$ and $R_{350/70}^{out/in}$ with time, suggesting cooling, but also the dependence on the mass of dust in that direction. One should be aware that $R_{350/70}$ can not be too far from 1 since the fluxes are similar. For most SNRs $R_{70/24}^{out/in}$ and $R_{350/70}^{out/in}$ do not become equal to 1 within the observed lifetime of the SNRs, from which follows that the impact of these objects on the ISM is longer than the period that we observe them ($\lesssim 10^4 - 10^5$ years). The effect does not only depend on the temperature, but also on the mass in the SNR direction and imbalance between the amount of dust in the remnants and outside of the remnants (later I will discuss that SNRs sputter the dust). Thus, SNRs in lower density have lower ratios even if they are almong the youngest (such as the two Ias in our sample, 0509−67.5 and 0519−69.0). On the other hand the most massive SNRs, N 63A and N 49, stand out in the second plot (later I will show that the column densities towards these two SNRs are among the highest in the sample of SNRs that clearly interact with the dust).

Also, I made plots of these ratios versus diameters for the whole sample of SNRs (Fig. 4.10, top and bottom). Even if some of the ratios from these plots do become equal to 1, some other ratio might still show the presence of that remnant as it can be seen in the enclosed DVD.

An interesting case is SNR N 103B (type Ia) which could be in a dense environment, because it is in the direction of a dusty cloud (see mass map in Fig. A.4, bottom). However, it is only visible on the $R_{70/24}$ ratio map, while other maps of ratios do not show its presence (see DVD). It might be that it is not resolved at longer wavelengths, but also that it expands in a relatively low-density environment (Dickel & Milne 1995) and therefore only $R_{70/24}$ can be distinguished, like in case of other Ias, 0509−67.5 and 0519−69.0.

In these plots I have found the errors of the ratios in the following way. We have $A = B \times C$ where $A = (F_{\nu_2}^{out}/F_{\nu_1}^{out})/(F_{\nu_2}^{in}/F_{\nu_1}^{in})$, $B = F_{\nu_2}^{out}/F_{\nu_2}^{in}$ and $C = F_{\nu_1}^{in}/F_{\nu_1}^{out}$. We

can find the errors σB and σC using the equations

$$\frac{\sigma B}{B} = \sqrt{\left(\frac{\sigma^{\rm out}_{\nu_2}}{F^{\rm out}_{\nu_2}}\right)^2 + \left(\frac{\sigma^{\rm in}_{\nu_2}}{F^{\rm in}_{\nu_2}}\right)^2} \tag{4.4}$$

and

$$\frac{\sigma C}{C} = \sqrt{\left(\frac{\sigma^{\rm out}_{\nu_1}}{F^{\rm out}_{\nu_1}}\right)^2 + \left(\frac{\sigma^{\rm in}_{\nu_1}}{F^{\rm in}_{\nu_1}}\right)^2}, \tag{4.5}$$

while we can find the final errors of ratios, σA using the equation

$$\frac{\sigma A}{A} = \sqrt{\left(\frac{\sigma B}{B}\right)^2 + \left(\frac{\sigma C}{C}\right)^2}. \tag{4.6}$$

In these equations F_ν are total measured fluxes per pixel, while $\sigma^{\rm in}_{\nu_i}$ and $\sigma^{\rm out}_{\nu_i}$ are total errors of fluxes, found using eq. 4.2, and then divided by the number of pixels, N.

I did also have a look at these ratios in the SMC – they behave similarly but they do not show such obvious evolution since the dust is rarer, the objects are older and the galaxy is further.

4.2.4 Maps of mass and temperature of SNRs and their environments

In Section 2.2.2 I described the methods of producing the mass and temperature maps; in Section 4.2.4.1 I discuss the uncertainties in mass and temperature maps; In Section 4.2.4.2 I present mass and temperature maps of SNRs and their surroundings, while in Section 4.2.4.3 I discuss the maps of the other remnants that are given in the Appendix A.

4.2.4.1 The uncertainties of the maps

The uncertainties of these maps can be estimated using Monte Carlo simulations or found directly from the fit. Monte Carlo simulation is done by adding random Gaussian noise with standard deviation equal to the error on the fluxes, and fitting the resulting

SED. In the contour plot in Fig. 4.11, top, is the distribution of values of mass and temperature using 10 000 simulated datasets. The white square marks the actual fit for the given pixel. The two spots in the (M, T) plot appear to suggest that Monte Carlo fits are bimodal with the frequency of M and T parameters from the fits tending to cluster around M=0.5 $M_\odot$ and T=22.6 K or M=0.4 $M_\odot$ and T=23.7 K. This implies the fit is degenerate, but the apparent bimodality in Fig. 4.11, top is simply due to the way the figure is plotted (colour coded by frequency). When we instead compare the standard deviation (1σ = 68% confidence interval of distribution) of M and T (orange cross presents the propagation of 1σ errors for M and T, derived from the FWHM of the Gaussians of distributions of M and T as in Fig. 4.12), we see that the parameter space is not really bimodal – the fit to the SED (white square) and the 1σ range on this fit encompasses these 2 spots. The actual fit for the given pixel is shown in Fig. 4.11, bottom.

In Fig. 4.12 I show the histograms of obtained values of mass and temperature for the same 10 000 data sets. From the width of the Gaussians I find the errors of the mass and the temperature for that pixel of 6.9% and 1.8% respectively; the average χ^2 was 1.45. These errors are different from pixel to pixel and from remnant to remnant. For low density SNRs, like 0506−675 and DEM L71 we can not use this method for finding errors since the flux can be too low (sometimes less than 3σ).

Because Monte Carlo simulations for every pixel and remnant would be time consuming, I find the uncertainties of mass and temperature from the MPFIT procedure itself. In Fig. 4.13 I give the distributions of the ratios of the uncertainties and corresponding parameters, for mass and temperature, respectively, for SNR N 49B and surroundings, using 9120 pixels, or 320×320 pc^2 (pixel size is $\sim 14''$). The maps of N 49B and its surroundings are representative for the LMC because there are enough faint and bright pixels to estimate the error distribution. These uncertainties are <40% for the mass and <13% for the temperature. The correlation between these parameters and their uncertainties and between temperature and mass are given in Fig. 4.14.

In Fig. 4.15 I show the histograms of the residuals (model minus data) divided by the corresponding surface brightnesses (Σ) at all wavelengths for SNR N 49B and

the surroundings (the same area as above). The residuals are of order of the surface brightness uncertainties (∼10%) and thus my adopted model describes the data well. More sophisticated models and error analysis can be found in Gordon et al. (2014), who used the same data but different κ and α_{IR} as free parameter.

4.2.4.2 The mass and temperature maps of several remnants

Here I present the maps of mass and temperature for several SNRs and their surroundings, while for the rest of the remnants they are given in Appendix A. The procedure I used for producing these maps is described in Section 2.2.2. As one can see on Fig. 4.16, the circle in the center shows the diameter of a SNR, while the other small circle in the corner is the size of the beam at the resolution of the 500 μm images, 36.3″. The conclusion I made from these maps is that there is often less mass and higher temperature within the remnants than towards their surroundings (see Sections 4.3.1 and 4.3.2). I explain this effect by sputtering and heating of the dust by SNR shocks. It is important to note that most of the remnants for which we see enhanced temperature in these maps (∼10 objects) are also detected with *Spitzer* and/or *AKARI* (Borkowski et al. 2006; Williams et al. 2006; Williams, Chu & Gruendl 2006; Seok et al. 2008; Seok, Koo & Onaka 2013). These mass and temperature maps, based on *Herschel* data are both a confirmation and extension of these previous observations but now include crucial long wavelengths information.

In Fig. 4.16, top I show the temperature and mass maps for SNR N 49 and its surroundings, mass maps on the left and temperature maps on the right side. From the mass map of this remnant I noticed that there is less dust within the remnant than in the regions that surround the remnant. The temperature map of SNR N 49 shows evidence of heating at the location of the remnant. In this remnant, the highest

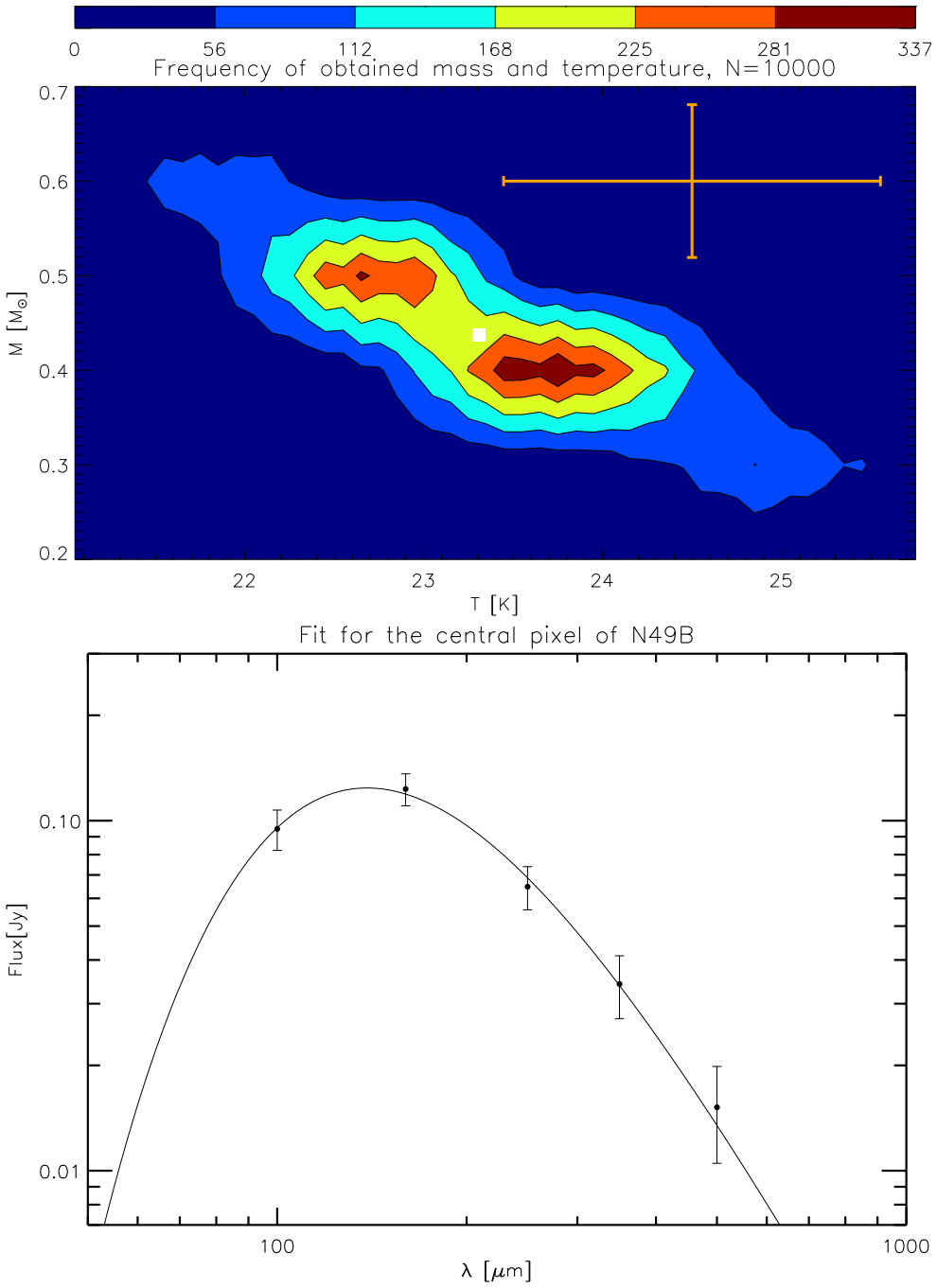

Figure 4.11: *Top:* The obtained values of mass and temperature for the central pixel in the image of N 49B, based on fits to 10 000 simulated datasets. The white square is the actual result of the fit for that pixel. The orange cross corresponds to the sizes of the error (2σ) for M and T, which were derived from the FWHM of the Gaussians of the distribution of M and T (similar as these at Fig 4.12). *Bottom:* Fitting of the SED of that particular pixel.

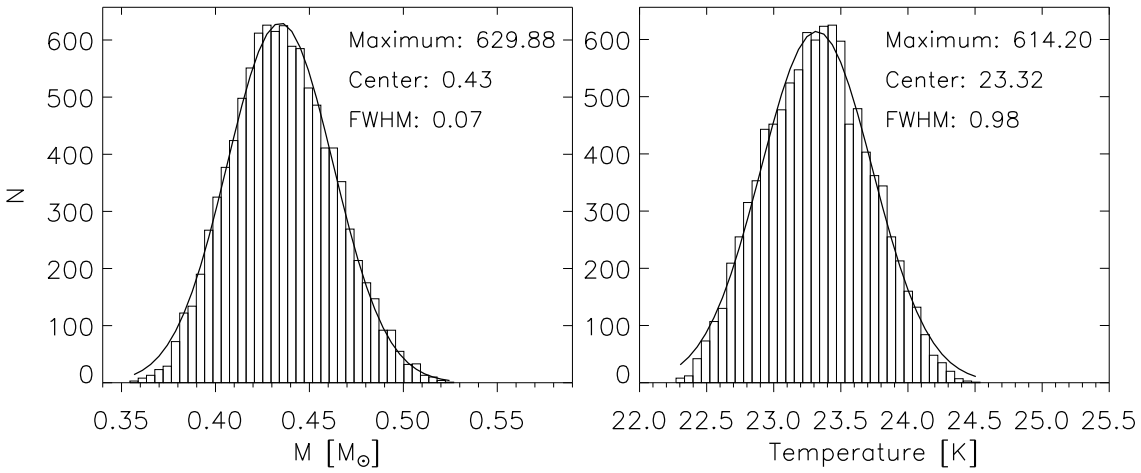

Figure 4.12: Histograms of the (*left*) mass and (*right*) temperature obtained for the 10 000 simulated datasets around the central pixel of SNR N 49B. From FWHM we can find the values of σ.

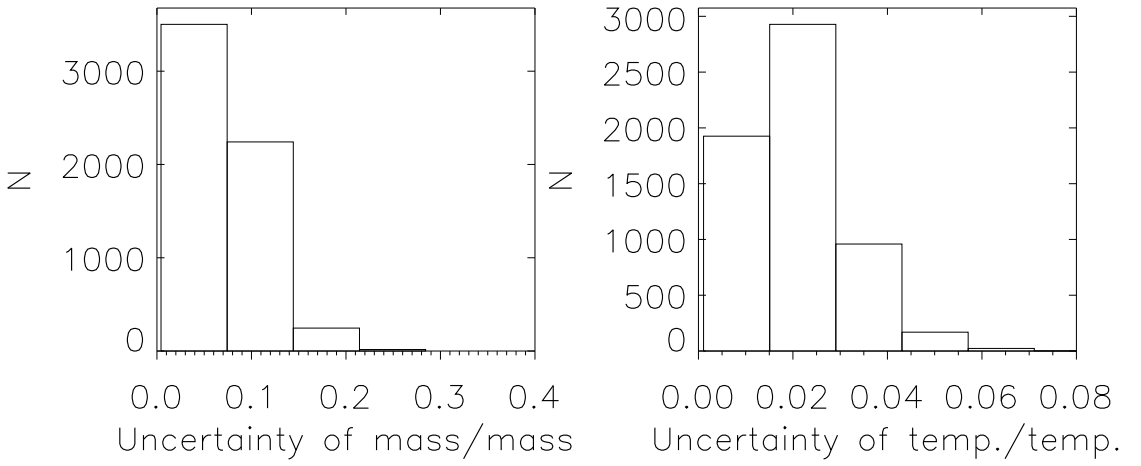

Figure 4.13: Histograms of the ratio of uncertainties of parameters and the parameters themselves for 9120 pixels of the N 49B image, for (*Left:*) mass and (*Right:*) temperature.

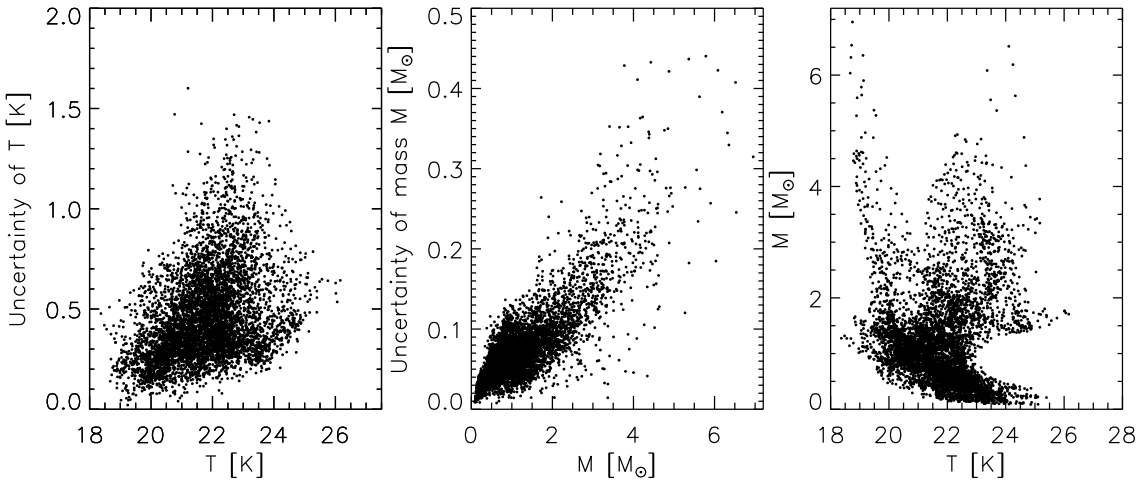

Figure 4.14: *Left:* Correlation between temperature and its uncertainty; *Middle:* between mass and its uncertainty; and *Right:* between temperature and mass. All three images are based on 9120 pixels of the N 49B image.

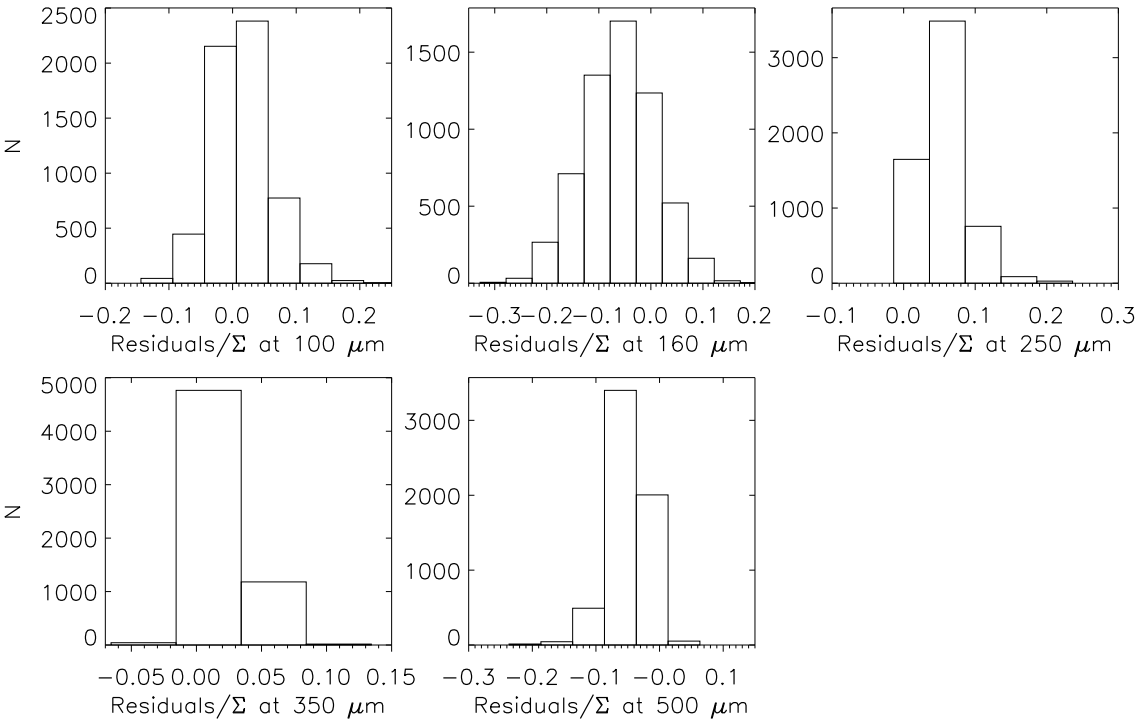

Figure 4.15: Histograms of the residual/Σ at all wavelengths for SNR N 49B and its surroundings (9120 pixels). These residuals are of order of the surface brightness uncertainties (∼10%) and therefore my adopted model describes the data well.

temperature is in of the 'blob' – which is the dust cloud that the SNR interacts with, present in the original images of this object of *Herschel* and *Spitzer* data (Williams, Chu & Gruendl 2006; Otsuka et al. 2010). From these maps I conclude that we see the 'blob' on *Herschel* and *Spitzer* images – not because it is massive – but because it is heated by a shock (of speed $\sim$ 45 km s^{-1}; Bon-Chul, in prep.). This remnant is possibly overlapping with two other older shells, one below, one above, as was observed by Payne, White & Filipović (2008), that might have caused some sputtering before N 49 itself, and might possibly be the reason why the column density is not dropping immediately at the edges of SNR N 49. The other possibility is that remnant has sputtered dust further out by X-rays or cosmic rays. More about N 49 and the other SNRs can be found in 4.1.1.

Similarly as for N 49, the maps of temperature and mass for SNR N 63A are given in Fig. 4.16, bottom. This remnant, probably from a massive progenitor (Hughes, Hayashi & Koyama 1998), is embedded in a large H II region on its North-Western side and is enhancing the temperature and probably reducing the dust mass on its position. The warmest, North-Western part of the SNR corresponds to the shocked lobes, which have a higher contribution from line emission – up to half of the 24-μm flux (Caulet & Williams 2012).

In Fig. 4.17, top are the maps for N 132D. The mass and temperature maps show the remnant surrounded by plenty of dust; it has warmed up and reduced the mass of dust. Fig. 4.17, bottom: N 49B, similarly as others – heating up and sputtering the dust. Fig. 4.18, top: DEM L71 and bottom: N 157B - both also show sputtering and heating. Fig. 4.19, top: SNRs DEM L316A and DEM L316B. Both remnants seem to sputter and heat the dust and they seem to belong to similar dust environment. Fig. 4.19, bottom: SNR N 23 seems to heat and perhaps sputter the dust.

4.2.4.3 Other SNRs

Many SNRs show signs of dust removal and/or heating. SNR Honeycomb is devoid of dust compared to its surroundings whilst lacking any signs of heating (Fig. A.10).

Other SNRs showing signs of dust removal and/or heating within the SNR include 0453−68.5 detected with *Spitzer* (Fig. A.2; Williams et al. 2006), N 4 (Fig. A.1), the type Ia – SNR 0519−69.0 detected with *Spitzer* (Fig. A.6; Borkowski et al. 2006), DEM L241 (Fig. A.11), N 23 (Fig. A.3), B 0548−70.4 (Fig. A.13) – detected with *Spitzer* (Borkowski et al. 2006), SNR 0520−69.4 (Fig. A.6; probably sputtering and heating on the edges), DEM L204 (Fig. A.7)– devoid of dust, DEM L109 and a nearby compact SNR candidate, J 051327 −6911 (Bojičić et al. 2007) appearing to heat a nearby dust cloud (Fig. A.5).

Several SNRs appear to interact with interstellar dusty features at their periphery. Young N 158A (0540−69.3) (progenitor of 20–25 $M_{\odot}$, Williams et al. 2008) is possibly interacting with a dense cloud to the North. Williams et al. (2008) detected its PWN with *Spitzer* at wavelengths ≤ 24 μm, but did not find any IR detection of the shell. They found dust synthesized in the SNR, heated to 50–60 K by the shock wave generated by the PWN. The data I have only show possible heating of the surrounding medium, but not an obvious influence by this SNR. Other SNRs interacting (or about to interact) with surrounding dusty structures include N 9, B 0507−7029, SNR 0450−709 and DEM L299.

Some SNRs are confused. DEM L218 (MCELS J 0530−7008), of type Ia (De Horta et al. 2012) is covered with the object that Blair et al. (2006) called SNR 0530−70.1. N 159 (0540−697) is in a complicated region, close to the black-hole high-mass X-ray binary LMC X-1 and a bright H II region to the South–West (Seward et al. 2010). SN 1987A is unresolved and on its dust mass map I can measure $\sim$1 $M_{\odot}$ of the dust (I remind the reader that these maps are constructed at the angular resolution of the 500-μm data).

4.2.4.4 Pulsar wind nebulae

Some SNRs contain a PWN, which could make a synchrotron contribution to the FIR spectrum or provide an additional mechanism to heat dust (Temim et al. 2012). The SNRs which have been connected with pulsars in the LMC are N 49 (Park et al. 2012),

N 206, 0453−68.5, B 0540−693 in N 158A, N 157B, DEM L241 (Hayato et al. 2006), and DEM L214 (Bozzetto et al. 2012a). On the other hand, while all PWNe are powered by pulsars, PWNe are known without a detected pulsar (Gaensler et al. 2003). An example of this is N 23 (Hayato et al. 2006). I did not find any evidence for the influence of pulsars on these maps.

For example, 0540−69.3 is the remnant whose pulsar was detected with *Spitzer* (Williams et al. 2008), but it was not detected in these maps. Probably the resolution of my maps is not good enough to detect the effects produced by pulsars.

4.3 Discussion

In Section 4.3.1 and Section 4.3.2 I discuss the influence of the population of SNRs on the interstellar dust mass and temperature. In Section 4.3.3 I argue for a lack of evidence for large amounts of dust having formed in SNRs and survived. I attempt to quantify the amount of sputtered dust in Section 4.3.4, based on the difference of column density between SNR surroundings and SNRs. I end with a brief discussion about the thickness of the interstellar dust layer (Section 4.3.5).

4.3.1 Influence of SNRs on the mass of the interstellar dust

In Fig. 4.20 (top panel) I present radial profiles of the average dust column density in and around SNRs as a function of radial distance to the centre of the SNR, for a sub-sample of 22 SNRs, where each successive bin comprises a 6.8 pc wide annulus. The blue circles mark where the SNR's radii end. While often less dust is seen towards the SNR – although sometimes the opposite is seen – the radial profiles are generally fairly flat; this indicates that the amount of (cold) dust that is destroyed is relatively small compared to the amount of dust in the LMC in that direction. These profiles also reflect a general relation between SN progenitor type and ISM density, as core-collapse SNe are usually seen in regions of recent star formation whereas SNe Ia often

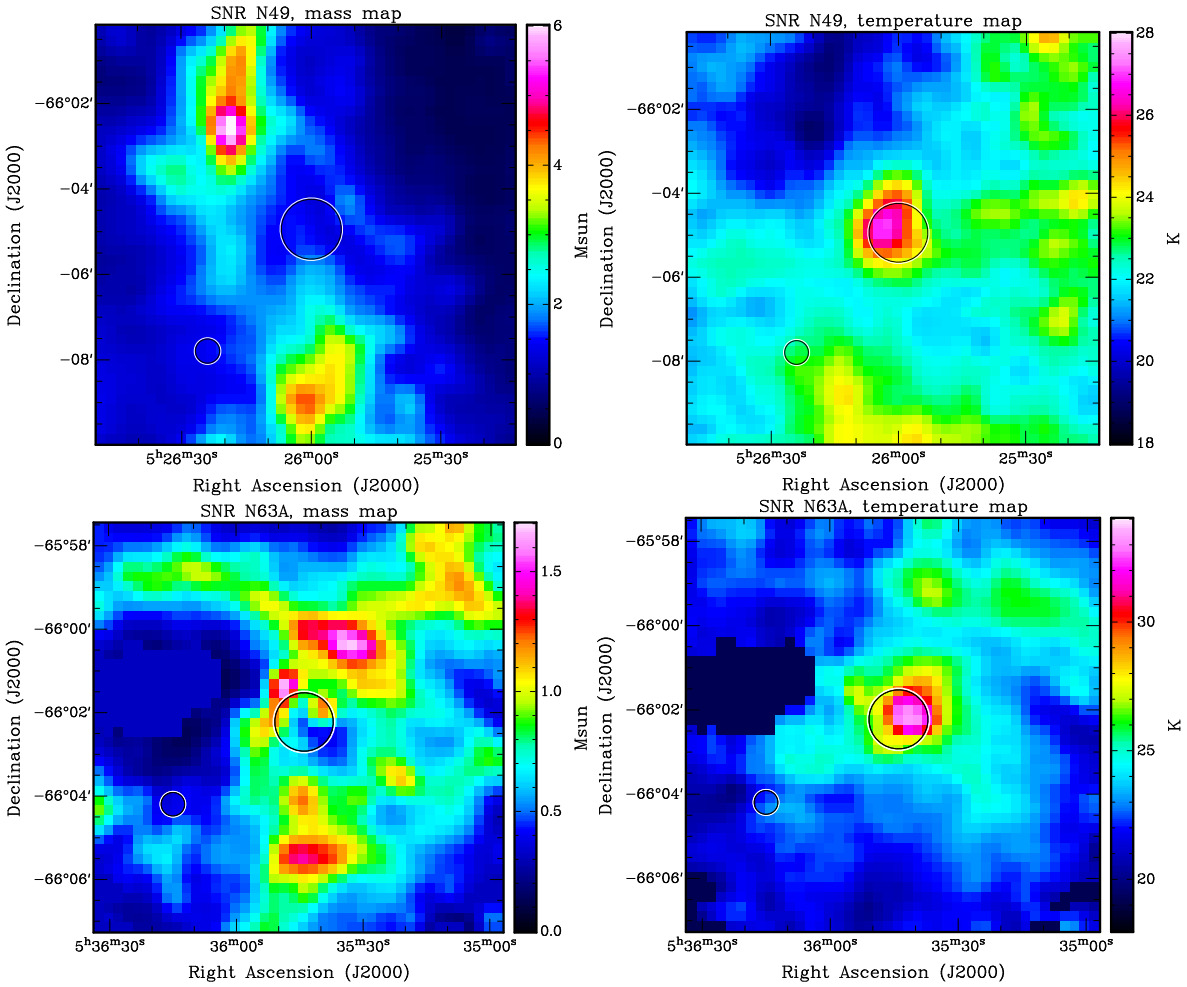

Figure 4.16: Images on the left side are mass maps and on the right side are temperature maps. Upper images are for N 49, lower are for N 63A. Smaller circle in left corner is the beam and the central big circle is the surface of the SNR.

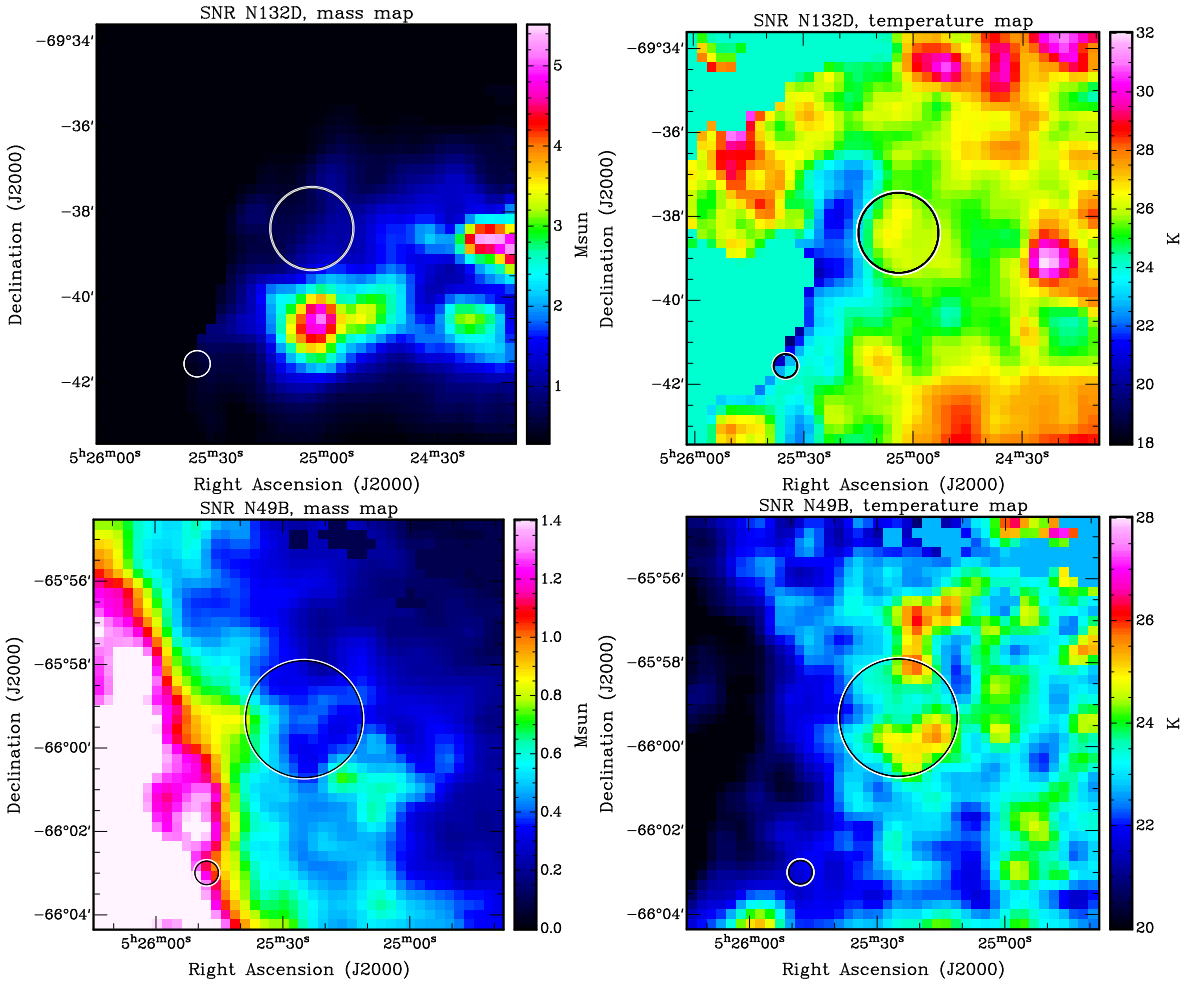

Figure 4.17: As Fig. 4.16, but for SNRs N 132D and N 49B.

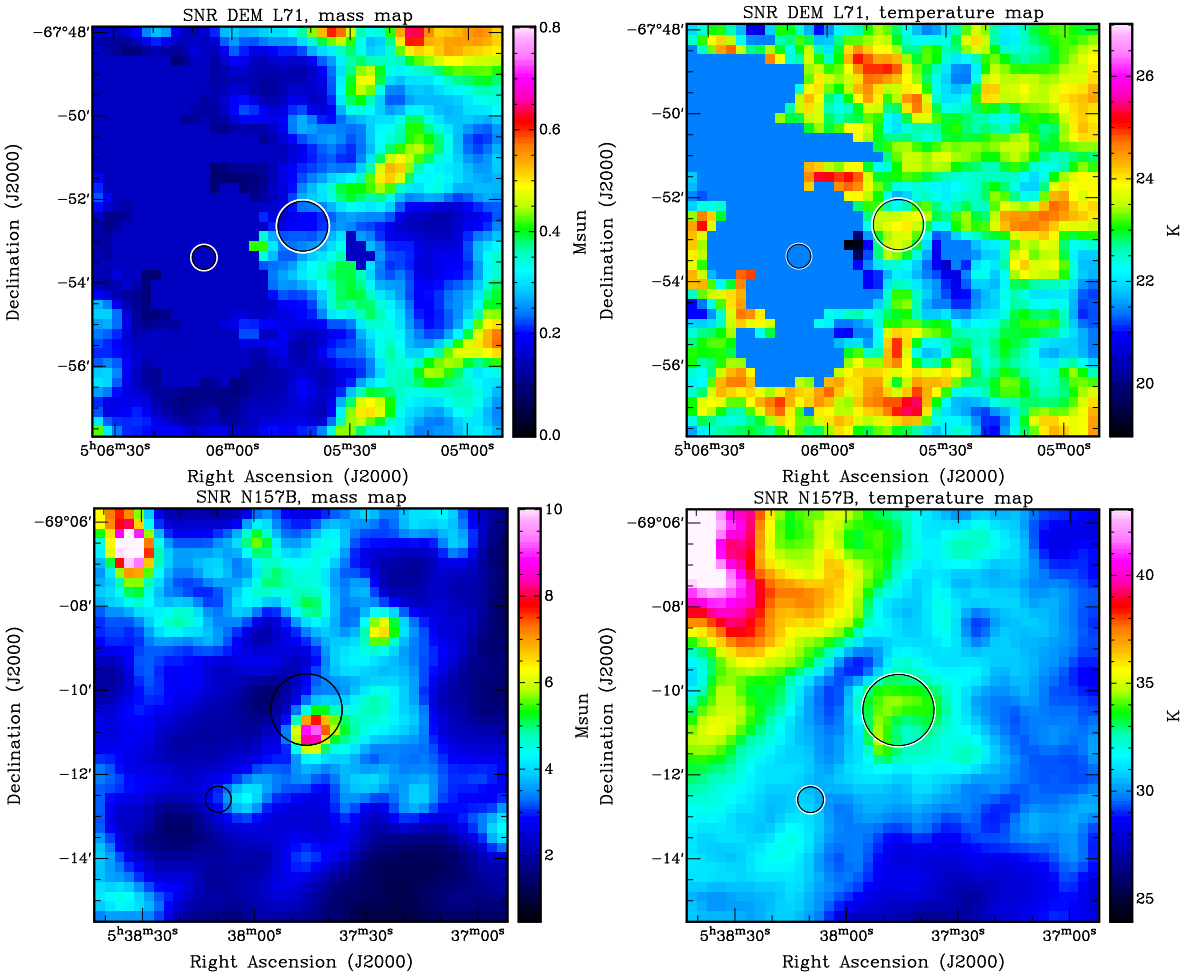

Figure 4.18: As Fig. 4.16, but for SNRs DEM L71 and N 157B.

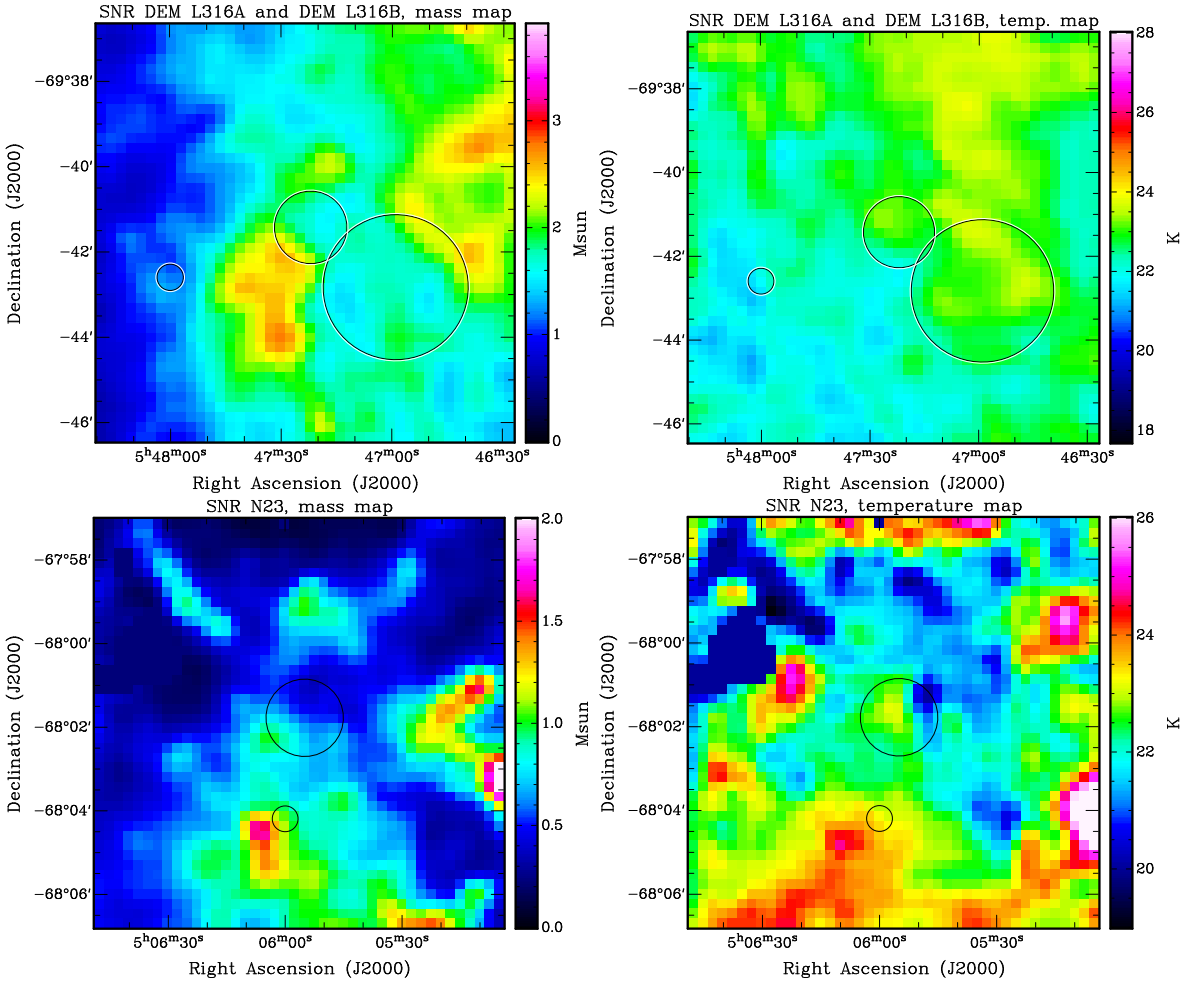

Figure 4.19: As Fig. 4.16, but for SNRs DEM L316A and DEM L316B (top) and N 23 (bottom).

bear no memory of their natal environment. On this basis, N 157B and N 159 stand out in terms of ISM density; they are bright at FIR and radio wavelengths and their progenitors are probably massive.

To examine the difference in ISM surrounding CC and Ia SNRs, in the bottom panel of Fig. 4.20 I show the distributions of average dust column density within the SNR diameter, separately for CC, Ia and for all SNRs together (for typing SNRs see Section 4.1.1). Ias are usually in dust-poor environments, but there are exceptions such as the probable prompt Ia SNRs DEM L316A and N 103B, that are seen in the direction of dense ISM. A K-S test of these two data samples gives a P value of 0.016 which means that there is 1.6% chance that these data are from the same population (distribution). For the Ia sample, the mean is 0.045 and median is 0.027, while for the CC sample, the mean is 0.079 and median is 0.059 $M_{\odot}$ pc^{-2}. In each dataset there are found the two outliers compared to the mean. We can conclude that having submm and FIR data we can not find out the SNR type, but we can have an insight in the probable SNR environment.

Some of the SNRs which in this work I believe to sputter dust are already claimed to be dust destroyers based on modeling of *Spitzer* observations (Williams 2010). With *Herschel* data the lack of dust within the SNR can actually be observed – for SNRs that have enough dust to interact with.

If it is possible that the dust were pushed out of the way and not sputtered, we should see dust piling up around the rims of SNRs – which we do not see. If the dust is significantly sputtered by SNR shocks, then for most of the remnants (D> 10 pc) the dust formed in the progenitor and its CSM should have been mainly sputtered in the early stages, while only a small part of it got to be re-formed. The winds of RSG SN progenitors are slow, $v \ll 100$ km s^{-1}, and such CSM is quickly over-run by the SNR (see, e.g. van Loon 2010). Only if the progenitor star was an early-type star, it could have formed an interstellar bubble of a size ∼30 pc (Castor, McCray & Weaver 1975), otherwise the dust around remnants is not directly connected with the CSM of the progenitor but is from pre-existing ISM dust, with possibly different densities depending on progenitor type.

According to the dust mass maps, many SNRs are close to, or at the rim, or in the direction of dusty structures. This could hide the influence of SNRs from the observer in two ways: if the cloud is irregular and inhomogeneous, we would not see a lack of dust inside SNRs; if the SNR is next to the cloud from our perspective, then it is more difficult to claim that it has sputtered any dust.

Initially I used annuli from 1–1.3 of diameters, but I found that 20 pc thick annuli are a better solution, since in the case of annuli of 1–1.3D, there would be a big difference between the areas of the annuli for SNRs of various sizes.

As I am using annuli that are 20 pc thick, large SNRs ($D > 100$ pc) subtend a larger area on the sky than the annulus, which tends to reduce the difference between average inner and outer column density, because the probability of back/foreground noise is higher towards the remnant than towards the annulus. Similarly, the annuli of the smallest SNRs are more likely to be more massive than areas within these remnants.

4.3.2 Influence of SNRs on the temperature of the interstellar dust

On my maps of dust temperature, there is often a slightly higher temperature towards SNRs than towards the surrounding annuli – even for the older remnants. Also, for older remnants the dust temperature often peaks near the edges or outside of the remnants which can probably also be a sign that the dust has been removed. In Fig. 4.21, top I show the ratio of inner and outer (from annuli 20 pc thick) temperature, $T_{\rm in}/T_{\rm out}$, where the sizes of the symbols represent the the column densities towards SNRs. $T_{\rm in}$ and $T_{\rm out}$ are defined as the average temperatures within the remnant and within its annulus, from the dust temperature maps. The errors of this graph are derived from standard deviations of the temperature values $\sigma_{\rm in}$ and $\sigma_{\rm out}$ as

$$\Delta\left(\frac{T_{\rm in}}{T_{\rm out}}\right) = \frac{T_{\rm in}}{T_{\rm out}}\sqrt{\left(\frac{\sigma_{\rm in}}{T_{\rm in}}\right)^2 + \left(\frac{\sigma_{\rm out}}{T_{\rm out}}\right)^2}. \quad (4.7)$$

We used the Spearman's Rho test to find that the R value of the plot on Fig. 4.21, top is –0.3, meaning the weak downhill (negative) linear correlation between $T_{\rm in}/T_{\rm out}$

and diameter. That means that $T_{\rm in}/T_{\rm out}$ decreases slightly as SNRs get old and that it is somewhat higher in younger and smaller SNRs than in older and larger remnants. Two-tailed value of P is 0.02, which is the probability of having this correlation to happen by chance. By normal standards, the association between the two variables would be considered statistically significant. This plot indicates that most of the SNRs do heat up the swept ISM and that the temperature of this dust is somewhat higher than the temperature of the ISRF. The heating of the dust is most prevalent in the more compact, presumably younger SNRs as well as the ones with a higher dust content.

On Fig. 4.21, bottom I show the average temperatures for the individual SNRs, also derived from the dust temperature maps. On that graph, the errors are standard deviations, themselves.

The temperature maps often show heating of dust on SNR locations, usually in SNRs that are detected with *Spitzer*, although here I use only *Herschel* data. Since the dust is being eroded and cools, this heating is only seen in young SNRs that interact with sufficient amounts of dust. It should be added that the temperature maps would show much more heating at the places of SNRs if the data at 24 and 70 μm are added, in the case of fitting with two dust components.

I do not exclude the possibility that the heated dust towards SNRs belongs to the closer ISM surroundings of SNRs.

4.3.3 Production of dust in SNRs

Even if all SNRs create some dust in their ejecta, it would not be possible to recognize with the mass maps I have. The youngest SNR in my sample, SN 1987A has produced ~ 0.6 M$_\odot$ of cold dust (Chapter 3). It stands out on the *Spitzer* and short-λ *Herschel* images but not at 500 μm. On my mass map, the mass is slightly higher at the place of that object (for about 1 M$_\odot$), but one could not recognize this mass without knowing that it is there.

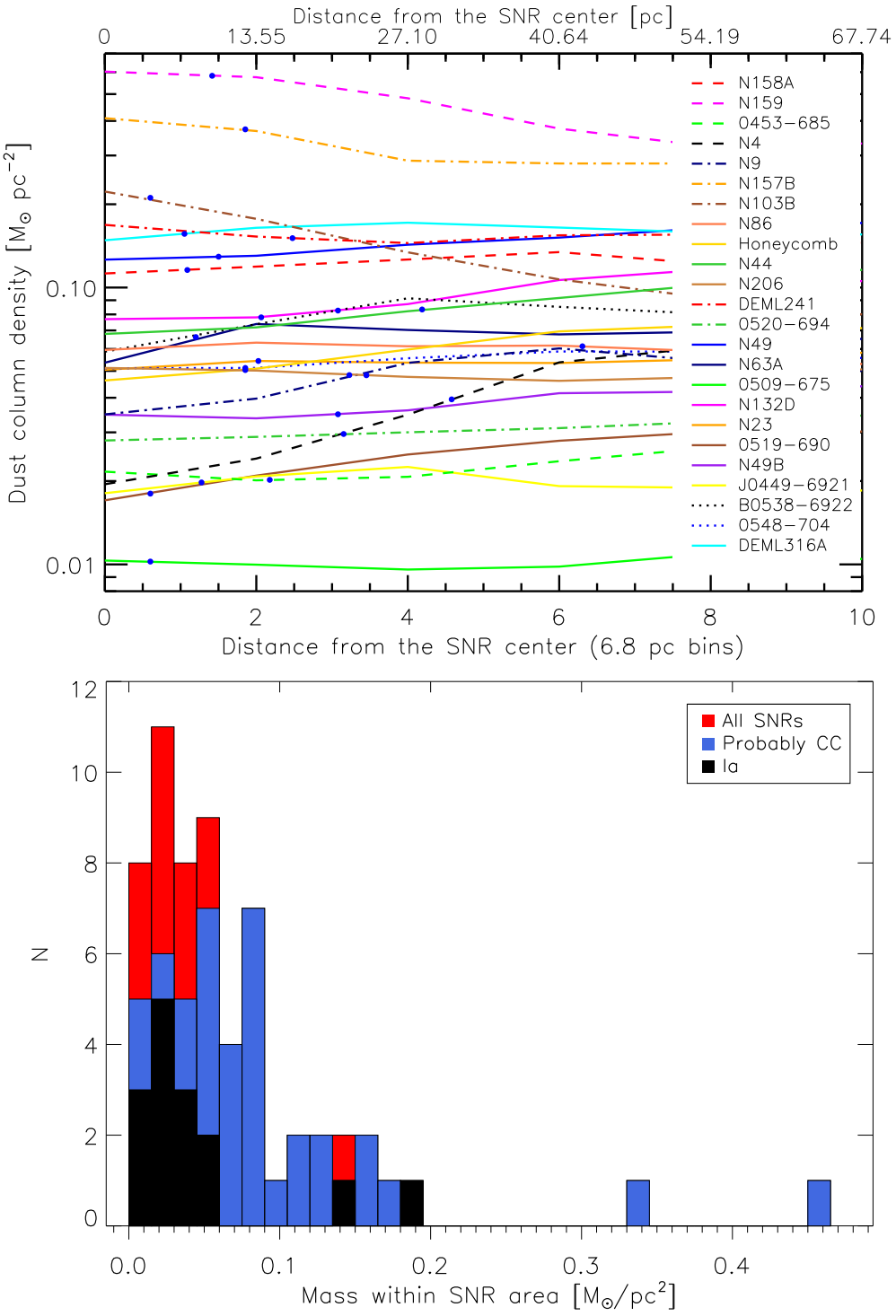

Figure 4.20: *Top:* Radial profiles of dust column density distribution across SNRs and their environment. On the x-axis is the number of bins; each bin is 6.8 pc wide annulus. The blue circles mark the ends of the radii of SNRs. *Bottom:* The distribution of the average dust mass ($M_\odot$ pc^{-2}) within one diameter of Ia, CC and all SNRs together.

Another object that is probably in the free expansion phase (other objects are in later stages – most of the material associated with them is swept up ISM) is N 103B. N 103B might not be resolved on the dust maps; but it has reduced $R_{70/24}$ compared to the surrounding ISM, while other ratios do not show that characteristic. It may indeed be in a rare environment, behind (or in front of) a massive cloud (Dickel & Milne 1995). I see no dust production here, but I do not expect it, since it is a Ia remnant.

Almost all other SNRs are larger than 50″, and cover > 50 pc^2. Even if 1 M$_\odot$ of dust were present in the ejecta, even if it is not spread over more than $\sim$3 arcsec^2 (like in the case of SN 1987A), this would correspond to a surface density < 0.009 M$_\odot$ pc^{-2}, i.e. often below that of the surrounding ISM ($\sim 0.01 - 0.6$ M$_\odot$ pc^{-2}; Fig. 4.20).

4.3.4 How much dust have SNRs sputtered?

I estimate the mass of dust that is removed from the ISM by the SNRs by comparing the average dust column density towards the SNR with that within a 20 pc thick annulus. Assuming that both reflect the ISM dust in those directions, the difference will correspond to the mass of dust that was removed (or added) by the SNR. In Table 4.5 I list the determinations for nearly all (60) SNRs. The average dust column density within the SNR is $N_{\rm in}$ and within an annulus surrounding the SNR is $N_{\rm out}$. I only quote the values for the removed dust mass M for those cases I am reasonably confident about (for these SNRs I believe that they did sputter dust and that the difference in dust mass is not caused by the accidental position of the SNR next to the cloud). The assumption that these objects are more confidently showing dust sputtering is made without any statistical method, using only the eye.

To find the sputtered mass by one SNR I use the formula $\mathrm{S} \times (N_{\rm out} - N_{\rm in})$, where S is the surface of the SNR, in pc^2. In Fig. 4.22 I show graphically the sputtered dust mass by all SNRs in the sample – given as $\pm\sqrt{|\mathrm{S} \times (N_{\rm out} - N_{\rm in})|}$, versus the dust column density in the annuli of SNRs, finding that 40 out of 60 SNRs have less dust within their diameters than in their annuli. The median value is indicated by the

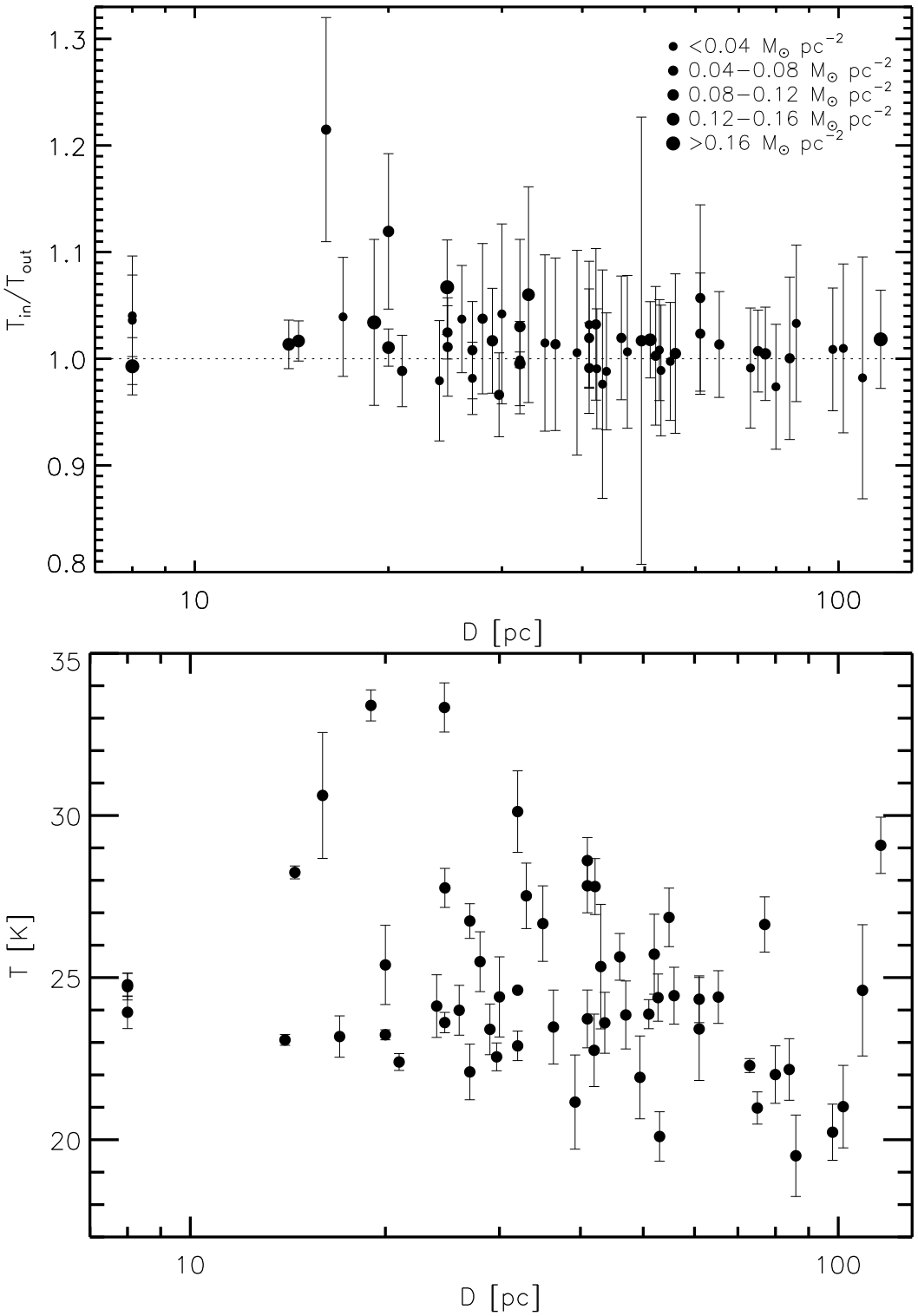

Figure 4.21: *Top:* ratio of average dust temperature within and outside the SNR vs. SNR diameter. The size of the symbol is proportional to the average dust column density in the direction of the SNR. *Bottom:* Average dust temperature towards SNRs vs. diameters. Both graphs are made using dust temperature maps.

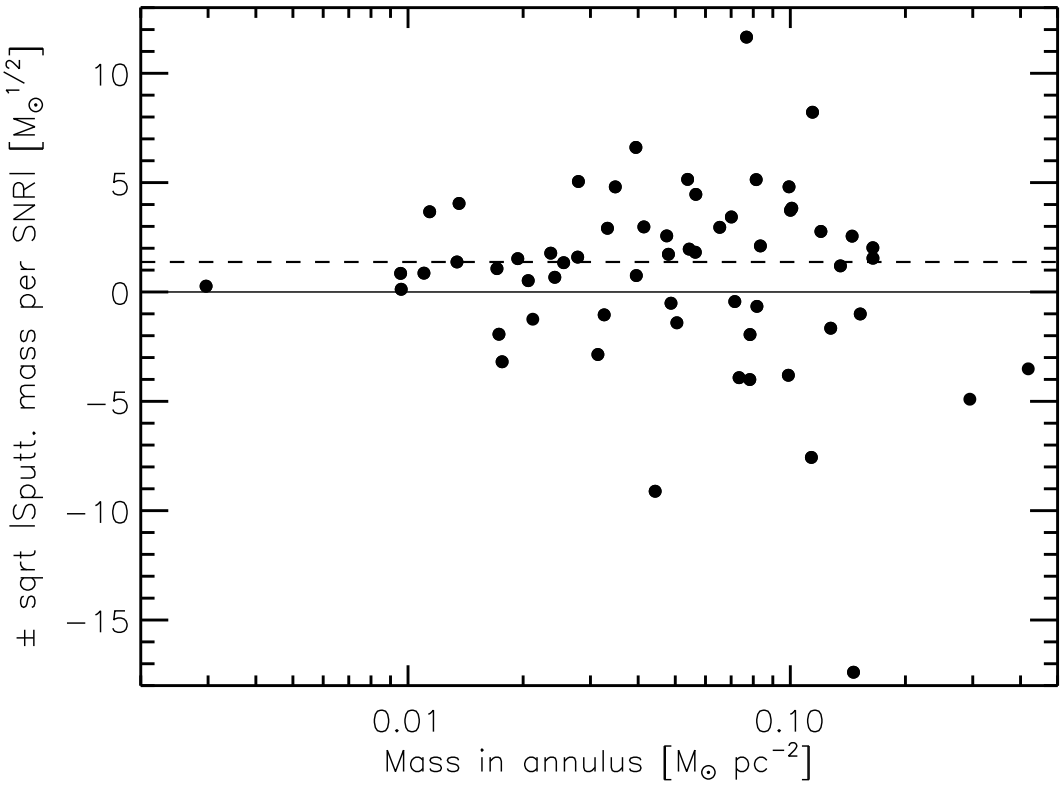

Figure 4.22: Sputtered dust mass vs. dust mass in an annulus surrounding the SNR. Square-root values are plotted to limit the dynamical range, with negative masses ($M < 0$) represented by $-\sqrt{-M}$. The median value is indicated by the dashed line.

dashed line.

In Table 4.5, the errors for $N_{\rm in}$ and $N_{\rm out}$ include the uncertainties of the fitting of all pixels, $\sigma_{i,\rm fit}$, obtained by MPFIT, as well as the uncertainty of κ which is $\sim$25% (Gordon et al. 2014). They are found by the formula:

$$\Delta N_{\rm in} = N_{\rm in}\sqrt{\left(\frac{\sqrt{\Sigma\sigma_{i,\rm fit}^{\ 2}}}{N_{\rm in}S}\right)^2 + \left(\frac{\Delta\kappa}{\kappa}\right)^2}, \tag{4.8}$$

and

$$\Delta N_{\rm out} = N_{\rm out}\sqrt{\left(\frac{\sqrt{\Sigma\sigma_{i,\rm fit}^{\ 2}}}{N_{\rm out}S_1}\right)^2 + \left(\frac{\Delta\kappa}{\kappa}\right)^2}, \tag{4.9}$$

where S_1 is the surface of the SNR annulus, in pc^2. Therefore, the uncertainties of M are found as

$$\Delta M = {\rm M}\times\sqrt{\left(\frac{\Delta'}{N_{\rm out}-N_{\rm in}}\right)^2 + \left(\frac{\Delta\kappa}{\kappa}\right)^2}, \tag{4.10}$$

where

$$\Delta' = \sqrt{\left(\sqrt{\Sigma\sigma_{i,\rm fit,in}^2}/S\right)^2 + \left(\sqrt{\Sigma\sigma_{i,\rm fit,out}^2}/S_1\right)^2}. \tag{4.11}$$

The SNRs that I am confident about that there is dust removed in them (15 objects) show a wide range of dust removed, but with a mean of 6.5 M$_\odot$ (and a median of $\sim$ 4 M$_\odot$) – well above the typically inferred amounts of dust that are produced in the ejecta ($<$ 1 M$_\odot$). If this is representative of the SNR population as a whole I would obtain $M_1 \sim 390$ M$_\odot$ of sputtered dust. If instead of the mean, I use the median value of these 15 SNRs, I would obtain $M_1' = 240$ M$_\odot$ of dust sputtered by 60 SNRs. The uncertainties for these estimates are the factor of three (see the following text) and are given in Table 4.6.

Now, I attempt to estimate the result for the entire sample of SNRs, including negative values, as follows:

$$M_2 \ = \ \sum_{i=1}^{N} \left[\pi(D/2)^2\times(N_{\rm out}-N_{\rm in})\right], \tag{4.12}$$

where D is the SNR diameter (in pc), and the sum is over N objects. Using this approach I obtain $M_2 = -13.6\pm47.5$ M$_\odot$ of dust sputtered by $N = 60$ SNRs in the

LMC. This result is driven by a few severe outliers for which the individual estimates are particularly uncertain (Fig. 4.22). If we perform $\sigma-$clipping, discarding the data points that deviate from the mean by more than 3σ (where σ is the standard deviation of this dataset), we can only discard SNR B0536–6914 (the datapoint in the bottom of Fig. 4.22). Without that data-point we obtain M_2 =288.9±26.4 $M_\odot$. We will keep the first calculation of M_2 to be more conservative (Table 4.6). The uncertainties in these two estimations are calculated as the standard deviations of these data sets.

My third estimate is based on the median rather than the sum (or average):

$$M_2' \;=\; 60 \times \mathrm{Median}_{i=1}^{N} \;\left[\pi(D/2)^2 \times (N_{\rm out} - N_{\rm in})\right]. \qquad (4.13)$$

Now, I obtain $M_2' \sim 113^{+278}_{-125}$ $M_\odot$. This, on the other hand, may exclude rare, but real, more prominent contributors to sputtering. The uncertainty in this estimation is calculated as the confidence intervals for 1σ (32%,68%) of the data set.

An alternative way of estimating the combined effect of the SNR population within the LMC is based on an empirical Monte Carlo simulation. I generate 10 000 sets of values for mass (m) and for diameter (D). These are drawn from the positive domain of a Gaussian, where the width is set by $\sigma = 0.13$ $M_\odot$ pc^{-2} for m and $\sigma = 44.4$ pc for D (Fig. 4.23). For each of these pairs of values (m, D) I derive the sputtered mass, from which I obtain the average sputtered mass per SNR and thence

$$M_3 \;=\; 60 \times \left\langle \pi(D/2)^2 \times m \times 0.09 \times \frac{40}{60} \right\rangle, \qquad (4.14)$$

where 40/60 is the probability that the SNR is sputtering the dust that we see in its direction – 40 is the number of SNRs with $(N_{\rm out}/N_{\rm in}) > 1$, in our sample of 60 SNRs; 0.09 is the average fraction of sputtered dust mass as compared to the dust mass that is seen in the direction of the SNR ($\langle N_{\rm out}/N_{\rm in}\rangle = 1.09$). I thus obtain $M_3 \sim 389 \pm 22$ $M_\odot$ sputtered mass per 60 SNRs. This result and its uncertainty are the average value and the standard deviation of the obtained values of M_3 based on 50 runs. This estimate is also given in Table 4.6.

While extrapolation of the 'cleanest sample', M_1 and Monte Carlo give high values, M_2 is too influenced by the fore/background of 3−4 very massive SNRs that

have $N_{\rm out} < N_{\rm in}$. I will adopt the average of these five values, i.e. 224 $M_\odot$ sputtered by the whole sample of SNRs.

The different approaches that I followed in the estimation of the sputtered dust give a range of a factor of ± 2, but the uncertainty of κ causes also a similar factor (we compared our κ_0 and λ_0 with the one that Gordon et al. (2014) have derived from fitting the MW diffuse emission SED for the SMBB[3] model, and we found that my dust masses are $\sim$60% of their masses due to κ uncertainty). Therefore, my estimate of the total error of sputtered mass is a factor of three.

For a SN rate in the LMC of $dN/dt = 10^{-2}$ yr^{-1} (Filipović et al. 1998a) and a mean lifetime $\tau_{\rm SNR} = 10^4$ yr for SNRs to be visible (Van den Bergh 2004), the number of SNRs existing in the LMC should be $N = \tau_{\rm SNR} \times dN/dt = 100$, i.e. almost double the sample considered here. Correcting for this, I deduce a total mass of sputtered dust by LMC SNRs of $M = 373$ $M_\odot$, within the range 124$-$1120 $M_\odot$. Thus, a dust destruction rate by SNRs in the LMC of $dM/dt = M/\tau_{\rm SNR} = 0.037$ $M_\odot$ yr^{-1} within a range of 0.012–0.11 $M_\odot$ yr^{-1}. For a total interstellar dust mass in the LMC of $M_{\rm dust} = 7.3 \times 10^5$ $M_\odot$ (Gordon et al. 2014) this would imply an interstellar dust lifetime of $\tau_{\rm dust} = M_{\rm dust}/(dM/dt) \sim 2 \times 10^7$ yr within a range (0.7$-$6) $\times 10^7$ yr. Of course, not all of the interstellar dust is affected by SNRs to the same degree, and some dust may survive a lot longer.

If SNe/SNRs are dust destroyers, then an alternative source of dust is needed to explain the dust in the high redshifts and in the local Universe. While some works show that the contribution of the AGB stars to the dust in the early Universe is not negligible, elsewhere an additional dust supply is needed to explain the large dust masses, such as quasar outflows (Mattsson 2011) or growth within dense ISM (Zhukovska 2014).

[3]SMBB model is a single temperature blackbody modified by a single power law emissivity.

Table: 4.5: Name of SNR, dust column densities within ($N_{\rm in}$) and outside ($N_{\rm out}$) the SNR in $M_\odot$ pc^{-2} and the total amount of dust which could be removed by the SNR ($M[M_\odot]$).

Name	$N_{\rm in} \pm \Delta N_{\rm in}$	$N_{\rm out} \pm \Delta N_{\rm out}$	$M \pm \Delta M$
B 0519−690	0.015 ± 0.004	0.024 ± 0.009	0.9 ± 0.3
DEM L71	0.019 ± 0.005	0.021 ± 0.006	0.20 ± 0.07
B 0509−675	0.009 ± 0.003	0.01 ± 0.003	0.04 ± 0.02
N 103B	0.19 ± 0.05	0.13 ± 0.04	-
0548−704	0.05 ± 0.02	0.06 ± 0.02	4 ± 2
DEM L316A	0.15 ± 0.04	0.16 ± 0.05	-
N 9	0.05 ± 0.02	0.05 ± 0.02	-
0534−699	0.034 ± 0.009	0.033 ± 0.009	-
DEM L238	0.009 ± 0.003	0.01 ± 0.003	-
DEM L249	0.04 ± 0.01	0.031 ± 0.008	-
0520−694	0.027 ± 0.007	0.033 ± 0.009	11 ± 3
DEM L204	0.008 ± 0.003	0.011 ± 0.003	-
0450−709	0.031 ± 0.008	0.035 ± 0.009	-
HP99498	0.019 ± 0.005	0.017 ± 0.005	-
DEM L218	0.023 ± 0.006	0.018 ± 0.005	-
N 23	0.05 ± 0.02	0.05 ± 0.02	4 ± 2
N 132D	0.08 ± 0.02	0.10 ± 0.03	-
N 157B	0.34 ± 0.09	0.29 ± 0.08	-
N 44	0.09 ± 0.03	0.11 ± 0.03	-
N 158A	0.13 ± 0.04	0.13 ± 0.04	-
N 206	0.05 ± 0.02	0.05 ± 0.02	-
N 120	0.08 ± 0.03	0.10 ± 0.03	-
N 49B	0.035 ± 0.009	0.04 ± 0.02	12 ± 4
N 49	0.12 ± 0.04	0.14 ± 0.04	6 ± 2
N 11L	0.07 ± 0.02	0.08 ± 0.03	4 ± 2
N 86	0.06 ± 0.02	0.04 ± 0.02	-
0453−685	0.019 ± 0.005	0.024 ± 0.007	-
N 63A	0.07 ± 0.02	0.07 ± 0.02	-
DEM L203	0.07 ± 0.02	0.08 ± 0.02	-
DEM L241	0.15 ± 0.04	0.15 ± 0.04	-
DEM L299	0.09 ± 0.03	0.10 ± 0.03	-
DEM L109	0.08 ± 0.03	0.07 ± 0.02	-
MCELS J0506-6541	0.025 ± 0.007	0.026 ± 0.007	-
0507−7029	0.031 ± 0.008	0.04 ± 0.01	-
0528−692	0.012 ± 0.004	0.013 ± 0.004	2.0 ± 0.8
DEM L214	0.0031 ± 0.0008	0.0033 ± 0.0008	-
0532−675	0.07 ± 0.02	0.07 ± 0.02	-
Honeycomb	0.05 ± 0.02	0.06 ± 0.02	10 ± 3
0536−6914	0.17 ± 0.05	0.15 ± 0.04	-
DEM L256	0.09 ± 0.03	0.08 ± 0.02	-
N 159	0.5 ± 0.2	0.4 ± 0.2	-
DEM L316B	0.15 ± 0.04	0.16 ± 0.05	-

to be continued on next page...

Table 4.5 – *Continued from previous page*

J0550−6823	0.05 ± 0.02	0.05 ± 0.02	-
B 0450−6927	0.14 ± 0.04	0.11 ± 0.03	-
0454−7005	0.012 ± 0.004	0.014 ± 0.004	-
DEM L214	0.009 ± 0.003	0.011 ± 0.003	-
MCELS J04496921	0.12 ± 0.03	0.10 ± 0.03	-
N 186D	0.05 ± 0.02	0.05 ± 0.02	-
0521−6542	0.04 ± 0.01	0.04 ± 0.02	-
MCELS J0448−6658	0.018 ± 0.005	0.020 ± 0.006	3.0 ± 0.8
N 4	0.05 ± 0.02	0.06 ± 0.02	-
RXJ0507−68	0.025 ± 0.007	0.028 ± 0.008	-
B 0528−7038	0.010 ± 0.003	0.017 ± 0.005	-
0538−693	0.08 ± 0.03	0.08 ± 0.02	-
0538−6922	0.08 ± 0.03	0.08 ± 0.03	-
B 0449−693	0.11 ± 0.03	0.12 ± 0.03	10 ± 3
J0508−6830	0.04 ± 0.02	0.08 ± 0.03	27 ± 7
J0511−6759	0.023 ± 0.006	0.028 ± 0.008	3.0 ± 0.8
J0514−6840	0.022 ± 0.006	0.021 ± 0.006	-
J0517−6759	0.05 ± 0.02	0.06 ± 0.02	-

4.3.4.1 How do these results compare with othere estimates from the literature

Similar results of the sputtered cold dust mass per SNR, of 2.7–6.1 $M_\odot$ is obtained by Temim et al. (2015), using the same *Herschel* data as we use in this work, but different techniques and models. Their destruction rates are close to these in our work and their dust lifetimes in SNR environment is similar to ours, (2–5)$\times 10^7$ yr. There are not many other observational estimates of the mass of the cold dust distroyed by SNRs in the literature, but there are many models how much dust is destroyed.

Bianchi & Schneider (2007) predict the survival of 2–20% of the initial dust mass survives the passage of the reverse shock, while an extreme model of Nath, Laskar & Shull (2008) predicts only 1–20% of the dust mass sputtered by the reverse shock. Nozawa et al. (2007) find the fraction of destroyed dust by the reverse shock from 0.2-1.0, depending on the energy and the density of the ISM. They believe that the small grains <0.05 μm are completely destroyed, grains 0.05-0.2 μm – trapped into the dense shell behind the forward shock, while very large grains $\gtrsim$0.2 μm are ejected into the ISM without decreasing their sizes significantly. However, most of these models consider

Table 4.6: Sputtered mass by known SNRs in LMC according to various methods (see text). The quoted errors on M_1 and M'_1 are the factor of 3 (see the text), the error for M_2 was estimated as the standard deviation of the data set, the errors for M'_2 were found as the confidence intervals of 1σ from the median of the dataset and the error of M_3 was found as the standard deviation of the obtained values of M_3 based on 50 runs.

ID	Method	Sputtered mass [$M_\odot$]
M_1	mean, good	390^{+780}_{-260}
M'_1	median, good	240^{+480}_{-160}
M_2	mean, all	-13.6 ± 47.5
M'_2	median, all	113^{+278}_{-125}
M_3	Monte Carlo	389 ± 22

young SNRs of ∼1000 years old, while in my work the mean age of the remnants for which ages are known (Table 4.2) is ∼14770 yr, while the rest of the objects are mostly older than that. Also, most of these models calculate survived ejecta mass after the passage of the reverse shock, while in this work I estimate the removal of interstellar dust in which the ejecta dust is contained.

In the modeling of galactic evolution (as in works of Dwek 1998, Dunne et al. 2011 and Zhukovska 2014), the mass of sputtered dust by SNRs is usually estimated by assuming SN rate and an amount of dust (or gas) removed by each SN. Therefore the work in this thesis chapter has implications for these models.

4.3.5 Thickness of the dust layer in the LMC

I can use the $N_{\rm out}$ and $N_{\rm in}$ values from Table 4.5 to estimate the thickness, d, of the dust layer within the LMC – and hence the average density – if I assume that all dust has been removed from within the SNRs. In that case, and assuming SNRs are spherical with diameter D and fully embedded within the dust layer, the volume in a column

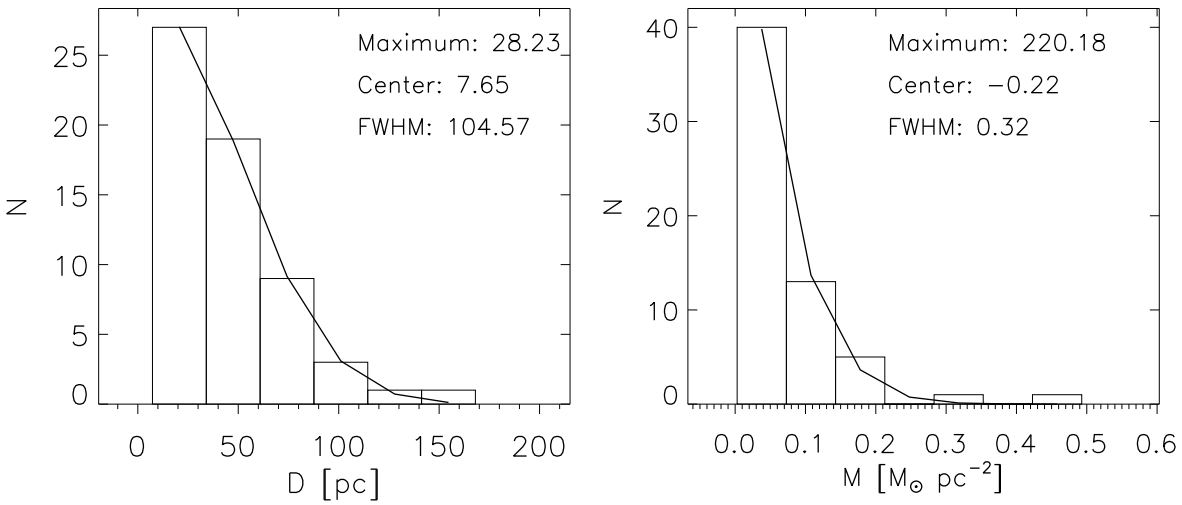

Figure 4.23: *Left:* Distribution of the diameters of the SNRs in my sample, fitted with a Gaussian curve. *Right:* Distribution of the column densities towards SNRs in my sample, fitted with a Gaussian curve.

with area $A = \pi(D/2)^2$ that contains dust is Ad outside the SNR and $Ad - \frac{4}{3}\pi(D/2)^3$ in the direction of the SNR. Dividing by A, I obtain column lengths of d and $d - \frac{2}{3}D$, respectively. Assuming a constant density, the inner and outer column densities would compare as $N_{\rm in}/N_{\rm out} = 1 - \frac{2D}{3d}$ and hence I could estimate a thickness of the dust layer in the LMC in pc,

$$d \;=\; \frac{2}{3}D\left(1 - \frac{N_{\rm in}}{N_{\rm out}}\right)^{-1}, \tag{4.15}$$

and average dust volume density $\rho = N_{\rm out}/d$ in $\mathrm{M}_\odot$ pc^{-3}.

I thus obtain a median value for the thickness of the dust layer within the LMC to be $d \sim 107$ pc.

4.3.6 The imperfections of the methods for the estimation of the removed dust in this work

Here we list the number of assumptions in this work which could significantly act to change the destruction timescales and the mass of dust destroyed that we derived in

Chapter 4.

1. The 100–500 μm SEDs of SNe and galaxies can be fit by a single modified blackbody, but though this is a physically inaccurate description of the dust emission, and the resulting dust masses from the SED fit are systematically too low by a factor of $\sim$2 (see Bendo et al. 2015 for a discussion) compared to what was expected when fitting modified blackbodies to components of the SED associated with different heating sources (e.g. two modified black bodies). Also assuming β =1.5 biases the dust mass to hotter dust (less mass).

2. As we said in Section 2.2.1, κ in this work is two times higher than in the literature (Draine & Lee 1984; James et al. 2002).The overestimation of κ for a factor of 2 implies that the mass in all calculations should be two times higher. Therefore, the sputtered dust by SNRs in LMC should be 746 $M_{\odot}$, sputtering rate would be $0.075^{+0.15}_{-0.05}$ $M_{\odot}$ yr^{-1}, which would yield the lifetime of dust in SNR environments of $9.78^{+19.56}_{-6.52}\times$ 10^6 yr, which is lower than the lifetime that we estimated before (2×10^7 yr).

3. The destruction timescale is estimated by assuming that all the dust removed by SNR is destroyed, but this can not be completely true. If grains are grown in SN or in the ISM, they are likely to be bigger and more resilient (>1 μm, Gall et al. 2014). Sputtering is likely to change the dust size distribution, but may not destroy all the dust (Bianchi & Schneider 2007). However, even if we assume that only 30% of dust removed by SNRs is actually destroyed, the dust lifetime would be $6.52^{+13.05}_{-4.35}\times10^7$ yr, which is still $\sim$2.5 times shorter than the timescale of dust formation in AGB stars of 500 Myr (Ventura et al. 2014), thus SNRs would still be the dust destroyers.

4. We are missing $\sim$40% of the remnants, and are not sure if there is some selection bias that would make the missing sources different to the ones in the known sample. It is possible that missing remnants are in the lower density, therefore

they could be destroying less dust. In that case, the sputtered masses would be still higher and the lifetime shorter than in the point 3.

4.4 Conclusions about the study of SNRs with *Herschel* and *Spitzer*

I presented the first FIR and submm analysis of the population of 61 SNRs in the LMC, based on *Herschel* images from the HERITAGE survey at 100, 160, 250, 350 and 500 μm in combination with *Spitzer* 24- and 70-μm images that were published before for some objects. These *Herschel* data allowed me to estimate the mass of the cold interstellar dust. I reach the following conclusions:

- Although the FIR/submm surface brightness of SNRs is very similar to the one of the ISM, it is slowly decreasing with time, meaning that SNRs cool down and/or dust is removed from them, or the dust is eroded. The radio surface brightness is somewhat correlated with that of the FIR/submm, as it was shown before by Gonçalves (2013).

- There is no evidence for large amounts of dust having formed and survived in SNRs. In fact, most of the dust seen in my maps seem to be pre-existing.

- The ISM is generally denser around core-collapse SNRs than type Ia, but significant variations are seen between individual SNRs of either type.

- SNRs sputter and heat cold interstellar dust by their hot plasma and shocks, which is evident from the maps of dust mass and dust temperature.

- The mass of sputtered dust for all SNRs in the LMC is estimated to be $\sim 373^{+746}_{-249}$ $M_\odot$; at a dust destruction rate of $\sim 0.037^{+0.074}_{-0.025}$ $M_\odot$ yr^{-1}, and thus the interstellar dust lifetime in the regions close to SNRs is $\sim 2^{+4}_{-1.3} \times 10^7$ yr.

- If SNRs are "empty" in terms of dust, then I estimate a typical thickness of the ISM dust layer within the LMC of ~ 107 pc.
- I conclude that it is unlikely that SNe/SNRs in the local Universe can resolve the observational conundrum of large dust reservoirs in high redshift galaxies since it seems that SNRs sputter more dust than they produce.

5 Synthesis of conclusions based on my work, and prospects for future work

5.1 Discussion of the results and their implications

5.1.1 The importance of the results from this thesis

There are two major important parts of this work. The first is about the submm and mm observations of SN 1987A, work that contributed to the unique scientific result about the $\sim$1 $M_{\odot}$ dust produced in SN ejecta that was observed with *ALMA* which at first glance implies SNe are significant dust producers. The second is the first observational estimation of the amount of sputtered dust by SNRs in one galaxy, the LMC. When these two effects are combined, it follows that in galaxies similar to LMC, in present time, SNRs do sputter more dust than they can produce. SNe and AGB stars still remain important creators of the chemical elements and dust in the Universe – that get to be reprocessed in the future formations of the stars and planets, but the effect that SNRs are possibly dust destroyers – at least for our sample in the LMC – could be important to account. This work could help to improve the understanding of the dust origin, destruction and the evolution in all galaxies. Maybe some alternative processes of dust creation need to be included to explain the origin of the dust both in the local Universe and high-z, such as within molecular clouds, or quasar outflows (Mattsson 2011) or in the ISM (Dunne et al. 2011; Zhukovska 2014).

5.1.2 The main implications of my work on SN 1987A

5.1.2.1 The first *APEX* and *ATCA* observations of SN 1987A

I have presented the observations of SN 1987A, from *ATCA* at 3.2 mm in 2005, and from *APEX* at 0.87 mm in 2007, that were publicly available. This was the first observation of a SN/SNR with *APEX* telescope and the first observation of that remnant at 3

mm. These data, together with new *Herschel* observations of Matsuura et al. (2011) – and later with *ALMA* (Indebetouw et al. 2014) – completing the gap in the spectrum between thermal and synchrotron components and revealing ∼1 $M_\odot$ of dust, at ∼22 K, connected to this object. The *APEX* data cover a similar wavelength range as the *Herschel* data in Matsuura et al. (2011), but provide significantly higher resolution than the *Herschel* long-wavelength observations. The *APEX* data were well fitted with the modified black body curve together with *Herschel* data. The *ATCA* data were lying on the extrapolation of the power law of other radio measurements, taken about the same time, and belonged to synchrotron radiation. However, the source was still not resolved.

My analysis of the *APEX* observations confirmed the measurements of Matsuura et al. (2011) and shown that the flux had not changed for more than ∼20% from the time of *APEX* to the time of *Herschel* observations (for ∼3 years). I estimated the upper limits on the presence of free-free emission in the ionized ejecta of this SNR to be ∼2 mJy.

5.1.2.2 The second *APEX* observations of SN 1987A

In mid-year 2011, we observed SN 1987A at 350 and 870 μm, with *APEX* telescope. The 350-μm image had superior angular resolution (∼8″) over that of the *Herschel* existing data (∼25″) and S/N was ∼8.5. The 870-μm observation (at ∼18″ resolution) was a repetition of the similar observations made in 2007. I showed that on these wavelengths the flux is not significantly changing on a timescale of ∼4 years. The achievement of my work was constraining all dust to be within 8″ (limited by the resolution of *SABOCA*), which strengthened the claims that the dust is in the ejecta. However, the source was still not resolved.

5.1.2.3 *ATCA* observations of SN 1987A at 3 mm

In mid-year 2011, I observed SN 1987A with *ATCA* at 3 mm with a 750B array configuration, with baselines between 61 and 765 m, and resolved it for the first time at this wavelength with a beam of 0.″7. The 3-mm detection is the faintest of all radio wavelengths and difficult to measure since it requires very good weather conditions. The radiation we detected was synchrotron radiation from the equatorial ring, characterised by moderately weak shocks. The flux density had doubled over the 6 years since the previous observations at 3 mm. The image had similar morphological characteristics as the other radio images and peaked on the Eastern part of the ring. I found no emission of different nature than the synchrotron, but the current limits do not rule out the presence of a pulsar, strong shocks or the dust in the centre of the remnant and I placed an upper limit of 1 mJy on any emission in the centre at 3.2 mm. If there is 1 mJy of the dust in the centre, at a temperature of 20 K, there could be $\sim$1.98 $M_{\odot}$ of dust (χ^2 =30.6; χ^2_{RED} =7.65; κ = 0.05 m^2 kg^{-1}; β =1.5; if the error at 3 mm is 20%). The large χ^2 suggests that it is not likely that there is dust at 3.2 mm having such high flux.

5.1.2.4 The importance of FIR, submm and mm observations of SN 1987A

Before *ALMA* data were available, my *APEX* and *ATCA* observations were the only ones to bridge the gap among FIR 350-μm and 0.8-cm radio observations, proving that the SN 1987A spectra can be well fit with a combination of a modified blackbody and power-law synchrotron model. My data contributed to the proposal and execution of *ALMA* observations. Also, my *ATCA* observations at 3 mm from 2011 still have better resolution than the ones from *ALMA* at that wavelength.

The FIR, submm and mm observations of SN 1987A provide the observational confirmation of the important scientific discovery of dust created in the ejecta of a SN. The produced mass of dust in this object ($\sim$0.7 $M_{\odot}$) is the highest mass ever observed in a SN/SNR, in agreement with many theoretical models (Kozasa et al. 2009; Nozawa

et al. 2003; Cherchneff & Dwek 2010; Todini & Ferrara 2001). 0.1−1 $M_{\odot}$ of dust per SN is required to form to explain the large dust content in high-z galaxies (Morgan & Edmunds 2003; Dwek, Galliano & Jones 2007; Gall, Hjorth & Andersen 2011; Rowlands et al. 2014). The only two other SNRs observed to have produced sufficient amounts of dust so that SNe can be dust suppliers at high-z are the young Crab nebula (Gomez et al. 2012b) and Cas A (Rho et al. 2008; Dunne et al. 2009; Barlow et al. 2010). On one hand, that gives proof for more similar objects to exist in the Universe, so that SNe can be important dust producers, but on the other hand exposes the problem of the non-detection of similar objects, opening the question why do we not detect them. Are dust producers special objects, are there selection effects causing us to systematically miss them, or does the dust in such objects have a short lifetime? The next decades will give us the answer.

Observations of a large mass of dust formed in SN 1987A caused many astronomers to keep researching dust properties of SNe/SNRs and the whole of this field of astronomy became more developed.

5.1.2.5 The future of SN 1987A and other SNe research

It will be interesting to observe SN 1987A in the following decades and centuries, to see if and when the dust properties will change. It is not known whether the dust in the ejecta was formed very soon after the explosion, within the next couple of years, or if this process still lasts and is continuous to this day. It would be important to confirm if the reverse shock is already in the equatorial ring (as it is believed) and how fast is it; perhaps in a decade or so it might be destroying some part of the dust in the ejecta (which will be more spread in the following years). On the other hand, the reverse shock might come later, as it is the case of Cas A (which is $\sim$ 300 yr old and its reverse shock is still bright and visible, less than half way toward the centre), and that might give us the chance to observe the evolution of the untouched dust in the next $\sim$100 years.

One of the expected directions is looking for a PSR or NS in SN 1987A – there

is not much known about young PSRs and there are not many of them in the neighborhood. There will be further research about the dust composition and evolution in SN 1987A, as this object is unique to observe dust formation (or removal). Monitoring of evolution at all wavelengths is expected because young objects conserve more information about the explosion and have faster evolution. There were some indications of possible sputtering of warm dust (Bouchet et al. 2006), while Dwek et al. (2010) noticed the increase in the flux of this object, but not yet the production of new dust.

Although our current understanding over the last $\sim$ ten years, based on observations of various galaxies suggests that an average SN produces 10^{-4}–10^{-2} $M_{\odot}$ of warm dust, which is too low to explain the formation of dust at high redshifts (Kotak et al. 2006; Silvia, Smith & Shull 2010), that does not mean that CC SN/SNRs do not produce significant (0.1–1 $M_{\odot}$) of dust for the two reasons: 1) the SNe studies are limited to MIR observations, and therefore cannot see the cold dust (<60 K) which dominates the dust mass. The cold dust is not visible in MIR data and can be as much as 10 – 1000 times larger in mass, as demonstrated with Crab, Cas A and SN 1987A (Gomez et al. 2012b; Barlow et al. 2010; Lakićević et al. 2012a). Therefore these studies could be providing only lower limits on the mass only. 2) These SNe studies are limited to the fact they only consist of young SNe (<3 yr old) and it is well known that significant dust mass is only seen in much older remnants (>20 yr; – Gall et al. 2014; Wesson et al. 2015). Therefore, it is important to continue research into dust in SNe/SNRs to understand the life cycle of dust in these objects.

The SNe dust research will be continued by monitoring the dust evolution according to SN type and host galaxy. With the advantage of *ALMA*, *APEX*, and future FIR research further details about the dust properties, formation, composition, duration of formation and survival in SN/SNRs will be revealed. The first remnant in the MCs that could show cold dust formed in the ejecta is E0102 because it is young ($\sim$2000 yrs), oxygen rich remnant, with a massive progenitor (Van der Heyden, Bleeker & Kaastra 2004), the reverse shock has only propagated through the outer layers of the ejecta (Finkelstein et al. 2006) and warm dust in the ejecta is already observed (Stanimirović et al. 2005).

The conditions in the early Universe were probably quite different from those in the local Universe. So far, the problems with the explanation of the dust at high redshifts have already produced a series of studies of alternative sources of dust, other than SNe and AGB stars, such as grain growth in the interstellar medium (Elvis, Marengo & Karovska 2002; Michalowski et al. 2011; Pipino et al. 2011; Dunne et al. 2011; Zhukovska 2014).

5.1.3 The main implications of the FIR and submm study of SNRs in LMC

5.1.3.1 The conclusions from FIR and submm study of SNRs in LMC

For the first time I have presented a FIR/submm analysis of the population of 61 SNRs in LMC, based on *Herschel* images from the *HERITAGE* survey, at 100, 160, 250, 350 and 500 μm, in combination with *Spitzer* 24- and 70- μm images from the *SAGE* survey. The long-wavelength data (100–500 μm) allowed me to create the mass and temperature maps of the cold dust towards the LMC, by fitting the SEDs of all SNRs and their surroundings (cold dust is $\simeq$90% of the dust mass in most galaxies; Dunne & Eales 2001).

Most of the dust seen in *Herschel* images is pre-existing interstellar dust. There is no evidence for large amounts of dust having formed and survived in SN/SNRs. These mass and temperature maps reveal heating and removal of dust by the SNR, therefore I concluded that SNRs sputter (and heat) significant amounts of interstellar dust. I presented the first crude and quantitative observational analysis of that dust sputtering by a whole population of SNRs in one galaxy.

The amount of sputtered dust for all SNRs in LMC is estimated to be $\sim 373^{+746}_{-249}$ $M_\odot$; at a dust destruction rate of $\sim 0.037^{+0.074}_{-0.025}$ $M_\odot$ yr^{-1}; while the interstellar dust lifetime in the regions close to SNRs can be $\sim 2^{+4.0}_{-1.3} \times 10^7$ yr. This result would be even easier to notice if SNRs were in denser environments, because the dust removal mass would increase and the effects of SNRs on their environments would be more visible in

the mass and temperature maps.

If SNRs are "empty" in terms of dust, then I estimate a typical thickness of the ISM dust layer within the LMC of ~ 107 pc.

The surface brightnesses of SNRs at FIR and submm wavelengths are somewhat decreasing with diameter/time, since SNRs cool down and perhaps dust erodes. The radio surface brightness is weakly correlated with that of the FIR (c. corr. of 0.5-0.6).

From submm data we can have an insight in the possible SNR environment because the mass maps do not always identify dust that is close/within the SNRs, but can be some foreground or background dust. The ISM is generally denser around core-collapse SNRs than around type Ia, but significant variations are seen between individual SNRs of either type. According to a K-S test, there is 98.4% chance that CC and Ia SNRs are in different environments. From mass maps we can not determine the SNR type because there are outliers in both CC and Ia datasets.

5.1.3.2 Concluding remarks

Future FIR observations will be used to re-calculate the results of dust sputtering in the LMC and refine theoretical estimates. I expect that new methods will be invented for the research of dust sputtering, not only by SNRs, but also possibly by other objects such as AGNs, stars, novae, intense X- and/or $\gamma-$ray radiation and not only using dust mass maps but possibly based on observations of CO or H I or other methods. It would be interesting to check if some dust from the SN environment is sputtered immediately after the SN explosion.

In this work and in the work of Gordon et al. (2014) dust mapping is performed, which is different from the traditional method of detection of an object. Dust mass/temperature mapping is used in many astrophysical studies, like H II regions, dark clouds, galaxies etc. In my study of SNRs the indication that the SNR has interacted with dust was the lack of dust and slightly warmer temperature present within the remnant. The most useful were young objects surrounded by plenty of dust, since their imprints on the dust were clearly detected and they helped me to interpret and

understand these data as it shown in Chapter 4. These mass/temperature maps show that the brightness does not always mean that the object is too massive, it can be just warm and dense enough (like the 'blob' of N 49). On the contrary, SN 1987A had about the same temperature as ISM in the LMC, but it was detected with *Herschel* because it was denser and physically distinguishable from the interstellar background. Also I discovered that some SNRs that are not detected at FIR/submm are often visible on the flux ratio maps.

It is well-expected that SNRs will have an effect on the global structure of the ISM in various ways, although it is a surprise finding that some objects that are not even directly visible on the FIR/submm images have such big impact. Though, it would be very important to explore the dust sputtering in a bigger sample of SNRs, in other galaxies, with better resolution and perhaps in higher dust density environments.

5.2 Future plans

5.2.1 Paper in preparation and other possible projects

The next project that I will work on is my *NTT (New Technology Telescope)* observations of MC SNRs from 2011, collected at the European Southern Observatory, La Silla Observatory, Chile (ESO No 87.D-0402), with the *SOFI* instrument. The *NTT* telescope is a 3.6 m optical and IR telescope, consisting of the *SOFI* and *EFOSC2* instruments. *SOFI* contains the infrared spectrograph and imaging camera, having the field of view of $4.92'$ and covering the wavelength range from 0.9–2.5 μm.

We observed with [Fe II], [H_2], Br_γ and continuum near-IR (NIR) narrow band filters together with H and K broad band filters in the following SNRs in the MCs: N 49 (0525–66.1), N 63A (0535–66.0), SN 1987A, N 132D (0525–69.6), E0102 (IKT 22; E0102–72.3), B0540–69.3 (N 158A), IKT 16 (0056–72.5), B0104–72.3 (IKT 25) and IKT 6 (0049–73.6) and detected in some of these lines 5 LMC SNRs and one SMC SNR, but continuum emission was found in all young SNRs including E0102. The res-

olution we obtain in this imaging is 0.7″–1.75″. The images of N 63A in Br_γ, [Fe II] and [H_2] lines are shown in Fig. 5.1a, b and c, respectively; while images of N 49 are given in the same order in Fig. 5.2, images of SN 1987A in Fig. 5.3 and the [Fe II] image of N 132D is in Fig. 5.4, top. The image of PWN B0540–693 in [Fe II] is given on Fig. 5.5, top, while the image of B0104–72.3 in [H_2] is shown on Fig. 5.5, bottom.

In many studies [Fe II]/Br_γ ratio is used for the estimations of the shocks velocity and the density and as the discriminant between collisionaly excited gas by shock and photo-ionised gas, since at H II regions this ratio is ∼0.06, while in most of SNRs is >30 (Graham, Wright & Longmore 1987; Koo et al. 2007).

H_2 ro-vibrational emission at 2.12 μm is probing the circum-burst medium, which is collisionaly excited by the SNR (Koo et al. 2007), and it provides the view of the coldest (but excited) structures, bound to progenitor mass loss and the impact of SNRs on the ISM. [Fe II] at 1.64 μm traces the ejecta from the supernova and/or the ionized iron in circumstellar material. Koo (2014) identified two groups of SNRs bright in [Fe II] emission: middle-aged SNRs interacting with molecular clouds (they are also often detected in H_2 line) and young CC SNRs in dense circumstellar medium. The Br_γ hydrogen recombination line at 2.17 μm maps cooling atomic gas in the SNR shocks and ISM.

While on Fig. 5.5, top we detect [Fe II] from ∼4″ PWN B0540–693 (already observed in J, H and Ks bands by Mignani et al. 2012, with resolution of ∼0.16, 0.12, and and 0.11″, respectively, who even resolved the pulsar itself), it is likely that radiation from the gas at these lines in in N 49, N 63A and B0104–72.3 is from the circumstellar shells from various phases of progenitors (RSG or other post-main sequence star) or perhaps from the ISM, as it is seen for some Galactic SNRs (Graham, Wright & Longmore 1987; Graham, Wright & Longmore 1989; Koo et al. 2007; Koo, Lee & Moon 2007; Lee et al. 2009; Lee et al. 2011). However, the radiation of [Fe II] is from the ejecta in case of SN 1987A and perhaps N 132D. In the case of the N 132D image in [Fe II] (Fig. 5.4, top), interesting shell-like emission is seen, which implies it should be from the ejecta of this SNR. When I compare my image with the images from Vogt & Dopita (2011) (Fig. 5.4, bottom), I find that the brightest part of [Fe II] filaments cor-

respond to optical [O III] and especially H_β emission. Although they claim that [O III] is from the ejecta, they believe that H_β emission has to be from the ISM. Therefore, we do not know yet if the [Fe II] from our image originates from the ejecta, or from the ISM or CSM.

Although there are many spatial congruences between the emission of these three lines in the case of N 49 (while it is clear that H_2 is probably from the cloud that the remnant interacts with), in the cases of N 63A and SN 1987A there are some similarities, but also many differences between the places of the emission of these lines, especially in the case of H_2.

One of my next projects could be to carry out a similar study to this work in the SMC and I hope that I will soon study some Galactic SNR using FIR data.

I am also interested to investigate if there is any spatial correlation or anti-correlation between *Herschel* data and radio data, knowing the well known relationship with dust detected with *Spitzer* and *Herschel* and radio data (Seok et al. 2008 and that I have shown in Section 4.2.1). The FIR-radio correlation might exist only because of the density of the particles that radiate; while it is unexplored how that correlation behaves in the SNRs and other parts of LMC, and how the synchrotron radiation contribute to FIR and submm radiation of these objects.

5.2.2 Proposals that we (will) write connected to this field

One (not accepted) proposal (PI: van Loon) is to observe N 49 with *ALMA*, because the results of my analysis of *Herschel* data show that a lot of dust has been sputtered by that object and because Otsuka et al. (2010) had connected it with 10 $M_\odot$ of dust (which is the highest dust mass that one SN/SNR has ever been matched with) from

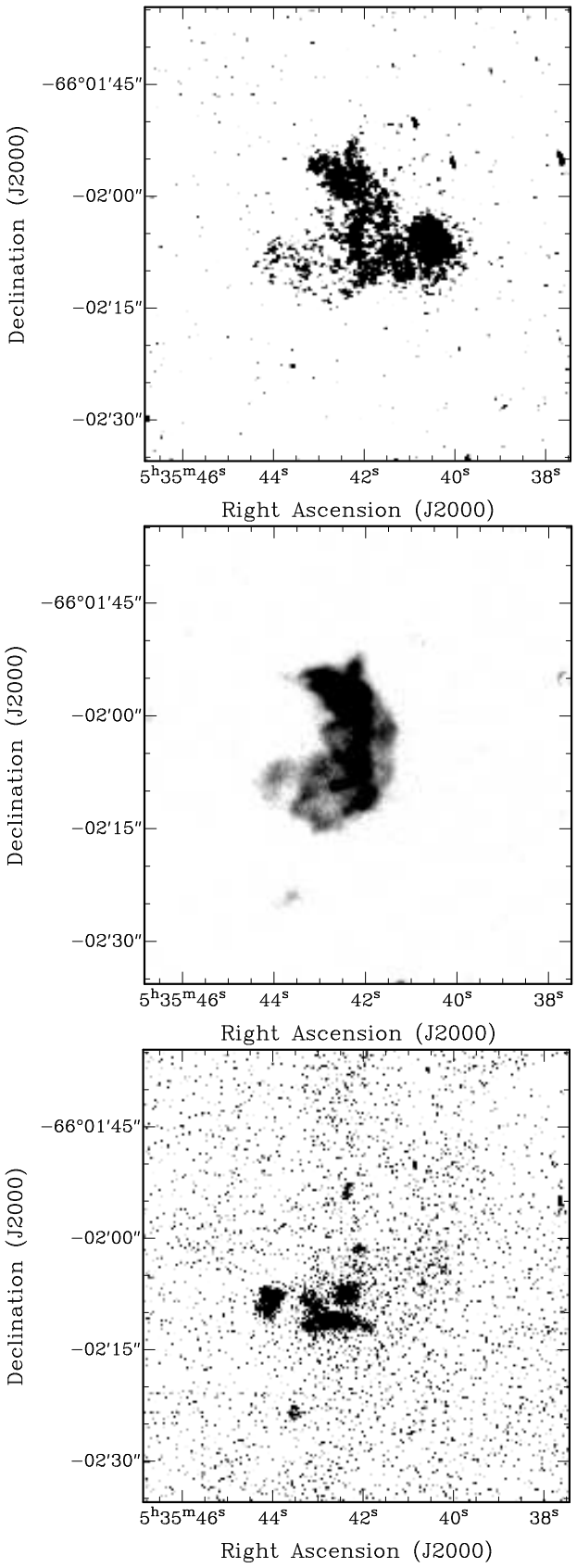

Figure 5.1: The *NTT, SOFI* images of SNR N 63A in *a:* Br_γ, *b:* [Fe II], *c:* H_2.

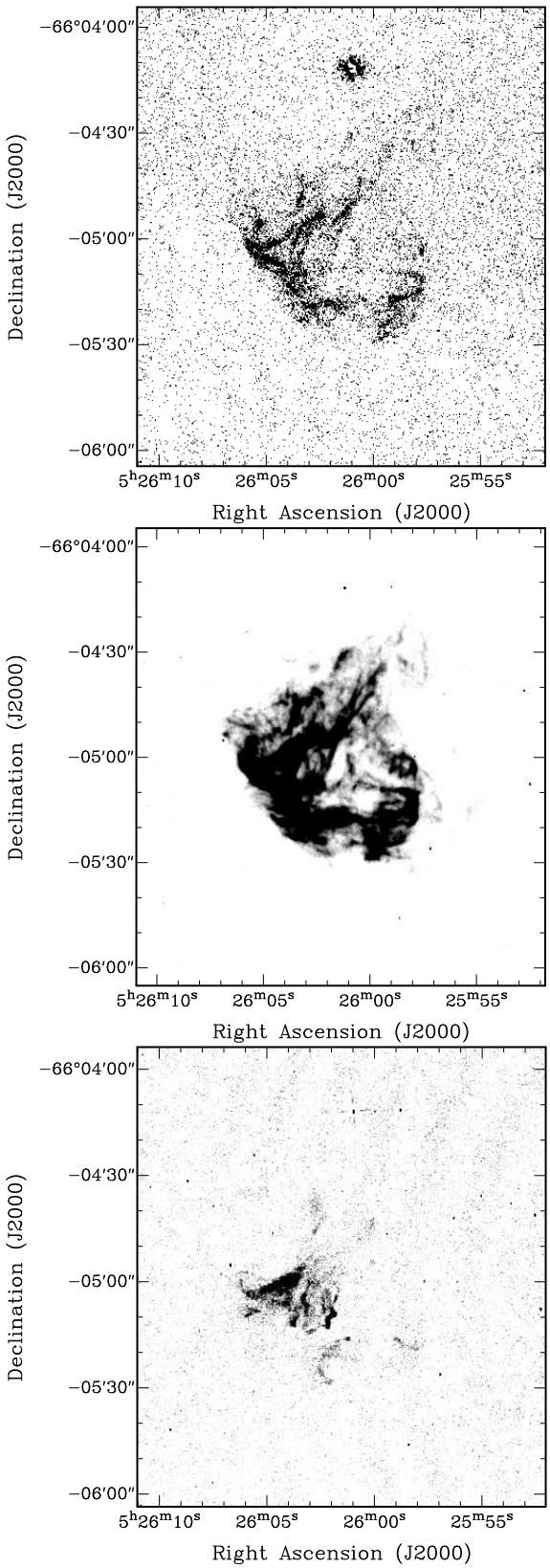

Figure 5.2: The *NTT, SOFI* images of SNR N 49 in *a:* Br_γ, *b:* [Fe II], *c:* H_2.

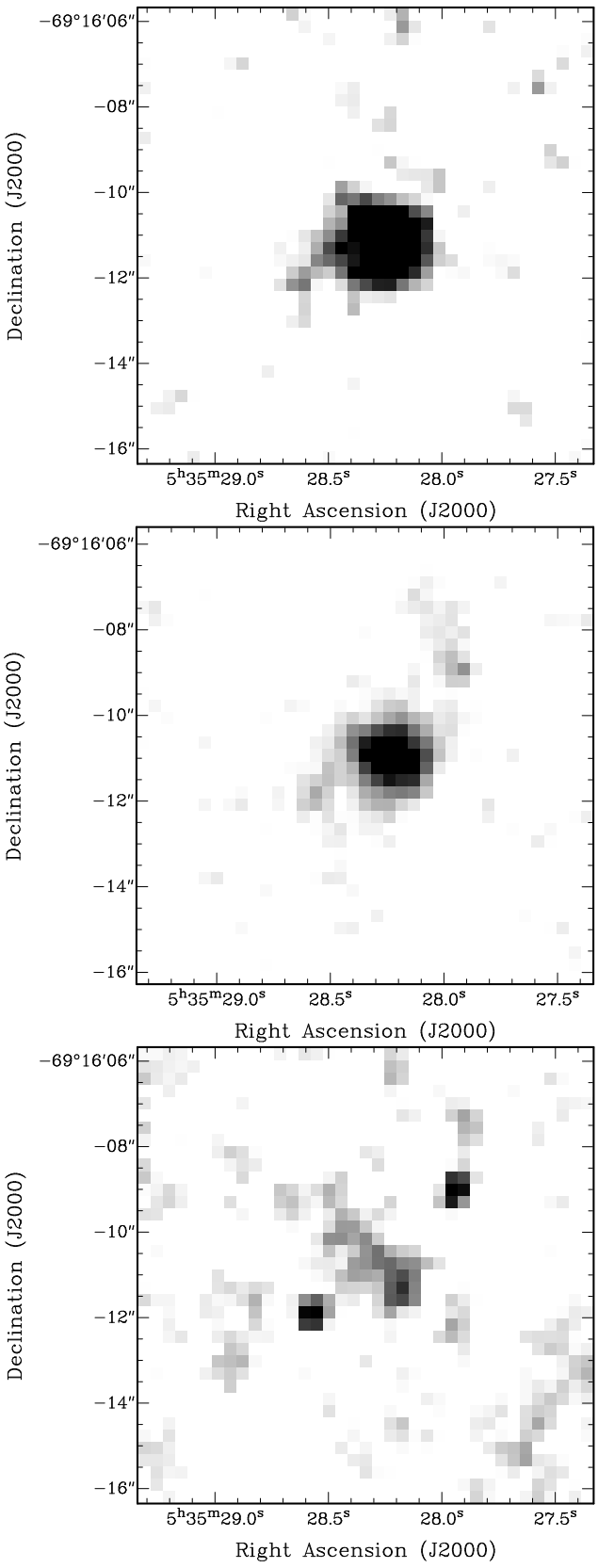

Figure 5.3: The *NTT, SOFI* images of SN 1987A in *a:* Br_γ, *b:* [Fe II], *c:* H_2.

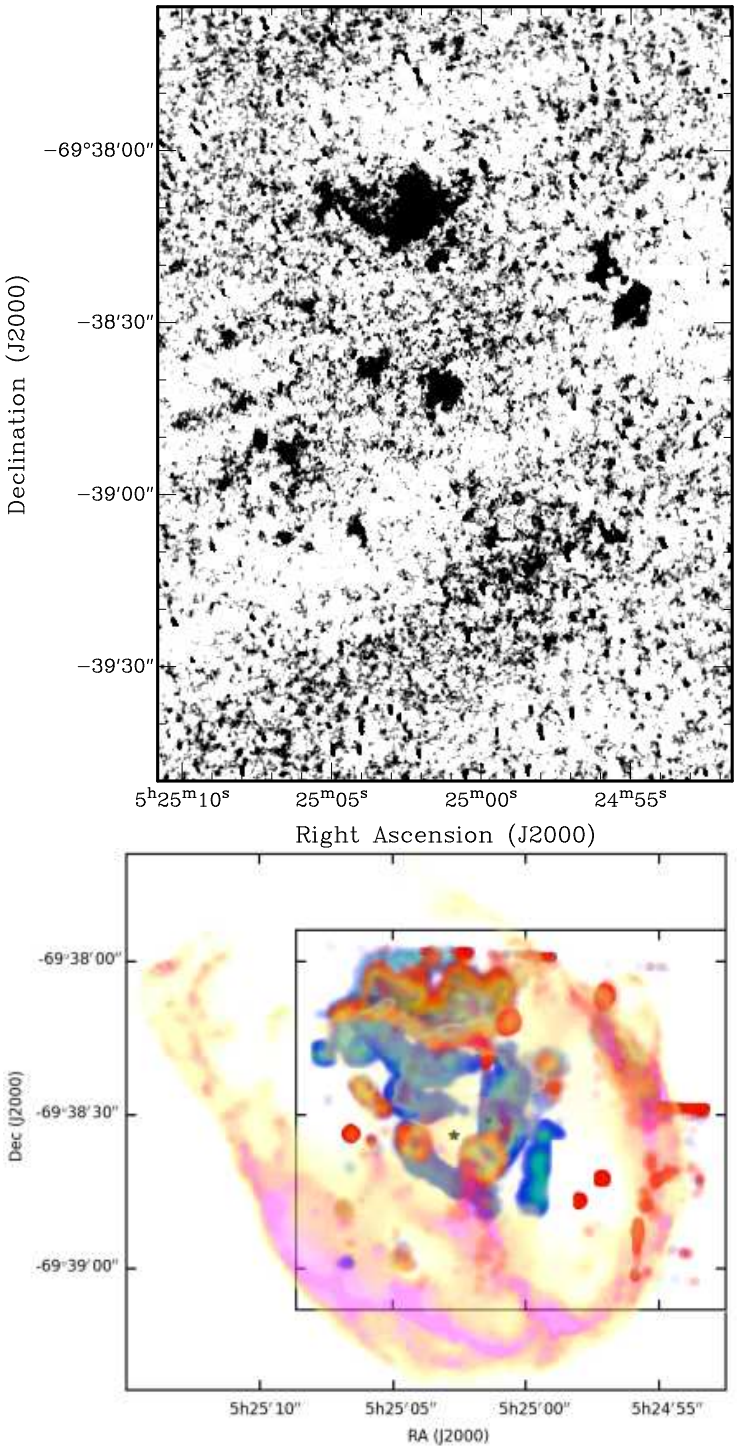

Figure 5.4: *Top:* The *NTT, SOFI* image of SNR N 132D in [Fe II]. *Bottom:* Chandra X-ray observation of SNR N 132D (in background) overlaid with the [O III] (blue-green) and H_β (yellow-red) emission (image taken from Vogt & Dopita 2011).

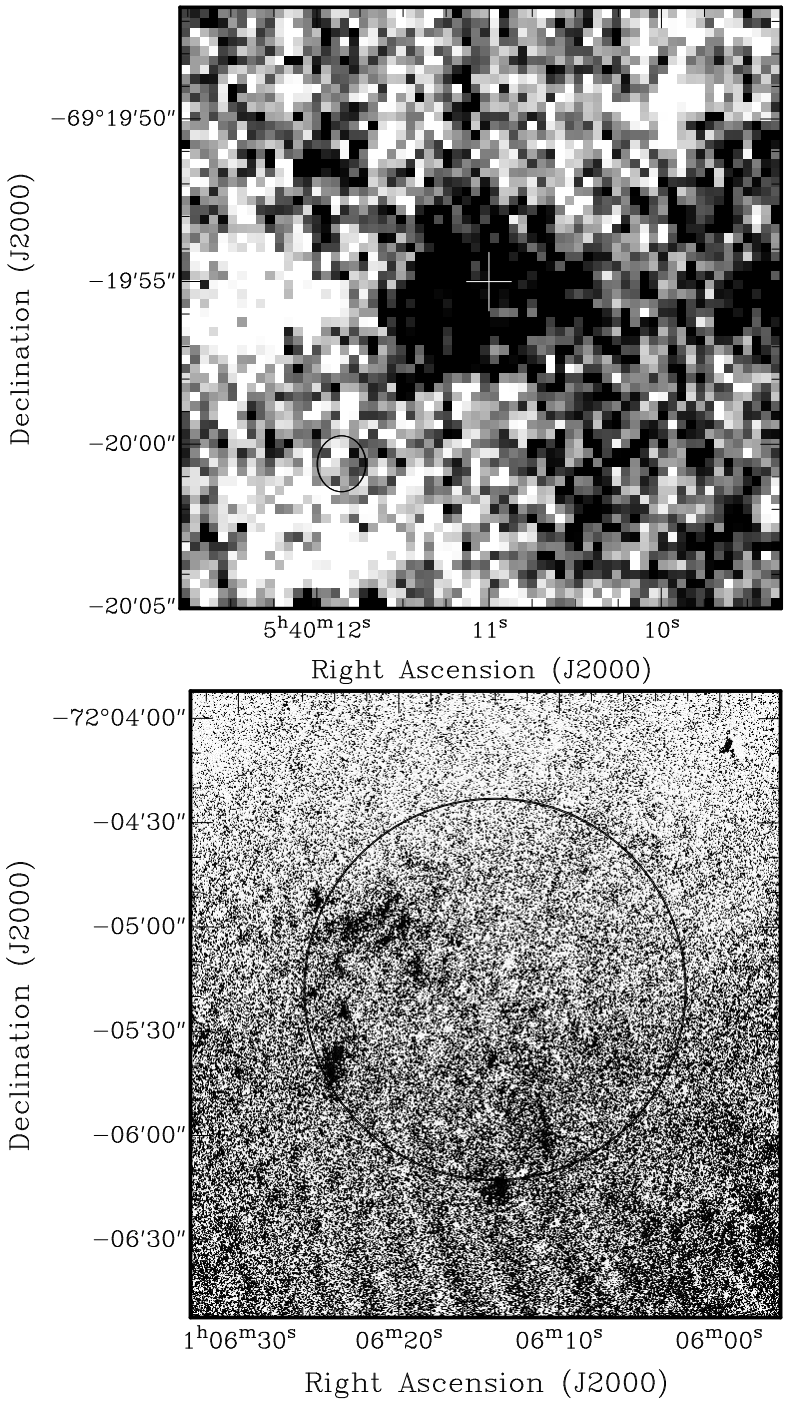

Figure 5.5: *Top:* The *NTT, SOFI* image of PWN in SNR B0540–693 in [Fe II]. *Bottom:* The *NTT, SOFI* image of SNR B0104–72.3 in H_2.

the molecular cloud with which the remnant is interacting. By imaging CO v = 0, $J = 2 \rightarrow 1$, we wanted to explore the unique case of the collision of this SNR with a bright molecular cloud, to reveal morphological indicators of interaction (compressed fronts, correspondence with filamentary structure on the SNR shell...). Observing of CO v = 0, $J = 1 \rightarrow 0$ would map undisturbed molecular material and form a reference against which to measure the excitation of CO into the $J = 2$ level. Finally, we wanted to estimate the amount and location of sputtered dust based on SiO v = 0, $J = 2 \rightarrow 1$ emission, since we believe that it arises from the products of sputtered small grains.

Also, we plan to write proposals to observe some MC SNRs with *APEX*.

5.3 Next 10 years

The *James Webb Space Telescope (JWST)* will observe MIR emission of SNRs at better resolution than *Spitzer*, with diameter of 6.5 m and the resolution from 0.024″ at 0.6 μm to 1.104″ at 28.5 μm. *JWST* will be one to two orders of magnitude more sensitive than current or recent NIR and MIR instrumentation (http://www.stsci.edu/jwst/science/sensitivity). It will observe molecular line emission, fine-structure lines, PAH, look into SNe/SNR details, give more information about the temperature, shocks, warm dust production and sputtering, following-up the existing *Spitzer* and *AKARI* data.

Observations with *ALMA*, *APEX* and other submm telecopes will look more deeply into the production and the sputtering of the dust by SNe and SNRs – investigating the composition, time scales, how much of the produced/interstellar dust survives the shocks and becomes the base for the formation of molecules; how do the elements and dust integrate in the interstellar environment to form molecules, stars and planetary systems and if there is some other important process of forming the dust in the Universe that we do not know of. Is it possible to connect the type of SN or the type of the galaxy with the amount and/or the composition of dust that it produced/sputtered? What happens when the dust is removed?

It is time to make radio surveys again, with better resolution than the one for

the last SMC survey (>12″ – Filipović et al. 2005, Filipović et al. 2008), to reveal more details about SNRs and compare the data with the observations from ∼50 years ago. There is a strong need to complete a homogeneous radio survey of LMC SNRs, since no such catalogue currently exists.

Will the reverse shock of SN 1987A come to the ejecta in the near future or in >300 years like in Cas A? Will the amount of dust in the ejecta and in the ring increase or decrease in the future and until when? Will some future observations of SNR N 49 in FIR resolve some detailed characteristics and will we finally understand its interaction with the 'blob'? Will other observations confirm my conclusions about the dust sputtering? The dust sputtering needs to be more explored.

Is there a better way to do the population study of dust sputtering than I have done in this thesis? Is it possible to do it in the Milky Way or some other galaxy? Since the submm data are new, they deserve to be continuously monitored in detail in order to notice any small changes, in any type of object.

Publications

Refereed

- Lakićević, M., van Loon, J.Th., Patat, F., Staveley-Smith, L., Zanardo, G., 2011, A&A, 532, L8.

- Lakićević, M., van Loon, J.Th., De Breuck, C., Patat, F., 2012, A&A, 541, L1.

- Lakićević, M., Zanardo, G., van Loon, J.Th., Staveley-Smith, L., Potter, T., Ng, C.-Y., Gaensler B. M., 2012, A&A, 541, L2.

- Matsuura, M., Dwek, E., Meixner, M., Otsuka, M., Babler, B., Barlow, M.J., Roman-Duval, J., Engelbracht, C., Sandstrom., K., Lakićević, M., van Loon, J.Th., Sonneborn, G., Clayton, G.C., Long, K.S., Lundqvist, P., Nozawa, T., Gordon, K.D., Hony, S., Panuzzo, P., Okumura, K., Misselt, K.A., Montiel, E., Sauvage, M., 2011, Science, 333, 1258.

- Kamenetzky, J., McCray, R., Indebetouw, R., Barlow, M. J., Matsuura, M., Baes, M., Blommaert, J. A. D. L., Bolatto, A., Decin, L., Dunne, L., Fransson, C., Glenn, J., Gomez, H. L., Groenewegen, M. A. T., Hopwood, R., Kirshner, R. P., Lakićević, M., Marcaide, J., Marti-Vidal, I., Meixner, M., Royer, P., Soderberg, A., Sonneborn, G., Staveley-Smith, L., Swinyard, B. M., Van de Steene, G., van Hoof, P. A. M., Th. van Loon, J., Yates, J., Zanardo, G., 2013, ApJL, 773, L34.

- Indebetouw, R., Matsuura, M., Dwek, E., Zanardo, G, Barlow, M. J., Baes, M., Bouchet, P., Burrows, D. N., Chevalier, R., Clayton, G. C., Fransson, C., Gaensler, B., Kirshner, R., Lakićević, M., Zanardo, G., van Loon, J.Th., Staveley-Smith, L., Potter, T., Ng, C.-Y., Gaensler B. M., Long, K. S., Lundqvist, P., Marti-Vidal, I., Marcaide, J., McCray, R., Meixner, M., Ng,

C.-Y., Park, S., Sonneborn, G., Staveley-Smith, L., Vlahakis, C., van Loon, J., 2014, ApJL, 782, L2.

- Zanardo, G., Staveley-Smith, L., Indebetouw, R., Gaensler, B. M., Baes, M., Barlow, M. J., Chevalier, R. A., Fransson, C., Kamenetzky, J. R., Lakićević, M., Lundqvist, P., Marcaide, J., Marti-Vidal, I., Matsuura, M., Meixner, M., Ng, C.-Y., Park, S., Sonneborn, G., Spyromilio, J., van Loon, J. Th., 2014, ApJ, 796, 82.

- Lakićević, M., van Loon, J. Th., Meixner, M., Gordon, K., Bot, C., Roman-Duval, J., Babler, B., Bolatto, A., Engelbracht, C., Filipović, M., Hony, S., Indebetouw, R., Misselt, K., Montiel, E., Okumura, K., Panuzzo, P., Patat, F., Sauvage, M., Seale, J., Sonneborn, G., Temim, T., Urošević, D., Zanardo, G., 2015, ApJ, 799, 50.

A FIR atlas of SNRs in the Large Magellanic Cloud: maps of dust mass and temperature

Here I give the continuation of maps of dust mass and temperature in and around SNRs in the LMC made using *Herschel* images at 100−500 μm, that are presented in Section 4.2.4. For each remnant on the left side is the mass map and on the right side the temperature map. The main conclusion based on these maps was that the SNRs sputter and heat up the dust.

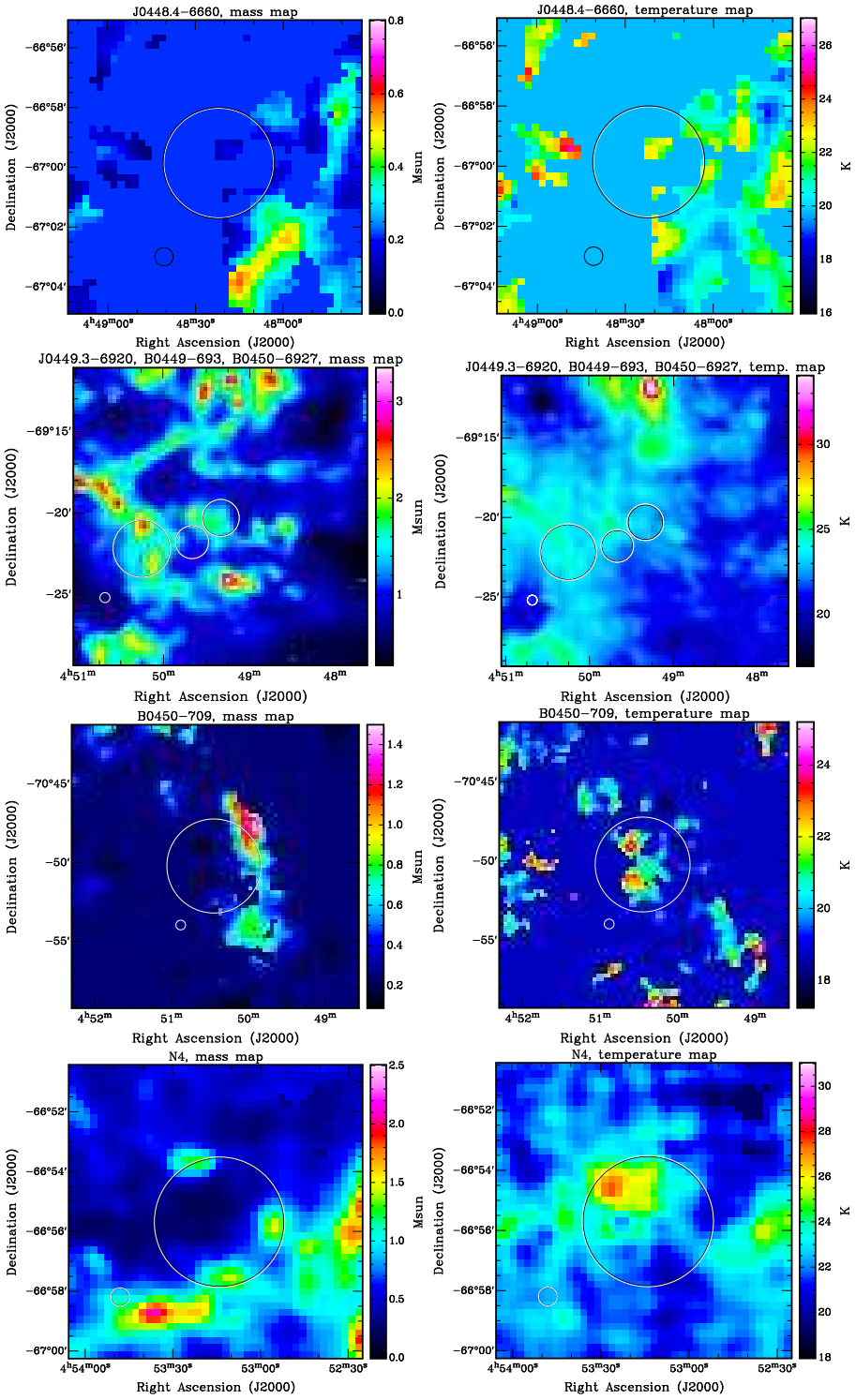

Figure A.1: *Left:* dust mass maps; *Right:* dust temperature maps. *a* and *b:* J0448 −6658; *c* and *d:* J0449.3−6920 (center of the image), B0449−693 (circle in the middle) and B0450−6927 (on the left); *e* and *f:* B0450−70.9; *g* and *h:* N 4.

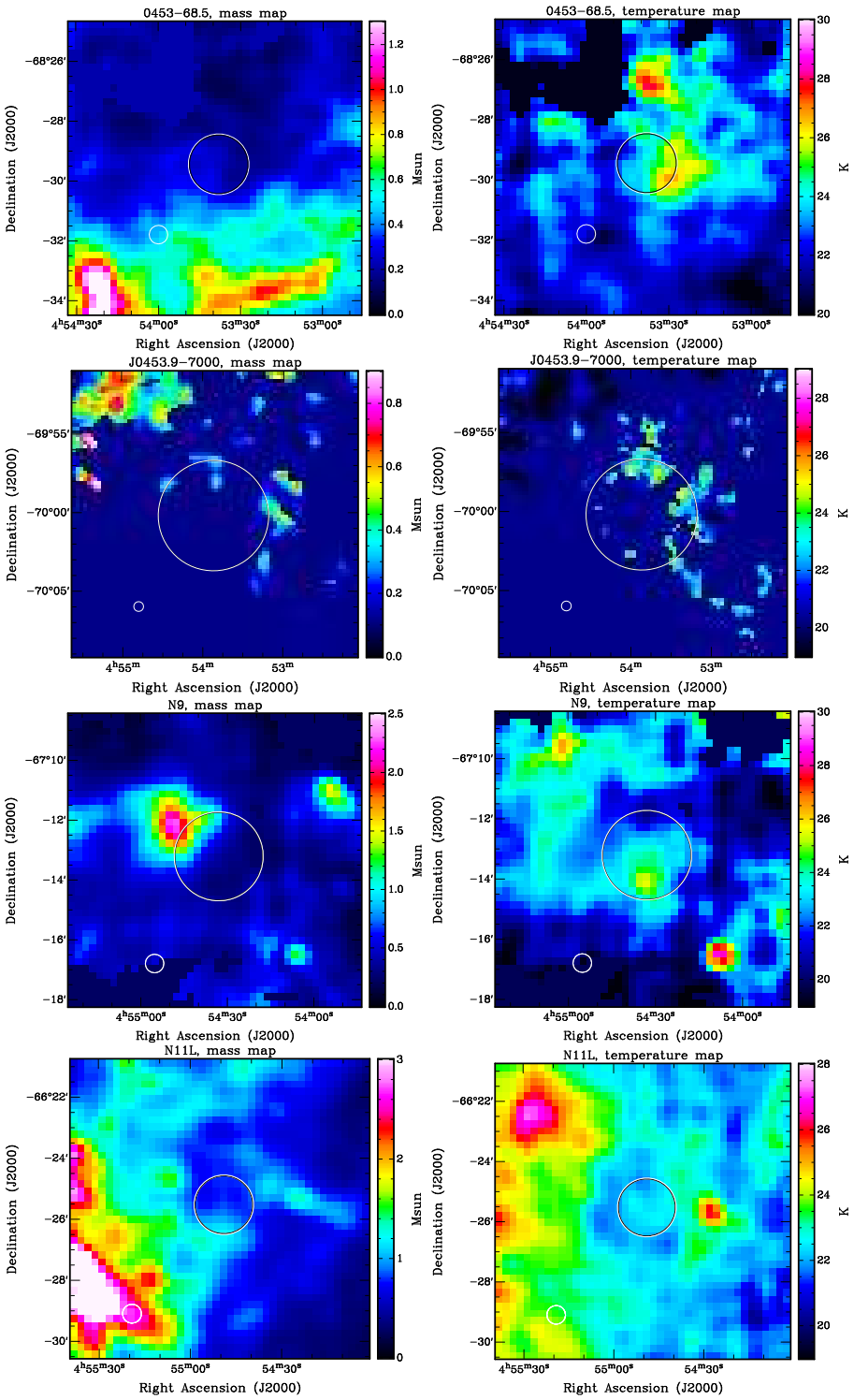

Figure A.2: SNR 0453−68.5, and SNR J0453.9−7000, SNR N 9, and SNR N 11L.

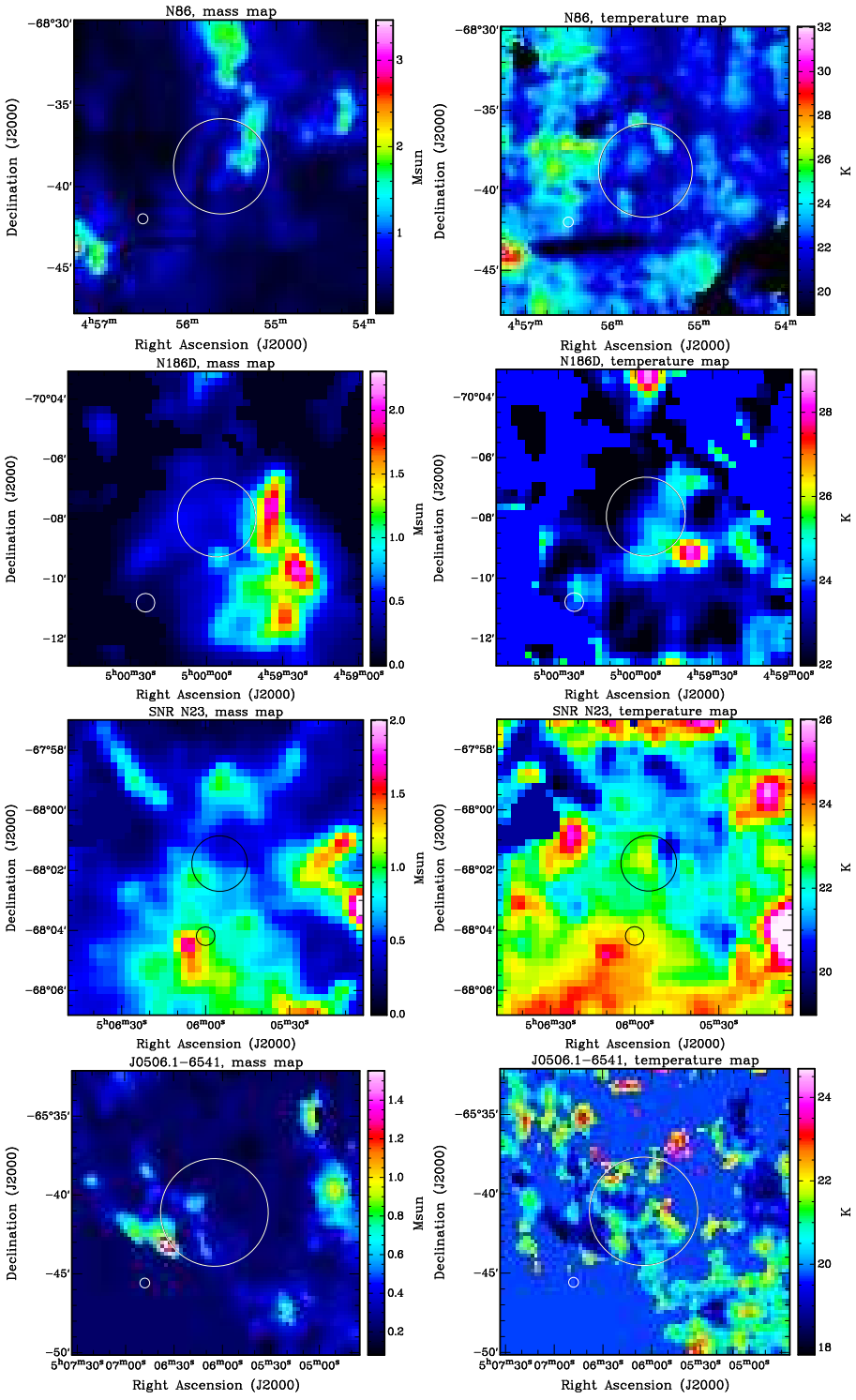

Figure A.3: SNR N 86, N 186D, N 23 and J 0506−6541.

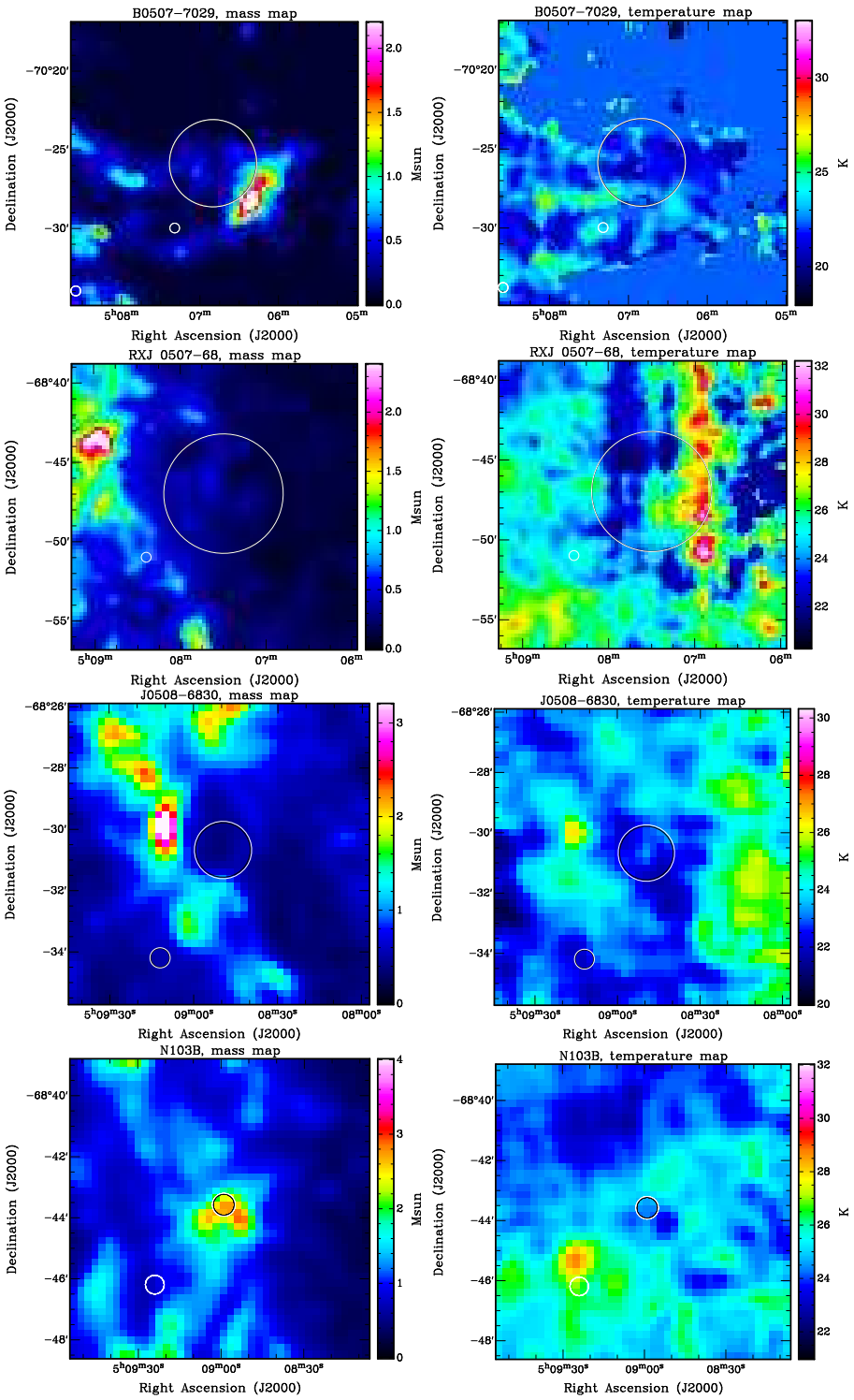

Figure A.4: SNR B 0507−7029, SNR RXJ0507−68, J 0508−6830 and N 103B.

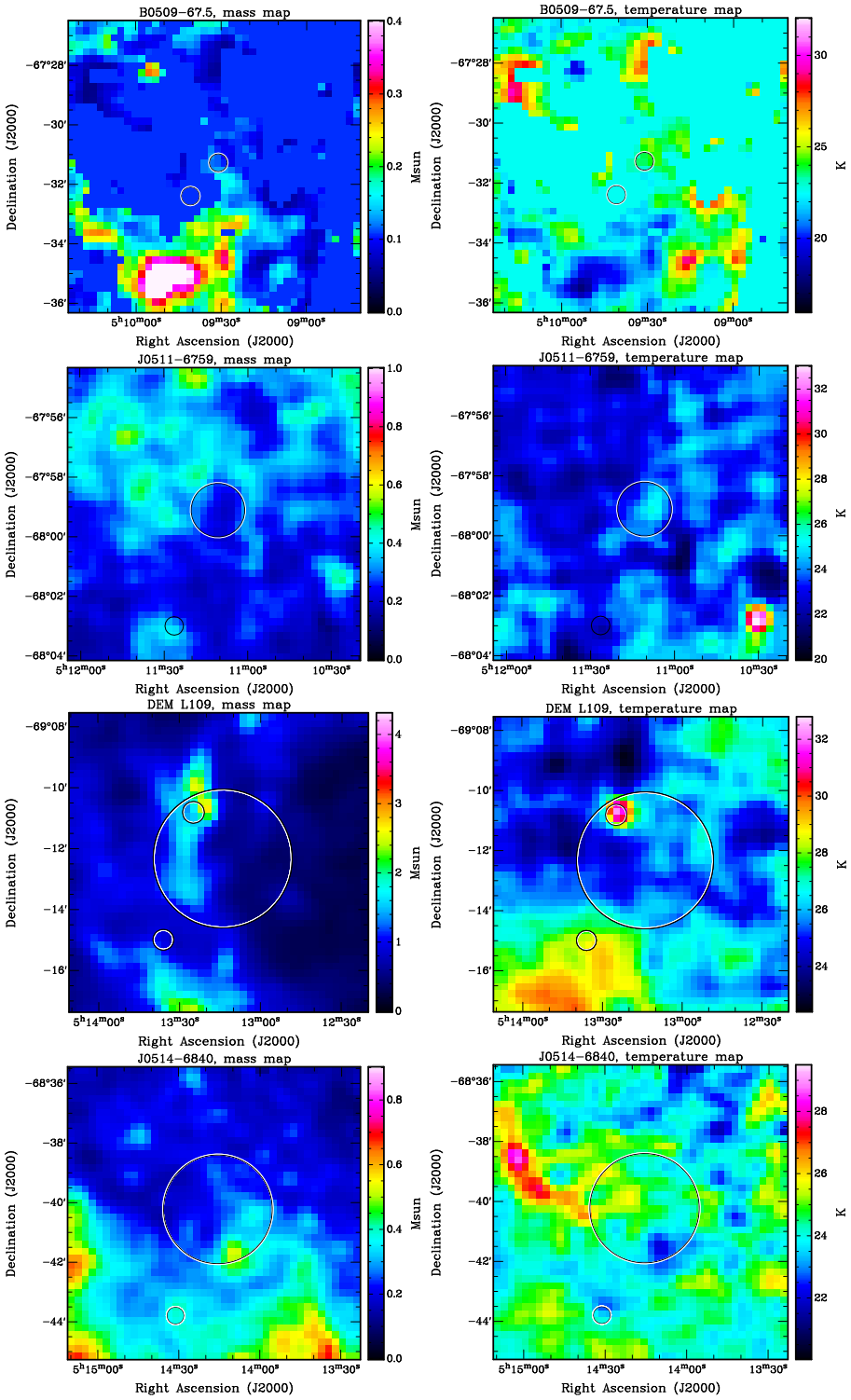

Figure A.5: SNR B 0509−67.5, J 0511−6759, DEM L109 (and the small candidate inside; Bojičić et al. 2007) and J 0514−6840.

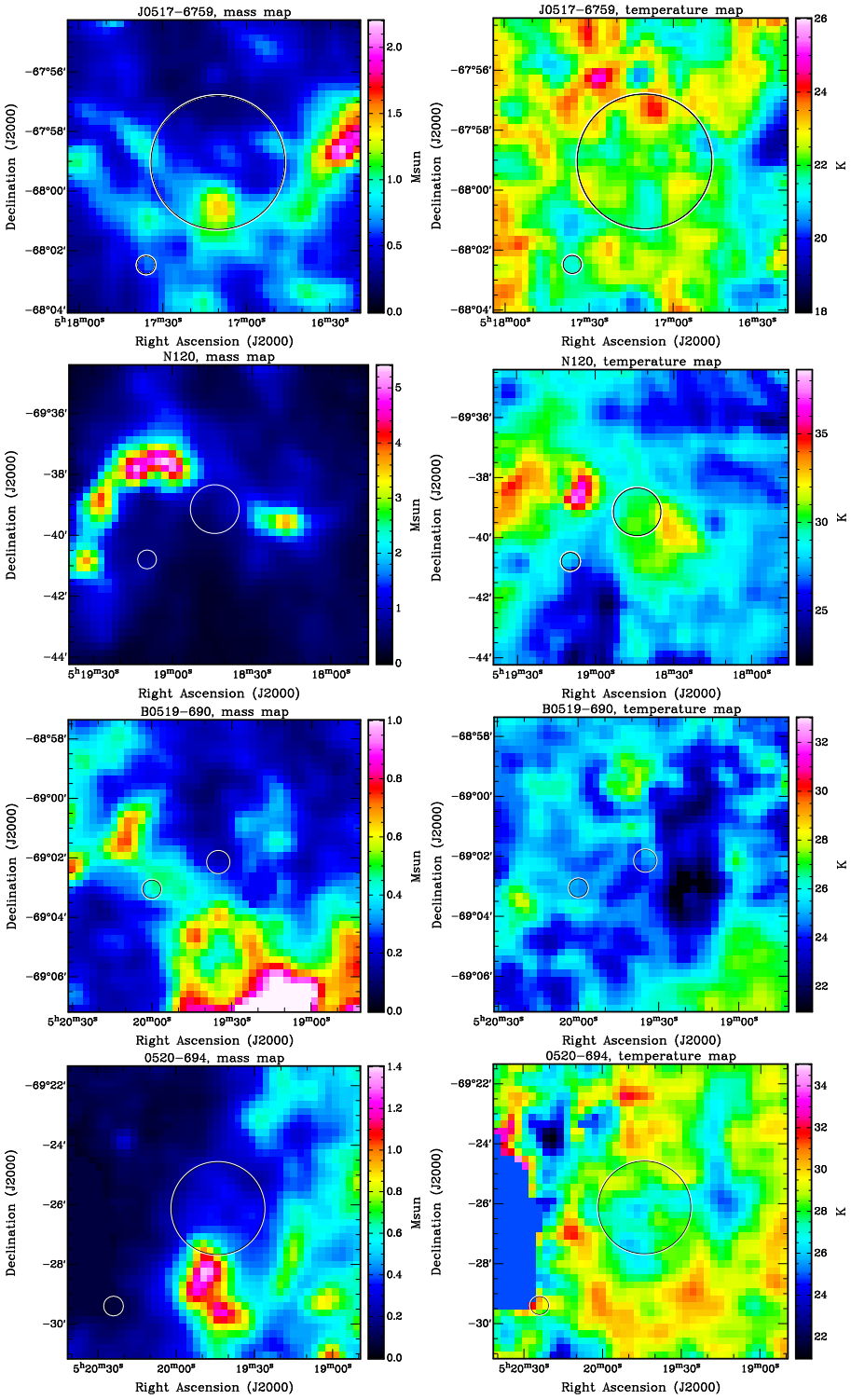

Figure A.6: SNR J 0517−6759, N 120, B 0519−690 and 0520−69.4.

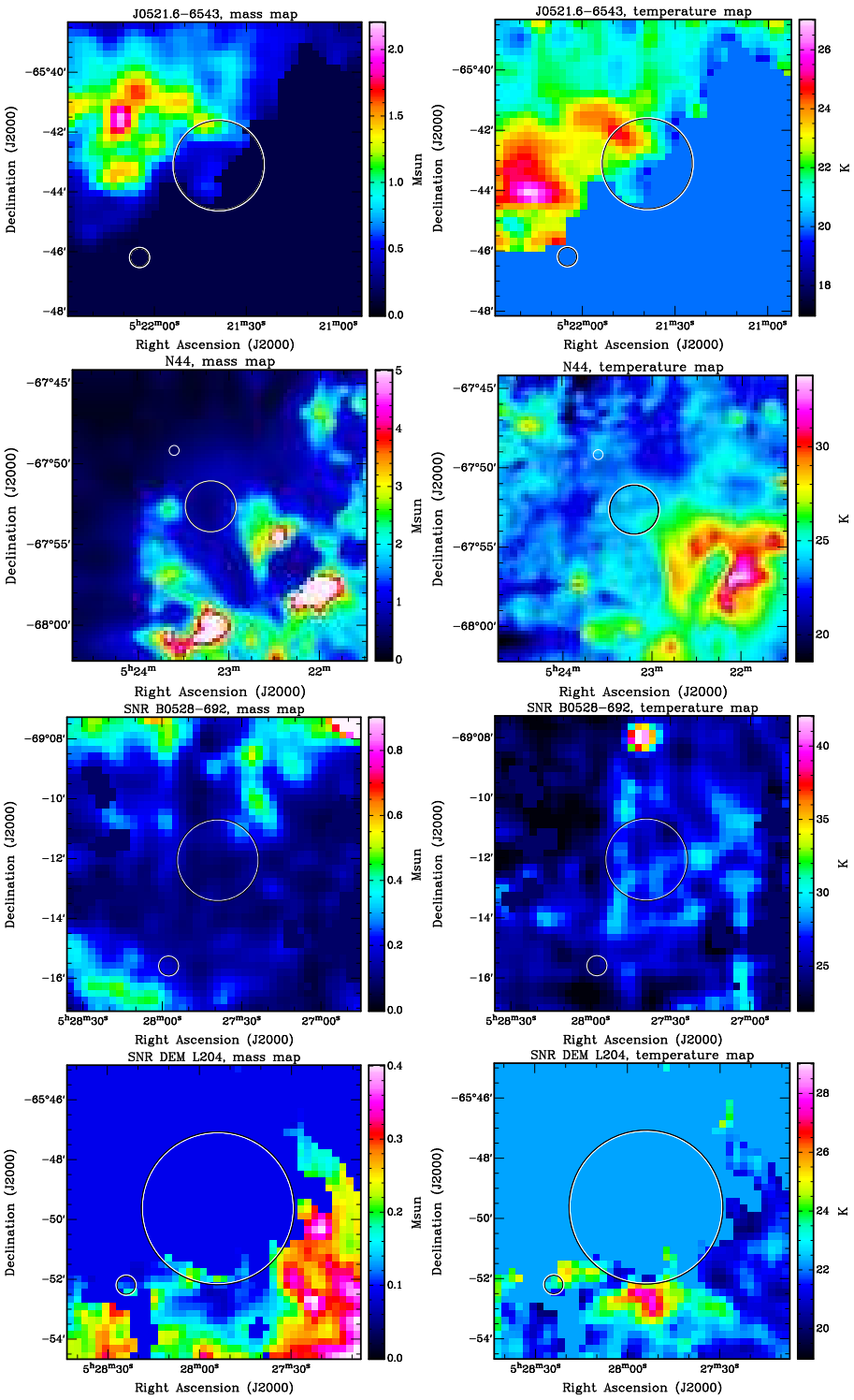

Figure A.7: J 0521.6−6543, N 44, 0528−692 and DEM L204.

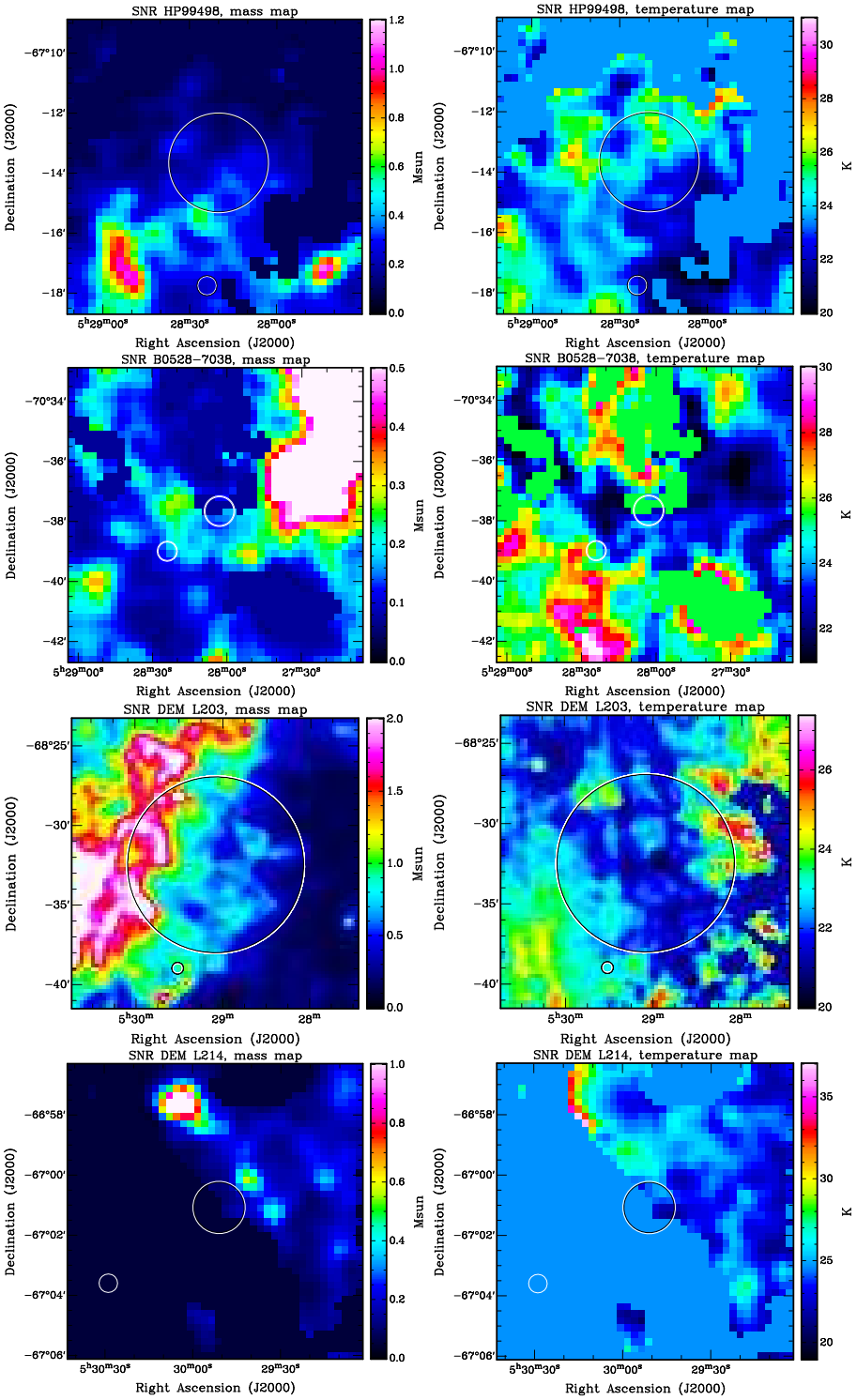

Figure A.8: SNR HP99498, B 0528−7038, DEM L203 and DEM L214 from Badenes, Maoz & Draine (2010).

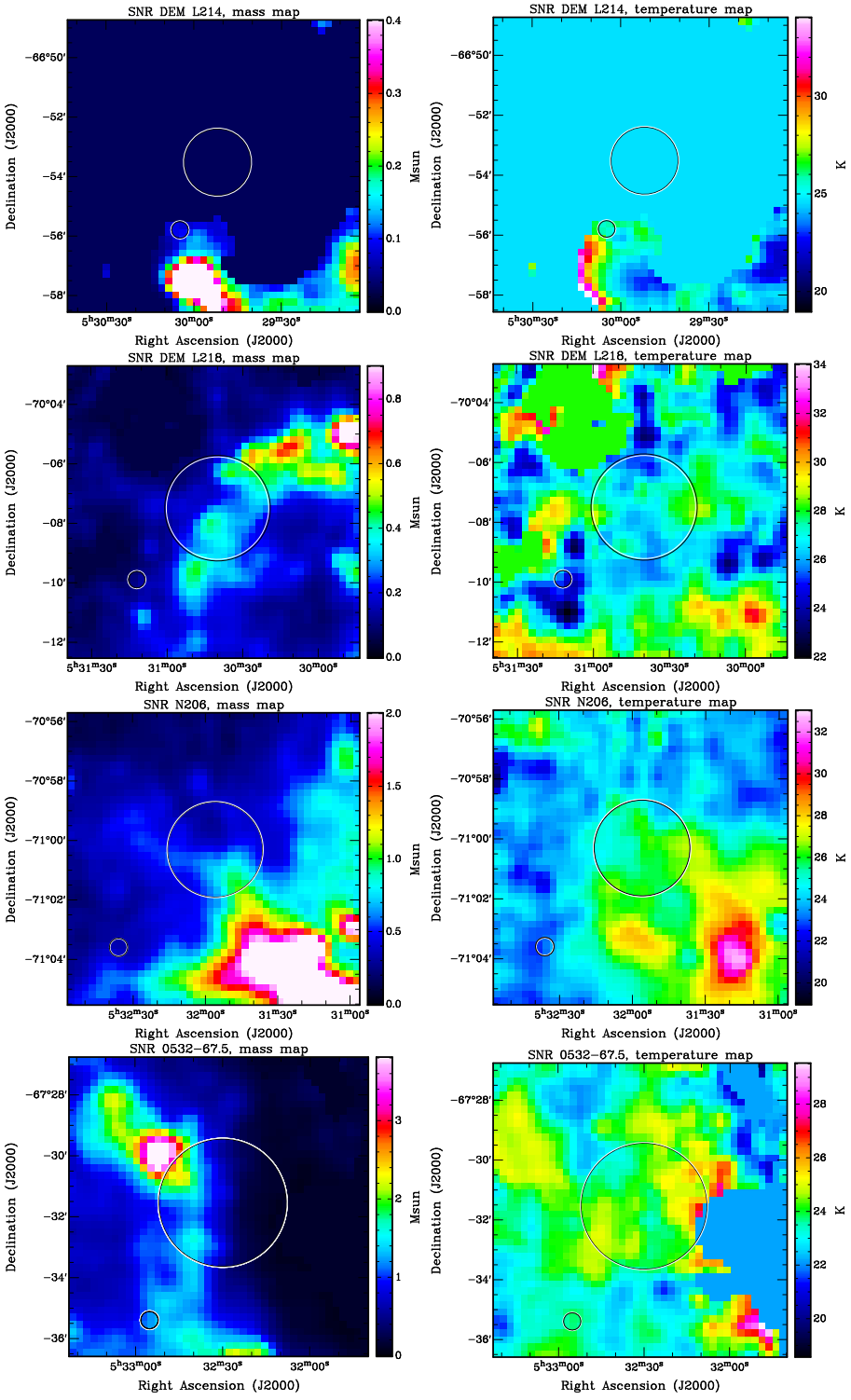

Figure A.9: SNR DEM L214 (Bozzetto et al. 2012a), DEM L218. N 206 and 0532−67.5.

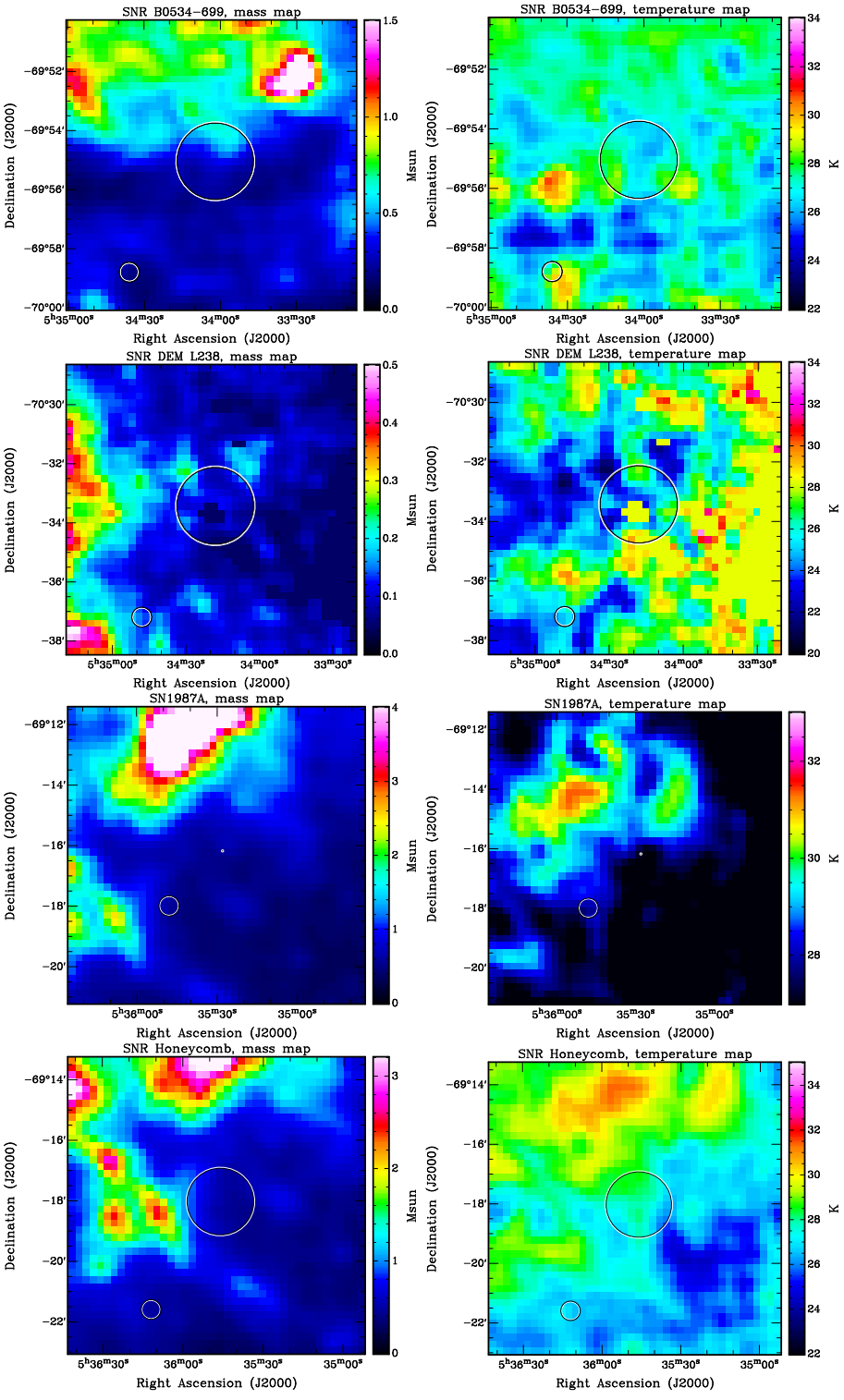

Figure A.10: B 0534−699, DEM L238, SN 1987A and SNR Honeycomb.

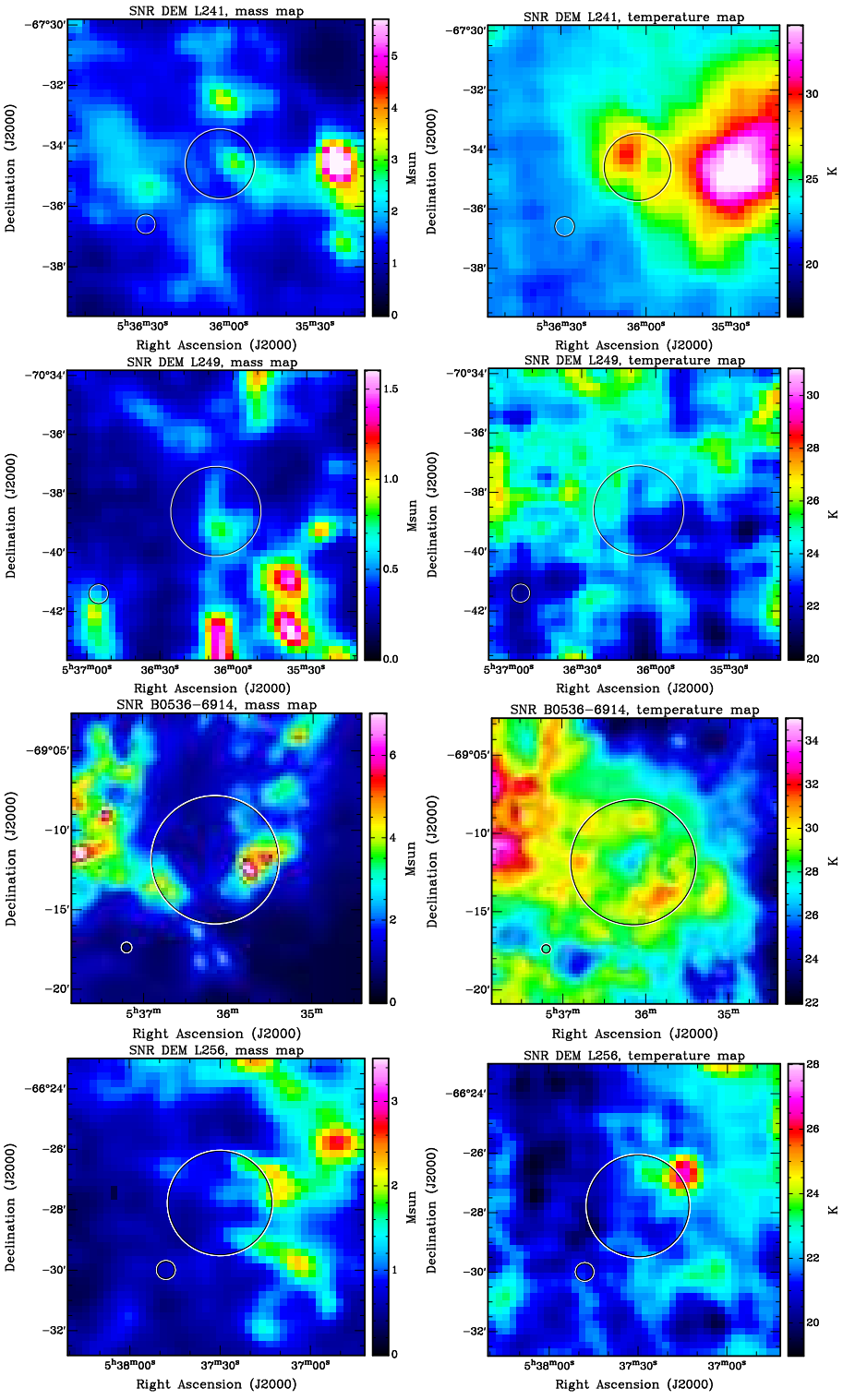

Figure A.11: SNRs DEM L241, SNR DEM L249, B 0536−6914 and DEM L256.

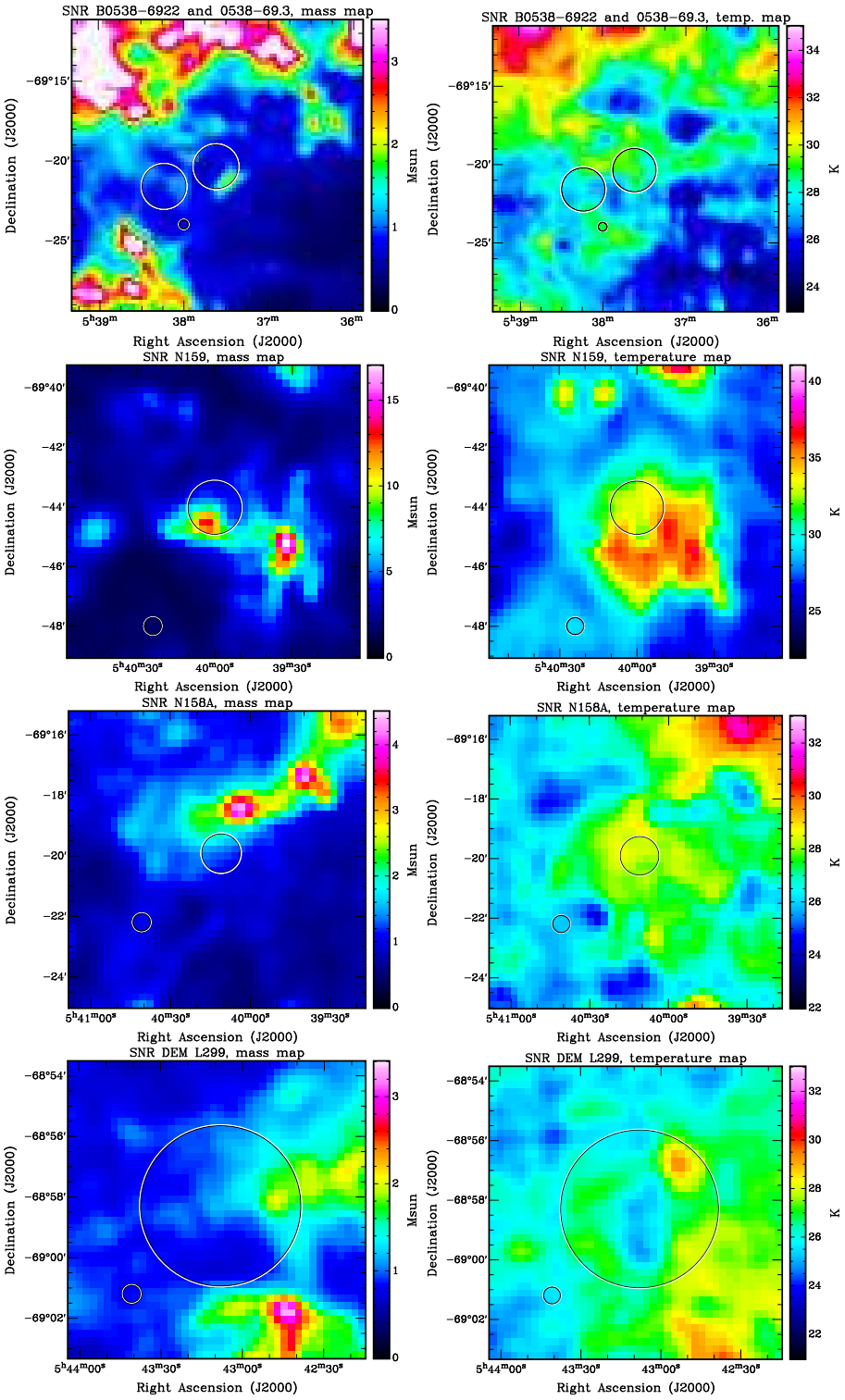

Figure A.12: B 0538−6922 (center) and 0538−693 (the second circle), N 159, N158 A and DEM L299.

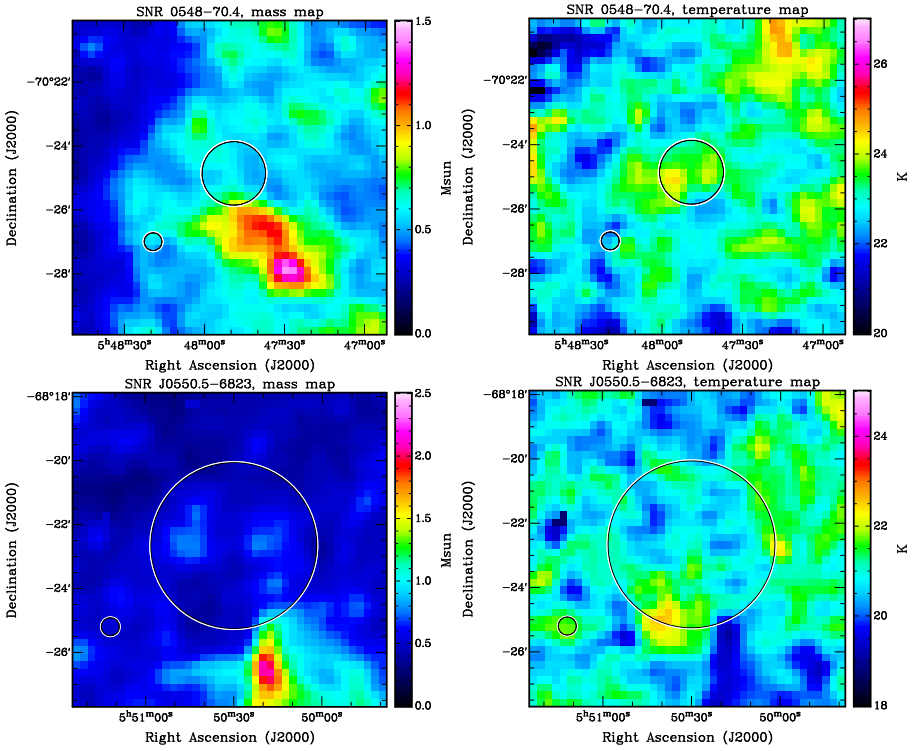

Figure A.13: 0548−70.4, and SNR J 0550.5−6823.

Bibliography

Andersen M. I., Hjorth J., Sollerman J., Møller P., Fynbo J. U. P., 2004, BaltA, 13, 247

Andersen M., Rho J., Reach W., Hewitt J., Bernard J., 2011, ApJ, 742, 7

Andrews J. E., Clayton C., Wesson R., Sugerman B. E. K., Barlow M. J., Clem J., Ercolano B., Fabbri J., Gallagher J. S., Landolt A., Meixner M., Otsuka M., Riebel D., Welch D. L., 2011, AJ, 142, 45

Aniano G., Draine B. T., Gordon K. D., Sandstrom K., 2008, PASP, 123, 1218

Arbutina B., Urošević D., 2005, MNRAS, 360, 76

Arbutina B., 2005, Importance of supernova type for the hydrodynamic and radio evolution of its remnant, MSc thesis, University of Belgrade edition

Arendt R. G., 1989, ApJS, 70, 181A

Arendt R. G., Dwek E., Blair W. P., Ghavamian P., Hwang U., Long K. S., Petre R., Rho J., Winkler P. F., 2010, ApJ, 725, 597

Arnett W., Bahcall J., Kirschner R., Woosley S., 1989, ARA&A, 27, 629

Badenes C., Harris J., Zaritsky D., Prieto J. L., 2009, ApJ, 700, 727

Badenes C., Maoz D., Draine B. T., 2010, MNRAS, 407, 1301

Bamba A., Yamazaki R., Hiraga J. S., 2005, A new age and distance indicator of SNRs with nonthermal X-ray filaments, Proceedings IAU Symposium, 230 edition

Bandiera R., Petruk O., 2010, A&A, 509, A34

Bandiera R., Neri R., Cesaroni R., 2002, A&A, 386, 1044

Barkat Z., Wheeler J. C., 1988, ApJ, 332, 247

Barlow M. J., Krause O., Swinyard B. M., Sibthorpe B., Besel M.-A., Wesson R., Ivison R. J., Dunne L., Gear W. K., Gomez H. L., Hargrave P. C., Henning T., Leeks S., Lim T. L., Olofsson G., Polehampton E. T., 2010, A&A, 518, L138

Bell A. R., 1978, MNRAS, 182, 147

Belloche A., Garrod R. T., Muller H. S. P., Menten K. M., 2014, Science, 345, 6204

Bendo G. J., Baes M., Bianchi S., Boquien M., Boselli A., Cooray A., Cortese L., De Looze I., di Serego Alighieri S., Fritz J., Gentile G., Hughes T. M., Lu N., Pappalardo S., Smith M. W. L., Spinoglio L., Viaene S., Vlahakis C., 2015, MNRAS, 448, 135

Berezhko E. G., Ksenofontov L. T., 2006, ApJ, 650, L59

Berkhuijsen E. M., 1986, A&A, 166, 257

Bernard J.-P., Reach W. T., Paradis D., Meixner M., Paladini R., Kawamura A., Onishi T., Vijh U., Gordon K., Indebetouw R., Hora J. L., Whitney B., Blum R., Meade M., Babler B., Churchwell E. B., Engelbracht C. W., For B.-Q., Misselt K., Leitherer C., Cohen M., Boulanger F., Frogel J. A., Fukui Y., Gallagher J., Gorjian V., Harris J., Kelly D., Latter W. B., Madden S., Markwick-Kemper C., Mizuno A., Mizuno N., Mould J., Nota A., Oey M. S., Olsen K., Panagia N., Perez-Gonzalez P., Shibai H., Sato S., Smith L., Staveley-Smith L., Tielens A. G. G. M., Ueta T., Van Dyk S., Volk K., Werner M., Zaritsky D., 2008, AJ, 136, 919

Bianchi S., Schneider R., 2007, MNRAS, 378, 973

Biermann P. L., Chini R., Haslam C. G. T., et al., 1992, A&A, 255, L5

Blair W. P., Ghavamian P., Sankrit R., Danforth C. W., 2006, AJ, 165, 480

Blair W. P., Ghavamian P., Long K. S., Williams B. J., Borkowski K. J., Reynolds S. P., Sankrit R., 2007, ApJ, 662, 998

Bojičić I. S., Filipović M. D., Parker Q. A., Payne J. L., Jones P. A., Reid W., Kawamura A., Fukui Y., 2007, MNRAS, 378, 1237

Borkowski K. J., Dwek E., 1995, ApJ, 454, 254

Borkowski K. J., Williams B. J., Reynolds S. P., Blair W. P., Ghavamian P., Sankrit R., Hendrick S. P., Long K. S., Raymond J. C., Smith R. C., Points S., Winkler P. F., 2006, ApJ, 642, L141

Borkowski K. J., Hendrick S. P., Reynolds S. P., 2006, ApJ, 652, 1259

Bot C., Ysard N., Paradis D., et al., 2010, A&A, 523, A20

Botticella M. T., Pastorello A., Smartt S. J., et al., 2009, MNRAS, 398, 1041

Bouchet P., Danziger I. J., Lucy L. B., 1991, AJ, 102, 1135

Bouchet P., Dwek E., Danziger J., Arendt R., De Buizer I., Park S., Suntzeff N., Kirshner R., P. C., 2006, ApJ, 650, 212

Bozzetto L. M., Filipović M. D., Crawford E. J., Haberl F., Sasaki M., Urošević D., Pietsch W., Payne J. L., De Horta A. Y., Stupar M., Tothill N. F. H., Dickel J., Chu Y. H., Gruendl R., 2012a, MNRAS, 420, 2588

Bozzetto L. M., Filipović M. D., Crawford E. J., Payne J. L., De Horta A. Y., Stupar M., 2012b, RMxAC, 48, 41

Briggs D. S., 1995, BAAS, 27, 1444

Burrows D. N., Michael E., Hwang U., et al., 2000, ApJ, 543, L149

Casoli F., Lequeux J., David F., 1998, Astronomie Spatiale Infrarouge, Aujourd'hui Et Demain Infrared Space Astronomy, Today and Tomorrow, Springer

Castor J., McCray R., Weaver R., 1975, ApJ, 200, L107

Caulet A., Williams R. M., 2012, ApJ, 761, 107

Chen Y., Wang Q. D., Gotthelf E. V., Jiang B., Chu Y.-H., Gruendl R., 2006, ApJ, 651, 237

Cherchneff I., Dwek I., 2009, ApJ, 703, 642

Cherchneff I., Dwek E., 2010, ApJ, 713, 1

Cherchneff I., Lilly S., 2008, ApJ, 683, L123

Cherchneff I., Sarangi A., 2011, IAU Symp. 280, The Molecular Universe, Cambridge Univ. Press, 228 edition

Chu Y., Kennicutt R. C., 1988, AJ, 96, 1874

Chu Y., Low M.-M. M., Garcia-Segura G., Wakker B., Kennicutt R. C., 1993, ApJ, 414, 213

Chu Y.-H., Dickel J. R., Staveley-Smith L., Osterberg J., Smith C. R., 1995, AJ, 109, 1729

Clayton D. D., 2011, New Astronomy Reviews, 55, 155

Compiègne M., Verstraete L., Jones A., Bernard J.-P., Boulanger F., Flagey N., Le Bourlot J., Paradis D., Ysard N., 2011, A&A, 525, A103

De Horta A. Y., Filipović M. D., Bozzetto L. M., Maggi P., Haberl F., Crawford E. J., Sasaki M., Urošević D., Pietsch W., Gruendl R., Dickel J., Tothill N. F. H., Chu Y.-H., Payne J. L., Collier J. D., 2012, A&A, 540, A25

Desai K. M., Chu Y. H., Gruendl R. A., Dluger W., Katz M., Wong T., Rosie, Chen C. H., Looney L. W., Hughes A., Muller E., Ott J., Pineda J. L., 2010, AJ, 140, 584

Dickel J. R., Milne D. K., 1995, AJ, 109, 200

Draine B. T., Fraisse A. A., 2009, ApJ, 696, 1

Draine B. T., Lee H. M., 1984, ApJ, 285, 89

Draine B. T., Li A., 2001, ApJ, 551, 807

Draine B. T., 1981, ApJ, 245, 880

Dunne L., Eales S. A., 2001, MNRAS, 327, 697

Dunne L., Eales S., Ivison R., Morgan H., Edmunds M., 2003, Nature, 285, 424

Dunne L., Maddox S. J., Ivison R. J., Rudnick L., DeLaney T. A., Matthews B. C., Crowe, C. M. Gomez H. L., Eales S. A., Dye S., 2009, MNRAS, 394, 1307

Dunne L., Gomez H. L., da Cunha E., Charlot S., Dye S., Eales S., Maddox S. J., Rowlands K., Smith D. J. B., Auld R., Baes M., Boneld D. G., Bourne N., Buttiglione S., Cava A., Clements D. L., Coppin K. E. K., Cooray A., Dariush A., de Zotti G., Driver S., Fritz J., Geach J., Hopwood R., Ibar E., Ivison R. J., Jarvis M. J., Kelvin L., Pascale E., Pohlen M., Popescu C., Rigby E. E., Robotham A., Rodighiero G., Sansom A. E., Serjeant S., Temi P., Thompson M., Tuffs R., van der Werf P., Vlahakis C., 2011, MNRAS, 417, 1510

Duric N., Seaquist E., 1986, ApJ, 301, 308

Dwek E., Cherchneff I., 2011, ApJ, 727, 63

Dwek E., 1998, ApJ, 501, 643

Dwek E., Petre R., Szymkowiak A., Rice W. L., 1987, ApJ, 320, L27

Dwek E., Arendt R. G., Bouchet P., Burrows D. N., Challis P., Danziger I. J., De Buizer J. M., Gehrz R. D., Park S., Polomski E. F., Slavin J. D., 2010, ApJ, 722, 425

Dwek E., Galliano F., Jones A. P., 2007, ApJ, 662, 927

Edwards Z. I., Pagnotta A., Schaefer B. E., 2012, ApJL, 747, L19

Elmhamdi A., Danziger I. J., Chugai N., et al., 2003, MNRAS, 338, 939

Elvis M., Marengo M., Karovska M., 2002, ApJ, 567, L107

Fabbri J., Otsuka M., Barlow M. J., Gallagher J. S., Wesson R., Sugerman B. E. K., Clayton G. C., Meixner M., Andrews J. E., Welch D. L., Ercolano B., 2011, MNRAS, 418, 1285

Filipović M. D., Haynes R. F., White G. L., Jones P. A., Klein U., Wielebinski R., 1995, A&AS, 111, 311

Filipović M. D., Haynes R. F., White G. L., Jones P. A., 1998a, A&AS, 130, 421

Filipović M. D., Pietsch W., Haynes R. F., White G. L., Jones P. A., Wielebinski R., Klein U., Dennerl K., Kahabka P., Lazendic J. S., 1998b, AASS, 127, 119

Filipović M. D., Payne J. L., Reid W., Danforth C., Staveley-Smith L., Jones P. A., White G. L., 2005, MNRAS, 364, 217

Filipović M. D., Haberl F., Winkler P. F., Pietsch W., Payne J. L., Crawford E. J., De Horta A., Stootman F. H., Reaser B. E., 2008, A&A, 485, 63

Finkelstein S. L., Morse J. A., Green J. C., Linsky J. L., Shull J. M., Snow T. P., Stocke J. T., Brownsberger K. R., Ebbets D. C., Wilkinson E., Heap S. R., Leitherer C., Savage B. D., Siegmund O. H., Stern A., 2006, ApJ, 641, 919

Forest T., Spenny D. L., Johnson W., 1988, PASP, 100, 683

Fox O., Skrutskie M. F., Chevalier R. A., Kanneganti S., Park C., Wilson J., Nelson M., Amirhadji J., Crump D., Hoeft A., Provence S., Sargeant B., Sop J., Tea M., Thomas S., Woolard K., 2009, ApJ, 691, 650

Franceschini A., 2000, High-Redshift Galaxies: The Far-Infrared and Sub-Millimeter View, Proceedings of the XI CANARY ISLANDS WINTER SCHOOL OF ASTROPHYSICS on Galaxies at High Redshift, I. Perez-Fournon, M. Balcells, F. Moreno-Insertis and F. Sanchez, Cambridge University Press edition

Fryer C. L., 2004, Stellar Collapse, Astrophysics and Space Science Library, 1 edition

Gaensler B. M., Hendrick S. P., Reynolds S. P., Borkowski K. J., 2003, ApJ, 594, L111

Gall C., 2010, Genesis and evolution of dust in early Universe, PhD thesis, Copenhagen University edition

Gall C., Hjorth J., Watson D., Dwek E., Maund J. R., Fox O., Leloudas G., Malesani D., Day-Jones A. C., 2014, Nature, 511, 326

Gall C., Hjorth J., Andersen A. C., 2011, Astron Astrophys Rev, 19, 43

Gomez H. L., Dunne L., Eales S. A., Edmunds M. G., 2006, MNRAS, 372, 1133

Gomez H. L., Vlahakis C., Stretch C. M., Dunne L., Eales S. A., Beelen A., Gomez E. L., Edmunds M. G., 2010, MNRAS, 401, L48

Gomez H. L., Clark C. J. R., Nozawa T., Krause O., Gomez E. L., Matsuura M., Barlow M. J., Besel M.-A., Dunne L., Gear W. K., Hargrave P., Henning T., Ivison R. J., Sibthorpe B., Swinyard B. M., R. Wesson R., 2012a, MNRAS, 420, 3557

Gomez H. L., Krause O., Barlow M. J., Swinyard B. M., Owen P. J., Clark C. J. R., Matsuura M., Gomez E. L., Rho J., Besel M. A., Bouwman J., Gear W. K., Henning T., Ivison R. J., Polehampton E. T., Sibthorpe B., 2012b, ApJ, 760, 96

Gonçalves D. P., 2013, Dust and gas in different Galactic environments, PhD Thesis, University of Toronto edition

Gordon K. D., Engelbracht C. W., Stansberry J., Wachter S., Frayer D. T., Rieke G., Noriega-Crespo A., Latter W. B., Young E., Neugebauer G., Balog Z., Dole H., Egami E., Hines D., Kelly D., Marleau F., Misselt K., Morrison J., Perez-Gonzalez P., Rho J., Wheaton W. A., 2007, PASP, 119, 1019G

Gordon K. D., Meixner M., Meade M. R., Whitney B., Engelbracht C., Bot C., Boyer M. L., Lawton B., Sewillo M., Babler B., Bernard J.-P., Bracker S., Block M.,

Blum R., Bolatto A., Bonanos A., Harris J., Hora11 J. L., Indebetouw R., Misselt K., Reach W., Shiao B., Tielens X., Carlson L., Churchwell E., Clayton G. C., Chen C.-H. R., Cohen M., Fukui Y., Gorjian V., Hony S., Israel F. P., Kawamura A., Kemper F., Leroy A., Li A., Madden S., Marble A. R., McDonald I., Mizuno A., Mizuno N., Muller E., Oliveira J. M., Olsen K., Onishi T., Paladini R., Paradis D., Points S., Robitaille T., Rubin D., Sandstrom K., Sato S., Shibai H., Simon J. D., Smith L. J., Srinivasan S., Vijh U., Van Dyk S., van Loon J. T., Zaritsky D., 2011, ApJ, 142, 102

Gordon K. D., Roman-Duval J., Bot C., Meixner M., Babler B., Bernard J.-P., Bolatto A., Boyer M. L., Clayton G. C., Engelbracht C., Fukui Y., Galametz M., Galliano F., Hony S., Hughes A., Indebetouw R., Israel F. P., Jameson K., Kawamura A., Lebouteiller V., Li A., Madden S. C., Matsuura M., Misselt K., Montiel E., Okumura K., Onishi T., Panuzzo P., Paradis D., Rubio M., Sandstrom K., Sauvage M., Seale J., Sewilo M., Tchernyshyov K., Skibba R., 2014, ApJ, 797, 85

Graham J. R., Evans A., Albinson J. S., Bode M. F., Meikle W. P. S., 1987, ApJ, 319, 126

Graham J. R., Wright G. S., Longmore A. J., 1987, ApJ, 313, 847

Graham J. R., Wright G. S., Longmore A. J., 1989, ESASP, 290, 169G

Gudipati M. S., Yang R., 2012, ApJL, 756, L24

Guillet V., Jones A. P., Pineau des Forêts G., 2009, A&A, 497, 145

Gull S. F., Daniell G. J., 1978, Nature, 272, 686

Gull S. F., 1973, MNRAS, 161, 47

Han J. L., Gao X. Y., Sun X. H., Reich W., Xiao L., Reich P., Xu J. W., Shi W. B., Furst E., Wielebinski R., 2013, Proceedings IAU Symposium, No. 296

Hayato A., Bamba A., Tamagawa T., Kawabata K., 2006, ApJ, 653, 280

Heinke C. O., Ho W. C. G., 2010, ApJL, 719, L167

Helmboldt J. F., Kassim N. E., 2009, AJ, 138, 838

Hendrick S. P., Borkowski K. J., Reynolds S. P., 2003, ApJ, 593, 370

Hjorth J., Sollerman J., Møller P., Fynbo J. P. U., Woosley S. E., 2003, Nature, 423, 847

Högbom J. A., 1974, A&AS, 15, 417

Hughes J. P., Hayashi I., Helfand D., Hwang U., Itoh M., Kirshner R., Koyama K., Markert T., Tsunemi H., Woo J., 1995, ApJ, 444, L81

Hughes J. P., Hayashi I., Koyama K., 1998, ApJ, 505, 732

Indebetouw R., Matsuura M., Dwek E., Zanardo G., Barlow M. J., Baes M., Bouchet P., Burrows D. N., Chevalier R., Clayton G. C., Fransson C., Gaensler B., Kirshner R., Lakićević M., Long K. S., Lundqvist P., Marti-Vidal I., Marcaide J., McCray R., Meixner M., Ng C.-Y., Park S., Sonneborn G., Staveley-Smith L., Vlahakis C., van Loon J., 2014, ApJL, 782, L2

Inserra C., Turatto M., Pastorello A., Benetti S., Cappellaro E., Pumo M. L., Zampieri L., Agnoletto I., Bufano F., Botticella M. T., Della Valle M., Elias Rosa N., Iijima T., Spiro S., Valenti S., 2011, MNRAS, 417, 261

James A., Dunne L., Eales S., Edmunds M. G., 2002, MNRAS, 335, 753

Joardar S., Bhattacharyya S., Hhattacharyya A. B., Datta C. R., 2010, Progress In Electromagnetics Research B, 22, 73

Johansson J., Amanullah R., Goobar A., 2013, MNRAS, 431, L43

Jones F. C., Ellison D. C., 1991, Space Sci. Rev., 58, 259

Jones A. P., Tielens A. G. G. M., Hollenbach D. J., McKee C. F., 1994, ApJ, 433, 797

Jones A. P., Tielens A. G. G. M., Hollenbach D. J., 1996, ApJ, 469, 740

Kamenetzky J., McCray R., Indebetouw R., Barlow M. J., Matsuura M., Baes M., Bolatto A., Decin L., Dunne L., Fransson C., Glenn J., Gomez H., Kirshner R., Lakićević M., Marcaide J., Marti-Vidal I., Meixner M., Soderberg A., Sonneborn G., Staveley-Smith L., Swinyard B. M., van Hoof P. A. M., van Loon J. T., Yates J., Zanardo G., 2013, ApJL, 773, L34

Koo B. C., 2014, Supernova Environmental Impacts, Proceedings IAU Symposium, 296

Koo B. C., Moon D. S., Lee H. G., Lee J. J., 2007, ApJ, 657, 308

Koo B. C., Lee H. G., Moon D. S., 2007, PASJ, 59, S455

Kotak R., Meikle P., Pozzo M., van Dyk S. D., Farrah D., Fesen R., Filippenko A. V., Foley R. J., Fransson C., Gerardy C. L., Hoflich P. H., Lundqvist P., Mattila, S. Sollerman J., Wheeler J. C., 2006, ApJ, 651, L117

Kovács A., 2008, Millimeter and Submillimeter Detectors and Instrumentation for Astronomy IV, SPIE, 7020, 45

Kozasa T., Nozawa T., Tominaga N., Umeda H., Maeda K., Nomoto K., 2009, COSMIC DUST - NEAR AND FAR, Dust in Supernovae: Formation and Evolution, ASP Conference Series, 414 edition

Krause O., Birkmann S. M., Usuda T., Hattori T., Goto M., Rieke G. H., Misselt K. A., 2008, Science, 320, 1195

Krishna S., 2005, Dust in the Universe: Similarities and Differences, World Scientific Series in Astronomy and Astrophysics, 1 edition

Lakićević M., van Loon J., Patat F., Staveley-Smith L., Zanardo G., 2011, A&A, 532, L8

Lakićević M., van Loon J., Stanke T., De Breuck C., Patat F., 2012a, A&A, 541, L1

Lakićević M., Zanardo G., van Loon J., Staveley-Smith L., Potter, T. amd Ng C.-Y., M. G. B., 2012b, A&A, 541, L2

Lakićević M., van Loon J. T., Meixner M., Gordon K., Bot C., Roman-Duval J., Babler B., Bolatto A., Engelbracht C., Filipović M., Hony S., Indebetouw R., Misselt K., Montiel E., Okumura K., Panuzzo P., Patat F., Sauvage M., Seale J., Sonneborn G., Temim T., Urošević D., Zanardo G., 2015, ApJ, 799, 50

Larsson J., Fransson C., Ostlin G., Groningsson P., Jerkstrand A., Kozma C., Sollerman J., Challis P., Kirshner R. P., Chevalier R. A., Heng K., McCray R., Suntzeff N. B., Bouchet P., Crotts A., Danziger J., Dwek E., France K., Garnavich P. M., Lawrence S. S., Leibundgut B., Lundqvist P., Panagia N., Pun C. S. J., Smith N., 2011, Nature, 474, 484

Leão M. R. M., Gouveia Dal Pino E., Falceta-Goncalves D., Melioli C., Geraissate F., 2003, Proceedings IAU Symposium, No. 259

Lee H. G., Moon D. S., Koo B. C., Lee J. J., Matthews K., 2009, ApJ, 691, 1042

Lee J. J., Park S., Hughes J. P., Slane P. O., Burrows D. N., 2011, ApJ, 731, L8

Lewis K. T., Burrows D. N., Hughes J. P., Slane P. O., Garmire G. P., Nousek J. A., 2003, AJ, 582, 770

Liu W., Dalgarno A., 1995, ApJ, 454, 472

Liu W., Dalgarno A., Lepp S., 1992, ApJ, 396, L679

Lucy L., Danziger I., Gouiffes C., Bouchet P., 1989, Structure and Dynamics of the Interstellar Medium, Proceedings of IAU Colloq., 120 edition

Lyman J. D., Bersier D., James P. A., 2014, MNRAS, 437, 3848

Maeda K., Nozawa T., Sahu, D. K. Minowa Y., Motohara, K. Ueno, I. Folatelli G., Pyo T.-S., Kitagawa Y., Kawabata K. S., Anupama G. C., Kozasa, T. Moriya T. J., Yamanaka M., Nomoto K., Bersten M., Quimby R., Iye M., 2013, ApJ, 776, 5

Maggi P., Haberl F., Kavanagh P. J., Points S. D., Dickel J., Bozzetto L. M., Sasaki M., Chu Y.-H., Gruendl R. A., Filipović M. D., Pietsch W., 2014, A&A, 561, A76

Manchester R. N., Gaensler B. M., Staveley-Smith L., Kesteven M. J., Tzioumis A. K., 2005, ApJ, 628, L131

Maoz D., Badenes C., 2010, MNRAS, 407, 1314

Markwardt C. B., 2009, ASPC, Astronomical Data Analysis Software and Systems XVIII, 411, 251

Mathewson D. S., Clarke J. N., 1973, ApJ, 180, 725

Mathewson D. S., Ford V. L., Dopita M. A., Tuohy I. R., Long K. S., Helfand D. J., 1983, ApJS, 51, 345

Mathewson D. S., Ford V. L., Dopita M. A., Tuohy I. R., 1984, AJSS, 55, 189

Mathewson D., Ford V., Tuohy I., 1985, AJSS, 58, 197

Matsuura M., Barlow M. J., Zijlstra A. A., Whitelock P. A., Cioni M.-R. L., Groenewegen M. A. T., Volk K., Kemper F., Kodama T., Lagadec E., Meixner M., Sloan G. C., Srinivasan S., 2009, MNRAS, 396, 918

Matsuura M., Dwek E., Meixner M., Otsuka M., Babler B., Barlow M. J., Roman-Duval J., Engelbracht C., Sandstrom. K., Lakićević M., van Loon J. T., Sonneborn G., Clayton G. C., Long K. S., Lundqvist P., Nozawa T., Gordon K. D., Hony S., Panuzzo P., Okumura K., Misselt K. A., Montiel E., Sauvage M., 2011, Science, 333, 1258

Matsuura M., Dwek E., Barlow M. J., Babler B., Baes M., Meixner M., Cernicharo J., Clayton G. C., Dunne L., Fransson C., Fritz J., Gear W., Gomez H. L., Groenewegen M. A. T., Indebetouw R., Ivison R. J., Jerkstrand A., Lebouteiller V., Lim T. L., Lundqvist P., Pearson C. P., Roman-Duval J., Royer P., Staveley-Smith L., Swinyard B. M., van Hoof P. A. M., van Loon J. T., Verstappen J., Wesson R., Zanardo G., Blommaert J. A. D. L., Decin L., Reach W. T., Sonneborn G., Van de Steene G. C., Yates J. A., 2015, ApJ, 800, 50

Mattila S., Lundqvist P., Groningsson P., et al., 2010, ApJ, 717, 1140

Mattsson L., 2011, MNRAS, 414, 781

McWilliam A., 2010, Proceedings of Science, 11th Symposium on Nuclei in the Cosmos

Meixner M., Gordon K. D., Indebetouw R., Hora J. L., et al., 2006, ApJ, 132, 2268

Meixner M., Panuzzo P., Roman-Duval J., Engelbracht C., Babler C., et al., 2013, AJ, 146, 62

Mennella V., Brucato J. R., Colangeli L., et al., 1998, ApJ, 496, 1058

Micelotta E. R., Brandl B. R., Israel F. P., 2009, A&A, 500, 807

Michalowski M. J., Murphy E. J., Hjorth J., Watson D., Gall C., Dunlop J. S., 2011, ASPCS, 446, 387

Mignani R. P., De Luca A., Hummel W., Zajczyk A., Rudak B., Kanbach G., Słowikowska A., 2012, A&A, 544, A100

Morgan H. L., Edmunds M. G., 2003, MNRAS, 343, 427

Morgan H. L., Dunne L., Eales S. A., Ivison R. J., Edmunds M. G., 2003, ApJ, 597, L33

Moseley S. H., Dwek E., Silverberg R. F., et al., 1989, ApJ, 347, 1119

Nath B. B., Laskar T., Shull J. M., 2008, ApJ, 682, 1055

Ng C.-Y., Gaensler B. M., Staveley-Smith L., et al., 2008, ApJ, 684, 481

Ng. C.-Y., Potter T. M., Staveley-Smith L., Tingay S., Gaensler B. M., Phillips C., Tzioumis A. K., Zanardo G., 2011, ApJL, 728, L15

Ng C.-Y., Zanardo G., Potter T. M., Staveley-Smith L., Gaensler B. M., Manchester R. N., Tzioumis A. K., 2013, ApJ, 777, 131

Nikolić S., van de Ven G., Heng K., Kupko D., Husemann B., Raymond J., Hughes J., Falcón-Barroso J., 2013, Science, 340, 45

Nozawa T., Kozasa T., 2006, ApJ, 648, 435

Nozawa T., Kozasa T., Umeda H., Meada K., Nomoto K., 2003, ApJ, 598, 785

Nozawa T., Kozasa T., Habe A., Dwek E., Umeda H., Tominaga N., Maeda K., Nomoto K., 2007, ApJ, 666, 955

Nozawa T., Kozasa T., Tominaga N., et al., 2010, ApJ, 713, 356

Osterbrock D. E., 1974, Astrophysics of Gaseous Nebulae, Freeman and Company, p79, 1 edition

Otsuka M., van Loon J., Long K., Meixner M., Matsuura M., Reach W., Roman-Duval J., Gordon K., Sauvage M., Hony S., Misselt K., Engelbracht C., Panuzzo P., Okumura K., Woods P., Kemper F., Sloan G., 2010, A&A, 518, L139

Owen R. A., Filipović M. D., Ballet J., Haberl F., Crawford E. J., Payne J. L., Sturm R., Pietsch W., Mereghetti S., Ehle M., Tiengo A., Coe M. J., Hatzidimitriou D., Buckley D. A. H., 2011, A&A, 530, A132

Paradis D., Bernard J.-P., Meny C., Gromov V., 2011, A&A, 534, A118

Park S., Burrows D. N., Garmire G. P., et al., 2002, ApJ, 567, 314

Park S., Burrows D. N., Garmire G. P., Nousek J. A., 2003a, ApJ, 586, 210

Park S., Hughes J. P., Burrows D. N., Slane P. O., Nousek J. A., Garmire G. P., 2003b, ApJ, 598, L95

Park S., Hughes J. P., Slane P. O., Burrows D. N., Warren J. S., Garmire G. P., Nousek J. A., 2003c, ApJ, 592, L41

Park S., Hughes J. P., Slane P. O., Mori K., Burrows D. N., 2010, ApJ, 710, 948

Park S., Hughes J. P., Slane P. O., Burrows D. N., Lee J. J., Mori K., 2012, ApJ, 748, 117

Patat F., Chandra P., Chevalier R., Justham S., Podsiadlowski P., Wolf C., Gal-Yam A., Pasquini L., Crawford I. A., Mazzali P. A., Pauldrach A. W. A., Nomoto K., Benetti S., Cappellaro E., Elias-Rosa N., Hillebrandt W., Leonard D. C., Pastorello A., Renzini A., Sabbadin F., Simon J. D., Turatto M., 2007, Science, 317, 924

Payne J. L., Filipović M. D., Reid W., Jones P. A., Staveley-Smith J., White G. L., 2004, MNRAS, 355, 44

Payne J. L., White G. L., Filipović M. D., Pannuti T. G., 2007, MNRAS, 376, 1793

Payne J. L., White G. L., Filipović M. D., 2008, MNRAS, 383, 1175

Peeples M. S., Werk J. K., Tumlinson J., Oppenheimer B. D., Prochaska J. X., Katz N., Weinberg D. H., 2014, ApJ, 786, 54

Pei Y. C., 1992, ApJ, 395, 130

Peters C. L., Lopez L. A., Ramirez-Ruiz E., Stassun K. G., Figueroa-Feliciano E., 2013, ApJL, 771, L38

Pilbratt G. L., Riedinger J. R., Passvogel T., Crone G., Doyle D., Gageur U., Heras A. M., Jewell C., Metcalfe L., Ott S., Schmidt M., 2010, A&A, 518, L1

Pipino A., Fan X. L., Matteucci F., Calura F., Silva L., Granato G., Maiolino R., 2011, A&A, 525, A61

Potter T. M., Staveley-Smith L., Ng C.-Y., et al., 2009, ApJ, 705, 261

Racusin J. L., Park S., Zhekov S., et al., 2009, ApJ, 703, 1752

Reach W. T., Rho J., Tappe A., Pannuti T. G., 2006, AJ, 131, 1479

Rest A., Suntzeff N. B., Olsen K., Prieto J. L., Chris, Smith R. C., Welch D. L., Becker A., Bergmann M., Clocchiatti A., Cook K., Garg A., Huber M., Miknaitis G., Minniti D., Nikolaev S., Stubbs C., 2005, Nature, 438, 1132

Rest A., Matheson T., Blondin S., Bergmann M., Welch D. L., Suntzeff N. B., Smith R. C., Olsen K., Prieto J. L., Garg A., Challis P., Stubbs C., Hicken M., Modjaz M., Wood-Vasey W. M., Zenteno A., Damke G., Newman A., Huber M., Cook K. H., Nikolaev S., Becker A. C., Miceli A., Covarrubias R., Morelli L., Pignata G., Clocchiatti A., Minniti D., Foley R. J., 2008, ApJ, 680, 1137

Reyes-Iturbide J., Rosado M., Velazquez P. F., 2008, AJ, 136, 2011

Reynolds J. E., Jauncey D. L., Staveley-Smith L., et al., 1995, A&A, 304, 116

Reynolds S. P., Borkowski K. J., Green D. A., Hwang U., Harrus I., Petre R., 2008, ApJL, 680, L41

Rho J., Kozasa T., Reach W. T., Smith J. D., Rudnick L., DeLaney T., Ennis J. A., Gomez H., Tappe A., 2008, ApJ, 673, 271

Rho J., Reach W. T., Tappe A., Rudnick L., Kozasa T., Hwang U., Andersen M., Gomez H., DeLaney T., Dunne L., Slavin J., 2009, Cosmic Dust - Near and Far, ed. Th. Henning, E. Grun, & J. Steinacker, ASPC, 414, 22

Rho J., Andersen M., Tappe A., Reach W., Bernard J., Hewitt J., 2011, PAHs and the Universe, EAS Publication Series, 46, 169

Rho J., Onaka T., Cami J., Reach W., 2012, ApJL, 747, L6

Rosado M., Laval A., Coarer E. L., 1993, A&A, 272, 541

Rowlands K., Gomez H. L., Dunne L., Aragon-Salamanca A., Dye S., Maddox S., da Cunha E., van der Werf P., 2014, MNRAS, 441, 1040

Saken J. M., Fesen R. A., Shull J. M., 1992, AJSS, 81, 715

Sakon I., Onaka T., Wada T., Ohyama Y., Kaneda H., Ishihara D., Tanabe T., Minezaki T., Yoshii Y., Tominaga N., Nomoto K., Nozawa T., Kozasa T., Tanaka M., Suzuki T., Umeda H., Ohyabu S., Usui F., Matsuhara H., Nakagawa T., Murakami H., 2009, AJ, 692, 546

Sandstrom K. M., Bolatto A. D., Stanimirović S., van Loon J. T., Smith J. D. T., 2009, ApJ, 696, 2138

Sankrit R., Williams B. J., Borkowski K. J., Gaetz T. J., Raymond J. C., Blair W. P., Ghavamian P., Long K. S., Reynolds S. P., 2010, ApJ, 712, 1092

Sarangi A., Cherchneff I., 2013, ApJ, 776, 107

Schaefer B. E., Pagnotta A., 2012, Nature, 481, 164

Seok J. Y., Koo B.-C., Onaka T., Ita Y., H.-G. L., Lee J.-J., Moon D.-S., Sakon I., Kaneda H., Lee H. M., Lee M. G., Kim S. E., 2008, PASJ, 60, S453

Seok J., Koo B.-C., Onaka T., 2013, ApJ, 779, 134

Seward F. D., Williams R. M., Chu Y. H., Dickel J. R., Smith R. C., Points S. D., 2006, ApJ, 640, 327

Seward F. D., Williams R. M., Chu Y. H., Gruendl R. A., Dickel J. R., 2010, AJ, 140, 177

Seward F. D., Charles P. A., Foster D. L., Dickel J. R., Romero P. S., Edwards Z. I., Perry M., Williams R. M., 2012, ApJ, 759, 123

Shklovsky I. S., 1960, AZh, 37(2), 256

Silvia D. W., Smith B. D., Shull J. M., 2010, ApJ, 715, 1575

Siringo G., Kreysa E., Kovács A., et al., 2009, A&A, 497, 945

Siringo G., Kreysa E., De Breuck C., et al., 2010, Msngr, 139, 20

Smartt S. J., Eldridge J. J., Crockett R. M., Maund J. R., 2009, MNRAS, 395, 1409

Smith R. C., Kirshner R. P., Blair W. P., Winkler P. F., 1991, ApJ, 375, 652

Smith N., Mauerhan J. C., Kasliwal M. M., Burgasser A. J., 2013, MNRAS, 434, 2721

Someya K., Bamba A., Ishida M., 2010, PASJ, 62, 1301

Spyromilio J., Leibundgut B., 1996, MNRAS, 283, L89

Spyromilio J., Meikle W. P. S., Learner R. C. M., Allen D. A., 1988, Nature, 334, 327

Stanimirović S., Bolatto A. D., Sandstrom K., Leroy A. K., Simon J. D., Gaensler B. M., Shah R. Y., Jackson J. M., 2005, ApJ, 632, L103

Suntzeff N. B., Bouchet P., 1990, AJ, 99, 650

Sutton E. C., 2012, Observational Astronomy: Techniques and Instrumentation, Cambridge University Press

Szalai T., Vinkó J., 2013, A&A, 549, A79

Tappe A., Rho J., Reach W. T., 2006, ApJ, 653, 267

Temim T., Slane P., Arendt R., Dwek E., 2012, ApJ, 745, 46

Temim T., Sonneborn G., Dwek E., Arendt R. G., Gehrz R. D., Slane P., Roellig T. L., 2013, ApJ, 753, 72

Temim T., Dwek E., Tchernyshyov K., Boyer M. L., Meixner M., Gall C., Roman-Duval J., 2015, ApJ, 799, 158

Tinsley B. M., 1980, A&A, 89, 246

Todini P., Ferrara A., 2001, MNRAS, 325, 726

Uchida H., 2009, X-ray Study of the Cygnus Loop Supernova Remnant, PhD Thesis, Department of Earth and Space Science, Graduate School of Science, Osaka University, Japan edition

Uchida H., Tsunemi H., Katsuda S., Kimura M., Kosugi H., Takahashi H., 2009, ApJ, 705, 1152

Urošević D., 2000, $\Sigma - D$ relation as an indicator of the origin of radio loops, PhD thesis, Belgrade University edition

Urošević D., 2002, SAJ, 165, 27

Urošević D., 2003, Ap&SS, 283, 75

Urošević D., Pannuti T. G., Duric N., Theodorou A., 2005, A&A, 435, 437

Van den Bergh S., 2004, The Galaxies of the Local Group, Cambridge Astrophysics Series, 35 edition

Van der Heyden K. J., Bleeker J. A. M., Kaastra J. S., 2004, A&A, 421, 1031

van Loon J. T., 2010, ASPC, 425, 279

van Loon J. T., 2013, EAS, 60, 307V

van Loon J., Oliveira J. M., Gordon K. D., et al., 2010, AJ, 139, 68

van Paradijs J., Bleeker J. A. M., 1999, X-Ray Spectroscopy in Astrophysics, Springer, Lecture notes in physics edition

Ventura P., Dell Agli F., Schneider R., Criscienzo M. D., Rossi C., La Franca F., Gallerani S., Valiante R., 2014, MNRAS, 439, 977

Vink J., 2012, AAR, 20, 49

Vinyaikin E. N., 2014, Astronomicheskii Zhurnal, 91, 720

Vogt F., Dopita M. A., 2011, Ap&SS, 331, 521

Vukotić B., 2006, On the magnetic field evolution in supernova remnants, MSc thesis, University of Belgrade edition

Vukotić B., Urošević D., Filipović M. D., Payne J. L., 2009, A&A, 503, 855

Walker A. R., 2012, Ap&SS, 341, 43

Wallstrom S. H. J., Biscaro C., Salgado F., Black J. H., Cherchneff I., Muller S., Berne O., Rho J., Tielens A. G. G. M., 2013, A&A, 558, L2

Wang Q. D., Gotthelf E. V., Chu Y. H., Dickel J. R., 2001, ApJ, 559, 275

Washimi H., Shibata S., Mori M., 1996, PASJ, 48, 23

Wesson R., Barlow M. J., Ercolano B., Andrews J. E., Clayton G. C., Fabbri J., Gallagher J. S., Meixner M., Sugerman B. E. K., L. W. D., Stock D. J., 2010, MNRAS, 403, 474

Wesson R., Barlow M. J., Matsuura M., Ercolano B., 2015, MNRAS, 446, 2089

Whitelock P. A., Catchpole R. M., Menzies J. W., et al., 1989, MNRAS, 240, 7

Wickramasinghe N. C., Wickramasinghe A. N., 1993, Ap&SS, 200, 145

Williams R. M., Chu Y.-H., 2005, ApJ, 635, 1077

Williams B., 2010, PhD thesis, North Carolina State University, arxiv:1005.1296

Williams R. M., Chu Y.-H., Gruendl R., 2006, AJ, 137, 1877

Williams R. M., Chu Y.-H., Dickel J. R., Smith R. C., Milne D. K., Winkler P. F., 1999, ApJ, 514, 798

Williams R. M., Chu Y.-H., Dickel J. R., Gruendl R. A., 2004, ApJ, 613, 948

Williams R. M., Chu Y.-H., Dickel J. R., Gruendl R. A., 2005, ApJ, 628, 704

Williams B. J., Borkowski K. J., Reynolds S. P., Blair W. P., Ghavamian P., Hendrick S. P., Long K. S., Points S., Raymond J. C., Sankrit R., Smith R. C., Winkler P. F., 2006, ApJ, 652, L33

Williams B. J., Borkowski K. J., Reynolds S. P., Raymond J. C., Long K. S., Morse J., Blair W. P., Ghavamian P., Sankrit R., Hendrick S. P., Smith R. C., Points S., Winkler P. F., 2008, ApJ, 687, 1054

Williams B., Borkowski K., S.P. R., Ghavamian P., Blair W., Long K., Sankrit R., 2012, ApJ, 755, 3

Williams S. C., Bode M. F., Darnley M. J., Evans A., Zubko V., Shafter A. W., 2013, ApJL, 777, L32

Wilson W. E., Ferris R. H., Axtens P., et al., 2011, MNRAS, 416, 832

Wooden D. H., Rank D. M., Bregman J. D., et al., 1993, ApJS, 88, 477

Woosley S. E., Heger A., Weaver T. A., 2002, MNRAS, 74, 1015

Xu J., Crotts A. P. S., 1999, ApJ, 511, 262

Yoshida T., Okita S., Umeda H., 2014, AIP Conf. Proc., 1594, 284

Zanardo G., Staveley-Smith L., Ball L., et al., 2010, ApJ, 710, 1515

Zanardo G., Staveley-Smith L., Ng C.-Y., Gaensler B. M., Potter T. M., Manchester R. N., Tzioumis A. K., 2013, ApJ, 767, 98

Zanardo G., Staveley-Smith L., Indebetouw R., Chevalier R. A., Matsuura M., Gaensler B. M., Barlow M. J., Fransson C., Baes M., Kamenetzky J. R., Lakićević M., Lundqvist P., Marcaide J. M., Marti-Vidal I., Meixner, M. Ng. C.-Y., Park S., Sonneborn G., Spyromilio J., van Loon J. T., 2014, ApJ, 796, 82

Zhekov S. A., McCray R., Dewey D., et al., 2010a, ApJ, 692, 1190

Zhekov S. A., Park S., McCray R., Racusin J. L., Burrows D. N., 2010b, MNRAS, 407, 1157

Zhukovska S., 2014, A&A, 563, A76